STUDY OF THE EFFECT OF ENRGETIC ION IRRADIATIONS ON $YBa_2Cu_3O_{7-x}$ SUPERCONDUCTOR

THESIS

Submitted in partial fulfilment
of the requirements for the degree of

DOCTOR OF PHILOSOPHY

By

SANJIT K. DAS

Under the supervision of
DR. P. K. ASHWINI KUMAR

BIRLA INSTITUTE OF TECHNOLOGY & SCIENCE
PILANI (RAJASTHAN) INDIA
1995

BIRLA INSTITUTE OF TECHNOLOGY & SCIENCE
PILANI RAJASTHAN

CERTIFICATE

This is to certify that the thesis entitled **STUDY OF THE EFFECT OF ENERGETIC ION IRRADIATIONS ON $YBa_2Cu_3O_{7-x}$ SUPERCONDUCTOR** and submitted by **Sanjit K. Das** ID. No. **91PZYF002** for award of Ph. D. Degree of the institute, embodies original work done by him under my supervision.

Signature in full of the Supervisor P.K. Ashwini Kumar

Name in capital block letters DR. P.K. ASHWINI KUMAR.

Date: 23 JUNE, 1995

Designation SCIENTIST – EI

ABSTRACT

After the initial exhuberence of the discovery of high Tc superconductivity, people concentrated on its application, mainly, in wire, tape and thin film form and using them in different environments. It had been of immense interest to see the behavior of these new materials in presence of some external perturbations, like, energetic particle radiation on them. It is from this motivation the irradiation studies on high Tc superconductors started and in present day the subject of these irradiation studies are not only limited to study the behavior of superconductors in radiative environment, but these studies are now being used to tailor the properties of the superconductors to use them in specific applications.

Present study, described in the thesis includes irradiation of high Tc $YBa_2Cu_3O_{7-\delta}$ superconducting system with energetic projectiles of energy $\sim$ 100 MeV. Since at this energy, the electronic energy loss due to inelastic collision, of a projectile with the electrons of the target atoms, shares major contribution to the total energy loss value, the projectiles are chosen with gradually increasing electronic energy loss value. The chosen projectiles according to this scheme are 75 MeV ^{16}O (S_e = 0.17 KeV/Å), 75 MeV ^{58}Ni (S_e = 1.45 KeV/Å) and 100 MeV ^{127}I (S_e = 2.09 KeV/Å). The first interest was to see that whether this YBCO system is sensitive to this electronic energy loss in terms of its change in properties. The next objective was that if this system is really responsive to these irradiations then whether it is possible to use these effects of irradiation in properties in making devices. The results of different experiments performed in the present study, demonstrated that the YBCO system responds differently to the irradiation of the projectiles with different S_e value, and it seems apparent that there is a threshold value of S_e above which the system changes its superconducting property significantly. Also it has been observed that after a certain dose value for a particular projectile, the normal state electrical conductivity of the system undergoes a drastic change. This fact can be used in future for ion beam lithography.

In the second part of the thesis deposition of buffer layers on Si, for subsequent growth of high Tc YBCO film on it, is undertaken to explore the feasibility of the integration between superconductor and semiconductor and also to explore the possibility of large area deposition of high Tc thin film on Si. Two different oxide materials, $SrTiO_3$ and MgO, has been deposited on Si by e-beam deposition method and subsequently characterised by different surface sensitive techniques like, AES, XPS, HIBS, ERDA and also by XRD. The integrity of the buffer layers are checked by heat treating them upto 900°C and subsequently characterising them. The results have confirmed that the deposited buffer layers are well integrated even after the heat treatment to such a high temperature and also there is no Si interdiffusion inside the film from the substrate. But the stoichiometry of the $SrTiO_3$ film and the crystalline orientation of both the films are still to be improved.

dedicated to.....

MY PARENTS

&

MY WIFE

ACKNOWLEDGEMENTS

Acknowledgements are not the full expression of one's gratitude towards the persons whose help is acknowledged, since language is an inadequate medium to express one's sentiments. But it is the only way one can record one's grateful indebtness to one's guide and benefactors. It is my first and foremost duty to express here my indebtness, with deep sense of gratitude, to my guide Dr. P. K. Ashwini Kumar, Scientist, National Physical Laboratory, New Delhi, under whose supervision this work has been done. His knowledge, experience, constant encouragement and support has helped me tremendously in completing this work.

I specially thank Dr. D. Kanjilal, Scientist, Nuclear Science Center, New Delhi, whose help and cooperation extended beyond mere academic help and suggestions. Without him, this work could never get the present form.

I would like to sincerely thank Dr. S. K. Sarkar (Scientist), Mr. M. L. Sharma (Scientist), Mr. Omprakash (J.T.A.) and Miss. Nimrat K. Duggal (J.R.F.) of our group, who have all been helpful in terms of scientific discussions and encouragement to complete this thesis.

I wish to convey my special thanks to Dr. S. M. Shivprasad, Scientist, National Physical Laboratory whose suggestions and cooperation has helped me a lot writing this thesis. I also thank Dr. B. R. Chakravarty (Scientist) and Dr. R. Bhattacharya (Scientist) who allowed me to use the computers in their respective departments. Thanks to Dr. A. K. Gupta (Scientist), for providing me high Tc thin films. I am grateful to Prof. J. K. N. Sharma, former Dy. Director of N.P.L., for permitting me to have my samples analysed by AES and XPS in his group.

I am grateful to Dr. D. K. Avasthi, Mr. L. Senapati, Mr. D. Kabiraj and all

other scientists and workers at Nuclear Science Center for extending their helping hands in performing the experiments at N.S.C. smoothly and also for giving their valuable suggestions time to time. I wish to acknowledge deeply Dr. G. S. Virdi's help in the low energy irradiation experiments in CEERI, Pilani.

I wish to express my indebtness to Prof. E. S. R. Gopal, the Director of N.P.L., for encouraging us to do such contemporary work in this field. I am also grateful to Prof. G. K. Mehta, the Director of N.S.C., for permitting me to work at his center and also for spending his valuable time in giving me suggestions.

I deeply acknowledge the financial assistance sponsored by Director N.P.L. fellowship and C.S.I.R. for my Junior and Senior research fellowships.

I wish to sincerely thank my friend Dr. Subrata Bose and Mr. D. Sarangi, who have given their lot of time during compilation of this thesis. I also would like to thank Mr. T. Mondal and Mr. A. Basu for providing me help in computer work. I specially thank my friend Dr. Santanu Bera (Ex. research scholar in Surface Physics Group), for helping me in AES and XPS analysis of my samples. I am thankful to all of my other friends at N.P.L., specially, Prabir, Sandip, Rupa and Suchita, who gave their valuable suggestions to understand and complete the work. Their association gave me enough recreation and pleasure in my daily life. I also wish to thank Indranil, Samit, Gopal and Susanta, whose company made my stay at N.S.C. charmful. I would like to thank Lalu, Asim, Amrit, Debu for their cooperation and help. I can not forget the contribution of Snehansu and Malay and my all other friends at Malda and Calcutta, who have been always encouraging me in this work and providing me support in other aspects of life.

I gratefully acknowledge the unbound love and encouragement from my parents, without whom I can not even enter the arena of higher education. I always felt their blessings and encouragement during each step of this work. I would like to sincerely thank my wife Shrabani, who apart from other materialistic supports has given me the much needed emotional support with the depth of her mind.

Her constant inspiration had been the source of great boost during the tough days of writing and compiling the thesis. I deeply acknowledge the limitless love and constant inspiration I have got from all the members of my family at Howrah. I wish to thank my brothers Sanjoy, Nirmalya, Bhuto and Raju, my sister in law Sheuli and my aunt without whose support, encouragement and love this work would not have been a success. I specially thank my four sweet nieces Munni, Munmun, Bachchu and Tultul, who have inspired me a lot with their love. I deeply acknowledge the help, cooperation and love from my sister, brother in law and my nephew and niece Aditya and Subhra at Sarojini Nagar. At last, but not the least, I convey my thanks to all of my other relatives for their love and good wishes to complete this work.

Sanjit K. Das

(SANJIT K. DAS)

Date : 23.6.95

National Physical Laboratory,

New Delhi, India.

LIST OF ABBREVIATIONS

HTSC	High Tc Superconductor
Tc	Superconducting transition temperature
Jc	Critical current
Hc	Critical magnetic field
YBCO	$YBa_2Cu_3O_7$
S_e	Rate of electronic energy loss
S_n	Rate of nuclear energy loss
MeV	Mega electron volt
KeV	Kilo electron volt
XRD	X-ray diffraction
SEM	Scanning elctron microscopy
AES	Auger electron spectroscopy
XPS	X-ray photoelectron spectroscopy
HIBS	High energy backscattering
ERDA	Elastic recoil detection analysis
R vs. T	Resistance versus Temperature

Contents

CHAPTER I

INTRODUCTION

1.1 Introdution

In the early twentieth century when Kammerlingh Onnes[1] was studying the resistance variation of Hg at liquid He temperatures, he observed a dramatic effect, namely, the element lost its resistance almost instantaneously when the temperature was around 4.2 K. Such a phenomenon was not observed in any of the metals studied till then. The most startling feature was the sudden drop in the resistance as shown in fig. 1.1. As this was a totally new effect, hitherto unobserved, he termed it as superconductivity and the temperature at which this occurred, was called the transition temperature. With this initial discovery, there was a burst in the experimental research to look for many more metals which would show the newly discovered phenomena. As a result of this, host of materials in elemental form showed the existence of superconductivity with widely varying transition temperatures (Table-1.1). All this was fine, but the questions arose : What superconductivity is due to ? Is it limited to only being seen at liquid helium temperatures and only in metals ? Can it be a reversible phenomenon ? What will happen to this state if external perturbations are applied or a continuously increasing current is passed through the sample ? To answer all these and many more questions, a systematic study of a large number of metals and alloys ensued, while a vigorous theoretical research started, to look into the mechanism of superconductivity. In so far as the effect of

TABLE 1.1

Elements	Transition Temperature (Tc)
Hg	4.1K
La	6.0K
Pb	7.2K
Nb	9.3K
Sn	3.7K

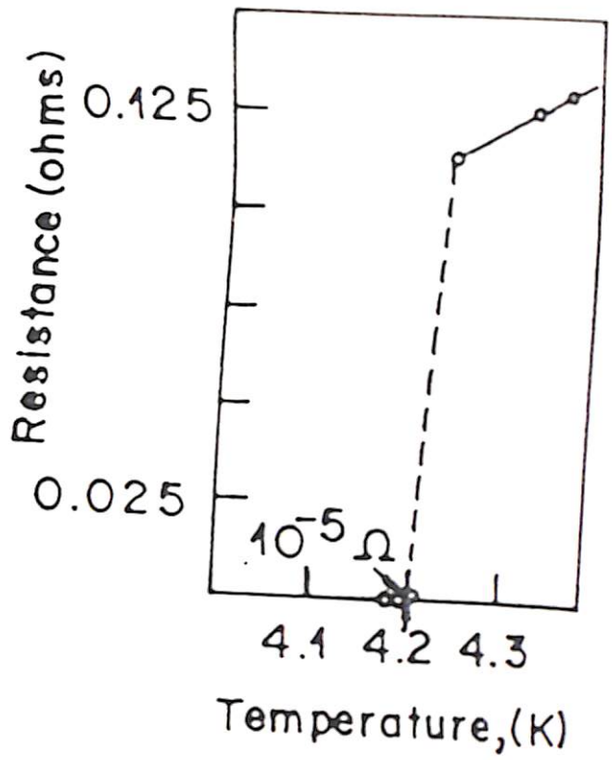

Fig. 1.1. Resistance versus absolute temperature of a specimen of mercury.

external perturbation on a superconductor is concerned, the first experiment was done by Meissner and Oschenfield[2] who observed that an applied field to a superconductor could not penetrate the material. Likewise, if superconductor in a magnetic field was cooled through the Tc, the field got excluded from the solid. These effects were attributed to be due to perfect diamagnetism of the solid (fig.1.2). It was observed that, with the field increasing upto a value called Hc, the critical field; the material retained its superconducting property while a small increment above Hc made the material to become normal. The subsequent decrease in the magnetic field resulted in restoration of the superconducting state. This merely implies: the superconductivity will be destroyed by a magnetic field greater than Hc, which is related thermodynamically to the difference in free energies between normal and superconducting state in zero field. Empirically Hc(T) has been found to be functionally dependent on temperature, by the following relation

$$Hc(T) = Hc(0) \left[1 - (T/Tc)^2 \right] \qquad (1.1)$$

The two above mentioned unique properties of a superconductor were first described by F and H London[3] by invoking the idea of microscopic electric and magnetic fields.

The gist of the London theory is: the phenomenon of

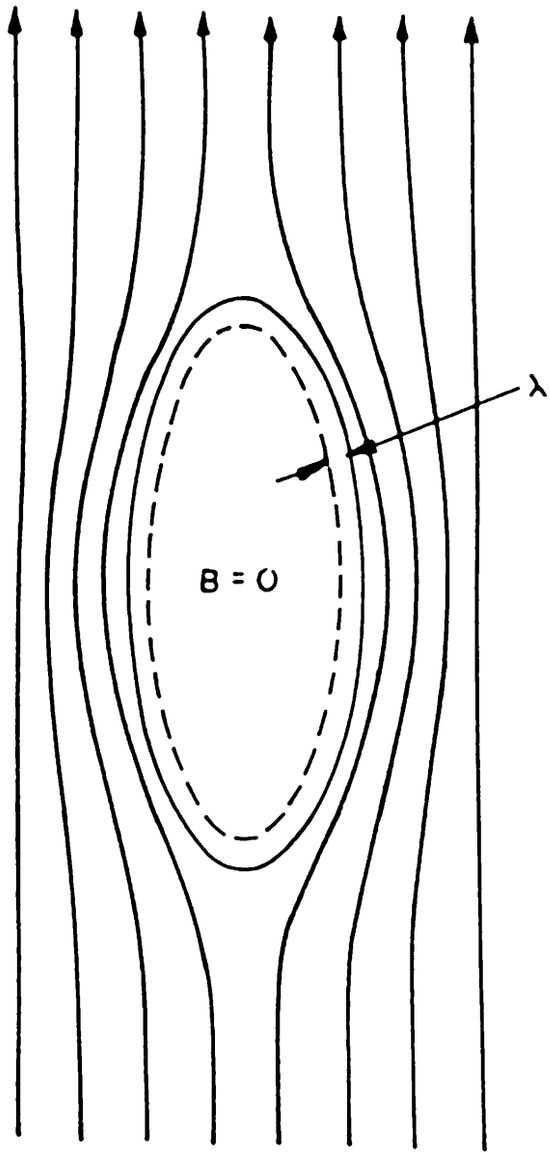

Fig. 1.2. Schematic diagram of exclusion of magnetic flux from interior of massive superconductor. λ is the penetration depth.

superconductivity is due to superconducting electrons described by a rigid wavefunction, leading to a density of electrons n_s, which can have an upper bound of n, the density of conduction electrons. A refinement in the London's formalism was brought about by Pippard [4] who introduced an additional concept of coherence length ξ_0 to have a similar characteristic dimension as wavefunction. The main argument behind this was, that only the electrons within ~kTc of Fermi energy can play a major role in the phenomenon which sets in at Tc. Pippard's theory was a good success in confirming the theoretical values with those of experiments on Tin and Aluminium and thus led pathway for development of the famous BCS theory[5] which introduced the concept of energy gap.

The center point of this epoch making theory is that the two electrons with opposite spins and momenta, can get bound via the virtual phonons. This interaction is characterized by an interaction parameter and is different for different superconductors. These bound electrons have been given the name "Cooper pairs" and are the Bosons with total spin equals to zero. As is characteristics of all Bosons, they also condense together to the zero energy state, the superconducting state. These Cooper pairs have the spatial extent of ξ_0. One of the crucial predictions of the theory is that these pairs possess a minimum energy $E_g = 2\Delta(T)$ needed to break them into two quasi particles. This energy gap parameter $\Delta(T)$ is supposed to increase from zero at Tc to a limiting value such that

$$E_g(0) = 2\Delta(0) = 3.528\ kTc \text{ for } T << Tc \qquad (1.2)$$

There was yet another landmark in the direction of understanding the superconducting state. This was the famous Ginzberg-Landau-Abrikosov-Gorokov theory or GLAG theory[6-8]. In this case, the emphasis is entirely on the superconducting state rather than on the excitations. The superconducting electrons, here, are defined by a pseudo wavefunction $\psi(0)$ defining the local density of Cooper pairs by $n_s = |\psi(x)|^2$. This function $\psi(x)$ is called the order parameter. This theory had a major breakthrough in explaining a peculiar phenomenon of intermediate state in a class of superconductors, the type-I superconductors. In this case, near Hc, the material is broken into laminae of normal and superconducting regions. The GLAG theory successfully explained this phenomenon and fig.1.3 depicts pictorially the situation with the concept of order parameter. Similar to the coherence length in Pippard's theory, GLAG theory introduces another characteristic length $\xi(T)$ which characterizes distance over which $\psi(r)$ can vary.

Far below from Tc ($T << Tc$) $\xi \sim \xi_0$. Now that few characteristic lengths have been generated, a new GL parameter κ was defined which is independent of the temperature. This parameter is related to ξ and λ by $\kappa = \lambda/\xi$. For a pure

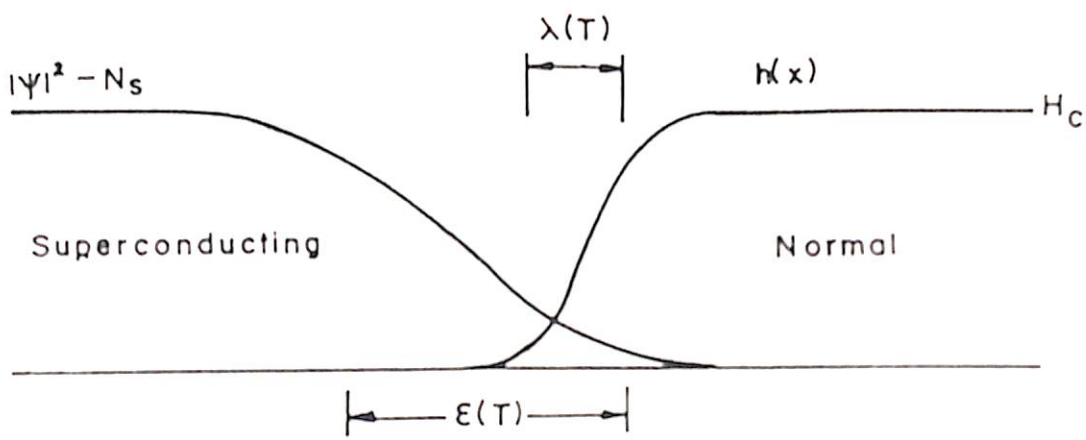

Fig. 1.3. Interference between superconducting and normal domains in the intermediate state.

superconductor $\kappa << 1$ as $\lambda < \xi$. This case relates to materials called Type-I superconductor. Abrikosov revolutionized the theoretical aspects by putting forward another interesting case in which $\xi < \lambda$, i.e., $\kappa > 1$. This was surely possible in some materials and these were called Type-II superconductors. It was shown that the exact break point was at $\kappa = 1/\sqrt{2}$, and for $\kappa > 1/\sqrt{2}$ the field penetrated not to give discrete laminae but to a continuous increase in flux starting at first at a field value Hc_1 and reaching maximum at a second critical field Hc_2 as shown in fig.1.4.

1.2 Materials

Since the discovery of superconductivity in 1911, many metals have been found to show this property in the liq. He temperature range. The temperature at which superconductivity occurs in metallic elements varies anywhere between 0.01 K and 10 K, with niobium showing the highest value. In addition to single elements and compounds, many metallic alloys also exhibit superconductivity. Niobium nitride was found to be superconducting at 16 K as early as in 1941. Then, another alloy Nb_3Ge was prepared which showed the superconducting transition temperature at 23 K. This temperature remained as the highest superconducting transition temperature till 1986, when Bednorz and Muller in their historic achievement, found that $LaCuO_4$ in which La was partly replaced

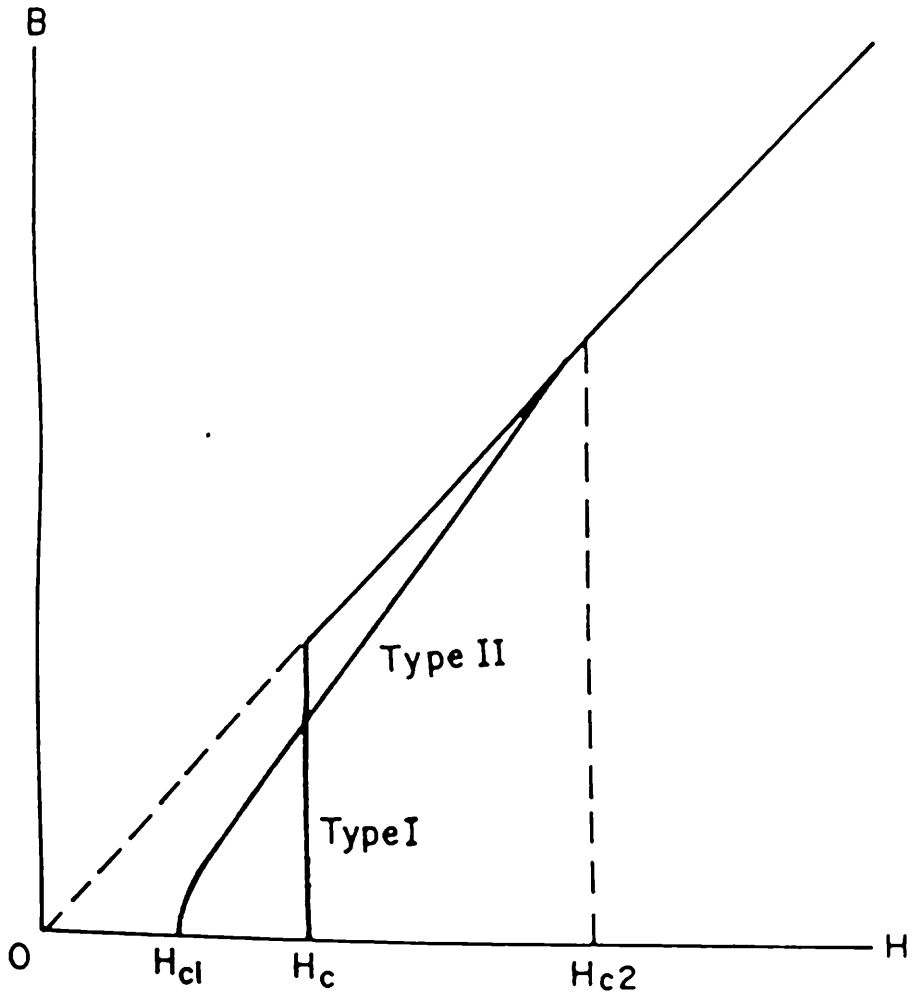

Fig. 1.4. Comparison of flux penetration behavior of type I and type II superconductors with the same thermodynamic critical field.

by barium shows superconductivity around 30 K. Confirmation of superconductivity in well characterized samples of $La_{2-x}Ba_xCuO_4$ and $La_{2-x}Sr_xCuO_4$ (x=0.08-0.25) started an unprecedented search for other oxide materials. In early 1987, several groups reported that compounds of the type $YBa_2Cu_3O_7$ become superconducting above the easily accessible liq. nitrogen temperature (77 K). Superconductivity thus came out of the very cold. Bednorz and Muller were awarded the Nobel Prize in 1988 for their pathfinding achievement leading to the so called high Tc materials. Several families of superconducting oxides have since been synthesized, with transition temperatures in the range of 40 K-130 K as shown in the fig. 1.5. These startling discoveries in Physical Science have probably the greatest potential for technological applications since the invention of the transistor or laser. Superconductors can thus be divided into two major categories. one which require liq. He and the other for which liq. N_2 is sufficient to produce their superconducting properties. Few of the properties of some of these new superconductors are described in Table 1.2.

1.3 Structures

All the oxide high Tc ceramic superconductors have one thing in common: they are structurally flawed members of a crystallographic family, known as perovskites[9]. Therefore, in the

TABLE 1.2

Material	T_c(K)	ξ(nm)	λ(nm)	κ	Eg/KT_c (from measurements
La Sr CuO	~35	~2	~220	~50-100	3-6
Y Ba Cu O	90-95	~2.2	~150	~75	3-5.5
Bi Sr Ca Cu O	105-120	4.2($\parallel$), 0.1($\perp$)			
Tl Ba Ca Cu O	110-125				

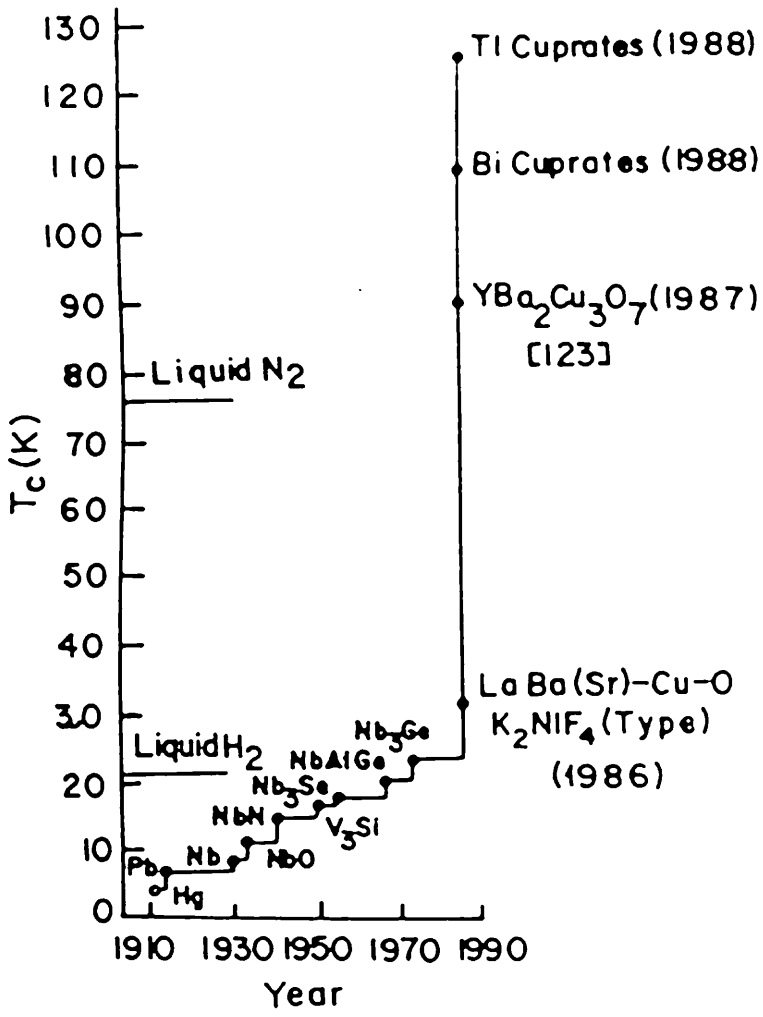

Fig. 1.5. Superconductivity through the years.

begining of this section perovskite structure will be introduced and then its relation with oxide superconductors will be indicated.

Perovskites, which derive their name from the specific mineral known as 'perovskite', are ceramics (solid materials combining metallic elements with non metals, usually oxygen) that have a particular atomic arrangement. They are the earth's most abundant minerals and have long been of interest to geologists for the clues they hold to the planet's history. Whereas a given crystal structure is usually associated with a specific electrical property, perovskites run the gamut from insulators to semiconductors, superionic conductors, metal like conductors and now high temperature superconductors. What accounts for this remarkable range of properties ? The answer is hidden in the fact that slight modifications of ideal perovskite structure often result in new features. There is no one-to-one correlation; a given modification does not automatically produce a particular degree of electrical conductivity. Yet any time the ideal structure is altered, the possibility of new electrical or other properties arises.

In their ideal form, perovskites, which are described by the generalized formula ABX_3, consists of cubes made up of three distinct chemical elements (A, B and X) which are present in a ratio of 1:1:3 (fig. 1.6(a)). The A and B atoms are metallic cations

and the X atoms are non metallic anions. An A cation - the larger of the two kinds of metals - lies at the center of each cube, the B cations occupy all eight corners and the X anions lie at the midpoints of the cube's twelve edges. One example of a perovskite structure is the ferroelectric $BaTiO_3$ (A=Ba, B=Ti and X=O). Above 200°C $BaTiO_3$[10] crystallizes into the ideal form of perovskite structure. Its unit cell consists of a single cube. The Ba in the A position is larger than the titanium in the B positions, and oxygen fill all 12 of the X sites. The lattice constant or length of unit cell is a=b=c=4.0118 Å. The crystal often grows into the shape of a cube or an octahedron, reflecting the symmetry of the atomic structure.

Many perovskites are somewhat distorted because the central cation is too small in relation to the B cations at the centers of the cubes. The disparity causes the X atoms, and sometimes the B's, to move out of position. Crystallographer often visualize such movements by thinking of ideal unit cell not as simple cube but as a cluster of polyhedrons (fig. 1.6(b)). Each B cation, which defines the corner of adjoining cubes, is surrounded by and closely bonded to six anions, one from each of the six cube edges that converge at the corner. The anions define the points of an octahedron. The A cation, formerly viewed as being at the center of a cube, is now considered to be surrounded by eight corner-

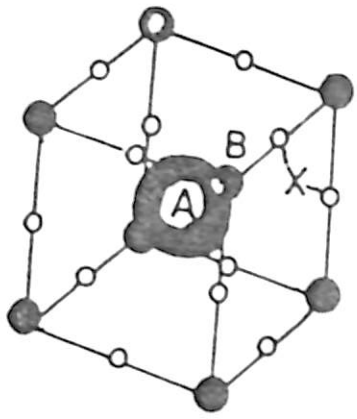

(a)

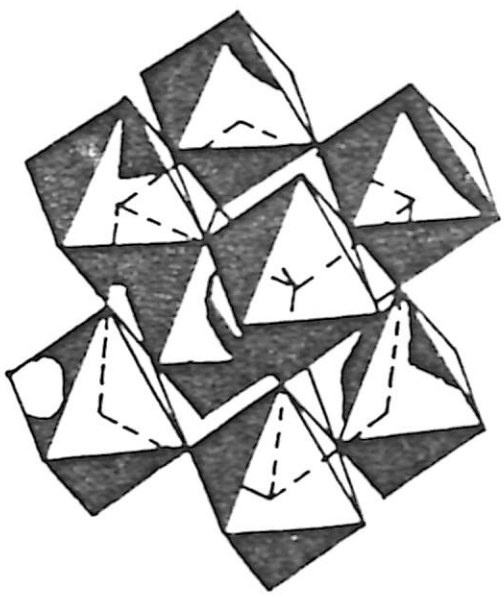

(b)

Fig. 1.6. (a) Basic cubic structural unit of perovskites. (b) Polyhedron model of perovskite structure.

sharing octahedrons, each of which contains a B cation in the center. When A cations are too small in relation to the B cations, the octahedrons, whose axes are aligned in an ideal perovskite, tilt and twist; the framework collapses around the A cations, lowering the symmetry and potentially altering the perovskite's optical, elastic, electrical and other physical properties. In tilted perovskites, B cations may remain at the center of the octahedron, as in the ideal form, or they can be shifted from their position. In the later case, this "off centering" of positive charge cation causes polarization of the material. In some materials direction of polarization can be changed with the influence of external electric field. These materials are known as ferroelectrics. BaTiO3 one such ferroelectric, having perovskite structure, is commercially widely used in electronic devices.

The variation from ideal perovskite structure can be of many more types. The A and B sites can be filled up by two or more type of cations and also by different valence state of same element. In Ca_2CaUO_6, Ca atoms take up the A position, but the B positions are distributed between Ca and U atoms. Similarly, in $(Mg,Fe)SiO_3$, A site is shared between Mg and Fe, with varying proportion. $BaBiO_3$ is a material with perovskite structure, where B sites are filled up by two charged states of Bi, namely, Bi^{3+} and Bi^{5+}. An almost ubiquitious feature of the perovskites is twining, which is

a large scale defect and is likely to be present in any sample which deviates from ideal cubic form. Twining can have dramatic effect - favorable or unfavorable - on electrical properties. Perovskites can be off stoichiometric also. In oxygen deficient calcium ferrite ($CaFeO_{2.5}$), the oxygen deficiency results in layers consisting of iron B cations that are surrounded by four oxygen atoms rather than the usual six. These layers are interspersed with ones featuring normal octahedrons.

All these complexities in perovskite structure can occur together in almost any combination and an infinite number of perovskite variants seems to be possible.

1.3.1 Perovskite type superconducting structure

In their first report on high temperature superconductors Bednorz and Muller referred to their samples as "metallic oxygen deficient ..... perovskite like mixed valent copper compounds"[10]. Subsequent work has confirmed that the new superconductors do indeed have these characteristics.

In oxide superconductors Cu takes up the B sites of the perovskite structure and in most cases retains the CuO_2 layering with two oxygens per copper in the layer. The other cationic sites

(A sites) are replaced by Bi, Ca, La, Sr, Tl and Y for the larger Ba, forming 'layers' containing only one oxygen or none per cation. We can divide these cations in four size groups as follows :

Cation	Ionic radius
Cu^{2+}	0.72 Å
Bi^{5+}	0.74 Å
Y^{3+}	0.94 Å
Tl^{3+}	0.95 Å
Bi^{3+}	0.96 Å
Ca^{2+}	0.99 Å
Sr^{2+}	1.12 Å
La^{3+}	1.14 Å
Ba^{2+}	1.34 Å

It is clearly evident from the above table that all other cations are significantly smaller than Ba. In all the oxide superconductors, one common feature is that the CuO_2 layers are planar or close to planar leading to fairly uniform lattice size in the a-b plane, viz., the parameters of compounds LaSrCuO (a=b=3.77 Å), YBaCuO (a=3.83 Å, b=3.89 Å), BiSrCaCuO (a=b=3.82 Å) and TlBaCaCuO (a=b=3.86 Å). In these oxide superconductors, few fundamental fcc unit cells of perovskite structure stack vertically to form the superconducting unit cell of that particular compound

with some oxygens removed in the process. This oxygen loss causes shrinkage of the vertical height or 'c' parameter of the superconducting unit cells from the value that would be expected for the stacking of perovskite cells.

In the next sections structures of some oxide superconductors are discussed according to their chronological order of evolution.

1.3.2 Lanthanum copper oxide

The structure of $(La_{1-x}M_x)_2CuO_{4-\delta}$ called the 21 structure, where M is usually Sr or Ba, is given in fig.1.7. It has tetragonal structure at room temperature and becomes orthorhombic at around 180 K. It has a quasi two dimensional structure of K_2NiF_4[11] described by the prototype compound $LaCuO_4$ corresponding $x = \delta = 0$, keeping in mind that in the superconducting compounds themselves some of the La atoms are replaced by a divalent cations such as Sr or Ba. Since La has a charge of +3 and both Ba and Sr have +2, whereas the charge state of oxygen is -2, it follows that all the copper is divalent (+2) when x=0, and some become trivalent for $x > 0$. Since the discovery of superconductivity in the cuprates of K_2NiF_4 structure, many other cuprates with considerably higher Tcs have been discovered, and all of them possess Cu-O sheets as an essential feature.

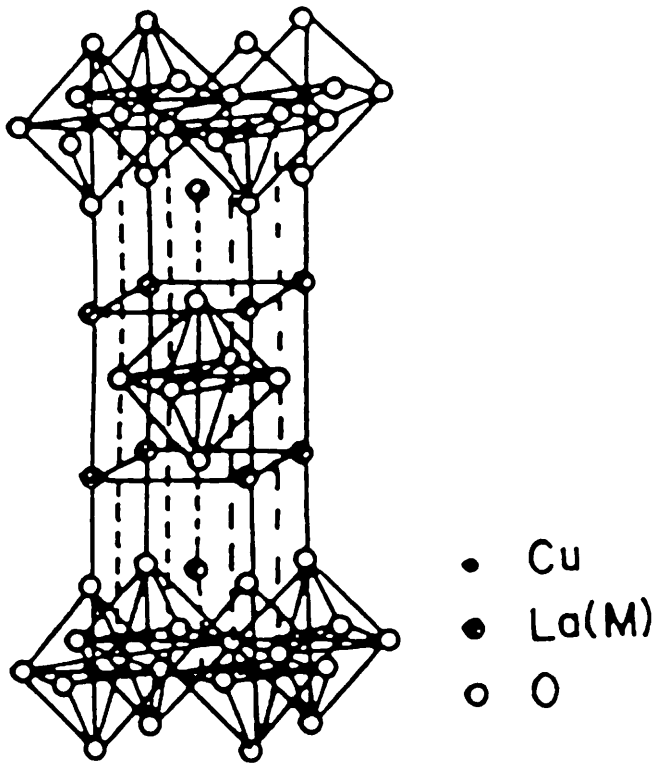

Fig. 1.7. K_2NiF_4 structure of $La_{2-x}M_xCuO_4$ (M = Ba or Sr).

1.3.3 Yttrium barium copper oxide

The structure $LnBa_2Cu_3O_7$ is called the 123 structure, where Ln's are rare earths(fig.1.8). Amongsts this family only $YBa_2Cu_3O_7$ will be described here, since the work described in this thesis is confined only on this phase, although this is not the most stable phase in the Y-Ba-Cu-O system. The 123 phase can occur both in tetragonal (a=b=3.9018 Å, c=11.9403 Å)(fig.1.9(a)) and in orthorhombic (a=3.827 Å, b=3.882 Å and c=11.682 Å)(fig.1.9(b)) structures. Usually, the orthorhombic phase is superconducting with few reported exceptions[12-15]. The compound is tetragonal at high temperatures and undergoes a second-order, order-disorder transition at about 700°C to the low temperature orthorhombic phase. The tetragonal phase at room temperature can be obtained by quenching the material from high temperature. In the tetragonal phase, the oxygen sites O(05) and O(01) sites are equivalent and therefore randomly occupied. But in orthorhombic phase, these sites are inequivalent and so a preferential occupancy takes place at O(01) site forming a Cu-O chain in the b direction. The vacancy at O(05) site causes the unit cell to compress slightly along 'a' to render a < b. The fractional site occupancy of the oxygens in the basal plane as a function of the heating temperature in oxygen atmosphere is given in fig.1.10. This also gives the x value of the formula $YBa_2Cu_3O_{7-x}$. Fig.1.11 shows the variation of the

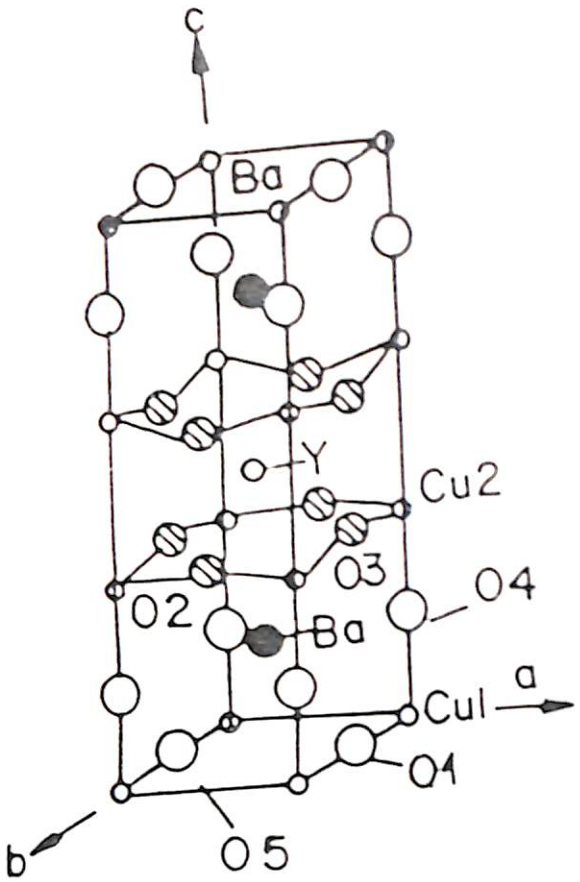

Fig. 1.8. Structure of $YBa_2Cu_3O_7$.

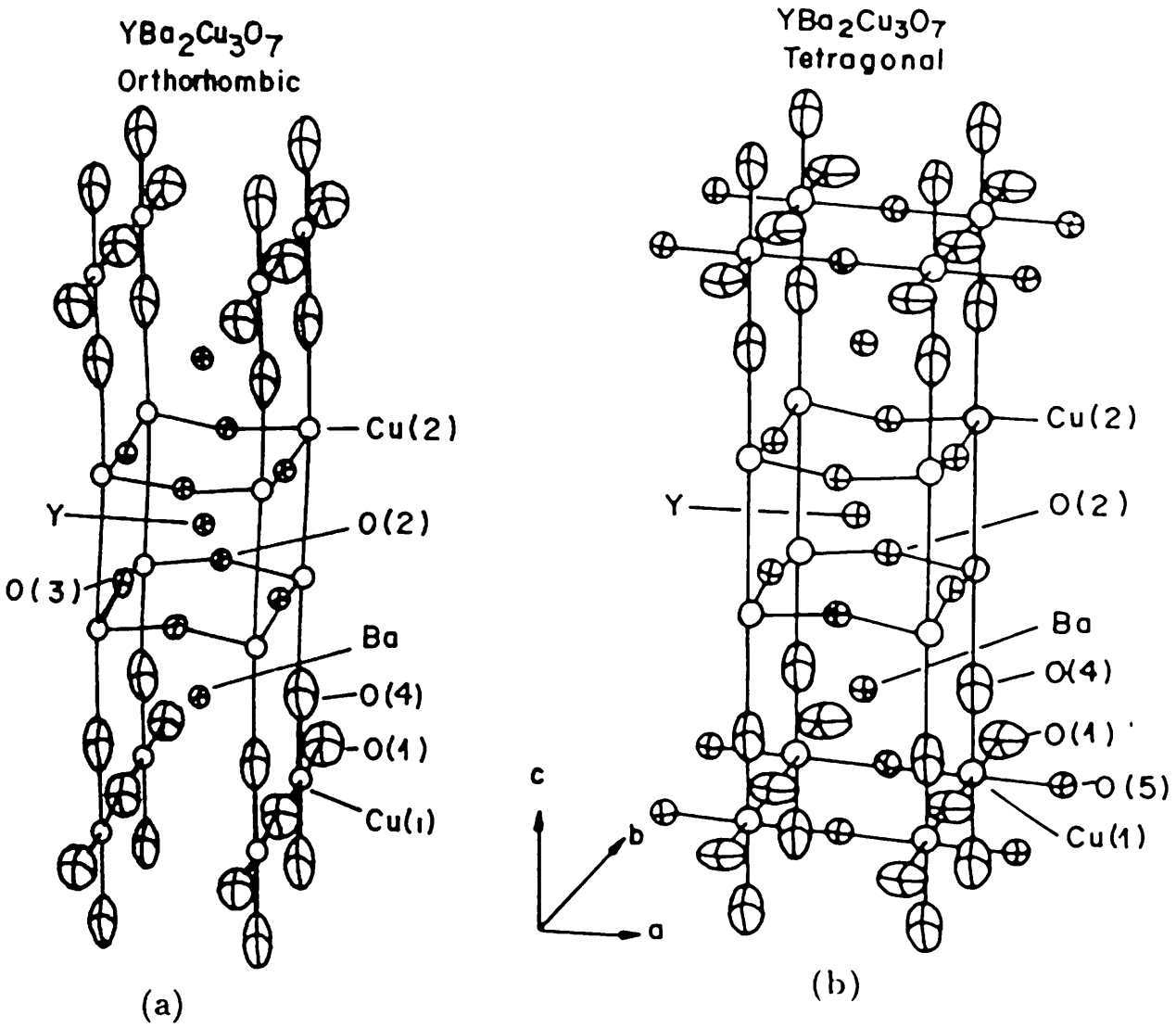

Fig. 1.9. (a) Orthorhombic, (b) Tetragonal structure of YBCO unit cell. Oxygens are randomly dispersed over the basal plane sites in the tetragonal structure. Thermal vibration ellipsoids are shown for the atoms.

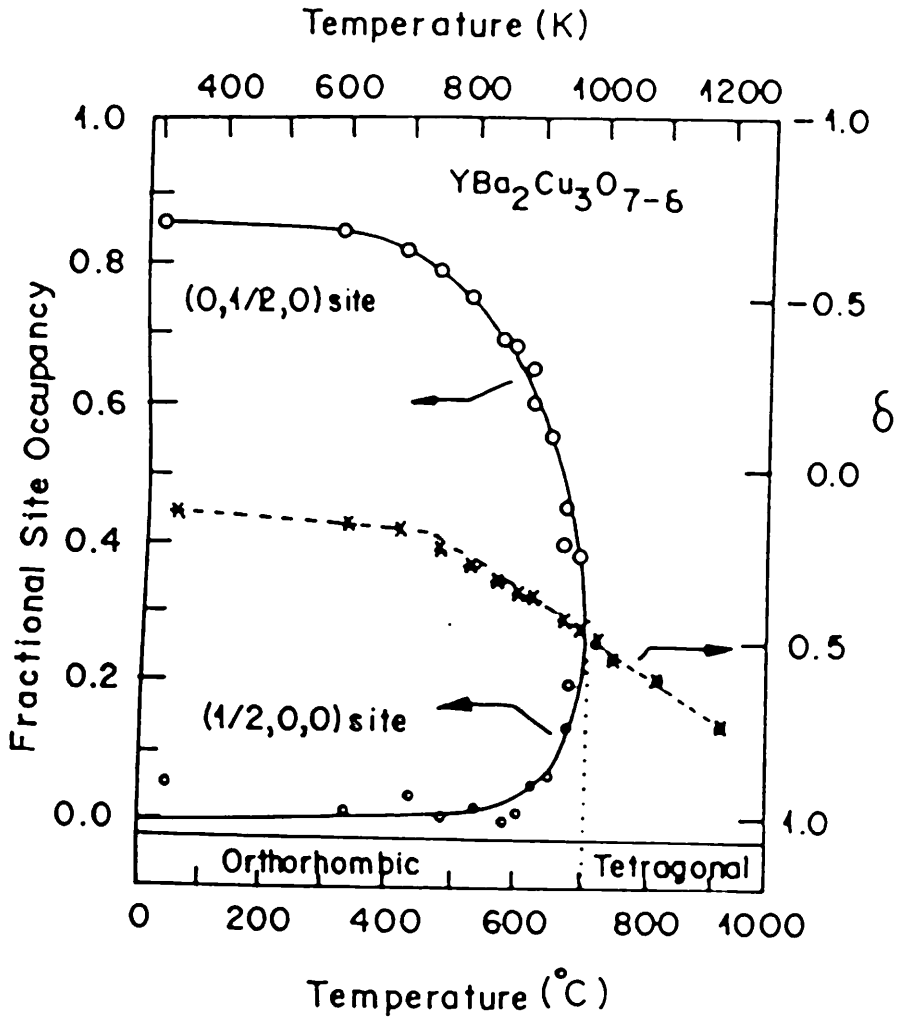

Fig. 1.10. Dependences of the fractional occupancies of the $(0,\frac{1}{2},0)$ and $(\frac{1}{2},0,0)$ sites and the oxygen content parameter δ on the quench temperature.

orthorhombic unit cell parameters of $YBa_2Cu_3O_{7-x}$ with oxygen stoichiometry x and fig.1.12 shows the variation of the superconducting transition temperature of $YBa_2Cu_3O_{7-x}$ with x. Structural studies revealed that in x = 0.5 composition, fully oxygenated Cu-O chains are present along the b axis, alternately with fully vacant O1 sites[11].

YBCO tetragonal structure can be visualized as made of three prototype perovskite fcc oxygen unit cells stacked one above another[10] (fig.1.13). For generation of YBCO, in the middle cube Ba atom at the center is replaced by Y and all the oxygens at the vertical edges of this cube are removed. To take up this unfilled space due to removed oxygen and also due to smaller size of Y, the middle cube is compressed and the oxygen on the vertical edges of the other two cubes are shifted toward the basal plane Cu. Therefore, in YBCO structure, there is a three fold layering sequence with median copper oxide planes adjacent to Y are much more closer together than they are to the basal planes. Also, because of the compression of the middle cube, the median Cu planes are slightly puckered whereas the basal planes are perfectly flat.

1.3.4 Bismuth-strontium-calcium-copper oxide

Bismuth cuprates of general formula $Bi_2(Ca, Sr)_{n-1}Cu_nO_{2n+4}$ were discovered in 1988 with Tc values of 90 and 100 K for

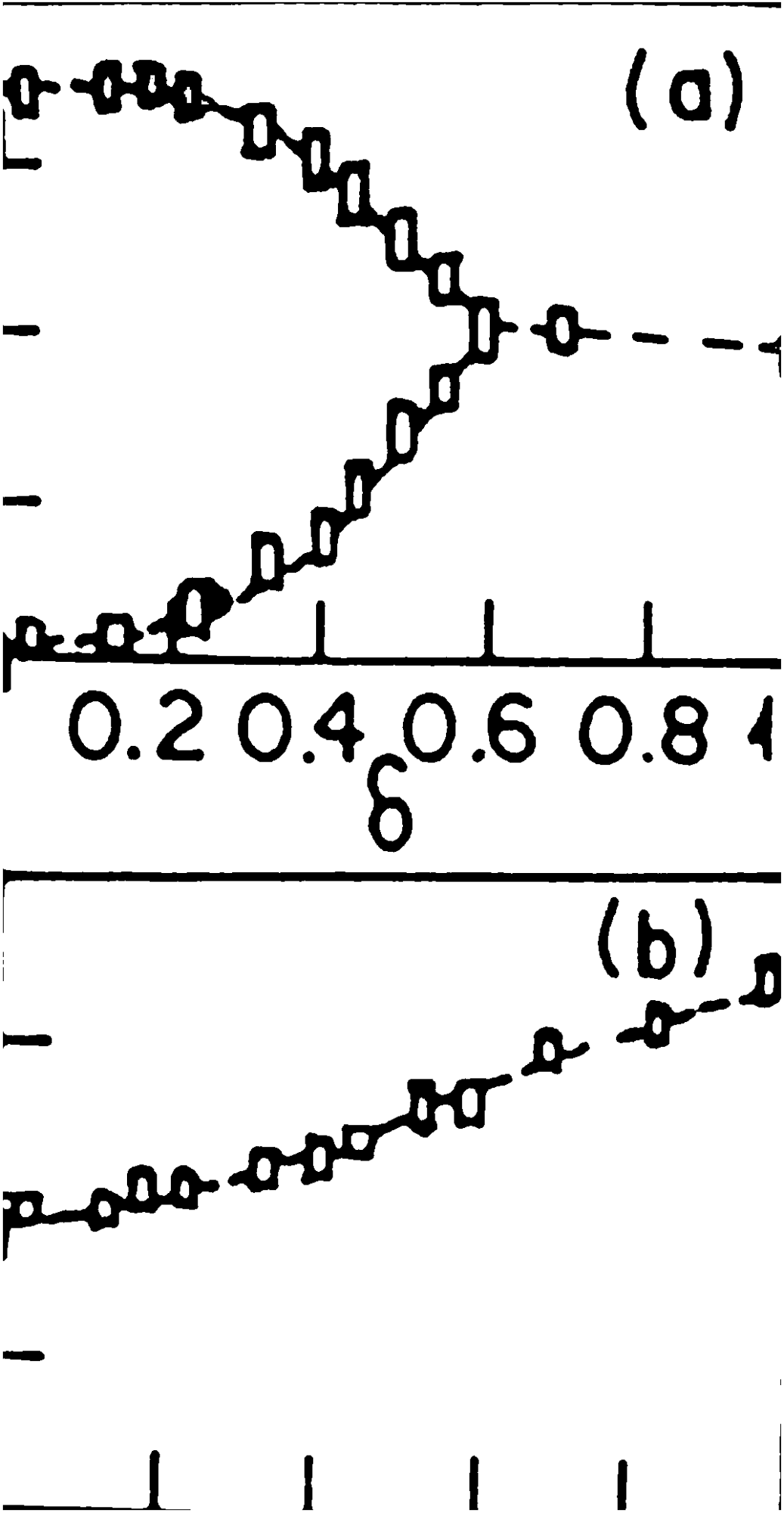
(a)
0.2
0.4
0.6
0.8
δ
(b)

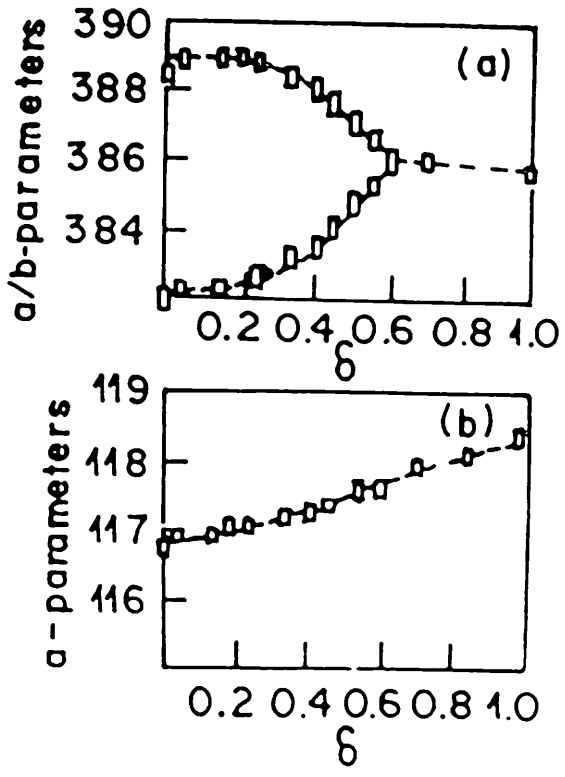

Fig. 1.11. Variation of the orthorhombic unit cell parameters of $YBa_2Cu_3O_{7-\delta}$ with oxygen stoichiometry δ.

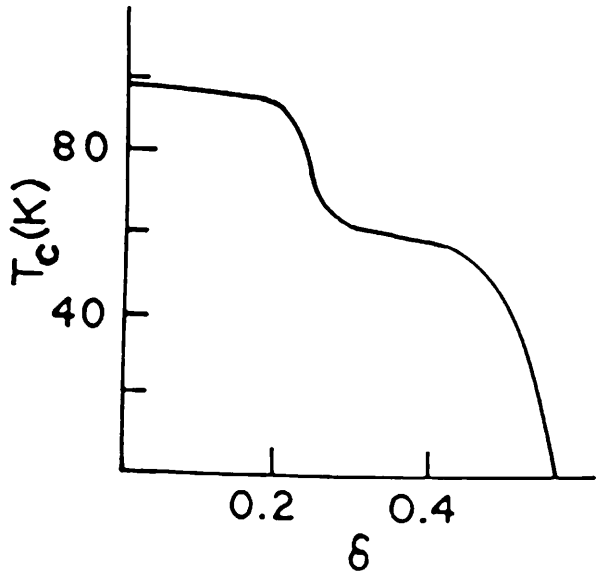

Fig. 1.12. Variation of the superconducting transition temperature of $YBa_2Cu_3O_{7-\delta}$ with δ.

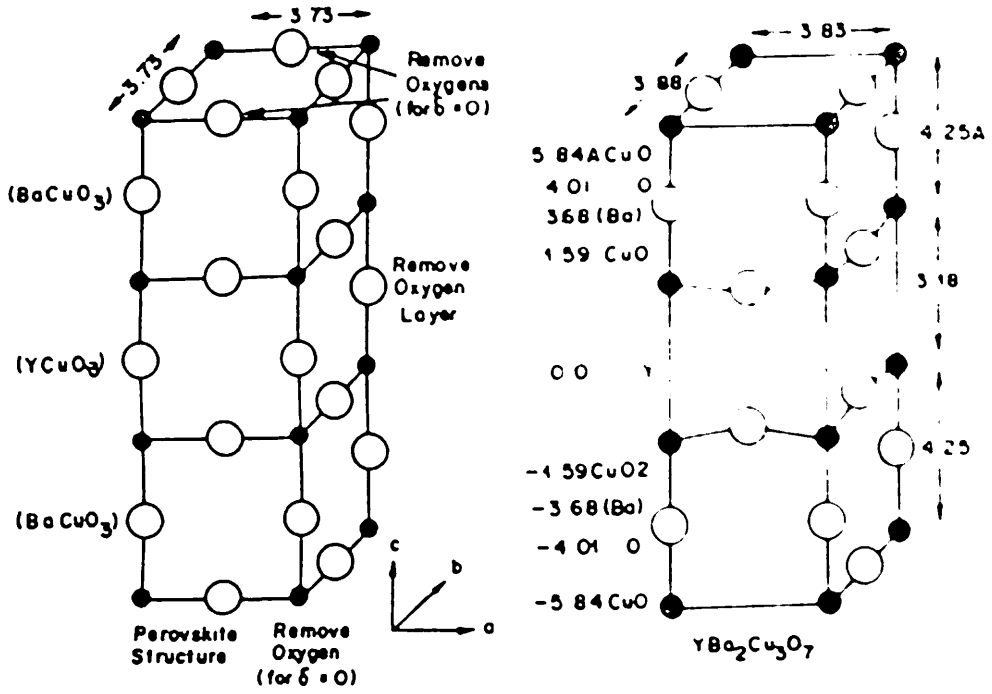

Fig. 1.13. Generation of the YBCO unit cell (right) from three stacked $BaCO_3$ perovskite unit cells (left) by the removal of oxygens on the yttrium level where Y replaces Ba.

n = 2 and n = 3 respectively. Fig.1.14 shows the structure of bismuth cuprate. These cuprates are orthorhombic and have Cu-O sheets besides two Ca, Sr-O layers. Crystals of these cuprates have mica like morphology. One of the problems with these bismuth cuprates is that they can never be produced with pure phase[11]. Thus, in a composition containing preponderantly the n=2 member, $Bi_2CaSr_2Cu_2O_8$, some n = 3 and n = 1 layers are usually present. This is, because these members can easily intergrow with each other at the unit cell level. Another aspect of these cuprates is that the actual cationic content is likely to be different from that given by the nominal formula. The divalent Ca ion can be replaced by a trivalent rare earth ion as in $Bi_2Ca_{1-x}Ln_xSr_2Cu_2O_{8-\delta}$ (Ln = Y or rare earth). The oxygen content, carrier concentration and Tc, all vary with x, with Tc and carrier concentration maxima at around x=0.25. Partial substitution of Bi by Pb seems to facilitate the formation of bismuth cuprates.

1.3.5 Thallium cuprates

These materials with highest known Tc have also been discovered in 1988. These superconductors are composed of thallium, barium, calcium, copper and oxygen with the general formula $Tl_mBa_2Ca_{n-1}Cu_nO_{m+2n+2}$. The structure is given in fig.1.15. Thallium is coordinated to oxygen in a large octahedron. The thallium-oxygen octahedron form a plane that rests on a plane of

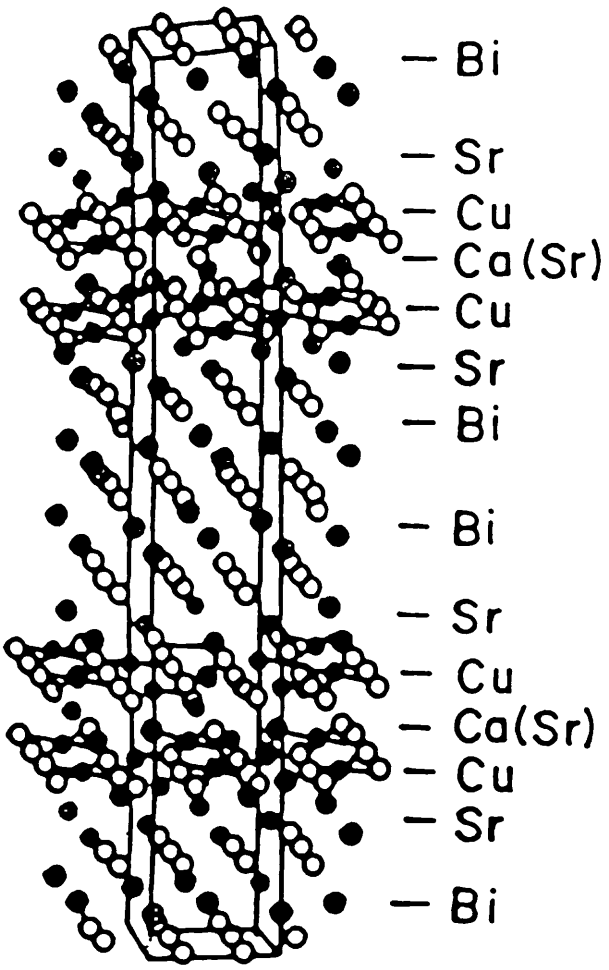

Fig. 1.14. Structure of bismuth cuprate containing two Cu O sheets.

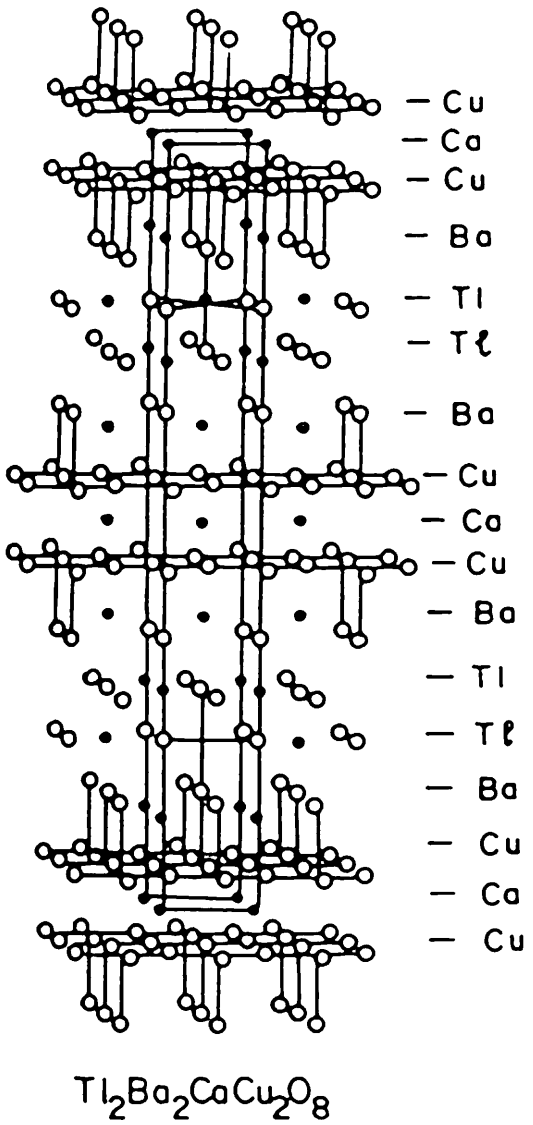

Fig. 1.15. Structure of $Tl_2Ba_2Ca_{n-1}Cu_nO_{4+2n}$ where n=1.

copper-oxygen octahedron or pyramids. The subscript 'm' in the general formula of these compounds describes the number of layers of thallium oxygen octahedra. Only compounds that have one or two layers are known. The number of copper layers (m) can vary from one to four. In these cuprates also, we encounter the problem of phasic inhomogenity. All compounds in the series are superconducting at high temperatures. The highest, at 125 K, is the superconductor $TlBa_2CaCu_3O_{10}$. The toxicity of thallium oxide makes handling the materials very risky and hazardous. Due to this, except under very carefully controlled laboratory conditions, using these materials is highly inadvisable and so their potential for commercial use is not yet explored.

The most common feature of all these cuprate family of superconductors is that they all contain Cu-O planes in them which, in turn, indicates the importance of the presence of these layers in the phenomenon of superconductivity. The increment of Tc with the increase of the number of Cu-O layers in bismuth and thallium compounds confirms this hypothesis. The present understanding says[11] that these two dimensional Cu-O sheets are primarily responsible for superconductivity, they have charge reservoirs in the form of Cu-O chains (123 compounds) or TlO (thallium compounds) or BiO (bismuth compounds) layers. Because of the presence of the two dimensional Cu-O sheets, properties of these

materials are anisotropic. Accordingly, these cuprates show very much higher normal state resistivity perpendicular to the a-b plane compared to that in the plane. The mica like morphology in bismuth cuprates underscores their anisotropic nature. Another important feature common to the cuprates is that they all are 'hole' superconductors. Earlier belief was that this hole resides on Cu site. But now the present general consensus[16-17] is that the excess positive charge resides on oxygen giving rise to O^{1-} type species rather than reside on copper giving rise to Cu^{3+}. This oxygen holes can dimerize in the form O_2^{2-}. Considerable evidence of the presence of such O^{1-} species have been found from X-ray absorption spectroscopy, photoemission studies and Auger electron spectroscopy; Cu^{3+} has not yet been identified in these materials. Tc of these cuprates varies with the hole concentration in the material with a maxima at an optimal hole concentration. Another feature common to these superconductors of cuprate families is that they generally have parent members which are antiferromagnetic insulators (e.g., La_2CuO_4, $YBa_2Cu_3O_6$, $BiCaSr_2LnO_8$).

So far the structures and properties of the oxide superconductors in bulk form have been discussed. Now the subject of discussion will be shifted to another important form of superconductors, namely, high Tc thin film. Also the methods of preparation of these high Tc thin films will be discussed briefly

in the next section. Lastly, the usefulness of different buffer layers for growing high Tc film on semiconducting substrate, namely, Si, will be described.

1.4 High Tc Thin Films

After the initial exhuberence of the discovery of the high Tc oxides, scientists all over the world started thinking about the applications of these exotic materials. Two immediate applications were apparent which involved the direct replacement of present technology current-carrying lines with superconductors, in order to reduce the heat generated and decrease the pulse dispersion which leads to higher packing densities and higher speed. So far processing of high Tc tapes and wires could not come up with expectations. The present status of superconducting current carrying lines entirely consists of thin films, which are used for on chip interconnects, and thick films, which are used for chip-carrier interconnects. The main importance of thin films comes from the fact that it has less imperfections in structure and greater current carrying capacity than those of the bulk materials. In good quality YBCO thin film, the critical current density can be as high as $10^7 A/cm^2$. High Tc thin films have their other applications too. One of the important usage of high Tc thin films is as an active device component (eg., Josephson Junction) which is being used in a wide range of fields. High Tc superconducting thin films are

also being used in the electronics of space vehicles, as space is thought to be ideal place of using high Tc materials because of its cooler atmosphere.

1.4.1 Preparation of thin films

Thin film processing has come through a long and tedious way of optimization and subsequent modifications with various techniques and in present days people can deposit few unit cell thick high Tc films with much more precision. Amongst the very many techniques, laser ablation[18-20] and magnetron sputtering[21-24] are the two most popularly used techniques to produce YBCO thin film because they are relatively less complicated and good quality stoichiometric high Tc YBCO thin films can be made reproducably by these two techniques. A brief description of these two techniques is given in the following subsections.

1.4.1.a Laser Ablation Technique

In this technique pulsed laser beam of appropriate wavelength (generally used laser beam wavelengths are 308 nm, 248 nm, 488 nm) and appropriate intensity is collimated through the quartz window of the chamber on the target at some incident angle. The target used is either stoichiometric $YBa_2Cu_3O_{7-x}$ bulk samples or sometime a composite target,

fabricated from a mixture of barium fluoride, yttrium oxide, and copper oxide powder. The energy dissipated from the laser beam on the target surface evaporates the material in molecular form which then condense on the substrate surface which is kept at a small distance from the target (the distance varies from few mm to few cm in different cases). The resulting film quality depends on the various processing parameters used in this technique. Most important factor for homogeneous film deposition is the laser energy density used. The optimum beam energy for homogeneous YBCO film deposition has been found to be 4-5 j/cm^2. So far good quality laser ablated YBCO film is made when substrate is kept at temperature ~700-800°C. Oxygen pressure in the deposition chamber is also important for the quality of the film grown. The lower limit of O_2 pressure for crystalline film growth is ~ 5 $X10^2$ mbar. The orientation of the deposited film also varies with oxygen pressure. Good quality c-axis oriented superconducting YBCO film has been prepared by laser ablation when chamber pressure of oxygen is between 0.1 mbar and 0.3 mbar. As the oxygen partial pressure is increased, above 0.4 mbar, 'a-b' axis oriented YBCO film growth takes place. It is also noticeable that the oxygen pressure required in laser ablation is more as compared with sputtering, another effective technique for good superconducting film deposition. The main reason is that in PLD technique,

deposition is not a continuous process like sputtering. In laser ablation relatively large amount of material is deposited in short burst of time(~ 0.5-1 Å/s). Naturally, large concentration of oxygen is required for effective oxidation of such a high concentration of fragments in each pulse. Like other techniques, substrate is a very important factor for depositing good quality superconducting films by laser ablation. So far best quality laser ablated YBCO film has been made on (100) $SrTiO_3$ substrate. A schematic diagram of standard laser ablation technique generally used for high Tc film deposition is given in Fig. 1.16.

1.4.1.b Magnetron sputtering technique

Single target sputtering is widely used for deposition of high Tc superconductors. In general, in cathode sputtering, a gas plasma is created by applying high voltage between two electrodes. The target is kept on the cathode and the positive ions, accelerated towards the cathode under the applied potential, sputter the material from the target. This sputtered material then condense on the substrate which is generally kept at ground potential in D.C. sputtering at a small distance from the cathode. In conventional D.C. sputtering the gas pressure in the chamber is kept high to create sufficient ions for sputtering. But the problem of high pressure sputtering is that the resulting films are contaminated with the impurities present in the chamber. To

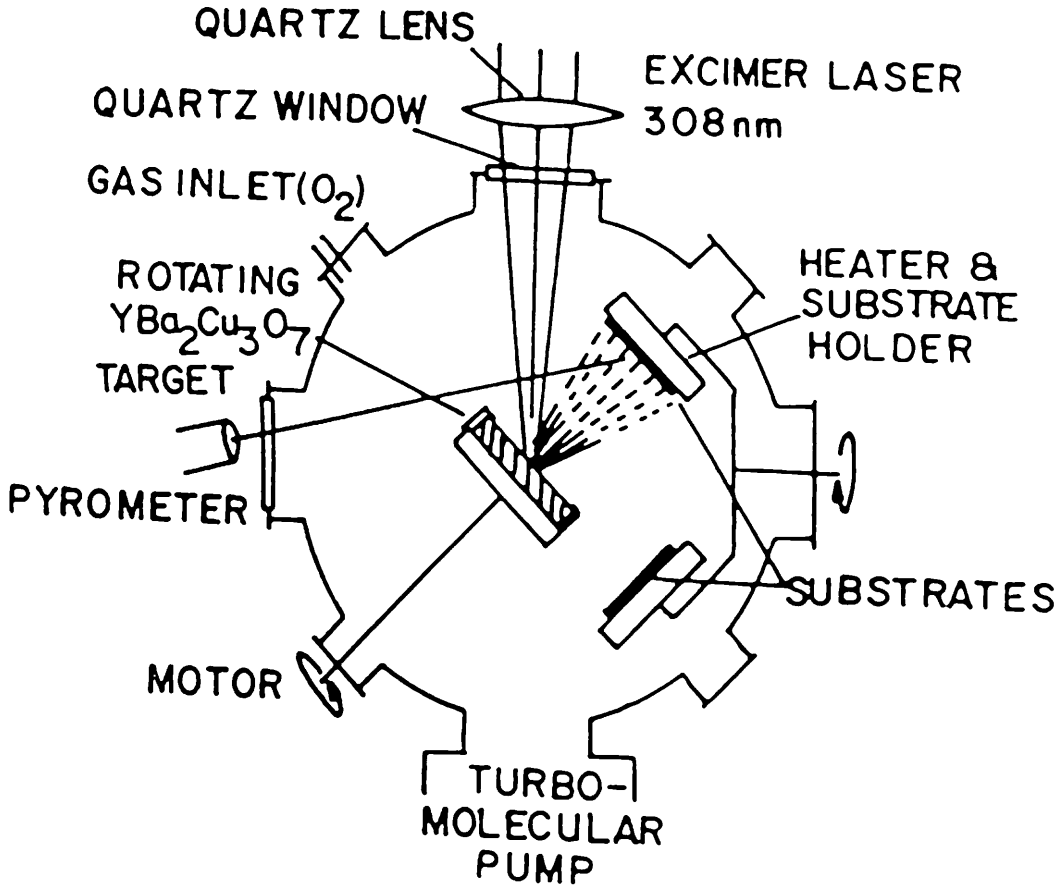

Fig. 1.16. Typical preparation chamber for laser evaporation.

avoid this difficulty a magnetic field is created in the plasma region by using a magnetic assembly behind the cathode. This magnetic field confines the electrons in the plasma for longer time so that they can experience more number of collisions inside the plasma and thereby create more number of ions. In this way sputtering with considerable rate can take place at low chamber gas pressure and even at low voltage. This is the basic process involved in magnetron sputtering.

The main advantage of sputtering with respect to other techniques is the relative ease of process control, repeatability of resulting sample characteristics, and reasonable processing time. Thin films of the high temperature superconductor $YBa_2Cu_3O_7$ have been sputter deposited with good result on variety of substrates such as Si, Al_2O_3, $SrTiO_3$, MgO and others.

The main disadvantage of this technique is the possible presence of oxygen resputtering effects which result in a film composition different from that of the target. In order to achieve a desired composition in the films, adjustment of the target composition is a method which is commonly employed. The resputtering problem involves heavy energetic particles produced at the target (cathode) or arising from the plasma which bombard the growing film and, in the case of YBCO, preferentially

resputter Ba from its surface. In some cases resputtering has been found to actualy etch the substrate. Resputtering is strongest when a strongly oxygenated target is used, or when anAr/O_2 mixture is used as the sputtering environment. The net effect of resputtering is a non-uniform thickness profile of the film and a film composition which can be signifiacntly different from that of the target. There are three type of particles which participate in resputtering effects :

1) Negative ions : Targets made by pressing Y_2O_3,BaO,CuO powders, or superconducting YBCO targets which are highly oxygenated, release negative oxygen ions from their surface. These ions are accelerated across the sheath and are subsequently neutralized in the plasma. They now have high kinetic energy and a small scattering rate and thus can reach the substrate where they preferentially resputter barium from its surface.

2) Neutral argon : Some Ar^+ ions are accelerated to the target where they are neutralized and are reflected back towards the film. This process is significant when the mass of the atoms constituting the target is larger than that of the Ar^+ ions. It has been reported that for YBCO targets this process is negligible.

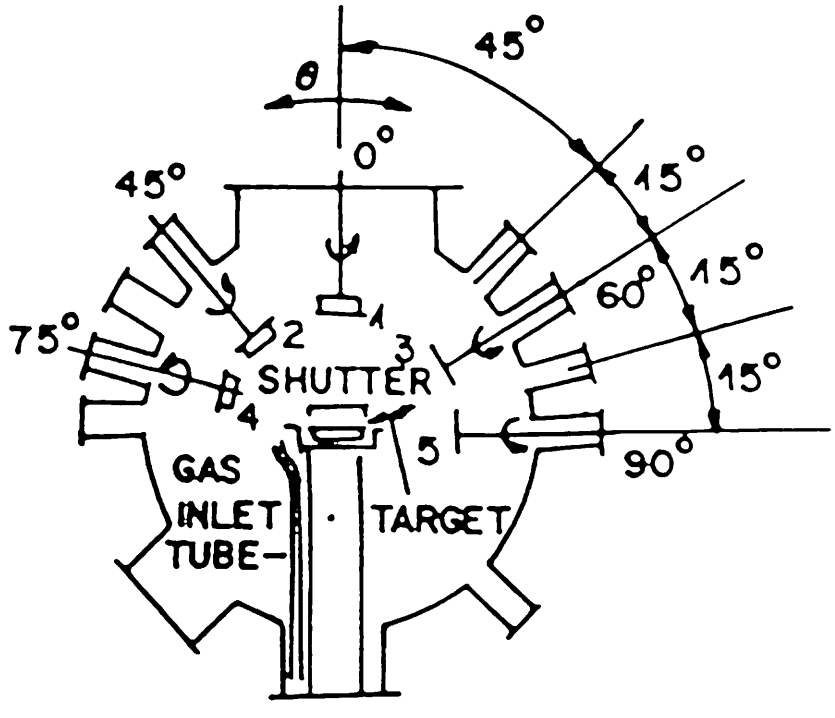

Fig. 1.17 Typical preparation chamber for sputter deposition.

during deposition and after deposition the film is slowly cooled down to room temperature in oxygen atmosphere. The YBCO film deposited below 400°C are all amorphous. So the films which are deposited at room temperature or below 400°C, have to go through post annealing at high temperature (~850°C). The main problem with post annealing of YBCO films is, since annealing of the film at ~850°C requires the film to pass through the temperature range 450°C-600°C and since at this "forbidden" temperature range for YBCO the nucleation of the other non-superconducting phases are thermodynamically feasible, the resulting film is often a polyphase mixture which has inferior superconducting properties (like current density etc.) than the insitu annealed films. This problem could be avoided by using BaF_2 as Ba source and wet oxygen annealing after traversing forbidden temperature range during which Ba is bound as a fluoride. This process has the advantage of precluding the formation of $BaCO_3$.

1.4.2 The Necessity Of Buffer Layers

It has been mentioned earlier that substrate is a very important factor in high Tc thin film deposition. The choice of the substrate depends on few factors. (1) Substrates should be stable at high temperature (~ 900°C) which is essential in the post deposition annealing technique in the high Tc thin film processing. (2) They should not react with the

superconductors during the thermal processing, failing to which, the superconducting properties are degraded and other unwanted phases occur. (3) Diffusion of film constituents into the substrate and those of the substrate into the film should be least, to make a good film-substrate interface. Even for the best substrate so far used, oxygen deficiency is observed in first few layers of YBCO thin film grown on them. (4) The lattice parameters of the substrat and their thermal expansion coefficients should match properly with those of the high Tc material. Otherwise mechanical strains which get, developed can make the film quality worst.

So far epitaxial high Tc YBCO has been made only on a few substrates like $SrTiO_3$[25-28], MgO[29-31], $LaAlO_3$[32,33], $LaNbO_3$[34] and Yttria stabilized Zirconia[35-39]. Among them single crystal $SrTiO_3$ has come out to give best quality YBCO films. But despite of being recognised as best substrate material, this crystalline $SrTiO_3$ has very little potential from the application point of view, because of its high cost, non-availability of large area substrates and above all, its high dielectric loss at microwave frequencies. Other single crystal substrates mentioned earlier, also suffer from some of these shortcomings. From this point of view, it is very much important and essential to make good high Tc films on semiconductor substrates. Much work has

been done to deposit YBCO on Si substrates due to the possible use of high Tc superconductors in microelectronics as passive interconnects or as superconductor/semiconductor devices[40-44]. These investigations have already provided useful data regarding the feasibility of the integration between superconductor and semiconductor.

Growing YBCO thin film on bare Si substrates poses several difficulties[45-48]. Although a few successes have been reported, the characteristics of resistivity vs. temperature was found to be semiconducting above onset temperature or to exhibit low temperature tail in the transition region when YBCO was directly deposited on bare Si substrate[30,49]. There are certain reasons for these degradations. Firstly, Si diffuses into the YBCO film, breaking the Cu-O bond to form SiO_2, thereby degrading the film quality severely. Also Cu diffuses very fast in Si at high temperature and significant Ba loss has also been observed at the film-substrate interface[50,51]. Therefore, several other phases are formed inside the film. In addition, because of the lattice constant and thermal expansion coefficient mismatch, cracking of the film and island formation takes place. The last difficulty can be avoided to some extent by depositing the YBCO film at higher substrate temperature. But to circumvent the problem of diffusion, deposition of a thin buffer layer on Si, which can act as a barrier to the diffusion

between Si and YBCO, is essential prior to the deposition of YBCO. Now the suitability of a material as a buffer layer depends on few of its properties. It should be chemically stable at higher temperature because the film has to be processed at high temperature. The most important requirement is that,there must not be significant amount of Si diffusion inside this material at high temperature. Also, it should restrict the reverse issue, i.e., the diffusion of the different constituents of YBCO inside Si, because this can lead to the formation of deep levels in Si[52,53] which in turn can serve as effective recombination centers, and hence degrade the performance of active devices, such as transistors and diodes, located on Si chip. Lastly, to grow good quality YBCO film on this material, its lattice constants and thermal expansion coefficients should have values nearer to those of YBCO.

The mostly used buffer layers on Si for YBCO thin film deposition, are the perovskite type oxides like $SrTiO_3$[54], $BaTiO_3$, $PbTiO_3$ etc. Also ZrO_2, YSZ, MgO, $SrTiO_3/MgAl_2O_4$, $BaTiO_3/MgAl_2O_4$, $PbTiO_3/MgAl_2O_4$ are also used successfully. Another group of buffer layers which are gaining more and more importance are the metallic buffer layers. The additional advantage of using metallic buffer layer is of two fold. One is, it provides a well controlled surface for the fabrication of the superconductor. Secondly, it enables the possibilities of practical applications

involving three dimensional device fabrications using superconductor/ metal/semiconductor materials. So far $CoSi_2$[55], RuO_2, Indium-tin-oxide have proved to be promising metallic buffer layers for YBCO.

1.5 Irradiation of High Tc Superconductors

Since its discovery, numerous ion irradiation experiments have been performed on high Tc superconductors, mainly with $YBa_2Cu_3O_{7-\delta}$. An overview of these irradiation studies is described in Chapter II. The energies of the different projectiles used in these experiments ranges from less than 1 MeV to several GeV. The main concern of most of these experiments has been the interpretation of effects of irradiation induced lattice defects on superconductivity and normal state properties of the copper-oxide-based high Tc compounds[56]. Copper-oxide superconductors are defect ridden[57] and the normal state conductivity of these systems cannot be understood from the details of fermi surface and conventional electron-phonon scattering[58,59]. The defects make the system to remain in a metastable state through lattice mismatch and co-ordination incompatibilities[60] and it is now believed that the superconductivity of these systems is closely associated with this metastability[61]. Therefore, one of the ways to understand few aspects of superconductivity is to create defects in it and ion irradiation is one such effective means of creating defects in the superconductors with the extra advantage that the high energy projectiles can cause

disorder at rather more stable lattice points[62] which is not possible with the other methods. Ion irradiation can also be effectively used to control the tailoring of properties of superconducting materials so that their behaviour in magnetic field and their current tarnsport capability can be changed favorably. Lastly, ion beam irradiation is used in a very important aspect, namely, superconducting device technology. Planar SQUID has been fabricated [63,64] by ion beam lithography.

1.6 Objective of the Thesis

The motivation behind the present work is of two folds. First is to investigate the effect of irradiation on the properties of superconductors with energetic ions in the energy range of 50-200 MeV. A systematic scheme has not been explored till now, though a good deal of data is available, yet the use of the projectiles, their energies and target conditions have been purely random, e.g., change of projectile has not been systematic with regard to energy and only low temperature irradiation have been studied. In this energy range of the projectiles used, energy loss due to electronic excitation of the target atoms is quite significant and it is very important, from the point of view of fundamental ion-matter interaction, to see the effect of irradiation on the properties of this superconducting system, i.e., to see whether this system is sensitive to electronic loss or not. The projectiles are,

therefore, chosen with increasing electronic loss parameter. Since nuclear loss effect is also present in the irradiated bulk sample, it has been tried to separate out the nuclear loss at the end of the projectile's range by using thin films of '123' material. Since the material is multi-atomic compound with complicated phonon distribution, it is interesting to see the effects of temperature during irradiation and the present work includes such study.

Secondly, the present study was aimed to correlate the irradiation effects to its possible place in device technology. This is the motivation behind the interest of growing superconducting films on semiconducting Si substrates and then the necessity of making suitable buffer layers between YBCO thin film and Si substrate is realized and undertaken. Although the present study does not include any direct experiment in the direction of device technology, the general irradiation experiments were motivated to find such applications. One such example is the search for the critical dose of irradiation at which the superconductor makes transition to insulator. Therefore, the motivation of the present work stems from both fundamental and applicational aspects of irradiation studies.

1.7 Outline of the Thesis

In this thesis an attempt has been made to consolidate the

results of the experiments and their interpretations in five chapters:

The PRESENT CHAPTER, CHAPTER 1 is an introduction and deals with the basic superconductivity phenomenon and the basic structures of the high Tc materials and their preparation and also describes briefly the motivation of the present work.

The SECOND CHAPTER is an overview of the irradiation studies so far carried out with different types of projectiles on superconducting materials, mainly on $YBa_2Cu_3O_{7-x}$.

CHAPTER 3 describes the experimental set-up used to prepare the materials, to irradiate them with both high and low energy particles and to characterize them with various techniques.

The CHAPTER 4 consists of three sections. The first section deals with the results of the irradiation experiments carried out on high Tc YBCO system with different projectiles of different energies after describing the results of the characterizations of the unirradiated samples and also with the discussion of these results. In second section the characteristics of the buffer layers grown on Si substrates are described after which the possible interpretation of the results are discussed. The third section is the conclusion of the present study which also indicates about the possible future

extension of the work and the limitations encountered in the present studies.

In APPENDIX-I a brief introductin about the computer simulation code TRIM (Transport and Range of Ions in Matter) is given.

References :

1. H. Kammerlingh Onnes, *Leiden Comm.*, 120b, 122b, 124c (1911).

2. W. Meissner and R. Ochsenfeld, *Naturwissenschaften*, **21**, 787 (1933).

3. F. and H. London, *Proc. Roy. Soc.* (London), **A149**, 71 (1935).

4. A. B. Pippard, *Proc. Roy. Soc.* (London), **A216**, 547 (1953).

5. J. Bardeen, L. N. Cooper and J.R. Schrieffer, *Phys. Rev.*, **108**, 1175 (1957).

6. V. L. Ginzburg and L. D. Landau, *Zh. Exsperim. i. Teor. Fiz.*, **20**, 1064 (1950).

7. L. P. Gor'kov, *Zh. Exsperim. i. Teor. Fiz.*, **36**, 1918 (1959). [*Soviet Phys.* JETP**9**, 1364 (1959)]

8. A. A. Abrikosov, *Zh. Eksperim. i. Teor. Fiz.*, **32**, 1442 (1957) [*Soviet Phys.*-JETP, **5**, 1174 (1957)]

9. Robert M. Hazen, *Scientific American*, June (1988) 52.

10. *"Copper Oxide Superconductors"* - Charles P. Poole, Jr., Timir Dutta, Horacio A. Farach, Willey Interscience Publication, John Willey & Sons (1988).

11. *'Superconductivity Today"* - T. V. Ramkrishnan, C. N. R. Rao, Willey Eastern Limited (1992).

12. I. Felner, I. Nowik and Y. Yeshurun, *Phys. Rev.*, **B36**,3923 (1987).

13. I. Felner and B. Barbara, *Phys. Rev.*, **B37**, 5820 (1988).

14. S. R. Ovshinsky, R. T. Young, D. D. Ailred, G. DeMaggio and G. A. Van der Leeden, *Phys. Rev. Lett.*, **58**, 2579 (1987).

15. G. Xiao, M. Z. Cieplak, A. Gavrin, F. H. Streitz, A. Bakhshai and C. L. Chien, *Phys. Rev. Lett.*, **60**, 1446 (1988).

16. C. N. R. Rao, *Advances in Superconductivity,* Proceedings of the 1st International Symposium on Superconductivity (ISS'88), August 28-31, Nagoya. **145**(1988).

17. Takato Machi, Atsushi Tanaka, Nobuo Kamehara and Kouichi Niwa, *Advances in Superconductivity,* Proceedings of the 1st International Symposium on Superconductivity (ISS'88), August 28-31, Nagoya, **187**(1988).

18. B. Raos, L. Schultz, G. Endres, *Appl. Phys. Lett.*, **53**, 1557 (1988).

19. R. E. Muenchausen, K. M. Hubbard, S. Foltyn, R. C. Estler, N. S. Nogar and C. Jenkins, *Appl. Phys. Lett.*, **56**, 578 (1989).

20. N. K. Jaggi, M. Meskob, S. F. Wahid, C. J. Rollins, *Appl. Phys. Lett.*, **53**, 1551 (1988).

21. Yasuyuki Kageyama and Yasunori Taga, *Appl. Phys. Lett.*, **55**, 1036 (1989).

22. M. Migluiolo, R. M. Belan and J. A. Brewer, *Appl. Phys. Lett.*, **56**, 2572 (1990).

23. Masao Nakao, Hideki Kuwahara, Ryohkan Yuasa, Hiromi Mukaida and Atsuo Mizukami, *Jap. Journal of Appl. Phys.*, **27**, L378 (1988).

24. M. Hong, S. H. Lion, D. D. Bacon, G. S. Grader, J. Kwo, A. R. Kortan and B. A. Davidson, *Appl. Phys. Lett.*, **53**, 2102 (1988).

25. J.J. Kingston, F. C. Wellstood, P. Lerch, A. H. Miklich and J. Clarke, *Appl. Phys. Lett.*, **56**, 189 (1990).

26. T. Terashima, Y. Bando, K. Lijima, K. Yamamoto and K. Hirata, *Appl. Phys. Lett.*, **53**, 2232 (1988).

27. C. H. Chen, J. Kwo and M. Hong, *Appl. Phys. Lett.*, **52**, 841 (1988).

28. B. M. Clemens, C. W. Nieh, J. A. Kittl, W. L. Jhonson, J. Y. Josefowicz and A. T. Hunter, *Appl. Phys. Lett.*, **53**, 1871 (1988).

29. A. B. Berezin, C. W. Wuan and A. L. Delozanne, *Appl. Phys. Lett.*, **57**, 2019 (1990).

30. P. Berberich, J. Tate, W. Dietsche and H. Kinder, *Appl. Phys. Lett.*, **53**, 925 (1988).

31. M. Naito, R. H. Hommond, B. Oh, M. R. Hahn, J. W. P. Hsu, P. Rosenthal, A. F. Marshall, M. R. Baseley, T. H. Geballe and N. Kapitulnik, *J. Mater. Res.*, **2**, 713 (1987).

32. A. E. Lee, C. E. Platt, J. F. Burch, R. W. Simon, J. P. Goral and M. M. Al-Jassim, *Appl. Phys. Lett.*, **57**, 2019 (1990).

33. Yong-Fen Hseih, Michael P. Siegal, Robert Hull and Julia M. Phillips, *Appl. Phys. Lett.*, **57**, 2268 (1990).

34. K. Imada, K. Yoshiara, I. Kawamata, F. Uchikawa, S. Ulsunomiya, T. Mizuochi, T. Kitayama and Y. Isoda, *Supercond. Sci. Technol.*, **4**, 473 (1991).

35. D. K. Fork, D. B. fenner, R. W. Barton, J. M. Phillips, G. A. Connel, J. B. Boyee and T. Geballe, *Appl. Phys. Lett.*, **57**, 1161 (1990).

36. X. D. Wu, R. E. Muenchausen, N. S. Nogar, A. Pique, R. Edwards, B. Wilkens, T. S. Ravi, D. M. Hwang and C. Y. Chen, *Appl. Phys. Lett.*, **58**, 304 (1991).

37. M. Myoren, Y. Hishiyama, N. Miyamoto, Y. Kai, Y. Yamanaki, Y. Osaka and F. Nishiyama, *Jpn. J. Appl. Phys.*, **29**, L955 (1990).

38. S. B. Oagle, R.D. Vispute and R. R. Rao, *Appl. Phys. Lett.*, **57**, 1805 (1990).

39. S. M. Garrison, N. Newman, B. F. Cole, K. Char and R. W. Barton, *Appl. Phys. Lett.*, **58**, 2168 (1991).

40. D. K. Fork, A. Barrera, T. H. Geballe, A. M. Viano and D. B. Fenner, *Appl. Phys. Lett.*, **57**, 2504 (1990).

41. P. Tiwart, S. M. kanetkar, S. Sharan and J. Narayan, *Appl. Phys. Lett.*, **57**, 1578 (1990).

42. T. Venkatasan, E. W. Chase, X. D. Wu, A. Inam, C. C. Chang and F. K. Shokoohi, *Appl. Phys. Lett.*, **53**, 243 (1988).

43. S. Miura, T. Yoshitake, S. Matshubara, Y. Miyasaka, N. Sohata and T. Satoh, *Appl. Phys. Lett.*, **53**, 1967 (1988).

44. Q. X. Jia, K. L. Xiao and W. A. Anderson, *J. Appl. Phys.*, **70**, 3364 (1991).

45. A. Mogro- Campero, B. D. Hunt, L. G. Turner, M. C. Burrel and W. E. Bulz, *Appl. Phys. Lett.*, **52**, 584 (1988).

46. C.T. Cheung and E. Ruckenstein, *J. Mater. Res.*, **4**, 1 (1989).

47. D. B. Fenner, D. K. Fork, J. B. Boyee, G. A. N. Connel and A. M. Viano, *Physica C*, **162-164**, 141 (1989).

48. A. Mogro-Campero, *Supercond. Sci. Technol.*, **3**, 155 (1990).

49. W. Y. Lee, J. Salen, V. Lee, T. Huang, R. Savoy, V. Deline and J. Duran, *Appl. Phys. Lett.*, **52**, 2263 (1988).

50. Tatsuo Teruayama, Tadatsugu Itoh and Hiroshi Takai, *J. Electrochem. Soc.*, **137**, 336 (1990).

51. B. J. Kellet, J. H. James, A. Gauzzi, B. Dwir, D. Pavuna and F. K. Reinhert, *Appl. Phys. Lett.*, **57**, 1146 (1990).

52. S. M. Sze, *Physics Of Semiconductor Devices*, 2nd edition (Willey, New York, 1981).

53. J. W. Chen and A. G. Manes, *Annu. Rev. Mater. Sci.*, **10**, 157 (1980).

54. F. Sanchez, M. Varela, X. Quercit, R. Aguiar and J. L. Morenza, *Appl. Phys. Lett.*, **61**, 2228 (1992).

55. Li Luo, R. E. Muenchausen, C. J. Maggiore, J. R. Jimenez and L. J. Schowalter, *Appl. Phys. Lett.*, **58**, 419 (1991).

56. B. Hensel, B. Roas, S. Henke, R. Hopfengartner, M. Lippert, J. P. Strobel, M. Vildic and G. Saemann-Ischenko, *Phys. Rev.*, **B42**, 4135 (1990).

57. B. Raveau, *Physics Today*, October, 53 (1992).

58. V. L. Ginzburg, *Physica C*, **209**, 1 (1993).

59. P. W. Anderson, *Physica C*, **185-189**, 11 (1991).

60. H. P. Mohapatra, D. Behera, B. Dash, N. C. Mishra and K. Patnaik, Physica C, **185-189**, 739 (1991).

61. A. W. Sleight, *Physics Today*, June, 24 (1991).

62. T. Terai, K. Kusagaya, T. Furuta, Y. Takahashi, Y. Enomoto and S. Kubo, *Physica C*, **185-189**, 2473 (1991).

63. V. Hardy, D. Groult, M. Hervieu, J. Provost, B. Raveau and S. Bouffard, *Nucl. Instrum. Meth.*, **B54**, 472 (1991).

64. B. Roas, B. Hensel, G. Saemann-Ischenko and L. Schultz, *Appl. Phys. Lett.*, **54**, 1051 (1989).

65. R. H. Koch, C. P. Umbach, G. J. Clark, P. Chaudhari and R. B. Laibowitz, *Appl. Phys. Lett.*, **51**, 200 (1987).

66. G. J. Clark, A. D. Marwick, R. H. Koch and R. B. Laibowitz, *Appl. Phys. Lett.*, **51**, 139 (1987).

CHAPTER II

RADIATION EFFECTS ON HIGH Tc SUPERCONDUCTORS

2.1. Introduction

The discovery of superconductivity above about 50 K in ceramic cuprates[1] led to a spurt in research in these materials to achieve higher and higher transition temperatures. Besides this parameter, attempts have been made to look into other properties like the critical current density and critical magnetic field. The objective was to make these materials in wire or tape form for making of superconducting magnets which could be used in a variety of situations and in particular in high energy nuclear physics experiments. The obvoius question arises: How these ceramic superconductors will behave in such radiative environments ? To be able to answer this, one obviously needs to study the high Tc superconductors, by intentionally exposing them to radiation like electrons, protons, neutrons and ions. The effect of irradiation with energetic particles on the properties of superconducting materials has been extensively studied and it has become an area of active research for the past few years. While good deal of work has been done with light particles, attempts have been made to expose the materials to high energy heavy ions over an energy interval of few 100 KeVs and upto GeV. Work has been reported in great detail on irradiation studies on thin films in the energy range upto 175 MeV[2] and in bulk samples in GeV range[3].

The subject of these irradiation studies is manifold. A host of material properties have been studied under the energetic irradiation, namely, change in critical current density, variation of Tc, the width of transition temperature, the change in lattice parameters, optical properties and transition from superconducting to semiconducting to insulator phases etc. From these studies it is envisaged that the properties of superconductors can be tailored according to specific applications. For example, the projectile induces pinning centers in the superconducting target materials and in this way Jc of the target can be improved. Many groups have found a systematic increase in Jc with increased radiation fluence accompanied by a slight decrese in Tc for a moderate radiation dose. Also, it is important to monitor the behaviour of superconductors under radiative environments. Superconducting magnets in fusion reactors, bending magnets in high energy particle accelerators, require materials having immunity to ion beam, neutron or γ-ray irradiation.During the expected lifetime of a fusion reactor, the superconductor of the magnet is exposed to fast neutron radiation of about 5 X $10^{18}/cm^2$.[4]

While normally the change in the crystal structure or any other ion induced effects have been observed by ex situ experiments of XRD and SEM/TEM, the insitu experiments have mainly included the study of change in resistivity of the samples with dose.

This experiment has been fruitfully used to establish a few critical parameters like the critical dose and also a threshold value of energy loss at which the sample changes any of its property rather abruptly. Another aspect of these irradiation studies is that these experiments are very effective approaches in probing the basic processes involved in superconductivity. For example, neutron diffraction measurement reveal the ordering of O vacancies in certain sites, resulting in one dimensional Cu-O chain parallel to the orthorhombic b-axis. These chains are absent in the tetragonal phase and shows no superconductivity. Therefore, it can be inferred that disordering the Cu-O chains might be the cause of any destruction of superconductivity due to irradiation.

There are two fundamental energy loss mechanisms of the energetic projectiles penetrating through matter. 1) Electronic Energy Loss and 2) Nuclear Energy Loss. In the first case, the projectiles share their energy with the orbital electrons of the target atoms and thereby excite them. These excited electrons can then produce more and more excited electrons and form cascades. These excitation can even end up in resulting a displacement of target atoms. The second process actually takes place at the end of the projectiles' range in the matter, when the energy becomes very low. The projectile then collides elastiacally with the target nuclei and gives some of its energy to the recoil. After few such collisions,

the projectiles get implanted inside the material. There is a spread of this implanted region about the range of the projectile, because of the statistical probability of collision of the ions inside the materials. This spread is called straggling. It has been found that in the low/medium energy regimes (upto ~ 3 MeV) the nuclear loss is mainly responsible for the change of the properties like superconducting transition temperature, normal state resistivity etc. and same has been attributed to the defects created in Cu-O lattice sites[5]. But for high energy projectiles at the begining of its path through matter, the ion loses most of its energy by electronic loss mechanism. It has been observed that in the high energy regime (≥150 MeV) there is a threshold value of the electronic loss of an ion in the system beyond which the material undergoes drastic changes and formation of latent tracks takes place[3,6]. Though an exact value is not proposed, but as a guiding factor it has been proposed that if $S_e/S_n = 2000$ for a typical S_e, then that value should be the threshold. The energy of the projectile required to attain such a threshold for a given target is different for different projectiles.

Thus, effect of energetic particles on the superconducting materials is necessarily to be correlated with the effect of either or both of the two losses. Keeping this in view, the following three types of projectiles are considered for a review in the present thesis.

In the actual work carried out it is the first aspect which has been addressed in the present project.

1) Effects due to ion beam irradiation,
2) Effects due to neutron irradiation,
3) Effects due to electron, proton and α particle irradiation.

2.2 Effects due to Ion Beam Irradiation

The properties on which the effects of ion beam radiation has been studied extensively, are, the normal state conductivity, superconducting transition temperature, critical current, change in crystallinity and structural phase transformation. Whatever be the incident energy of the particle, it is known that at least one of the above mantioned property will change. This change can be either for the worse or for the good. This change (good or bad) will be decided by the magnitude of the energy and the final state of the projectile i.e., whether it loses all its energy within the material and sits there (implantation) or passes through the material. When the projectiles used for bombardment are of low energy (100 - 200 KeV), it is the surface of the sample (both bulk and thin film) which is affected and the projectile get implanted inside the target. Here the elastic collision between the

target atoms and the projectiles, plays the major role in affecting the material properties. But in case of high energy (few hundred MeV to few GeV) irradiation, specially in case of thin film target, it is totally the inelastic energy loss through electronic excitation that plays the dominant role in changing the properties of the target and the projectile penetrates through the sample. For bulk it is the combined effect of the two energy loss mechanisms, if the range is less than the thickness. Out of the number of irradiation experiments, so far carried out on high Tc superconductors, only few important ones will be discussed in this report.

One of the most common effect of irradiation on superconductors is the change in crystallinity. For a polycrystalline $YBa_2Cu_3O_{7-x}$ (YBCO) film irradiated by 500 KeV O^- at relatively low dose ($2X10^{13}/cm^2$), the amorphous zones first appear at the kinks or sharp turns at the grain boundaries. These amorphous zones weaken the coupling between the superconducting grains and result in large degradation of $Tc_{downset}$. When irradiated at higher dose ($6X10^{13}/cm^2$), the grain boundary becomes completely surrounded by a thin (15 nm) layer of amorphous phase which destroys the phase coherence between the grains. The film becomes insulator at low temperature. On the other hand, these amorphous zones are not seen in epitaxial YBCO films, for which, under 1 MeV O^+ irradiation, Tc_{onset} moves to lower temperature[7]. In these

situations it is the nuclear loss which seems to be playing a decisive role although electronic loss is also coexistant.

Another important effect is the structural change induced by ion beam irradiation. A linear expansion of c-axis parameter with dose has been observed (fig. 2.1), and is probably due to build up of defect concentration[8]. Ion radiation also induces orthorhombic to tetragonal (OTT) transition[9]. It is suggested that such a phase transition is due to preferential radiation induced disordering of O in the Cu-O basal plane. If the radiation level has not induced the complete disappearence of twinning, i.e., some part of the sample has remained in the orthorhombic phase, then the induced OTT is reversible upon annealing to room temperature. The reversibility of OTT further indicates that such a transition is not due to O loss from the sample but due solely to O disordering. For Bi system, transition from Orthorhombic to Perovskite structure is observed for 50 KeV He^+ irradiation[10].

One of the most important aspects of ion beam modification of high temperature superconductors is the possibility of enhancing the critical current density (fig. 2.2), Jc. Defects introduced from ion irradiation can act as pinning centers for magnetic flux lines or vortices. The critical current density in as grown HTSs is typically limited by weak pinning energies for these fluxoids in

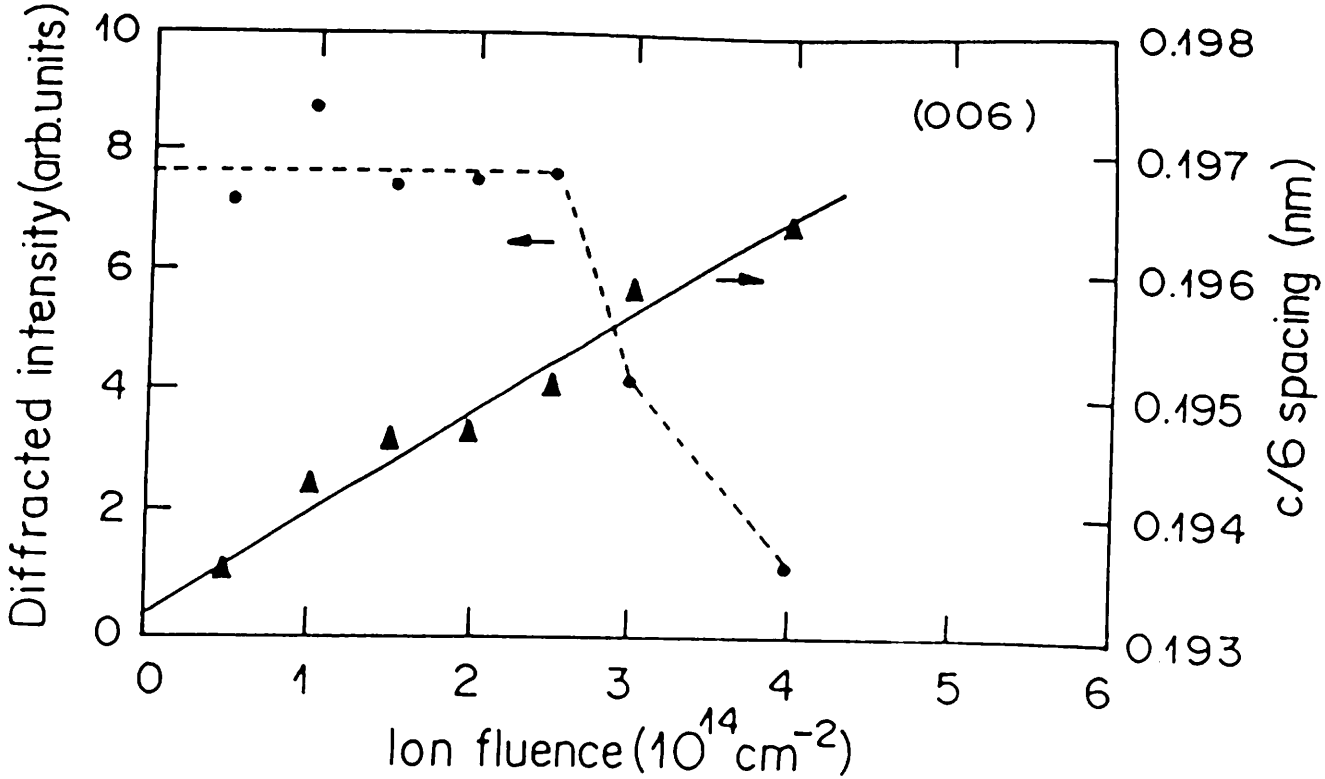

Fig.2.1. Intensity of the [006] X-ray diffraction peak as a function of ion fluence for a 500 keV oxygen irradiation. Also shown is the angular position of the diffraction peak, expressed as the interplanar spacing in the c-axis direction.

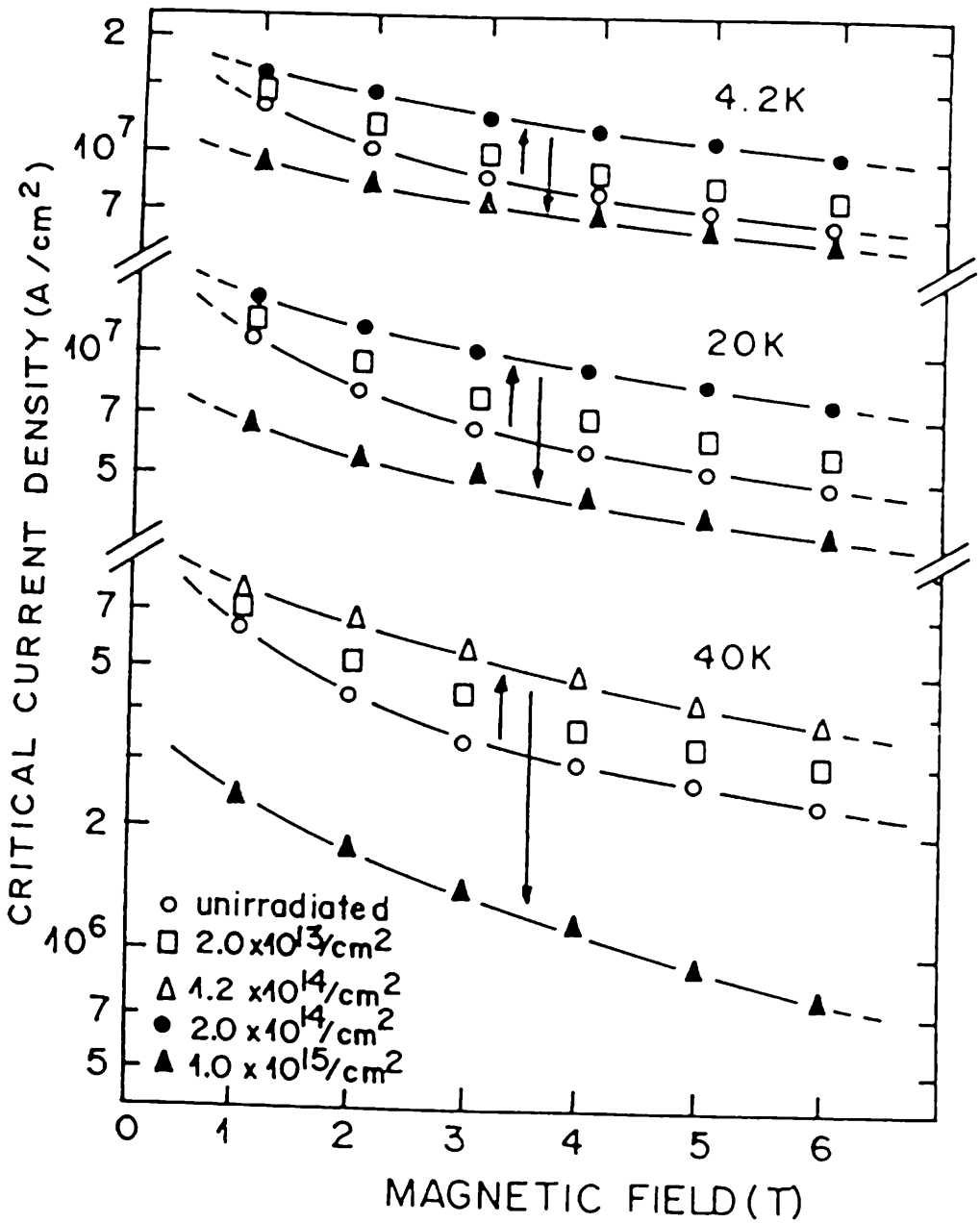

Fig.2.2. Magnetic field dependence of Jc at 4.2, 20 and 40 K after irradiation with various oxygen fluences.

comparision with thermal energies for activating flux motion; therefore an irradiation induced increase in pinning can give rise to an increase in Jc. The results of few investigations along this direction are summarised in the table-2.1.

TABLE-2.1

Sample (before irradiation)	Ion used	Jc enhancement (after irradiation)	Reference
$YBCO/SrTiO_3$ Jc = $6X10^4$ A/cm^2	514 Kev O^+ Rp=5500 Å $Q=2X10^{12}O^+/cm^2$	Jc_{trans} + 10%	T.Masegi et al. Jpn.J.Appl. Phys. 28(1989)L1521
YBCO single crystal 0.8X0.8X0.2 mm^3 Jc=$9X10^4$ A/cm^2 at 70 K	2-3.5 MeV H^+ Rp=0.045mm (3 MeV) $Q=3X10^{16}H^+/cm^2$	Jc_{mag}+few times	R.B.Van Dover et al., Appl. Phys.Lett., 56(1990) 2681
YBCO twinned crystal 1X1X0.3 mm^3	3 MeV H^+	Jc_{mag} + order of magnitude	L.Civale et al. Phys.Rev.Lett., 65(1990)1164
YBCO epitaxial film Appl.Phys.Lett., Jc=$5.2X10^6$ A/cm^2 at 77 K	25 MeV O^+	Jc_{trans}(B=3T) + two times	B.Roas et al., 54(1989)1051

It should be noted here that except for the case of 514 KeV O^+, in all the cases nuclear energy loss and hence the damage cascade is very less inside the film. In the last case mentioned in the table, Jc enhancement is still observed after annealing up to 300 K[11]. This could be an indication that the relatively heavily damaged regions should be most important for the pinning. Track induced enhancement of critical magnetisation current density Jc(M) is observed for 5.3 GeV Pb ion irradiation on bulk sintered samples at low fluences ($\phi t = 3X10^{11}$ cm^{-2})[12]. But it was very sensitive to orientation of the applied magnetic field with respect to the track formed. Similarly, improvement of critical transport current density Jc(T) had been seen for 173 MeV Xe ion irradiation when the magnetic field was aligned parallel to the tracks. A detailed study on the correlation between Jc enhancement and the microstructure of the radiation damage, such as the work of Kirk et al.[13], is important to the understanding of the mechanism.

Fig. 2.3 (a) and 2.3 (b) show the Resistance vs. Temperature result of two typical irradiation experiments on YBCO thin film. The superconducting transition temperature Tc has been seen either to be decreased or to remain constant in most cases of irradiation experiment.In case of low energy irradiation Tc degradation has

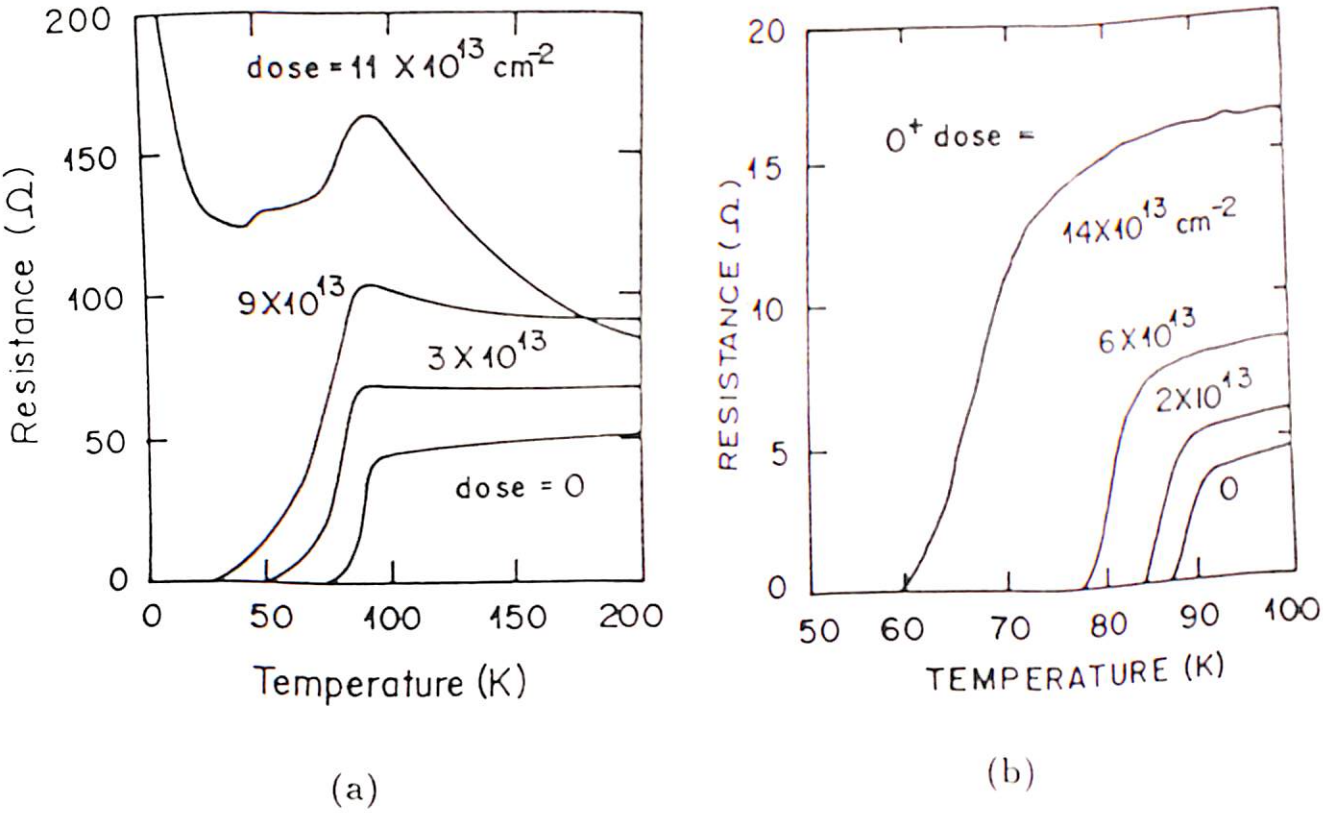

Fig.2.3. R vs. T plots for various doses of (a) 500 keV O ions and (b) 25 Mev O ions.

been observed to be proportional to nuclear energy loss[14,15]. But in some cases it has been seen to be improved. Shirashi et al.[16] irradiated sequentially single phased YBCO pellets with 200 KeV nitrogen ions and had seen an increase in Tc when measured with current density greater than 25 kA m^{-2} (fig. 2.4). The optimum dose for enhancement of zero resistance temperature was about $1X10^{14}$ m^{-2} and at a measuring current of 100 kA m^{-2} Tc had increased from 86.5-87.1 K to 90.9 K. Radiation induced increase in Tc has also been seen in La_2CuO_4 by 2.9 GeV Kr^{+} bombardment for Kr fluence of $1X10^{12}$ to $3X10^{12}/cm^2$.[17]

Transition of the conducting behaviour of YBCO from metallic to semiconducting was observed by 2 MeV As and 1 MeV O ion irradiation[18] with slightly different activation energies of the resulting semiconductor. This was explained as an example of a metal-insulator transition due to damage induced disorder.

One of the important application of ion irradiation is patterning of the material. The fact that irradiation can change YBCO sample into amorphous phase, has been used to pattern circuits onto YBCO film[19,20]. Ion beam patterning can be used to produce planar structure in YBCO with a simple processing sequence involving the formation of a metallic mask over the areas that are to remain superconducting followed by suitable implantation

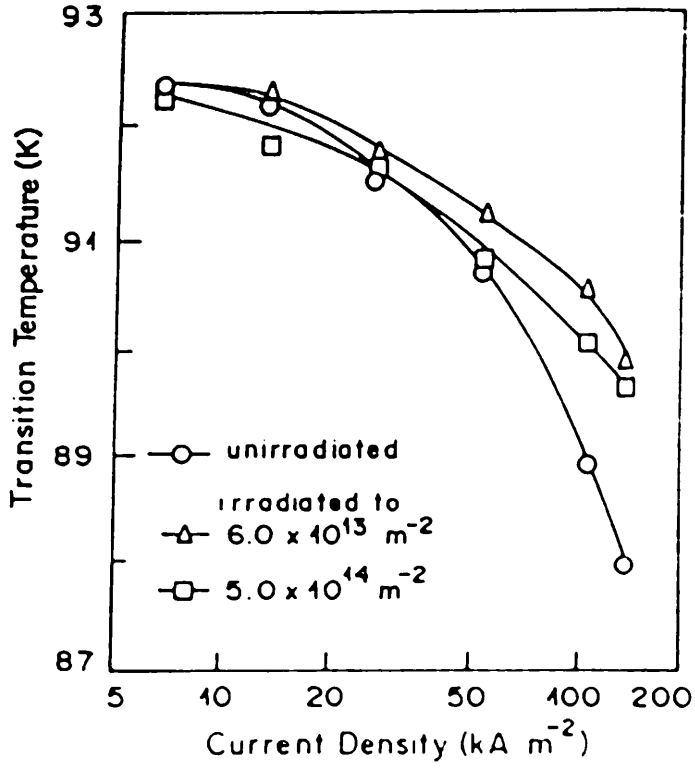

(a)

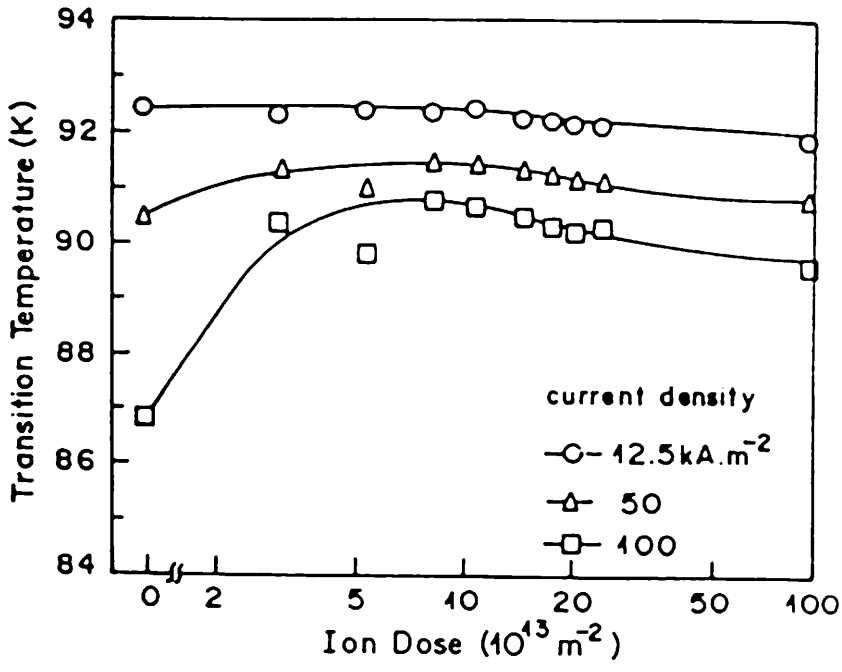

(b)

Fig.2.4. Variation of transition temperature of a 200 keV N irradiated bulk $YBa_2Cu_3O_7$ sample as a function of (a) measuring curent density and (b) dose.

to sufficient dose to render the surrounding material non superconducting and effectively insulating. A d.c. SQUID has been made in this way, operating at liquid N_2 temperature[18]. Patterned films are also important for measurement of critical current. The other way to make patterned HTS is, to use an ion beam to decompose metallo-organic precursors[21,22]. An alternative technique of patterning is to turn an insulating material into superconducting one by using ion implantation to introduce alloy constituents[23].

Another application of these experiments is composition adjustment through doping by ion implantation (fig. 2.5). Lot of investigations have been carried out for this purpose with different degrees of success[24,25]. But there are some problems associated with composition adjustment and ion doping. Considering the doping by chemical means, the amount of impurity required for HTSs is a few percent of the atomic concentration. This implies that an ion implantation dose of 10^{16} to 10^{17} ions/cm^2 or even higher is needed. Such high doses will make the superconductor completely amorphous. Post annealing may restore the crystalline structure and thus the annealing behaviour of the impurities in HTSs needs to be studied. During annealing, Ba segregation has been observed[26]. Ion implantation at elevated temperature is often used for doping in semiconducting materials such as GaAs and GaP for effective insitu reduction of the damage caused by ion bombardment. This

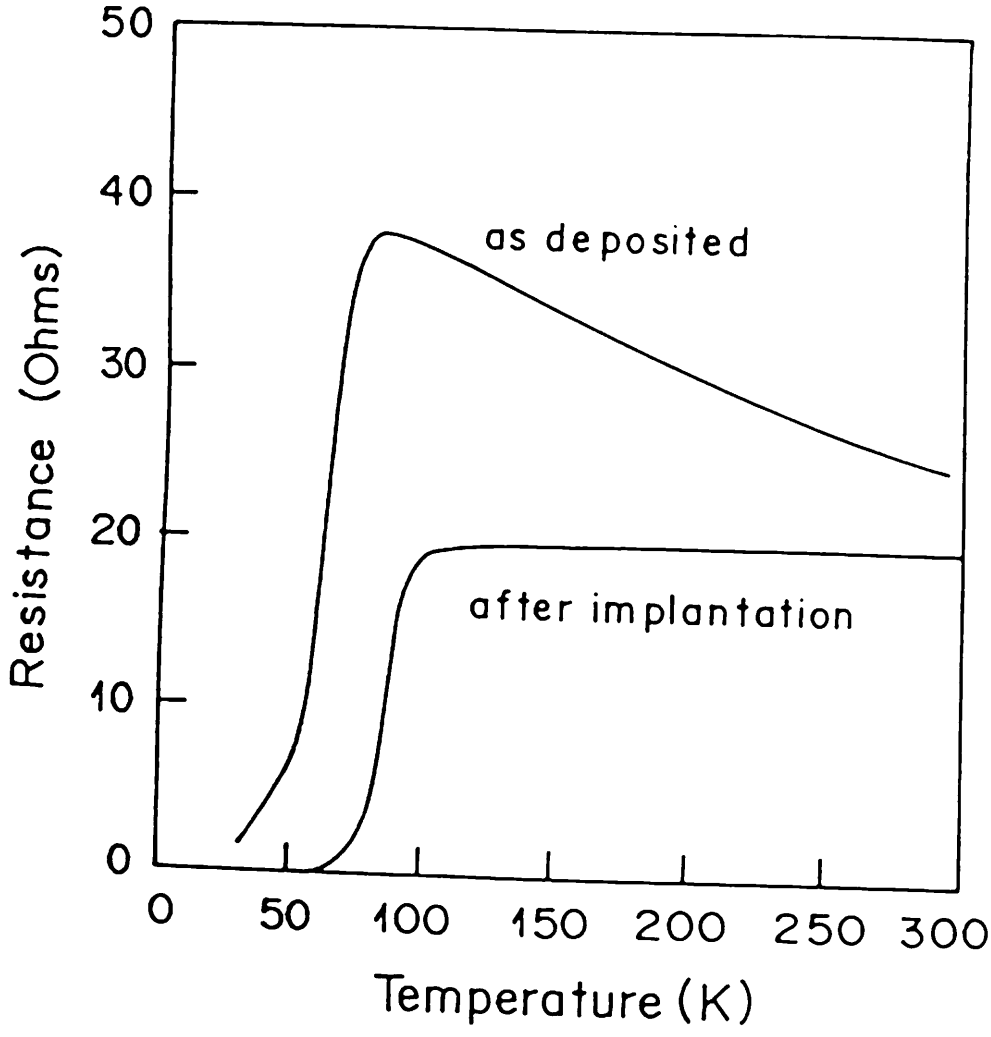

Fig.2.5. R vs. T of a YBCO film before and after ion implantation of Cu. The composition ratios were Ba/Y = 1.8 and Cu/Y = 2.5 as deposited, increasing to Cu/Y = 2.8 after implantation.

method may be useful for ion implantation in HTSs. Out diffusion of oxygen at elevated temperatures and surface decomposition may be expected.

2.3 Neutron Irradiation Effect

Unlike the case of charged particle irradiation effects, the accelerated neutral projectiles (neutrons) can directly collide with the nuclei of the host target without much of an interaction with the electron cloud. In neutron bombardment experiments on HTSC, Tc increase has been observed in La_2CuO_4 indicated by fast neutrons (E > 0.1 MeV)[27]. By irradiation with reactor fast neutrons (E > 0.1 MeV), a Tc improvement of 7 K in a YBCO pellet made by solid state reaction method has been reported by Okada et al.[28]. The irradiation was carried out at low temperature (20 K) and the sample was maintained at 77 K during the measurement and during storage. Such Tc improvements was repeatedly observed on the same sample over a period of more than 10 days. However, when irradiated at room temperature, there was no improvement in Tc of the sample. The origin of these Tc abnormalities has not been fully understood yet. In almost all the neutron irradiation experiments[29-32] transport Jc has been seen to increased while the magnetisation Jc is found to decrease. This is explained on the basis of creation of intragrain pinning sites and destruction of the weak links along the grain boundaries. The effect of neutron

irradiation is different from the effect of ion beam radiation on Jc. Most of the ion bombardment experiments show a systematic decrease in Jc with the dose, except that by Civale et al.[33] and Dover et al.[34]. In the case of neutron irradiation, almost all experiments show a systematic increase of Jc with neutron fluence up to a moderate dose of about $5X10^{17}/cm^2$. The reason behind such a difference is that there are differences of collision processes by ions and neutrons. The nuclear cross section of neutron collisions with target nuclei is less than the Rutherford cross section of ions by a factor of 10^{-7} to 10^{-8}. The penetration range of 100 KeV O^+ ions in YBCO is about 1.5 μm, but the characteristic ten times attenuation length of neutrons of same energy is of the order of a meter. Therefore, a bulk sample of a few milimeters is very transparent for fast and thermal neutrons. In contrast to ion irradiation with a fixed sample position to the incident ion beam direction, the interaction of neutrons with the superconducting sample is totally uniform. The Rutherford cross section of ions is proportional to Z^2 of the target atomic number. So the interaction with Ba (Z=56) is much more probable than the interaction with O (Z=8). In the case of neutron interaction with target atoms, the probability with different target lattice atoms is more or less equal which is clear from the table 2.2 for relative cross section.

TABLE-2.2

Particles	Relative Cross Sections			
	O	Cu	Y	Ba
Proton	1	13	24	49.4
α Particle	1	14.8	27	55.6
Neutron	1	1.8	2	1.6

2.4 Electron, Proton & α Particle Irradiation Effect

Contrary to neutron or ion irradiation where the strong increase of the transition width points to the damaging of weak links between the grains, electron seems to affect only intragrain (bulk) properties of $YBa_2Cu_3O_7$. 30 MeV electron irradiation[35] at very low temperature (5 K) and subsequent annealing at 105 K has been seen to cause an increase in Tc by about 2K at a moderate dose of $1X10^{18}$ cm^{-2} beyond which Tc seems to be saturated. Electron irradiation at higher temperature (at 185 K and 375 K) has been found to decrease the Tc (fig. 2.6). It is suggested that in case of low temperature (5K) irradiation followed by the annealing at 105K (which is slightly above the onset temperature of the superconducting transition of the particular sample), a low

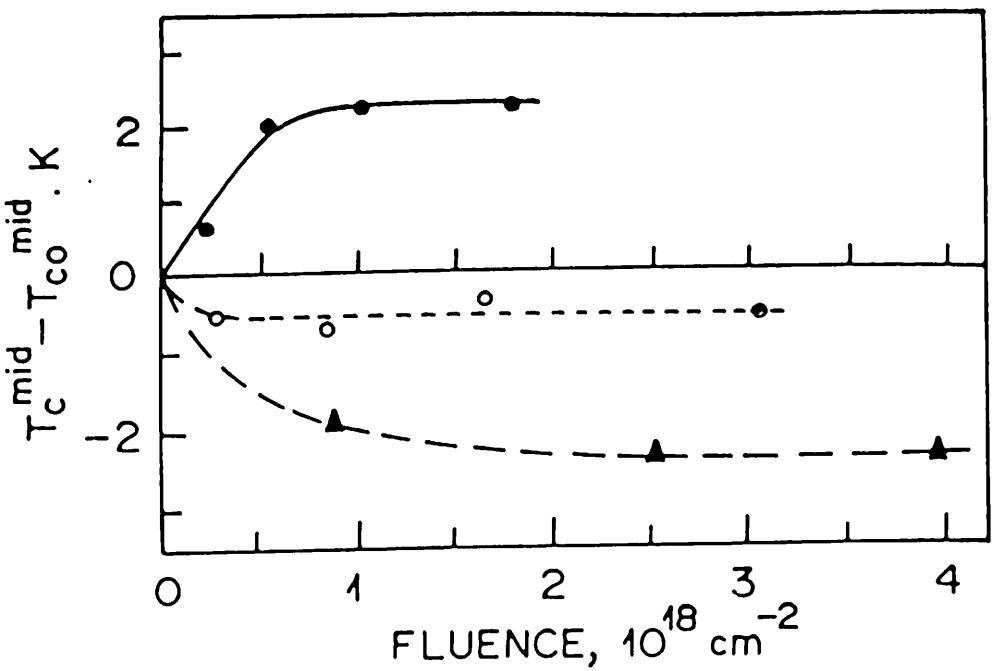

Fig.2.6. Dose dependences of midpoint temperature of the superconducting transition for YBCO samples irradiated with 30 MeV electrons at different temperatures : 5K, •; 185K, ○; 375K, ▲.

thermal mobility of vacancies may be realized. Then, in the YBCO systems, rather perfect atomic chains O-Cu-O-Cu-O may be formed with the resulting Tc increase. The saturation of the Tc value at rather low fluences was probably due to the balance achieved between formed and decaying O-Cu-O chains. The changes in the Tc behaviour at irradiation temperatures of 185 K and 375 K was attributed to an essential enhancement of vacancy mobility. In that case, the enhanced oxygen diffusion through vacancies might disturb the perfection the O-Cu-O chains and thus cause the Tc decrease. The annealing behaviour of YBCO samples irradiated by 2.7 MeV electron beam at low temperature (T_{irr} < 40 K) showed some important features[36]. The isochronal annealing behaviour of Tc after irradiation showed a significant step at 180 K overlaid by a continuous nearly temperature independent recovery of 0.1%K. As high as 40% of radiation damage has been seen to get annealed out at 320 K. This behaviour was explained as the recovery of Frenkel pairs, created by the electron irradiation, at temperatures below RT, 1) in an uncorrelated way responsible for the continuous annealing behaviour, 2) in a correlated way leading to the step at 180 K. Only few works have so far been reported about the effect of electron irradiation on critical current. Takayuki et al.[37] have found that by 28 MeV electron irradiation with a fluence of $4.7X10^{16}$ electrons cm^{-2}, Jc determined from I-V characteristics at temperatures from 75 to 85 K was enhanced by about 8%. Surprisingly in this experiment both Tc_{onset} and $Tc_{downset}$ remained

unaffected. A very systematic study of electron irradiation effect on bulk YBCO was carried out by Basu et al.[38]. They used 100, 150, 200, 250 and 300 KeV electrons at 83 and 300 K and they have shown that YBCO is insensitive to 100 KeV electron irradiation. But irradiation by higher energy electron leads to irradiation induced oxygen disordering of the oxygen atoms and vacancies, mainly by single displacement events. Their results suggest, that the displacement threshold energy for oxygen in YBCO is around 18 eV and that irradiation induced oxygen reordering occurs in YBCO at 300 K, but not at 83 K. Radiation damage of $YBa_2Cu_4O_y$ (124) superconductors induced by 1 MeV electron beam was studied by ultra high resolution high voltage electron microscopy[39] and it was found that small spots with nearly amorphous structure are formed mainly at the $(CuO)_2$ double chain layers at an early stage of irradiation and the area gradually increases with irradiation time. It was suggested that amorphization was induced by direct knock-on displacements of atoms by collisions with high energy electron beam.

Effect of proton irradiation on critical current has already been mentioned in Table-2.1 and a typical result of 2 MeV proton irradiation on YBCO is shown in fig. 2.7. Number of workers have found the critical current to increase as a result of proton irradiation[29]. Proton radiation effect was also studied on

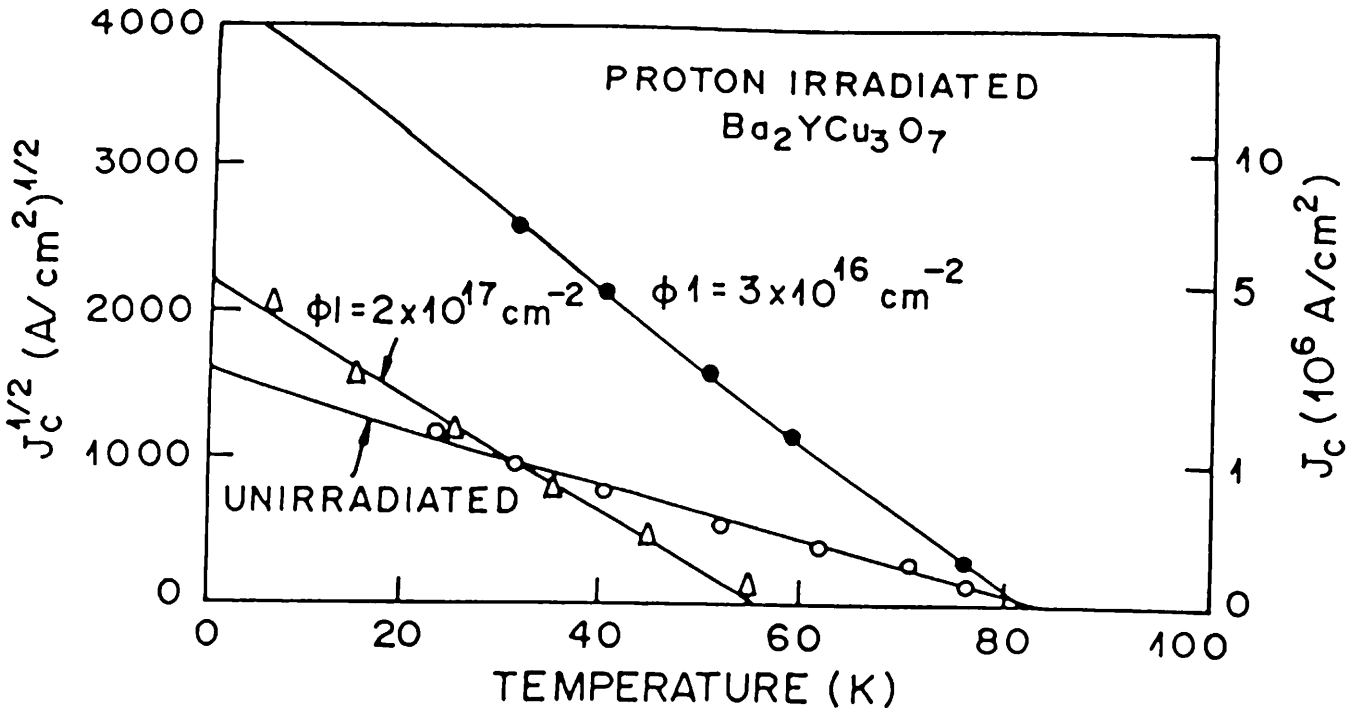

Fig.2.7. Temperature dependence of the critical current for three representative crystals at an applied magnetic field H = 1T. The lines are linear regression for $Jc^{1/2}$ (T).

superconducting ring resonator made from thin film of YBCO[40]. It has been seen that 2 MeV proton irradiation made the superconducting transition temperature Tc to decrease predictably with fluence. For temperatures below about 0.9 Tc, there was no significant change in the transmission coefficient, the center frequency, or the quality factor Q of the resonator, even for doses in excess of $4X10^{16}$ protons/cm^2 (0.04 dpa). Similarly, the low temperature surface resistance R_s of an unpatterned film did not change with irradiation. This experiment helped to evaluate theories ascribing the residual resistance R_o to weak links, flux pinning, impurities and lattice imperfections.

Irradiation with 200 KeV α particles on YBCO thin film was carried out by Vadlamannati et al.[41]. The changes in the superconducting properties was attributed to both oxygen loss as well as oxygen and cationic displacement by irradiation. This was demonstrated by study of recovery of these defects by plasma oxidation and relatively low temperature (600°C) annealing in oxygen. Plasma oxidation of films irradiated to low fluences enabled the replacement of oxygen atoms in the lattice leading to substantial recovery of Tc_0, Jc and normal state resistivity. Irradiation induced oxygen and cationic displacements and other microscopic defects were further annealed out at relatively low temperature leading to an almost full recovery of Tc_0, normal state

resistivity and even caused a slight increase of zero field Jc. A TEM study of irradiated films showed evidence that they were struturally disordered.

Based on the brief review presented above it is sure that the high Tc superconductors offer fascinating possibilities in both technology and basic science and studies of ion implantation and irradiation can potentially contribute both to the application of these materials, and to better understanding of their properties. The results have been reviewed of a series of experiments in which energetic particles were used to synthesize and modify thin films and bulk samples of high Tc superconductors. Although most of the irradiation works with high Tc superconductors were performed on YBCO system, experiments with other systems discovered later have been coming up gradually.

REFERENCES :

1 . J.G. Bednorz and K.A.Muller, *Z. Physik.* **B64,** 189(1986).

2 . D. Bourgault, S. Boufford, M.Toulmonde, D. Groult, J. Provost, F.Studer, N.Nguyen and B. Raveau, *Phys. Rev.*, **B39,** 6549(1989).

3. V. Hardy, D. Groult, M.Hervieu, J.Provost, B. Raveau and S.Bofford, *Nucl. Instru. Meth.*, **B54,** 472(1991).

4. Wei-Kan Chu Jia Rui Liu and Zuttua Zhang, *Nucl. Instr. Meth.*, **B59/60,** 1447(1991).

5. G.P.Summer, E.A.Burke, D.B.Chrisley, M.Natasi and J. Tessmer, *Appl. Phys. Lett.*, **55,** 1469(1989).

6. B.Hensel, B. Raos, S. Henke, R. Hopfengartner, M. Lippert, J.P.Stobbel, M.Vildic and G. Saemann-Ischenko, *Phys. Rev.* **B42,** 4185(1990).

7. G. J. Clark, A. D. Marwick, F. Legones, R. B. Laibowitz, R. Koch and P. Madakson, *Nucl. Instr. Meth.*, **B32,** 405(1988).

8. S. Matsui, H. Matsutera, T. Yoshitake and T. Sato, *Appl. Phys. Lett.*, **53,** 2096(1988).

9. M. O. Ruault, H. Bernas, J. Lesneur, L. Dumoulin, M. Nicolas, J. P. Burger, M. Gasgnier, H. Noel, P. Gaugeon, M. Potel and J. C. Levet, *Euro Phys. Lett.*, **7**, 435(1988).

10. M. D. Ruault and M.Gasgnier, *Mater. Sci. Eng.*, **B5**, 57(1989).

11. V. Hardy, D. Groult, M. Hervieu, J. Provost, B. Raveau and S. Bouffard, *Nucl. Instr. Meth.*, **B54**, 472(1991).

12. B. Roas, B. Hensel, G. Saemann-Ischenko and L. Schultz, *Appl. Phys. Lett.*, **54**,1051(1989).

13. A Karik, M.C.Frisehherz, J.Z.Liu, L.R. Greenwood and H.W. Webar, *Philos. Mag. Lett.*, **62**, 41(1990).

14. G. C. Xiong, H. C. Li, G. Linker and O. Meyer, *Phys. Rev.*, **B38**, 240(1988).

15. G. P. Summers, E. A. Burke, D. B. Chrisey, M. Nastasi and J. R. Tesmer, *Appl. Phys. Lett.*, **55**, 1469(1989) .

16. Kensuke Shiraishi, Hiroshi Itoh and Yasushi Akoi, *Jpn. J. Appl. Phys. Lett.*, **30**, L25(1991).

17. F. Studer, S.Provost, D.Groult, B.Raveau, S.Bouffand, M.Toulemonde, J.C. Jousset and F. Rullier-Albenque *Mater. Res. Soc. Symp. Proc.*, **99**, 877(1988).

18. A. D. Marwick and G. J. Clark, *Nucl. Instr. Meth.*, **B37/38,** 910(1989).

19. R. H. Koch, C. P. Umbach, G. J. Clark, P. Chaudhari and R. B. Laibowitz, *Appl. Phys. Lett.*, **51,** 200(1987).

20. G. J. Clark, A. D. Marwick, R. H. Koch and R. B. Laibowitz, *Appl. Phys. Lett.*, **51,** 139(1987).

21. J. V. Mantese, A. B. Catalan, A. H. Hamdi and A. L.Michell, *Appl. Phys. Lett.*, **52,** 1741(1988).

22. M. E. Gross, W. L. Brown, S. B. Disenzo, E. H. Hartford, Jr. J. J. Yeh and M. Hong, *Appl. Phys. Lett.*, **53,** 802(1988).

23. M. Natasi, J.R. Tesmer, M. G. Hollander, J. F. Smith and C. J. Maggiore, *Appl. Phys. Lett.*, **52,** 1729(1988).

24. P. N.Peters, R. C. Sisk, E. W. Urban, C. Y. Huang and M. K. Wu, *Appl. Phys. Lett.*, **52,** 2066(1988).

25. Ram P. Gupta, W. S. Khokle, J. P. Pachauri, C. C. Tripathi, B. C. Pathak and G. S. Virdi, *Appl. Phys.Lett.*, **54,** 570(1989).

26. J. C.McCallum, C.W.White and L.A. Boatner, *Nucl. Instr. Meth.*, **B40/41,** 608(1989).

27. Hiroyuki Yoshida and Kazo Atobe, *Physica C*, **156,** 225(1988).

28. M.Okada and T.Kawakubo, *Radiation Effects and Defects in Solids*, **38**, 137(1989).

29. J. R.Cost, J. O. Willis, J. D. Thompson and D. E. Peterson, *Phys. Rev.*, **B37,** 1563(1988).

30. A. Umezawa, G. W. Crabtree, J. Z. Liu, H. W. Weber, W. K. Kwok, L. H. Nunez T. J. Moran and C. H. Sowers, *Phys.Rev.*, **B36,** 1751(1987) .

31. A.C.Bodi, J.Crikai, R.Pepelnik, I.Halasz, I.Kirsehner, Gy.Kovacs, T.Porjesz and T.Trager, *Physica C*, **165**, 83(1990).

32. R. B.Van Dover, E. M. Gyorgy, L. F. Schneemeyer, J. W.Mitchell, K. V. Rao, R. Puzniak and J. V. Waszczak,*Nature*, **342**, 55(1989).

33. L. Civale, A. D. Marwick, M. W. McElfresh, T. K. Worthington, A. P. Malozemoff, F. H. Holtzberg, J.R.Thompson and M. A. Kirk, *Phys. Rev. Lett.*, **65,** 1164(1990).

34. R. B. Van Dover, E. M. Gyorgy, A. E. White, L. F. Schneemeyer, R. J. Felder and J. V. Waszczak, *Appl. Phys.Lett.*, **56,** 2681(1990).

35. V. F. Zelenskij, I. M. Neklyudov, Yu. T. Petrusenko, A. N.Slepstsov and V. A. Finkel, *Physica C*, **153-155**, 850(1988).

36. A. Hofmann, P. Schole, N. Moser, H.Kronmoller, H.Jager and F. Dworschak, *Physica C*, **153-155**, 341(1988).

37. Takayuki Terai, Tamaki Masegi, Yoichi Takahashi, Youichi Enomoto and Shugo Kubo, *Jpn. J. Appl. Phys.*, **29**, L2053(1990).

38. S. N. Basu, T. E. Mitchell and M. Nastasi, *J. Appl. Phys.*, **69**, 3167(1991).

39. Yoshio Matsui, Kasumi Yanagisawa and Naohito Fujiwara, *Jpn. J. Appl. Phys.*, **30**, L1375(1991).

40. B. D. Weaver, J. M. Pond, D. B. Chrisey, J. S. Horwitz, H. S. Newman and G. P.Summers, *Appl. Phys. Lett.*, **58**, 1563(1991).

41. S. Vadlamannati, P. England, N. G. Stoffel, R. Ramesh, T.S.Ravi, D. M. Hwang, A. Findikoglu, Q. Li, T. Venkatesan and W. L.McLean, *Appl.Phys. Lett.*, **57**, 2265(1990).

CHAPTER III

EXPERIMENTAL TECHNIQUES

This chapter is mainly devoted to the description of the various experimental procedures used in carrying out the sample preparation, characterisation and electrical measurements. The general outline of the chapter is given below.

3.1 Ceramic Preparation

This section deals with the details of synthesis of the high Tc superconductor in the bulk form. A brief description is given of the press and high temperature furnace used in the processing.

3.2 Characterization of the Samples

This section deals with the description of the various characterisation techniques used to evaluate the samples whether in bulk or thin film form. The section is devoted to a brief description of the following:

(i) X-ray diffraction (XRD)

(ii) Scanning Electron Microscopy (SEM)

(iii) Auger Electron Spectroscopy (AES)

(iv) X-ray Photoelectron Spectrocsopy (XPS)

(v) Rutherford Back Scattering Spectroscopy (RBS)

(vi) Elastic Recoil Detection Analysis (ERDA)

(vii) Iodometry to determine oxygen concentration

3.3 Ion Beam Radiation

This section devotes to the description of the low and high energy ion beam irradiation techniques, instruments & methodology of irradiation.

3.4 Thin Film Preparation

This section devotes to the method of thin film preparation of the buffer layers on Si. A brief description is given of the systems used for the thin film preparation.

3.5 Electric Measurements

Details are given of the experimental techniques used for measurement of electrical parameters of both bulk and thin film samples. Special mention is made of the on line measurements of the variation of the resistance with ion dose in case of high energy irradiation experiments.

3.1 Ceramic Preparation

Preparation of any ceramic[1] involves mainly few essential steps regardless of the fact whether it is conducting or not. The first step is to know exactly the chemical reaction due to heat treatment of a mixture of salts which results in the formation of the desired ceramic in its stoichiometric composition. Next step is the thorough mixing in an agate pestle-mortar of the weighed constituents of the salts required to synthesise the ceramic. This mixed powder is then pressed to uniform circular discs of suitable diameter and thickness in a hydrostatic press. This first stage is then referred to as pelletising. After this step the pelletised mixture is heat treated to initiate reaction process among the basic constituents. Normally the temperature required to achieve this is in excess of 800°C and the time frame used is anywhere between 6 hrs to 24 hrs. This process is called **calcination**. This step is just to decompose the constituents and help in the reaction of the components to create the ceramic. However, this step is not the final stage as the desired properties do not get acquired at this stage due to the large amount of crystalline imperfections and compositional and macroscopic variation within the bulk of the sample. These are then removed and tailored by further heat treatment in a controlled way. This step is called sintering and is not undertaken straightway after calcination. Instead, the

calcined pellet is reground thoroughly and then pelletised again and heat treated. In many situations multiple calcinations are also done to ensure uniform composition. Thus, after the final calcination the pellets are reground, pelletised and then sintered. In sintering process also there are variation in heat treatment process as demanded by the desired property of the ceramic. The sintering can be done in gas flow or air and the heating cooling cycles can be chosen. The sintering stage again can be chosen as a multiple step of grinding pelletising to achieve the desired properties. The sintering temperature is also set normally above 800°C for times anywhere between 1 hr to 100 hrs.

Now, the press used to make pellets in any of the steps mentioned above is briefly described here. The schematic of the press is shown in Fig. 3.1.

This press used is a hydraulic "Proto lifting and hoisting" type having a lift of its central piston of 150 mm. The base of the press is 2" thick iron square plate which at it's four corners house four 1" dia iron rods. On the top of these four rods rest another 1" thick square iron plate which can be fixed by bolts at any desired height. This upper square plate is used for adjusting the vertical lift of the central piston and therefore the vertical movement of the central piston can be adjusted to the required

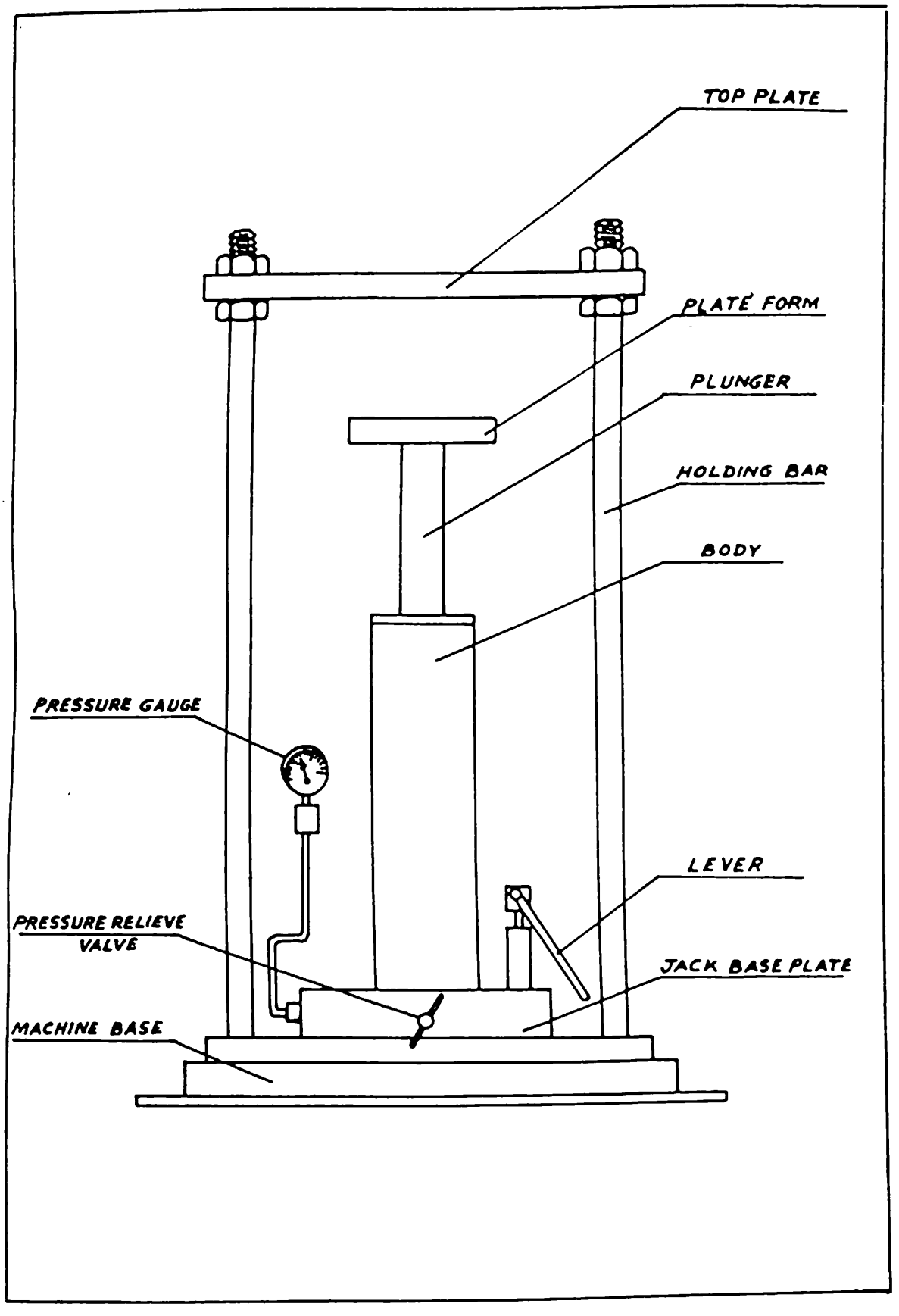

Fig. 3.1. Schematic diagram of the hydraulic press used for pelletising YBCO powders.

height. Base plate also houses one cylindrical oil filled air tight container which when pressed by another hand driven piston conveys the pressure to the central piston in turn. A small hole is driven into the base plate for air release. This hole can be air tightened using a screw and o-ring arrangement. The powder to be pressed is taken in a die-steel die of 1" diameter & kept on the main piston which is hoisted by applying a pressure through another hand driven piston until the upper part of the die rests against the upper square iron plate and when the required pressure is reached then air is leaked through base plate for lowering the central piston and the tablet.

The high temperature treatment in all the sample preparations (bulk, thin film) was done in a microprocessor controlled Furnace OMEGA Junior-I by Tempress (USA). The most important aspect of this instrument is the precise control of ramp up or ramp down time of heating or cooling schedules and the constancy of set temperature over a large linear zone between low temperature (~50°C) and high temperature (1100°C). The constancy in temperature is ± 0.1°C over a hot zone as long as 25 cm. The ramp up or down schedules can be programmed between 0.1°C min to 100°C/min. The other notable feature is that of the facility of loading 16 different recipes involving such data as ramp (in % min), temperature (T°C). At any point of time any desired

recipe can be executed as per the process. A typical photograph of the furnace used is shown in Fig. 3.2.

3.2 Characterization of the Samples

It is essential to know the nature of the sample with regard to the reproducibility in their structure and morphology and also the effect, the external perturbation have on these properties. To achieve this goal, all the samples were examined by a combination of variety of characterisation techniques, for their reproducibility in the structural, and compositional properties. Samples were characterised also to see the changes produced due to thermal and ion radiation treatments.

3.2.1 X-ray diffraction

To do X-ray, Siemens X-ray Diffractrometer was used in θ2θ Bragg-Brentano mode with the angle scanned between 3-63°. All the samples were examined without any cooling or heating. In a few cases to resolve the ambiguity in the presence of different phases the experiment was done in a slow scan mode at the peak of interest. The diffractogram was continuously received on a computer. The X-ray source was Cu at 25KV and the diffraction pattern was taken with the adjustments of the sensitivity of the intensity scale.

3.2.2 Scanning electron microscopy

Scanning electron microscopy was used to evaluate the surface microstructure of the virgin and the irradiated samples. The study of the surface morphology is very essential in order to correlate the changes occuring in the samples due to any parameter varying in the preparation of samples or to study the changes taking place due to external perturbations acting on the specimens. A JEOL SEM Model was used to study the sample. The specimens to be examined were cut into small pieces and mounted on a holder which could be inserted into the electron microscope via a load lock mechanism. Large number of samples were examined at a time to see for the relative changes in the surface morphology due to variation in the irradiation parameters or heat treatment schedules. In order to eliminate any electron beam induced modification the beam current was maintained to 10^{-10} A range.

3.2.3 Auger electron spectroscopy

The Auger electron spectroscopy technique for chemical analysis of surface is based on the Auger radiationless process. When core level of a surface atom is ionized by an impinging electron beam, the atom may decay to a lower energy state through

an electronic rearrangement which leaves the atom in doubly ionized state. The energy difference between these two states is given to the ejected Auger electron which will have a kinetic energy characteristic of the parent atom. The process is, therefore, specified by three parameters, the core from which the elastic electron is emitted, the core from which the electron fills up the vacancy and the core from which the Auger electron is emitted, e.g., KLM, MNN etc. The Auger process is shown in fig. 3.3. From the fig. the kinetic energy of the Auger electron is given by the equation,

$$E_0 = E_K - E_{L_1} - E_{L_{2,3}} - \Phi_0$$

where E_K is the energy of the level from which the elastic electron is emitted, E_{L_1} is the energy of the level from which the electron fills up the vacancy and $E_{L_{2,3}}$ is the energy of the level from which the Auger electron is emitted. ϕ_0 is the work function of the target. When the Auger transition occurs within a few angstrom of the surface, the Auger electron may be ejected from the surface without loss of energy and give rise to peaks in the secondary electron energy distribution function. The energy and shape of these Auger features can be used unambiguously to identify the composition of the solid surafce.

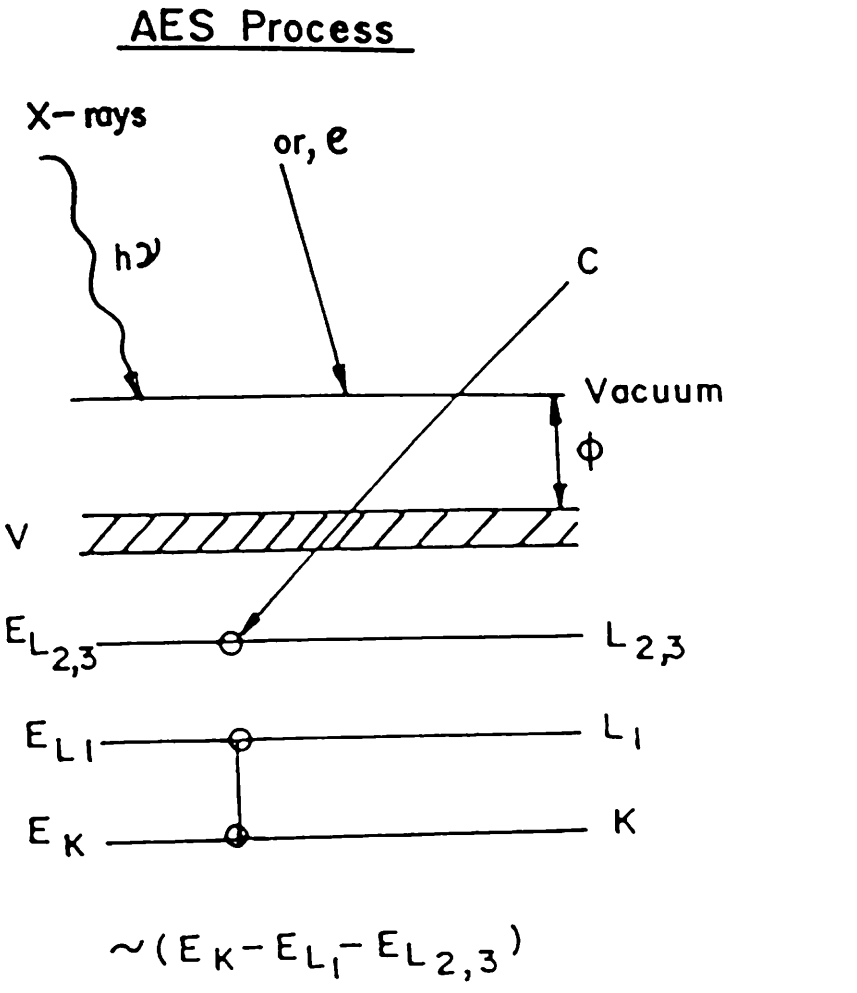

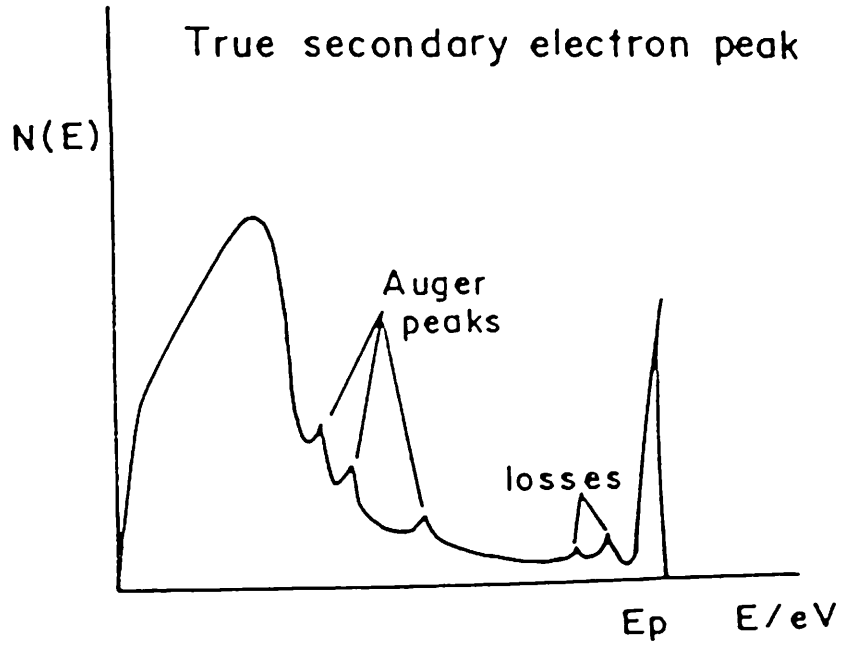

Fig. 3.3. Schematic representation of AES. The one electron energy diagram at the top is for an ideal free atom. The graph at the bottom shows the electron energy distribution leaving the solid.

An Auger electron spectroscopy system consists of an ultrahigh vacuum system, an electron gun for specimen excitation, and an energy analyzer for detection of Auger electron peaks in the total secondary energy distribution. Because the Auger peaks are superimposed on a rather large continuous background, they are more easily detected by differentiating the energy distribution function N(E). Thus the conventional Auger spectrum is the function dN(E)/dE. Electronic differentiation is readily accomplished with a velocity analyzer by superimposing a small a.c. voltage on the energy selecting voltage and synchronously detecting the output of the electron multiplier. The peak-to-peak magnitude of an Auger peak in a differentiated spectrum generally is directly related to the surface concentration of the element which produces the Auger electrons.

Unlike X-ray diffraction or scanning electron microscopy, Auger electron spectroscopy (AES) is a destructive technique. In spite of this minor shortcoming AES is a very powerful technique for materials study and characterisation when it comes to the investigation of small compositional variations and tracing of impurities in minute quantities distributed in the thickness of sample. The sensitivity of the Auger technique is determined by the transition probability of the Auger transition involved, the incident beam current and energy, and by the collection efficiency

of the analyzer. With a 3 KV, 50 μA beam and a high sensitivity cylindrical mirror analyzer, the limit of detection for the elements varies between approximately 0.02 and 0.2 atomic percent with spectrum scanning rates of 1 eV per second. All elements above helium produce Auger peaks in the 0-2000 eV range. The power of this technique lies in its capability of precise depth profiling of the samples by accurately controlled sputter etching by low energy Ar ion gun. The interference of background environment is eliminated as the samples are analysed by AES in clean ultra high vacuum condition with pressure in the range of ~ 10^{-9} torr. The amplitude of the Auger signal is dependent on the exciting beam energy and current, the transmission and resolution of the analyzer, the amplitude of the modulation voltage, the multiplier gain, and the sensitivitry setting of the lock-in-amplifier.

In the present case AES technique has been used to study the bulk and thin film samples to get to know the composition at the surface and in the depth of the material. In the case of insulating samples like MgO or $SrTiO_3$ thin film the problem of charging by primary electron beam is overcome by putting a dot of silver on the sample.

The samples to be studied are cut into small pieces and are put on a 15 position carousel which is mounted on a goniometer

in the Auger analysis chamber. The sample to be analysed is positioned in front of the probing e-beam by rotating the goniometer mounted on top of the UHV chamber. The primary e-beam energy is chosen to be 3 KeV and the Auger electrons extracted from the samples are energy analysed by a single pass Cylindrical Mirror Analyser. The relative atomic concentration of the elements were dtermined from the corresponding peak-to-peak height by using the formula,

$$C_x = \frac{I_x}{S_x d_x} / \sum_a \frac{I_a}{S_a d_a}$$

where I_x is the peak-to-peak Auger amplitude of the element x, S_x is the relative sensitivity of the element x which can be found from the Auger Handbook[2] and d_x is the scale factor of the element x, which here is taken as unity for all the elements. The summation is over one peak per element.

3.2.4 X-ray photoelectron spectroscopy

Like AES, XPS, more commonly known as electron spectroscopy for chemical analysis (ESCA), is a surface sensitive technique that uses the energy distribution of secondary electrons ejected from a target (usually, a thin film) for elemental and quantitative analysis. Surface analysis by XPS is accomplished by

irradiating a sample with monoenergetic soft X-ray and energy analysing the electrons emitted. The emitted electrons have kinetic energies given by,

$$K.E. = h\nu - B.E. - \Phi_s$$

where $h\nu$ is the energy of the photon, B.E. is the binding energy of the atomic orbital from which the electron originates, and ϕ_s is the spectrometer work function.

The surface sensitive nature of XPS is a result of the short inelastic mean free path (IMFP) of the emitted electrons and in XPS, one can assure surface sensitivity by using optimal (low) photon energies. In the laboratory most commonly used X-ray sources for XPS are Mg $K_{\alpha 12}$ (1253.6 eV) and Al $K_{\alpha 12}$ (1486.6 eV), giving rise to photoelectron energies in the desired range.

Fig. 3.4 shows the XPS process. The typical laboratory equipment includes an x-ray source that floods the sample with radiation characteristic of the anode material. In addition to the photoelectrons emitted in the photoelectric process, Auger electrons are also emitted among others due to relaxation of the energetic ions left after photoemission. The ionization occurs to a depth of few micrometers. But since the probability of interaction

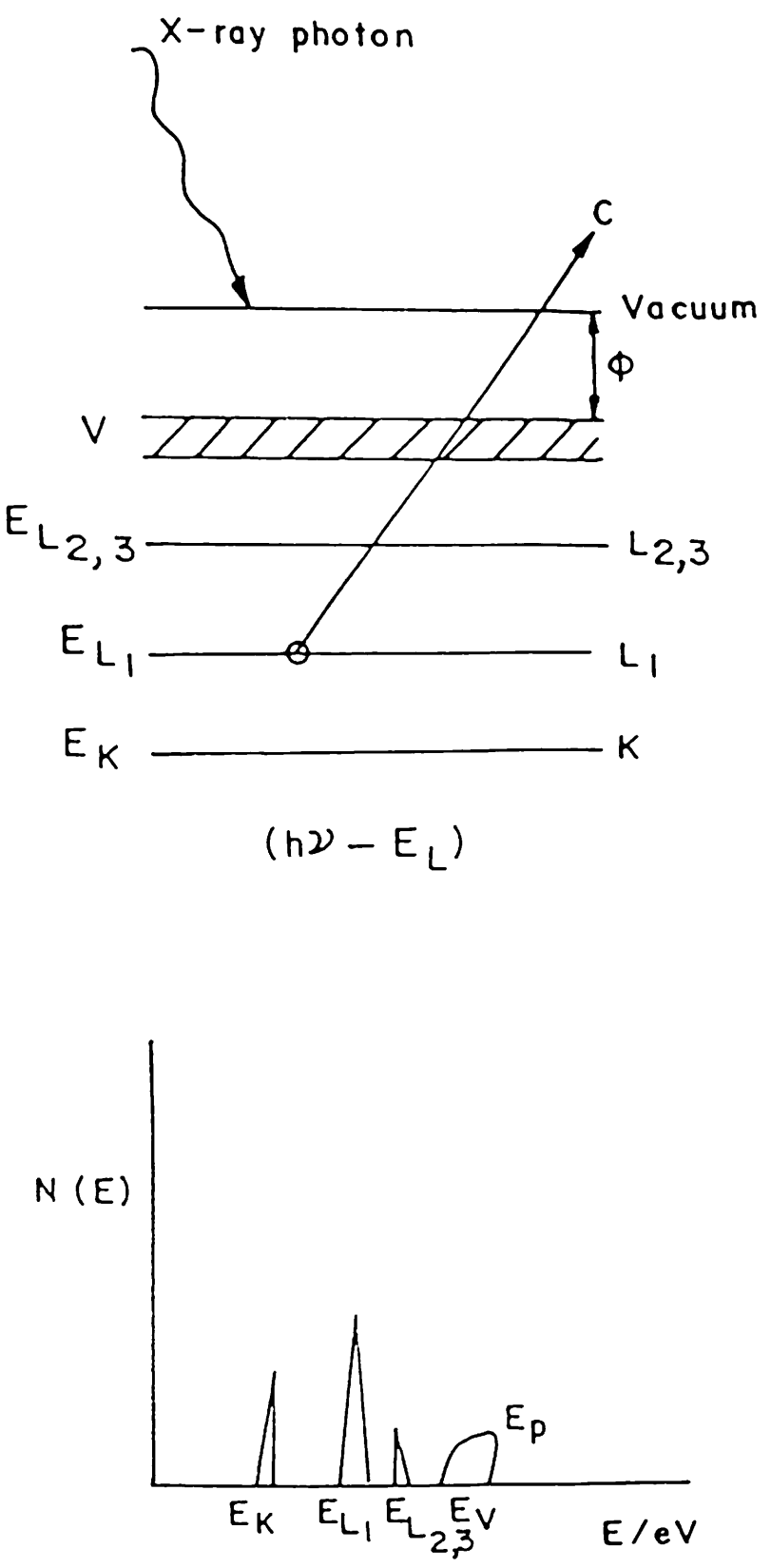

Fig. 3.4. Schematic representation of XPS. The one electron energy diagram at the top is for an ideal free atom. The graph at the bottom shows the electron energy distribution leaving the solid.

of electrons with matter exceeds those of the photons, only those electrons that originate within tens of angstroms below the solid surface, will not suffer any energy loss and are most useful in XPS studies. Nevertheless, few electrons which undergo loss before emerging from the background, are also present and are useful in many other interpretations. The electrons are detected by an electron spectrometer according to their kinetic energy. The analyser accepts only those electrons having an energy within the range of a fixed energy "window", referred to as the pass energy. Different energies are scanned by applying a retarded electrostatic field. Electrons are detected as discrete events, and the number of electrons for a given detection time and energy is stored digitally or recorded using analog circuitry.

XPS data are typically presented with the binding energy scale reversed so that kinetic energy increases to the right. For quantitative analysis the background in the XPS spectra due to the inelastically scattered electrons is subtracted by various methods and the peaks integrated to give the intensity. The quantitative analysis requires that the intensities be referred to a standard sample. The most common means of normalising intensities is to use tabulated sensitivity factors or to use laboratory-specific references. The sensitivity factors represent the relative intensities obtained in the pure elemental form. Normalization consists of

dividing the experimentally determined intensity for an element by its sensitivity factor. A better method is to use a laboratory-specific reference - a measurement of the pure element with the same equipment under the same conditions.

One of the many advantages of using X-rays rather than electrons to excite the specimen is the absence of backscattering effects. But one notable disadvantage of this scheme is that the area of the sample probed is only defined by the acceptance of the analyser, resulting in poor spatial resolution. However, with the advent of recently developed X-ray microprobes, which can produce micron or submicron spot sizes, dramatic improvement has been achieved in spatial resolution of XPS. Argon ion etching is commonly used to clean the sample surface and also to probe the composition as a function of the depth of the sample.

In the present case thin films of MgO on Si substrate has been analysed in Perkin Elmer (Model 1257) system with nonmonochromatised dual anode (Mg K_α and Al K_α) X-ray source. The sample was mounted on x, y, z, θ high precision manipulator and placed in a chamber evacuated to a pressure ~ 10^{-10} torr. The analyser is a 280 mm diameter hemispherical analyser with resolution of 25 meV. In situ cleaning of the sample was done by rastering a 2 KeV Ar^+ ion beam. The experimental data was

obtained by using PC interfaced data acquisition system using pulse counting technique. The quantitative analysis was done by normalising with sensitivity factors of different elements using ϕ–handbook. The expression for determination of the atom fraction of any constituent in a sample, C_x, is obtained by using the expression

$$C_x = \frac{n_x}{\sum_i E_i n_i} = \frac{I_x / S_x}{\sum_i E_i (I_i / n_i)}$$

where n_i, I_i and S_i are the atomic concentration, I_i is the intensity of the peak and S_i is the sensitivity factor respectively of the i th. element in the sample.

3.2.5 Heavy ion Rutherford backscattering and elastic recoil detection analysis

Ion Scattering techniques are very powerful and versatile for material characterization. Rutherford Back Scattering (RBS) spectrometry is a well established tool for material analysis[4]. The advantages of this technique are : the speed of the technique is fairly high, it does not require ultra high vacuum and most important of all is that its ability to percieve non-destructively the depth distribution of atomic species below the surface of the material and the quantitative nature of the results. In backscattering

experiments a collimated beam of energetic particles from a particle accelerator is made to fall on a target material (either in the bulk form or thin film) which is to be characterized. The projectile beam either falls at normal incidence or at an angle to the sample surface. A detector, which is generally a solid state detector (silicon surface barrier detector (SSBD)), is placed at some back angle which transforms the particle counts at that angle into equivalent electrical signal. This signal after preamplification and amplifiacation in successive steps is then fed into a multichannel analyser (MCA). The signal is then processed by the MCA, which subdivides its magnitude into a series of equal incremants. Each increment is numbered and is referred to as a channel. Modern MCAs contain thousands of channels. An event whose magnitude falls within a particular channel is registered there as a count. At the termination of the experiment, each channel has registered a certain number of counts. The output of MCA is thus a series of counts contained in various channels. Therefore, the count is equivalent to signal height, i.e., the concentration of the atomic species and the channel number is equivalent to energy of the backscattered projectile. The high energy edge of the signals from different masses appear at different places. The signals from the heavy masses will appear at higher energies and that of light masses at low energies because of the energy transfer to the target atoms. In case of thin films the low energy edge of the signals

depend on the depth of the films and also on the specific energy loss value of the projectile inside the target. Therefore, the energy scale can be converted into depth scale. The mass resolution is the minimum mass seperation that can be detected by the detector. The depth resolution is defined by the energy width between the positions at 12% and 88% of the full height of a signal that corresponds to an abrupt change in sample composition. For projectiles with same energy and flux, the scattering cross section gives the scaling factor for the scattering yoelds from different elements. The relative concentration ratio of two elements transforms into relative yields by a ratio given essentially by cross section ratio of the elements or by $(Z_1/Z_2)^2$ with some correction, where Z_1 and Z_2 are atomic numbers of the elements under study. Therefore, from output spectra of MCA, one can determine the stoichiometric abundance ratio in compound target, surface impurities, impurity distribution in depth, thickness of a thin film target etc. depending upon the requirements of the characterization.

In conventional RBS 2 MeV He ions are used as the ptojectiles. Now a days heavy ion backscattering (HIBS) is being used with greater advantages in the characterization procedures[5]. The advantages associated with the use of heavy ions are :

1) In conventional RBS with light target projectiles (He^{++}) mass

resolution becomes poorer for heavy target elements. But using heavy projectiles, better matching of projectile's mass with that of the target atoms for heavy targets is achieved. Also the energy seperation δE corresponding to a given mass seperation δM is increased with the use of heavy projectiles. Thus, the mass resolution is improved by using heavy projectiles.

2) Higher stopping power, which, under the right scattering conditions, can lead to eqivalent or better depth resolution than that achievable with normal RBS.

3) The optimum depth resolution can be achieved at higher angles of incidence to the surface with HIRBS reducing the effect of surface roughness on the attainable depth resolution.

4) The higher scattering cross section leads to greater scattered particle yield per projectile.

In backscattering it is very difficult to take out the signals from light target atoms, viz., O, N, among the other heavier target species. Elastic Recoil Detection Analysis (ERDA)[6] is a complimentary technique to avoid this difficulty of backscattering. In this technique the detector detects the recoils of light target particles at a suitable forward angle. In ERD it is in principle possible to perform virtually background free analysis of light

elements in surface layers. In order to fulfil the requirements for background free detection one has to stop the unwanted particles. In the conventional set up of ERD the heavy particles are stopped in an absorber foil infront of SSBD and only the energy of the tarnsmitted particles is determined. Due to the differences in energy loss of the different recoil elements, the presence of the absorber foil results in mass seperation.

In the present case e-beam evaporated $SrTiO_3$ thin films has been analysed by simultaneous HIBS and ERDA using 55 MeV Si ions from 15UD Pelletron at Nuclear Science Centre, New Delhi. Also the behaviour of the films under different annealing temperature has been studied with these techniques.

Collimated Si ions were bombarded on the sample which was mounted on a 1.5 m diameter general purpose scattering chamber. The chamber has detector arm which is concentric with rotation axis of the sample holder. The beam spot was about 2 mm in diameter and the current was 1 to 2 pna. The target was tilted at an angle of 30° so that the detection of elestic recoils and backscattered ions can be carried out simultaneously. It allows investigating Sr and Ti in backscattered ion spectrum at 135° and O in recoil spectrum at forward angle of 45°. Silicon surface barrier detector of 60 μm depletion depth with a 2X4 mm^2 slit infront

of it, was used for recording recoil energy spectrum. The detector subtended a solid angle of 0.4 millisteraradian (msr) and an angle of 1°. A 30 μm polypropylene foil was used infront of the detector to stop unwanted recoils of Si, Sr and Ti. Backscattered ions were detected in a 600 mm^2 surface barrier detector of 60 μm depletion depth. Detector was kept at a distance of 140 mm and it subtended a solid angle of 30.6 msr. A schematic description of the simultaneous HIBS and ERDA experiment is given in fig. 3.5.

3.2.6 Iodometry to determine oxygen concentration

Iodometry is a destructive but sufficiently accurate chemical test to determine the 'y' value in $YBa_2Cu_3O_y$ and this test is important because the 'y' value plays a detrimental role in the superconductivity of this family of compounds. The different steps of the method and the procedure to calculate the 'y' value is described as following.

Titration I :

1. The powdered sample of weight W_1 (~ 30-40 mg) is taken in a three neck flask.

2. Cover the sample in the flask with 1 gm of KI.

3. Create inert gas (say N_2) atmosphere in the flask.

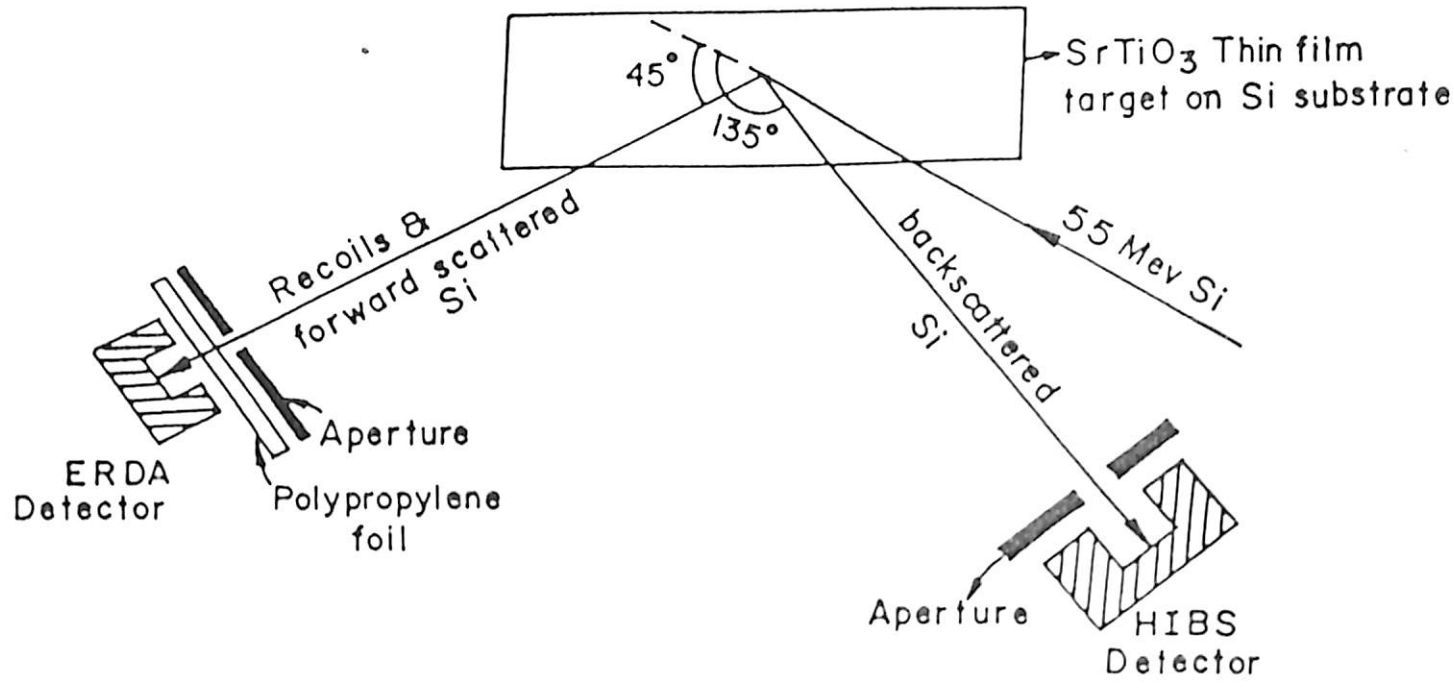

Fig. 3.5. Schematic description of the simultaneous HIBS & ERDA experiment.

4. Add 5 ml of 6N HCl in the flask.

5. Stir with a magnetic stirrer till the sample is completely dissolved. The colour of the solution turns from reddish to yellow. Care is taken that no black specks of the YBCO is left undissolved.

6. Add 5 ml 6N NH_4OH to the flask. The colour of the solution changes to a persistent greenish blue colour.

7. Add 2 ml 85% concentrated H_3PO_4 and the colour turns reddish yellow

8. Titrate the solution in the flask with 0.01N $Na_2S_2O_3$ until the colour slowly changes to pale yellow.

9. Add 1 ml freshly prepared starch solution and the colour of the solution immediately changes to black violate.

10. Continue titration with 0.01N $Na_2S_2O_3$ till the end point of the titration is reached when the solution becomes totally colourless. Then the volume of the $Na_2S_2O_3$ spent in titration is noted down and is denoted by V_1.

Titration II :

1. Take powdered YBCO sample of weight W_2 (30-40 mg) in the three neck flask.

2. Dissolve in 5 ml 6N HCl and the solution becomes colourless.

3. Add 10 ml water and raise the temperature of the solution to 60°C.

4. Add 6N NH_4OH to this hot solution and the colour changed to persistent blue.

5. Add 2 ml of conc. (85%) H_3PO_4 and as a result the solution turns colourless.

6. Cool the solution to room temperature and create neutral atmosphere (N_2 in the present case) inside the flask.

7. Add 10 ml KI to the solution and the colour becomes deep yellow.

8. Continue titration with the same recipe as described from step 8 of titration I and the volume V_2 of $Na_2S_2O_3$ spent in the titration is measured.

Calculation to determine 'y' :

The oxygen valency in the compound is given by the formula

$$P = (V_1/W_1)/(V_2/W_2) + 1$$

The oxygen content y = total +ive valency (except Cu)/2 + 1.5P

and, therefore, in case of $YBa_2Cu_3O_y$, $y = 3.5 + 1.5P$

A set of titration has been done and the value of (V_1/W_1)

and (V_2/W_2) has been calculated from different combinations in the set of data. The 'y' values are calculated from these values of (V_1/W_1) and (V_2/W_2) and those values of 'y' exceeding 7 are discarded. The 'y' value of the sample under study is then determined by averaging the valid 'y' values.

3.3 Ion Beam Radiation

The center point in the present thesis on the study of high Tc superconductors is to examine the effect of energetic particles on the material properties. The energy range of the projectiles employed was 75-100 MeV, although few samples are also irradiated with 150 KeV ^{14}N. The low energy irradiation was done in the VARIAN implanter of CEERI, Pilani. All the high energy irradiation experiments were carried out with the 15 UD Pelletron acceleartor in Nuclear Science Centre, New Delhi. In this context it is considered essential to go into a brief description of the Pelletron accelerator where majority of the irradiation experiments described in this thesis were performed.

3.3.1 The pelletron at NSC

The 15 UD 16MV Pelletron accelerator at Nuclear Science Centre (NSC) is a large tandem van de graff type electrostatic

accelerator capable of accelerating almost any ion beam from hydrogen to uranium to energies from a few tens of Mev to hundreds of Mev. A schematic diagram showing the basic principle of acceleration of ions in a tandem accelerator is given in fig 3.6. Fig 3.7. shows a schematic diagram of the accelerator facility at NSC. Different important parts of the accelerator at NSC are described briefly in the following few subsections.

3.3.1.a The injector system

Negative ions are produced in an ion source housed in a high voltage deck biased to a negative potential (e.g. -400 KV at NSC). An accelerator tube system having proper insulation and voltage gradient follows the high voltage deck and pre-accelerates the ions produced in the source travelling to the ground potential. The required ion beam is then selected using the injector magnet. The injector is equipped with three types of ion sources:

i) Source of negative ions by cerium sputtering (SNICS) which can produce negative ions of almost all elements (except He, Ne, Ar, Kr and Xe).

ii) Alphatross for marinly He ions and

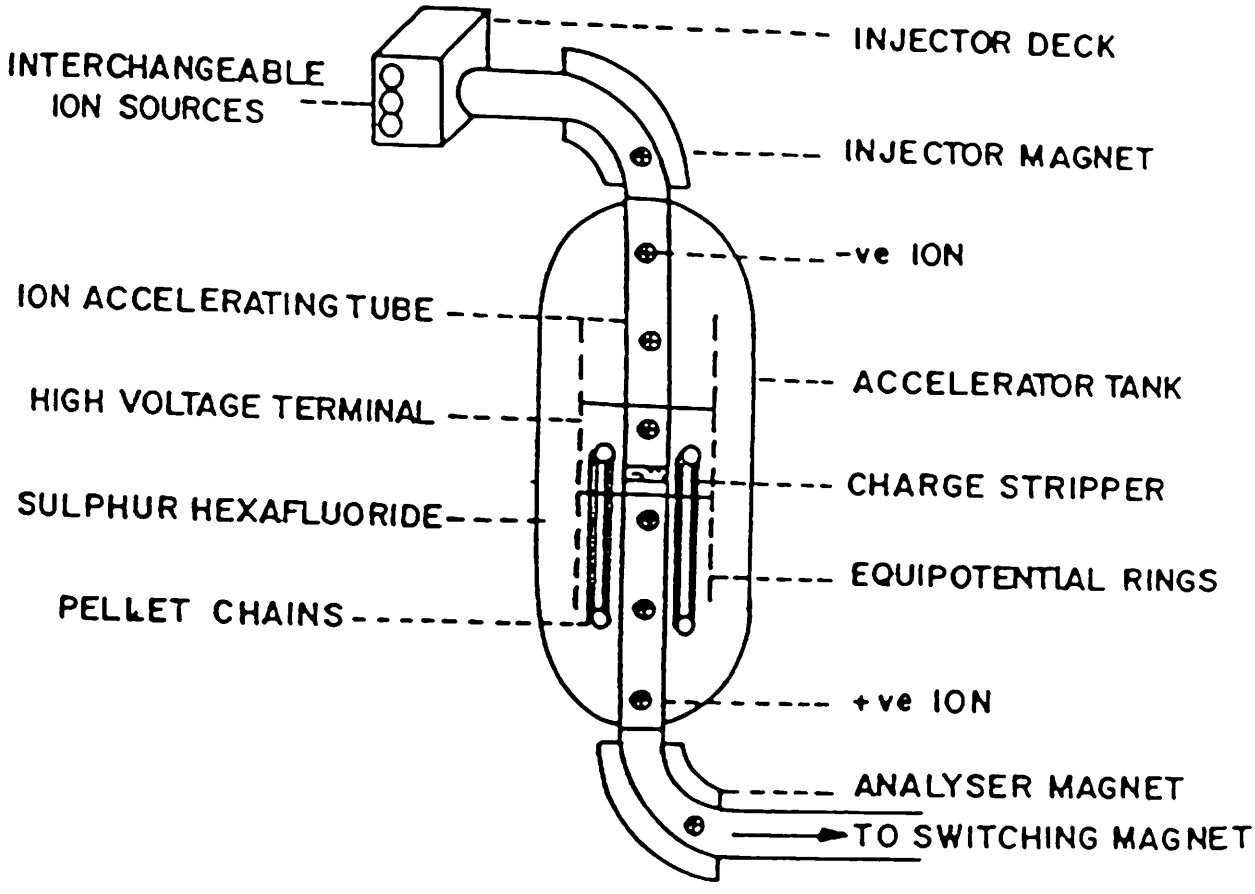

Fig. 3.6. The basic principle of acceleration of ions in a tandem accelerator.

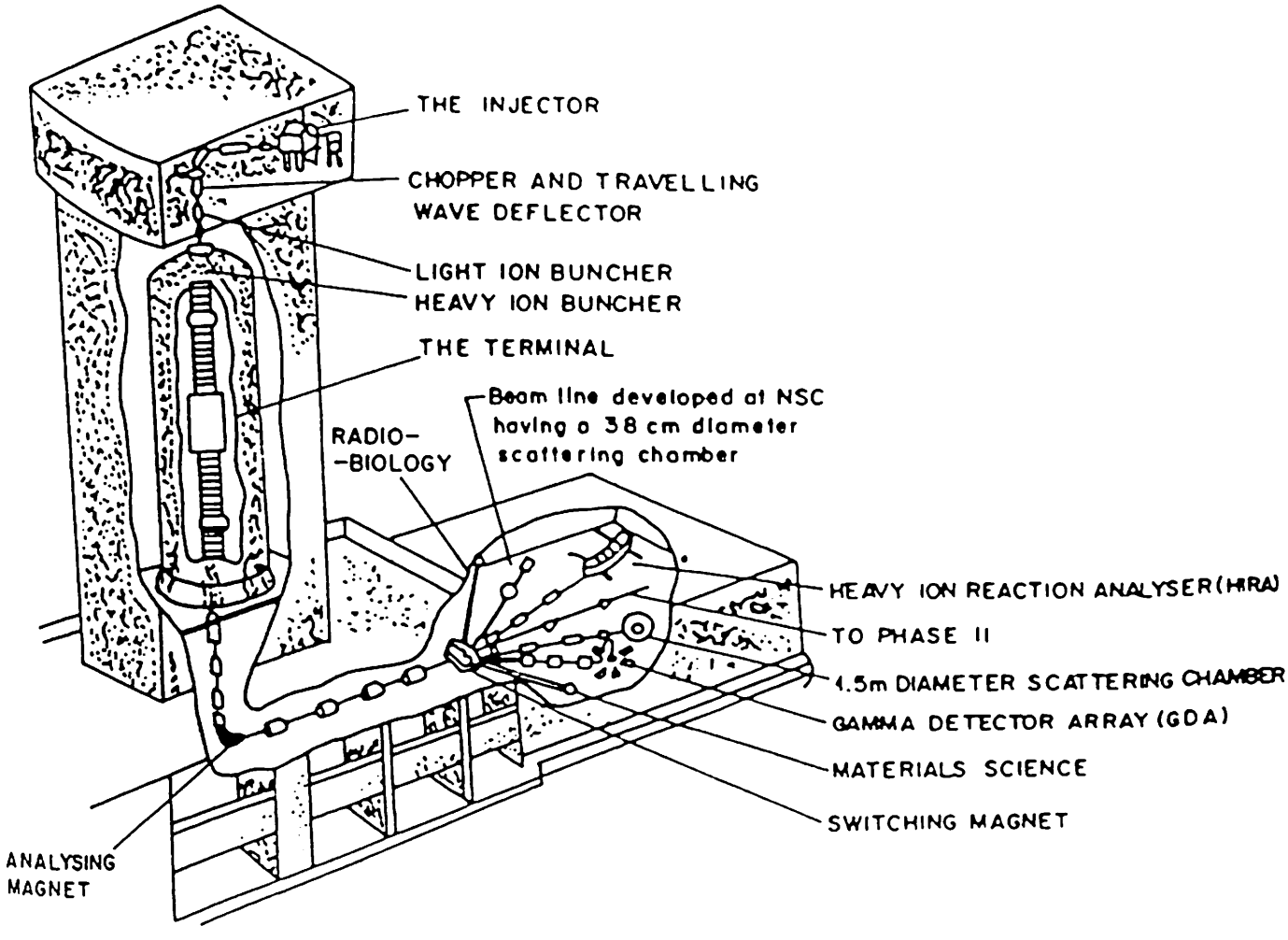

Fig. 3.7. The schematic diagram of the accelerator facility at NSC.

iii) Duoplasmatron mainly for high quality H^- ions.

3.3.1.b Description of the accelerator

This electrostatic accelerator at NSC is installed[7] with a vertical configuration in an insulating tank which is 26.5 m long and 5.5m in diameter & filled up with SF_6 as an insulating gas. Inside this tank, is the high voltage terminal about 1.52 m in diameter and 3.81 m in height. This terminal can be charged to a high potential that can be varied from 4 to 15 MV. This terminal is connected to the tank vertically through ceramic titanium tubes called accelerating tubes. A potential gradient is maintained through these tubes from high voltage to ground from top of the tank to the terminal, as well as from terminal to the bottom of the tank.

Negative ions from the ion source are injected in the accelerator & accelerated towards the terminal. In the terminal, negiative ions are stripped off a few electrons & thereby converted to positive ions, which are further accelerated as they proceed to the bottom of the tank at ground potential. As a result the ions emerging out of the accelerator gain energy given by

$$E \simeq V(q+1)\ MeV$$

Where V is the terminal potential (in MV) and q is the charge state of the ions after stripping. These high energy ions are then analysed to the required energy with the help of a 90° bending magnet known as analyser magnet directed to the desired experimental area with the help of a multiport switching magnet which can deflect the beam into any of the seven beam lines in the beam hall.

The insulating column which supports the high potential terminal consists of thirty 1 MV modules, 15 on either side of the terminal. The upper portion of the column is referred to as the low energy section while the portion below the terminal as the high energy section. Two shorted sections with no potential gradient, commonly known as dead sections, are provided one each in the low and high energy column sections for equipment housing. Both are provided with an electron trap and a sputter ion pump. The low energy dead section (LEDS) is also provided with an electrostatic quadrupole triplet lens while the High Energy Dead Section (HEDS) is equipped with a second foil stripper assembly. A shorting rod system is also provided for temporarily shorting selected column modules without entering the pressure vessel.

Running a normal cable from power source at ground potential to a device sitting at high potential is quite difficult

because of problems associated with insulation. Two insulating shafts run from each ground end to the terminal and are used to drive four 400 cps generators, which provide power for the equipment such as pumps, strippers, beam diagonostic and control equipments etc. housed in the dead sections and the terminal.

3.3.1.c Vacuum System

For the production, transport and acceleration of the ions it is very essential to have the smallest possible number of air atoms/ molecules present in their path. The presence of these atoms/ molecules will cause scattering and recombination of the ion beam and eventually lead to its loss. Because of this the ions always travel through tubes evacuated to very low pressure. For this, different types of vacuum pumps are used at different locations to establish very high vacuum from the ion surce to the experimental areas. The beam line upto the target chamber was maintained at 10^{-9} torr by means of a series of ion pumps.

3.3.1.d The Charging System

An important aspect of the pelletron accelerator is the generation of the high voltage at the terminal. This is done using the two charging chains present in the accelerator. The chain

comprises of alternating conducting and insulating links[8]. The conducting links are hollow cylindrical steel structures, approx. 3.2 cm long, called pellet (hence the name pellelron). The insulating links are made of a material which has small elongation, high Young's modulus, high dielectric constant, low reactivity with insulating gases like SF_6 and freon and high resistance to repeated bending. In this system, there are two chains run at 15m/sec, which carry approximately 150 μA per chain. The chains are located in the high energy section.

The pelletron charging system is shown in fig. 3.8. The functions of the different components are described below.

1) I_1 is held at -V and induces positive charge q on the pellet, negative charge flowing to ground through P_1.

2) The charged pellets are carried to the terminal. On reaching the terminal they come in contact with P_2 and transfer their charge to the terminal.

3) I_5 forms a capacitative gap with pellets. Now since Vq/c, for a given charge, if we decrease crpacittance, potential increases and vice versa. Hence capacittance as I_5 is adjusted to hold potential V. This allows W_1 to pick up charge and transfer it to I_3. Since I_5 is connected to

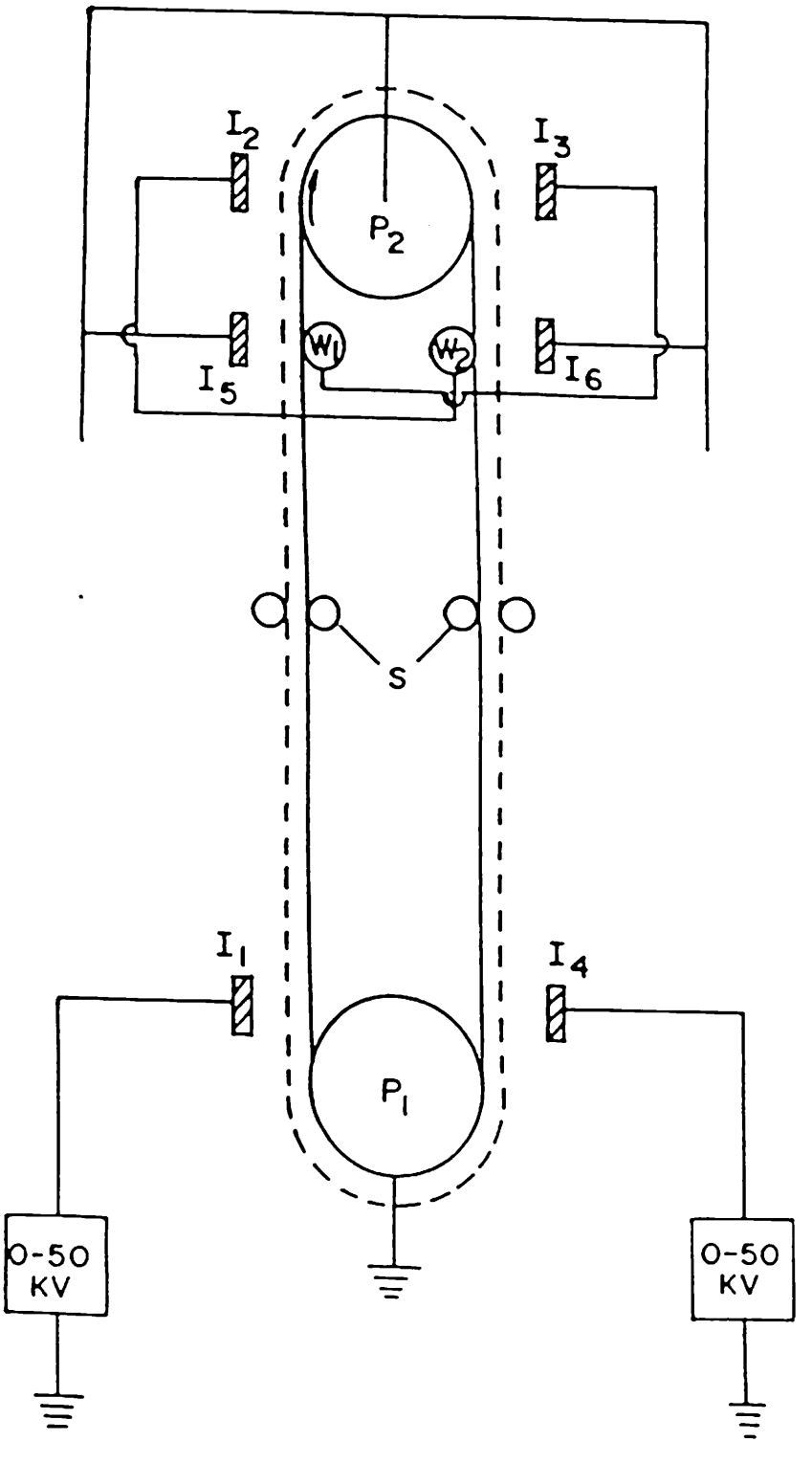

Fig. 3.8. The schematic diagram of the charging system in the pelletron.

terminal and if terminal potential is zero, W_1 picks up charge and transfers it to I_3 till potential of I_3 is raised to 0+V.

4) Since I_3 is at potential V w.r.t. terminal, it induces negative charge on the pellets, hence doubling the charging current.

5) Negative charges are carried to the motor end where they come in contact with P_1 and are carried to ground.

6) Pellets approaching either pulley are at a considerably higher potential w.r.t. them. When they come into contact with them charge is drained very quickly and sparking occurs. I_6 forms a capacitative gap with pellets and allows W_2 to pick up charge and transfer it to I_2. Again, I_6 is connected to terminal and is at terminal potential. Hence, I_2 is charged to 0-V. There is a high potential difference between P_2 and the pellets and as the distance between the two decreases, a high field develops which can lead to sparking. However, the negative potential on I_2 neutralizes the effect of the field and suppresses sparking. Also I_2 holds the charge on the pellets and retards the proccess of discharging of the pellet.

7) I_4 is held at potential V with the help of a power supply and performs a function similar to I_2, that of suppressing negative charge at P_1.

Spacing between the pellets and inductors plays a very important role in the charging process. Generally, I_1 to I_4 are equally spaced whereas I_5 and I_6 are adjusted such that I_2 is at -V and I_3 at +V w.r.t. terminal.

3.3.1.e The Control System

The accelerator is controlled from the control room using a control software running on a PC-AT 386 computer with EGA graphics and running under MS-DOS. The hardware consists of a main CAMAC (Computer Automated Measurement and Control) crate connected to the PC through a crate controller supporting the Auxiliary controller Bus (ACB). The status display and the meters help in the continuous monitoring of the status of the important parameters.

The devices to be controlled at the various locations of the accelerator are connected to the CAMAC crates provided nearby and the signals from the computer through the main CAMAC crate in the control room to the crates placed at other locations and vice versa are sent through a CAMAC serial highway.

The devices located at high potentials (i.e, the terminal, the dead sections and the high voltage deck) are connected to the CAMAC by using fibre optics cables. In this method the voltage

signal going to a device or coming from a device is first converted to a frequency signal (using voltage - to - frequency converters or frequency-to-voltage converters). These frequency signals can then be transmitted as optical pulses.

For irradiation experiment on bulk samples, the samples were cut into small rectangular bars and were mounted on specially designed target holders housed in the metal chambers having a base pressure of at least 10^{-7} torr. For low temperature irradiation, the samples were mounted on patterned glass epoxy board which were fixed on a cold finger cooled by liquid nitrogen. The glass epoxy mount ensured that the temperature of the material was above the transition temperature. This factor is important for insitu R vs. dose measurement in case of low temperature irradiation. In all the irradiation experiment with high energy beams the ion fluence was varied between ~10^{10}/cm^2 to ~10^{16}/cm^2. The fluence of the beam was determined by counting the number of particles bombarding the sample using a current integrator and a counter. The secondary electrons coming out of the sample were suppressed by an electrostatic suppressor.

3.4 Thin Film Preparation

Thin film samples used in the present work were prepared

by physical vapour deposition employing electron beam evaporation, d.c. magnetron sputtering and laser evaporation.

In the case of thin film preparation for $YBa_2Cu_3O_7$, MgO, YSZ, $SrTiO_3$ or $LaAlO_3$ single crystal substrates of $1cm^2$ size were used. The dielectric films on Si were deposited by e-beam evaporation of pressed pellets of $SrTiO_3$ and MgO powders. The depositions were done in an oil free ion pumped Varian VT118A UHV system having a base pressure of $1x10^{-8}$ mbar. The system used is as shown in Fig. 3.9. The preparation chamber, 18" in diameter, is of stainless steel with Meander type water cooling arrangement. Rough pumping of the chamber is done by three sorption pumping units and the final base pressure is obtained by seven triode ion pumps of 110 l/s speed each. Essentially the system contains two e-guns of 10 KW each with a water cooled hearth of 40 cc crucible. The substrates are mounted on a stainless steel planetary holder which can be fixed to a rotary feed through. 2" diameter Si wafers were used in all the depositions. The thickness of the samples for deposition is monitored with the help of an INFICON XTC quartz crystal microbalance fitted in the stainless steel evaporation chamber. The pressure in the chamber is measured by 890 Ar Varian ionization gauge of Bayerd-Alpert type. As the dielectric used are highly non conducting great care had to be exercised in the evaporations. Before the actual

Fig. 3.9. The Varian VT118A UHV system used for e-beam deposition of thin films.

evaporation could be commenced the charge in the electron gun hearth had to be carefully degassed at the minimum of the power. This outgassing normally resulted in large pressure outbursts resulting in tripping of the system. Thus, after ascertaining the stable vacuum condition of the system the actual deposition of the film was carried out. In this way, the buffer layers of $SrTiO_3$[9] and MgO films were deposited on Si for further usage for deposition on YBCO thin or thick film. Before depositing the thin films on Si substrates they are cleaned by standard RCA cleaning procedure. The cleaning steps are as follows :

1. Ultrasonic cleaning in trichloroethelene (duration 10-15 min.).

2. Keep wafers in boiling trichloroethelene (duration 10-15 min.).

3. Rinsing in acetone (duration 10-15 min.).

4. Ultrsonic cleaning in acetone (duration 10-15 min.).

5. Keep wafers in boiling acetone (duration 10-15 min.).

6. Rinsing in deionised (DI) water (resistivity 18 M-ohm cm) (duration 10-15 min.).

7. Keep the wafers in boiling Di water (duration 10-15 min.).

8. Keep the wafers in boiling solution of NH_4OH : H_2O_2 : H_2O :: 1 : 1 : 5 (duration 10-15 min.).

9. Rinsing in DI water.

10. Keep in boiling DI water.

11. Keep in boiling solution of HCl : H_2O_2 : H_2O :: 1 : 1 : 6 (duration 10-15 min.)

12. Rinsing in DI water.

13. Keep in boiling DI water.

14. Give 1-5 sec dip in buffered HF (buffer is NH_4F)

15. Rinse in DI water for 10 min.

16. Blow dry the substrates in N_2 gas.

17. Keep in boiling solution of HNO_3 : HF :: 10 : 1.

Step 1 to step 7 is necessary to remove dirt and grease on the surface. Step 8 to step 13 is needed to remove metallic impurities on the surface. Step 14 is necessary to remove oxide layer on the substrates. For immediate use of substrates, cleaning upto step 16 is sufficient. They can remain oxide free for about 30 min. after cleaning. But for longer duration oxide passivation, step 17 is necessary.

The YBCO thin films are deposited by d.c. magnetron sputtering and by laser ablation technique in other laboratories.

3.5 Electric Measurements

Standard four terminal network was used to conduct the routine electrical resistance measurements. The Tc measurements were done by a set of Keithly current source and Keithly multimeter using a laboratory made cryostat shown in Fig. 3.10. The measurement of the low energy irradiated samples was done ex situ after the implantation by using the Keithly set of instruments. In the case of high energy irradiations the R vs. dose measurements were done on line as a function of ion dose up to a dose ~ 10^{16} ions/cm^2. In this case the Keithly set of instruments were connected to a PC and an automatic data acquisition was done at each ion dose in both the direction of sample current.

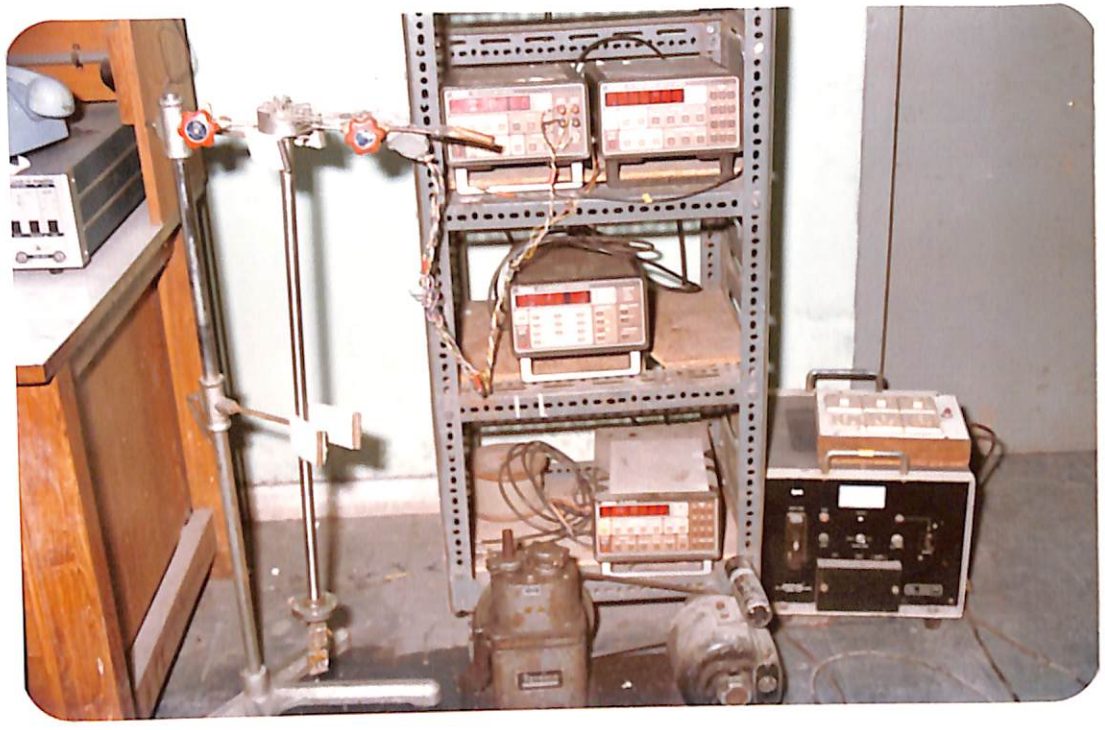

Fig. 3.10. The laboratory designed cryostat used for R vs. T measurement. The photograph at right shows the close view of a typical four probe sample connection on the cryostat.

References

1. W.D. Kingery, *Introduction to Ceramics*, John Willey & Sons, Inc.

2. *Hand Book Of Auger Electron Spectroscopy*, Lawrence E. Davis, Noel C. MacDonald, Paul W. Palmberg, Gerald E. Rinch and Roland E. Weber, PERKIN ELMER CORP. (1978).

3. *Hand Book Of X-Ray Photoelectron Spectroscopy*, C. D. Wagner, W. M. Riggs, L. E. Davis, J. F. Moulder, G. E. Muilenberg (Editor), PERKIN ELMER CORP. (1979).

4. Nei-Kan Chu, James W. Mayer, Marc-A Nicolet, *Backscattering Spectrometry*, Academic Press (1978).

5. P. Muller, G. Ischenko, *J. Appl. Phys.*, **47**, 2811 (1976).

6. J. L. 'Ecuyer, C. Brassad, C. Cardinal, B. Terrcault, *Nucl. Instr. Meth.*, **149**, 271 (1978).

7. D. Kanjilal, S. Chopra, M. M. Narayanan, I. S. Iyer, V. Jha, R. Joshi and S. K. Dutta, *Nucl. Instr. Meth.*, **A328**, 97 (1993).

8. R. G. Herb, *Nucl. Instr. Meth.*, **122**, 267 (1974).

9. Sanjit K. Das, P. K. Ashwini Kumar and S. K. Sarkar, *J. Phys.: Condens. Matter*, **6**, L445 (1994).

CHAPTER IV

RESULTS, DISCUSSION & CONCLUSIONS

The present chapter deals in total the presentation of the various results, and their discussions. It has been subdivided into three sections. The first section describes the results of all the irradiation experiment carried out in the present study and their possible interpretations. The chapter IV B is devoted to a special issue of study of buffer layers for the growth of YBCO thin film on large area substrates for application oriented studies. Based on the experiments presented, the final conclusions and scope for future work are given in the sub chapter IV(C).

CHAPTER IV A

IRRADIATION STUDIES ON $YBa_2Cu_3O_7$ SYSTEM

4a.1 Unirradiated Bulk Samples

In this section, results of various experiments on different properties of the virgin $YBa_2Cu_3O_{7-x}$ (YBCO) samples are described. As mentioned earlier, bulk YBCO samples were prepared by standard solid state technique by using weighed quantities of Y_2O_3, $BaCO_3$ and CuO powders in stoichimetric ratio. Different recipes of sintering temperature have been used to optimize the superconducting properties of the YBCO pellets. Here, only the results on the optimized samples will be described. The thermal schedule used to prepare such samples are given below.

TABLE 4a.1

Component used	Calcination temp. and duration	Sintering temp. and duration
Y_2O_3, $BaCO_3$, CuO	850°C (± 0.1°C) 12 hrs.	930°C (± 0.1°C) in O_2 atmosphere twice sintered. 10 hrs. each. Slowly cooled to 200°C atramp 2°C/minute

4a.1.1. Results of R vs. T measurements

After the preparation of the bulk samples, the first experiment was to evaluate the superconducting transition of the specimens. Fig. 4a.1(a), (b), (c) show the R vs. T variation of the YBCO bulk samples at different measuring currents; 1 mA, 10 mA and 50 mA. It is clearly seen that the samples are superconducting with transition temperature ~ 90 K and with metallic behavior in resistance variation near room temperature. The transition is quite sharp (ΔTc ~ 1K) and the $R_{(T\ 300K)}/R_{(T\ 100K)}$ ratio is ~ 2 in each case. Transition temperature is seen to decrease with increase in measurung currents.

To ascertain the correctness of the Tc measurement by R vs. T technique, susceptibility was also measured. Fig. 4a.2 shows the results of the a.c susceptibility measurement carried out on the bulk YBCO. The Tc from this measurement is seen to be 90.5 K. From the value of the real part of the susceptibility ($\underline{X}'$) when the sample is in superconducting state, it can be inferred that the sample is 90% volume superconducting. This indicates the good quality of the sample and thus the suitability of the thermal recipe used to prepare the specimen.

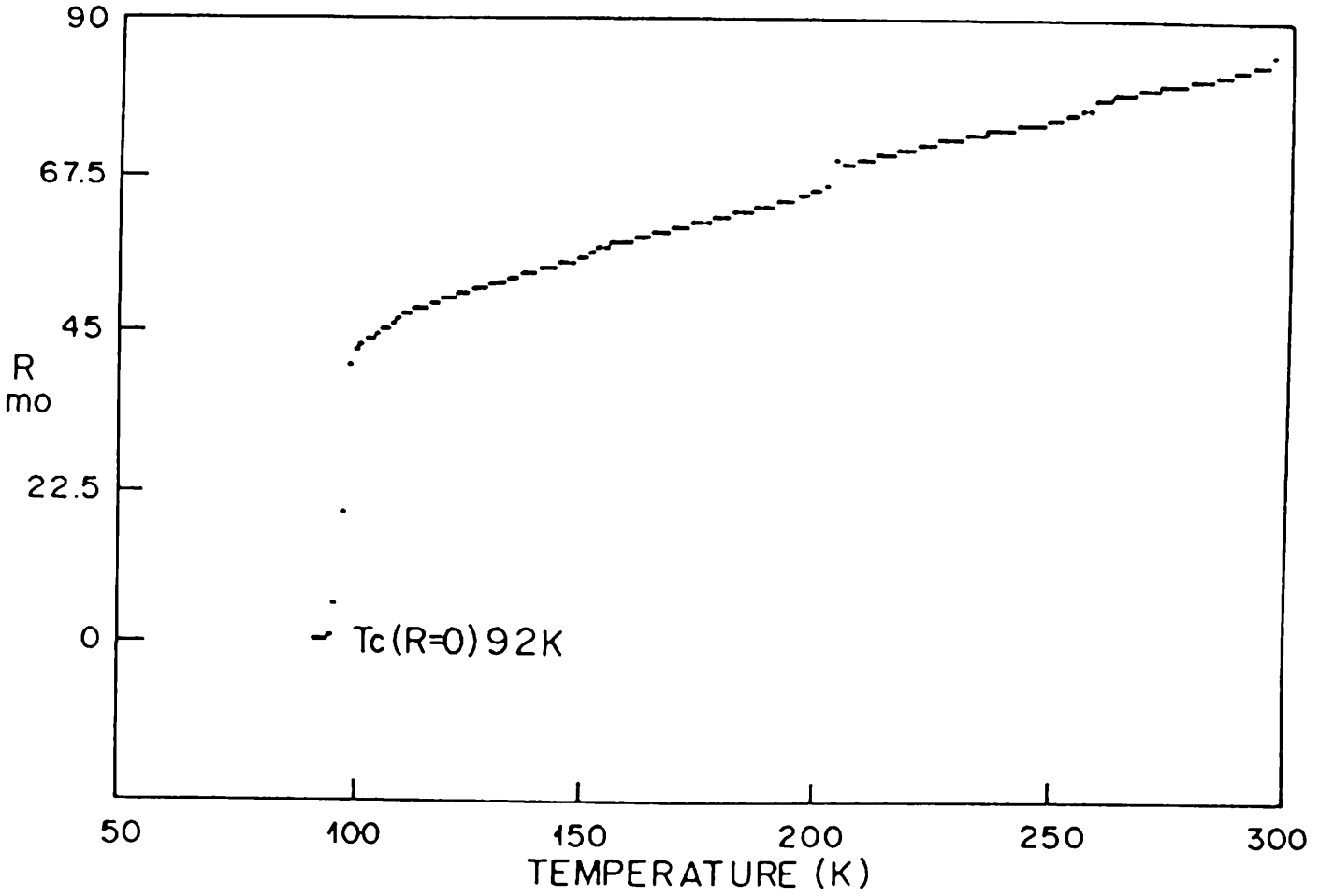

Fig. 4a.1. (a) R vs. T of the unirradiated bulk YBCO sample with measuring current 1 mA.

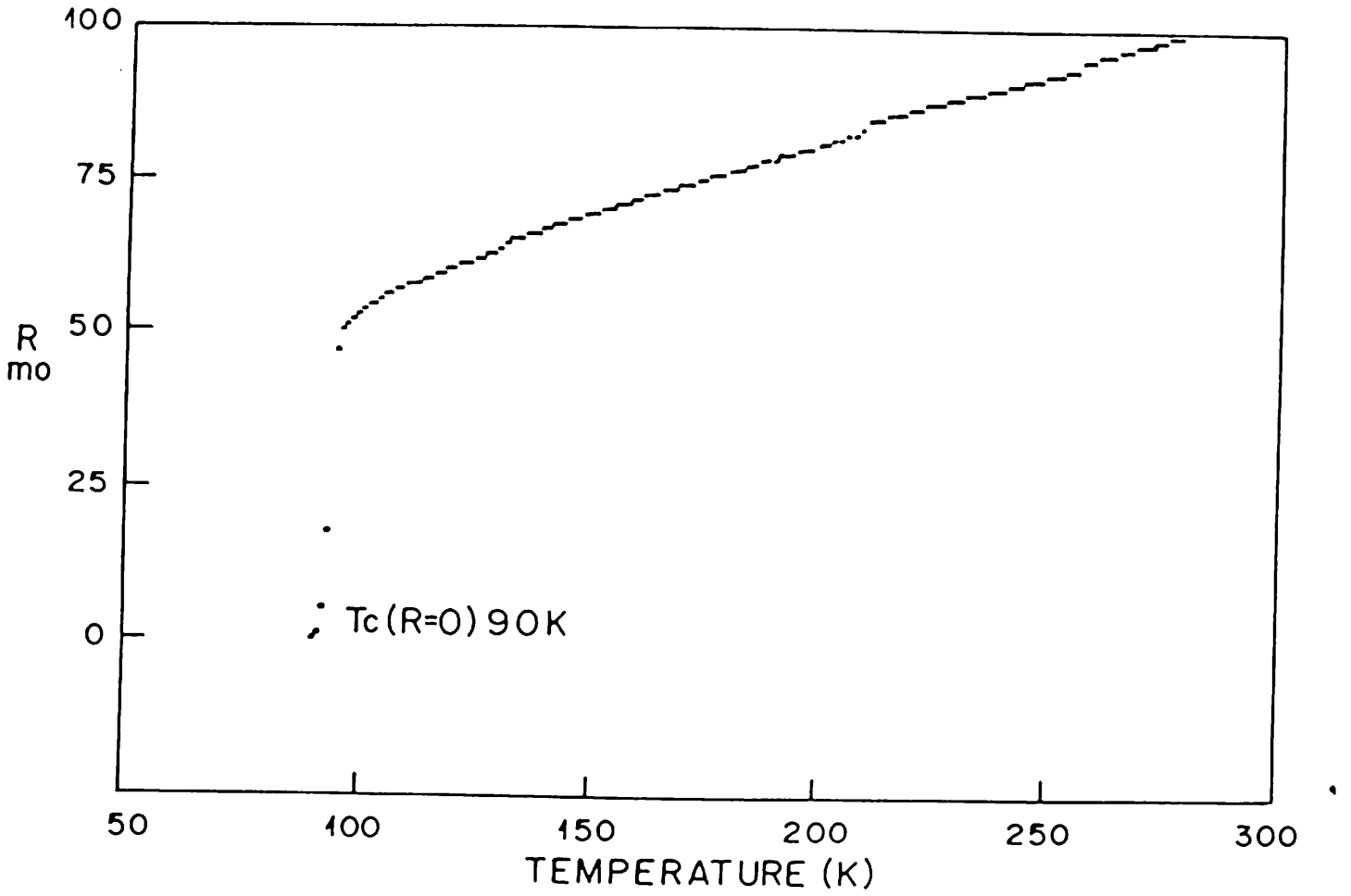

Fig. 4a.1. (b) R vs. T of the unirradiated bulk YBCO sample with measuring current 10 mA.

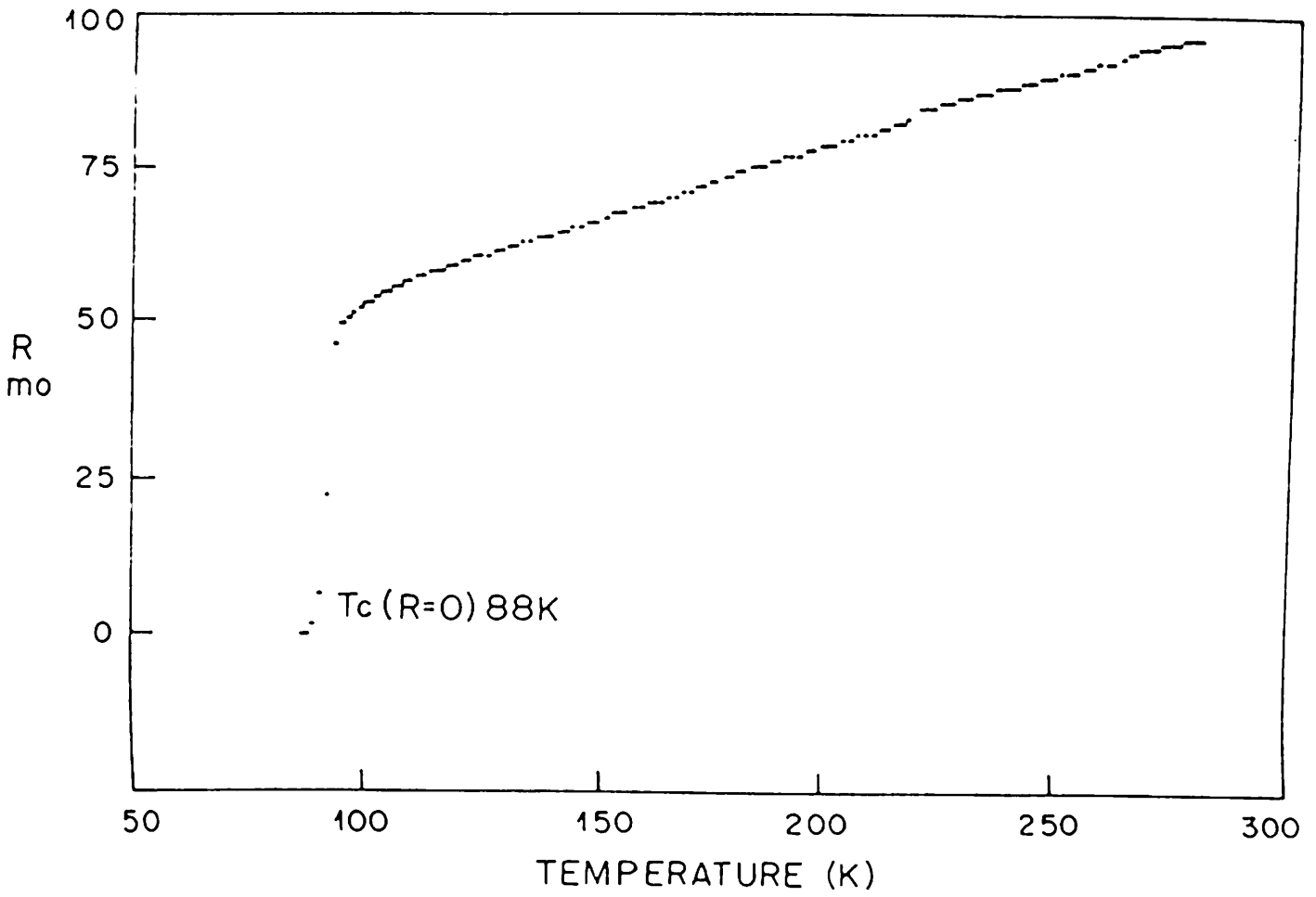

Fig. 4a.1. (c) R vs. T of the unirradiated bulk YBCO sample with measuring current 50 mA.

4a.1.2. Results of the iodometric test

We know that the value of 'y' in the formula $YBa_2Cu_3O_y$ plays a very crucial role. Hence, it is essential to know this and also to correlate this with the measured Tc values. To do this, the value of 'y' was determined by iodometric analysis. Table 4a.2.a, 4a.2.b. and 4a.2.c give the results of the iodometric measurement. The measurement shows that the value of 'y' in the formula of YBCO in the present sample is 6.95.

Table 4a.2.a. TITRATION I

Sl. No.	Weight of the sample (W_1)	Volume of Na_2SO_3 spent in mg. for titration (V_1) in ml.
1.	27.5	32.6
2.	30.6	40.7
3.	26.3	33.1

Table 4a.2.b TITRATION II

Sl. No.	Weight of the sample (W_2) in mg.	Volume of Na_2SO_3 spent for titration (V_2) in ml.
1.	28.6	28.4
2.	28.5	28.6
3.	33.3	24.9

Table 4a.2.c Determiantion of oxygen concentration

Combination used from table 4.2.a and table 4.2.b to calculate V_1/W_1 and V_2/W_2	The value of valency (P) using $P=(V_1/W_1)/(V_2/W_2) + 1$	Value of 'y' in the formula $YBa_2Cu_3O_y$ using $y=3.5+1.5P$	Average value of 'y' discarding those values which are much above 7
1,1	2.1938	6.7907	
2,2	2.3254	6.9881	
3,3	2.6831	7.5247	
2,1	2.3394	7.0091	6.95
3,2	2.2542	6.8812	
1,3	2.5854	7.3781	
$(123)_{avg.}$, $(123)_{avg.}$	2.3929	7.08938	

4a.1.3. Results of XRD

As is well known, YBCO system is superconducting only if it has orthorhombic structure. While R vs. T and a.c. susceptibility techniques give Tc and ΔTc yet one can not really ascertain whether the sample is really 100% uniform with regard to its desired crystalline property. To do this, it is necessary that X-ray diffraction be done. Fig. 4a.3 (a) shows the X-ray diffraction pattern of the bulk YBCO pellet. This is a plot of intensities from different (hkl) planes as a function of twice the Bragg diffraction angle θ. The YBCO (123) peaks are identified and are designated by the corresponding (hkl) value in the fig. The lattice parameters a, b and c are calculated by using the formula

$$d = \frac{1}{\sqrt{(\frac{h}{a})^2 + (\frac{k}{b})^2 + (\frac{l}{c})^2}} \qquad \text{(4a.1)}$$

where d is the spacing between the palnes. Taking different (hkl) values and the associated d values in the diffraction spectrum, the lattice parametrs are calculated as 'a' = 3.8076Å, 'b' = 3.8649Å and 'c' = 11.5947Å. It is clear from the inequality of the 'a' and 'b' values that the sample structure is orthorhombic.

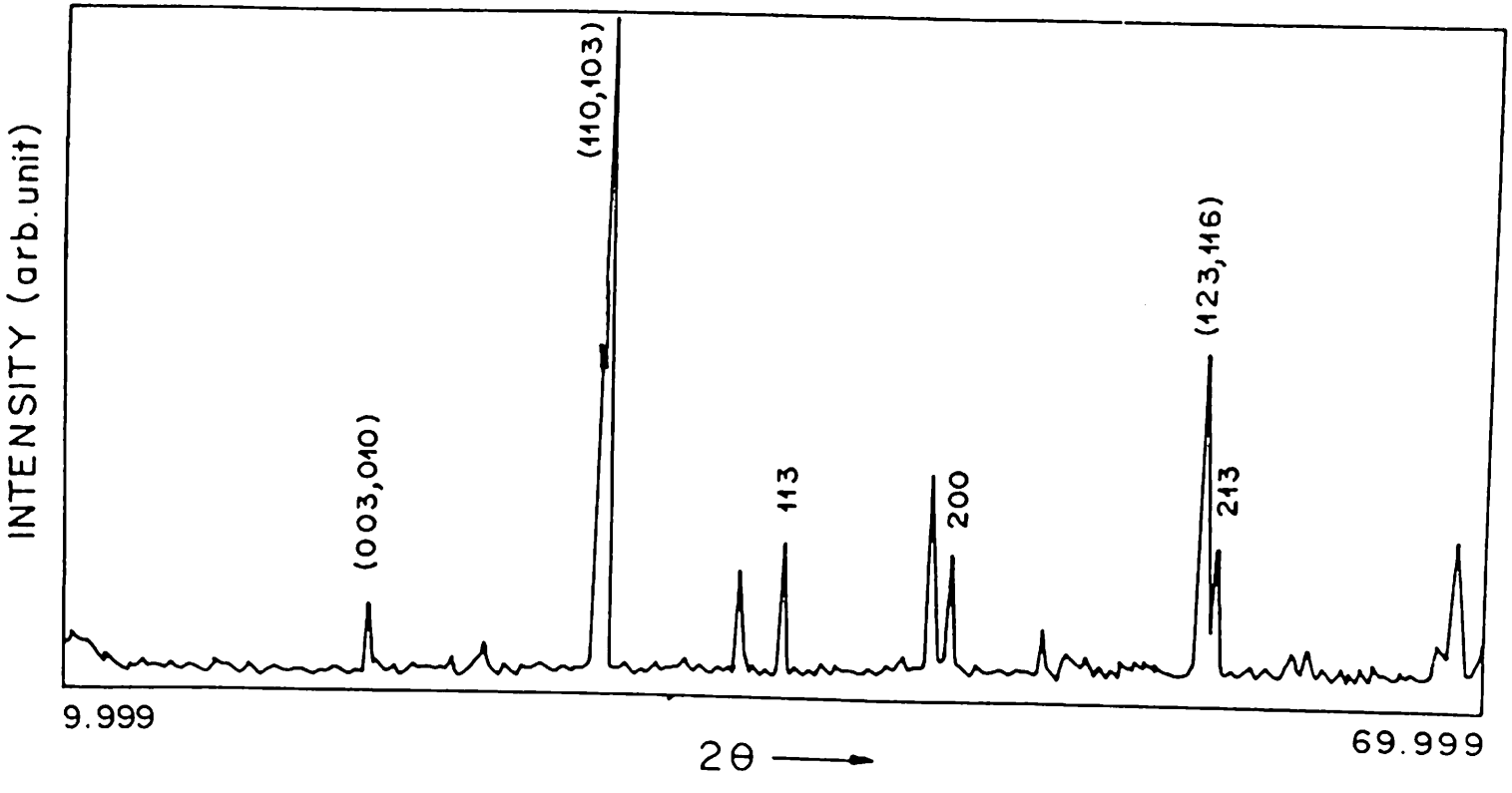

Fig. 4a.3. (a) XRD spectrum of the unirradiated YBCO bulk pellet.

The orthorhombicity is generally determined from the orthorhombic splitting (a,b) using the angular values of the lines (102) and (012). But, it is difficult to seperate out these two peaks, because the intensity is rather low (at 2θ= 28.034° in Fig. 4a.3 (a)) and they occur in a region where many intense peaks of some impurities increase the noise level.Therefore, few other pair of peaks are concentrated upon for this purpose. Some of them are the peaks at 2θ = 32.6°(hkl = 013) and 2θ = 32.9°(hkl = 103, 110), the peaks at 2θ = 46.7° (hkl = 020, 006) and 2θ = 47.7°(hkl = 200) and peaks at 2θ = 58.3°(hkl = 123, 116) and 2θ = 58.9°(hkl = 213). Clearly, the splitting of (013) (2θ = 32.699°) and (103) (2θ= 32.967°) peaks in fig. 4a.3 (a) shows the orthorhombicity of the sample. In the next few sections, to show the changes in crystallainity and structure produced by irradiation, the variations will always be referred to w.r.t. these peaks. Fig. 4a.3 (b) shows a slow scan of the diffraction spectrum of the virgin YBCO sample between the angles 46° and 48°.

4a.1.4. Results of SEM

X-ray studies gave us the clue of the presence of the various crystalline phases of the same material. Ideally all the samples should also be structurally homogeneous with regard to grain size

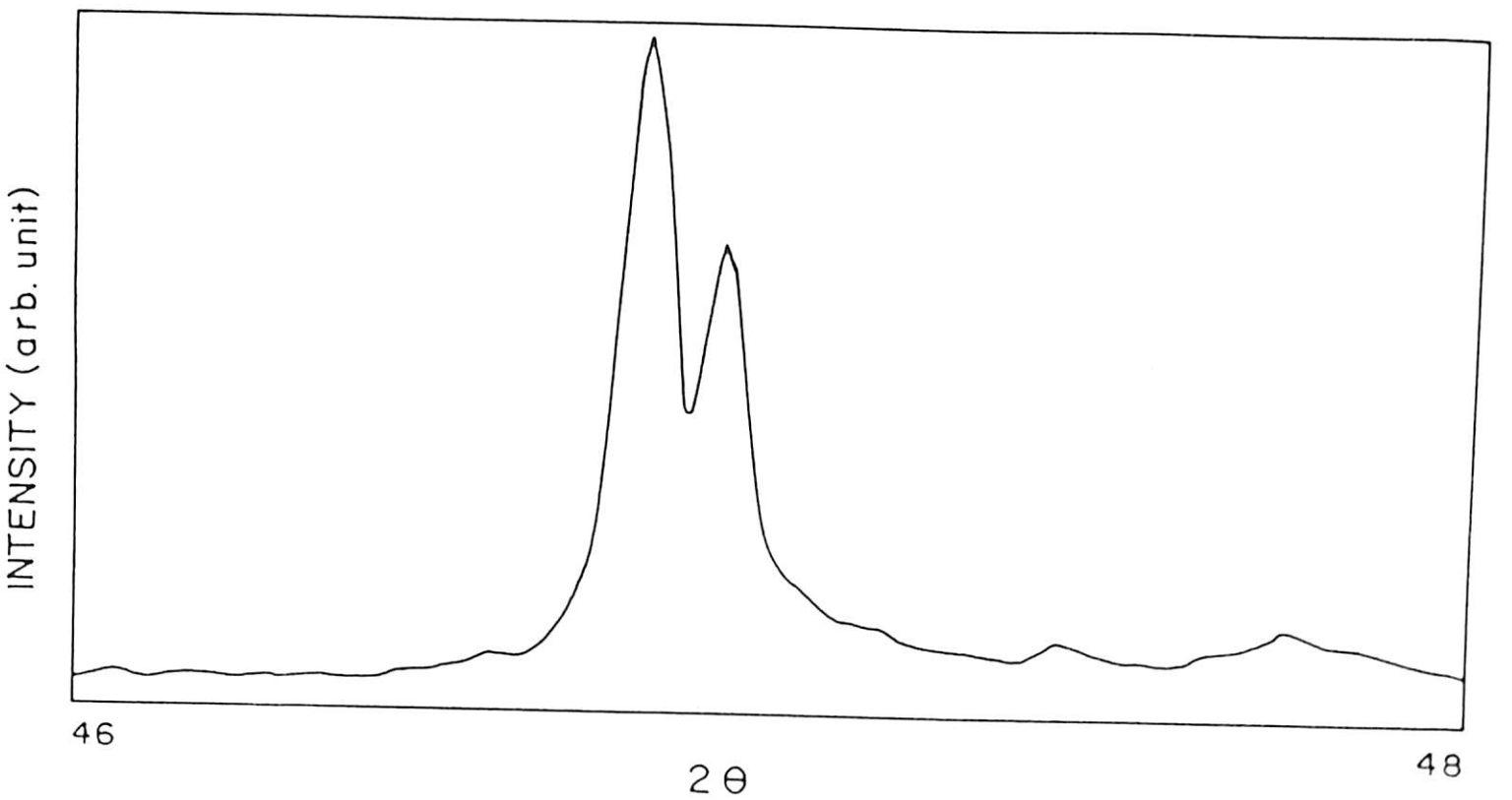

Fig. 4a.3. (b) Slow scan of the XRD spectrum of YBCO pellet between 46° and 48°

uniformity. This is best judged by performing SEM on the same sample at different locations. Fig. 4a.4 (a), 4a.4 (b) show the SEM pictures of the surface of a typical YBCO sample at two different positions. While Fig. 4a.4 (a) shows quite big and packed grains, Fig. 4a.4 (b) shows litle bit smaller grains with relatively less packing density. This shows that, even after such a prolonged heat treatment, there is still some inhomogenity of grain sizes at different parts of the sample.

After having described the basic properties of the virgin samples now we turn to the results on the effect of ion irradiation on the aforementioned properties. The various ions used are oxygen, nickel and iodine and also low energy nitrogen and the results are presented sequentially.

4a.2. Results of Oxygen Irradiation

This section describes the results of the 75 MeV ^{16}O irradiation on YBCO samples in bulk form.

4a.2.1 Projectile Parameters

The 75 MeV ^{16}O beam was derived from a tandem type Van de Graff accelerator, the 15 UD Pelletron. The charge state varies from 5^+ to 7^+ in different experiments to maintain an energy of

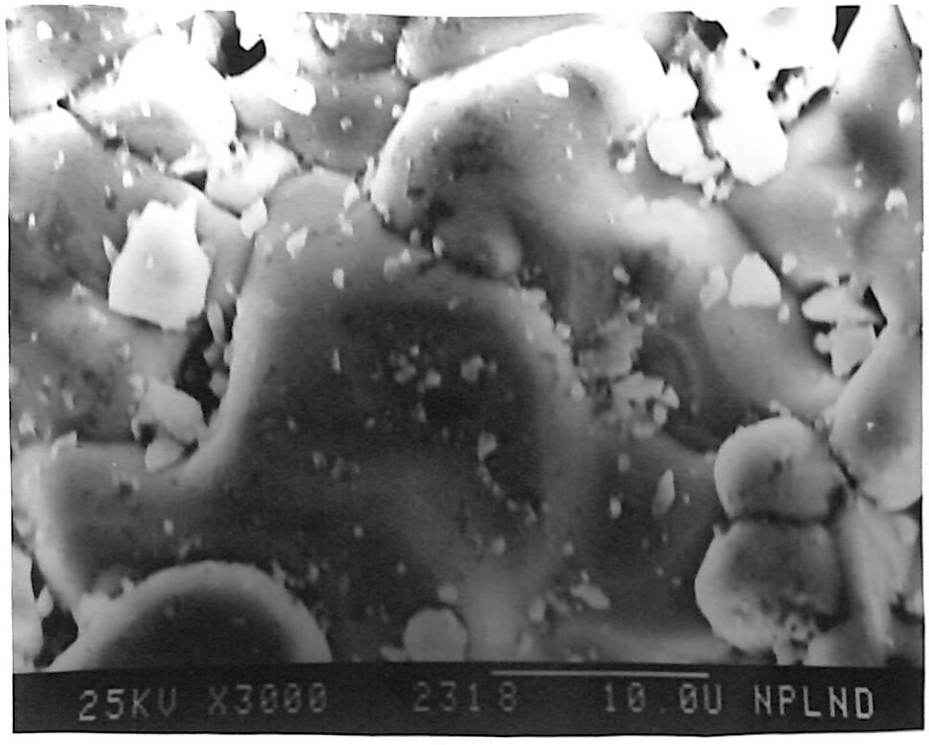

(a)

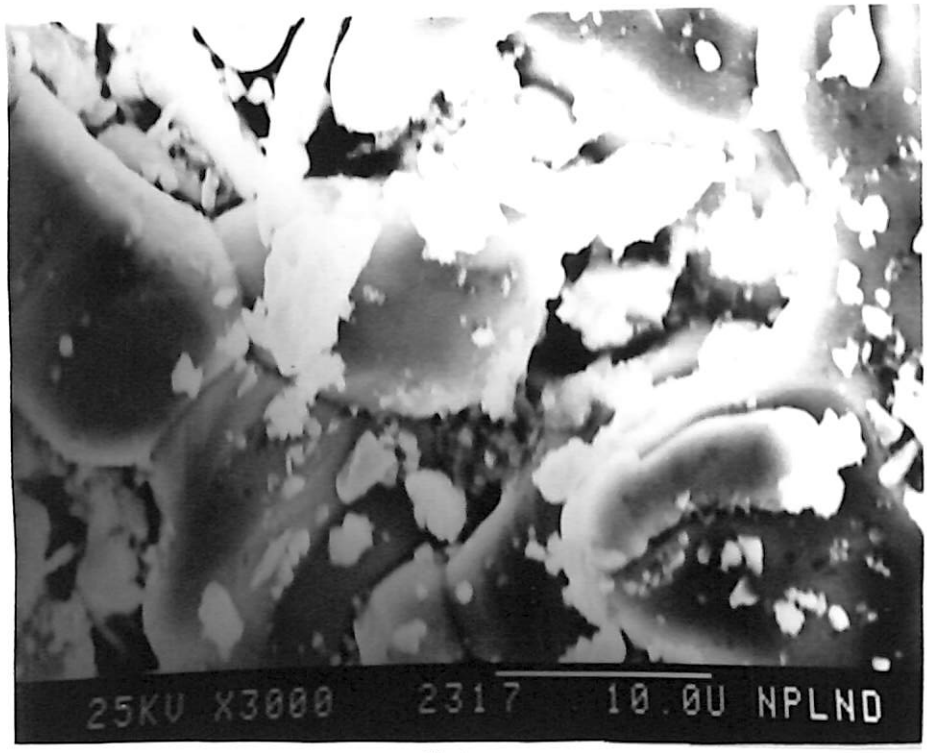

(b)

Fig. 4a.4. (a),(b) SEM pictures of unirradiated bulk $YBa_2Cu_3O_{7-\delta}$ sample at two different locations.

75 MeV as dictated by terminal voltage used. The enrgy loss parameters of this beam and the recoils, vacancies etc. created by it in YBCO target as calculated from computer simulation programme TRIM are shown in Fig. 4a.5 (a), 4a.5 (b), 4a.5 (c), 4a.5 (d) and 4a.5(e) and results are summarised in table 4a.3.

TABLE 4a.3

Beam Species	Energy	Rate of Electronic energy loss $(dE/dX)_e$ in eV/Å	Rate of Nuclear energy loss $(dE/dX)_n$ in eV/Å	Range
^{16}O	75 MeV	1.72 E+02	1.06 E-01	32μm
	10 KeV	1.55 E+01	2.39 E+01	139 Å

The various experimental results in the light of the various properties described in section 4a.1 are given sequentially in the following subsections. The main additional parameter included in this, is the study of variation of resistance with dose. This parameter helps in judging apriori what prominent properties will show changes.

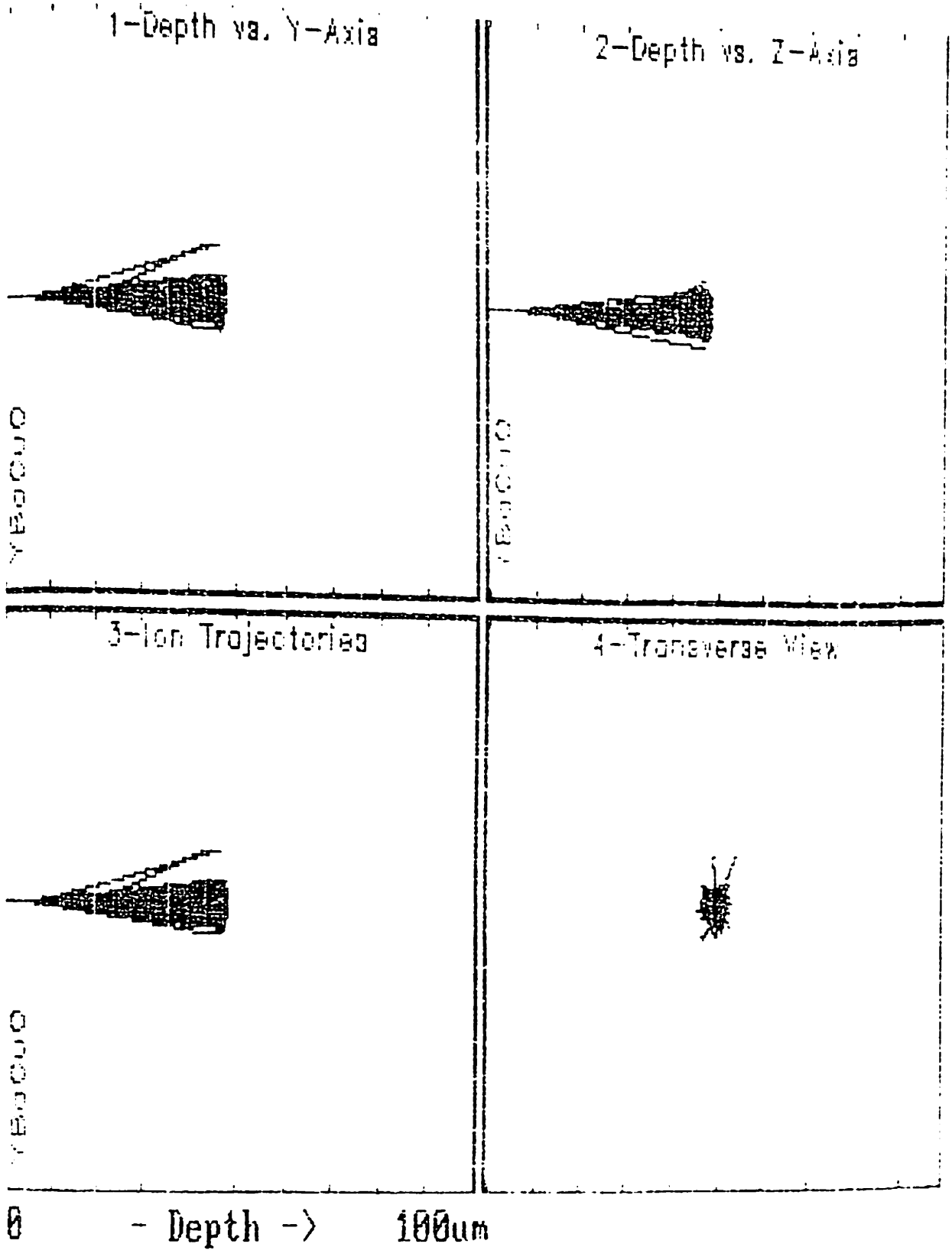

Fig. 4a.5.(a). TRIM plot of 75 MeV oxygen trajectory in $YBa_2Cu_3O_7$

$YBa_2Cu_3O_7$

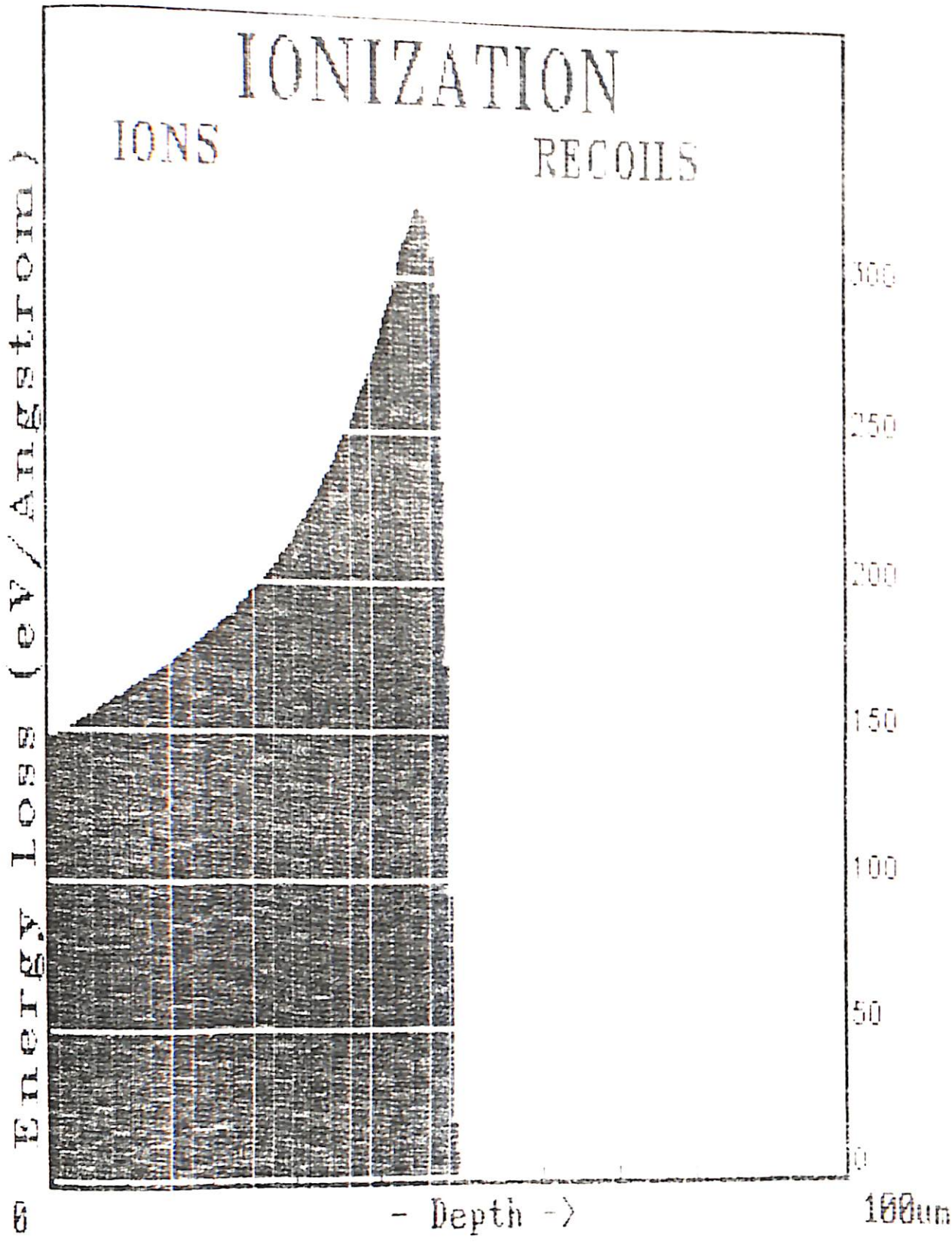

Fig. 4a.5.(b). TRIM plot of ionization by 75 MeV oxygen ions and also by the recoils created by the bombarding ions in $YBa_2Cu_3O_7$

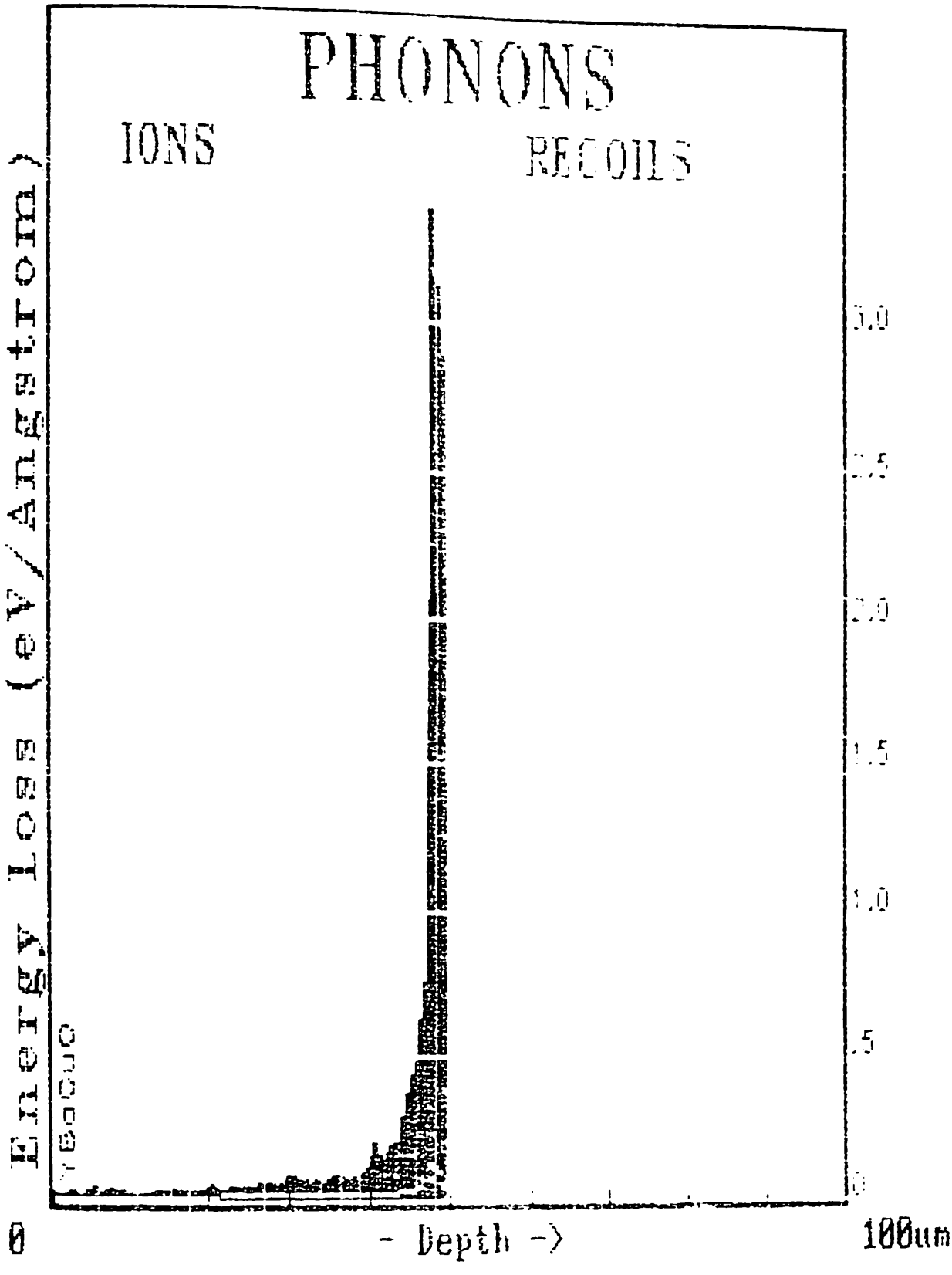

Fig. 4a.5.(c). TRIM plot of phonons created by 75 MeV oxygen ions in $YBa_2Cu_3O_7$

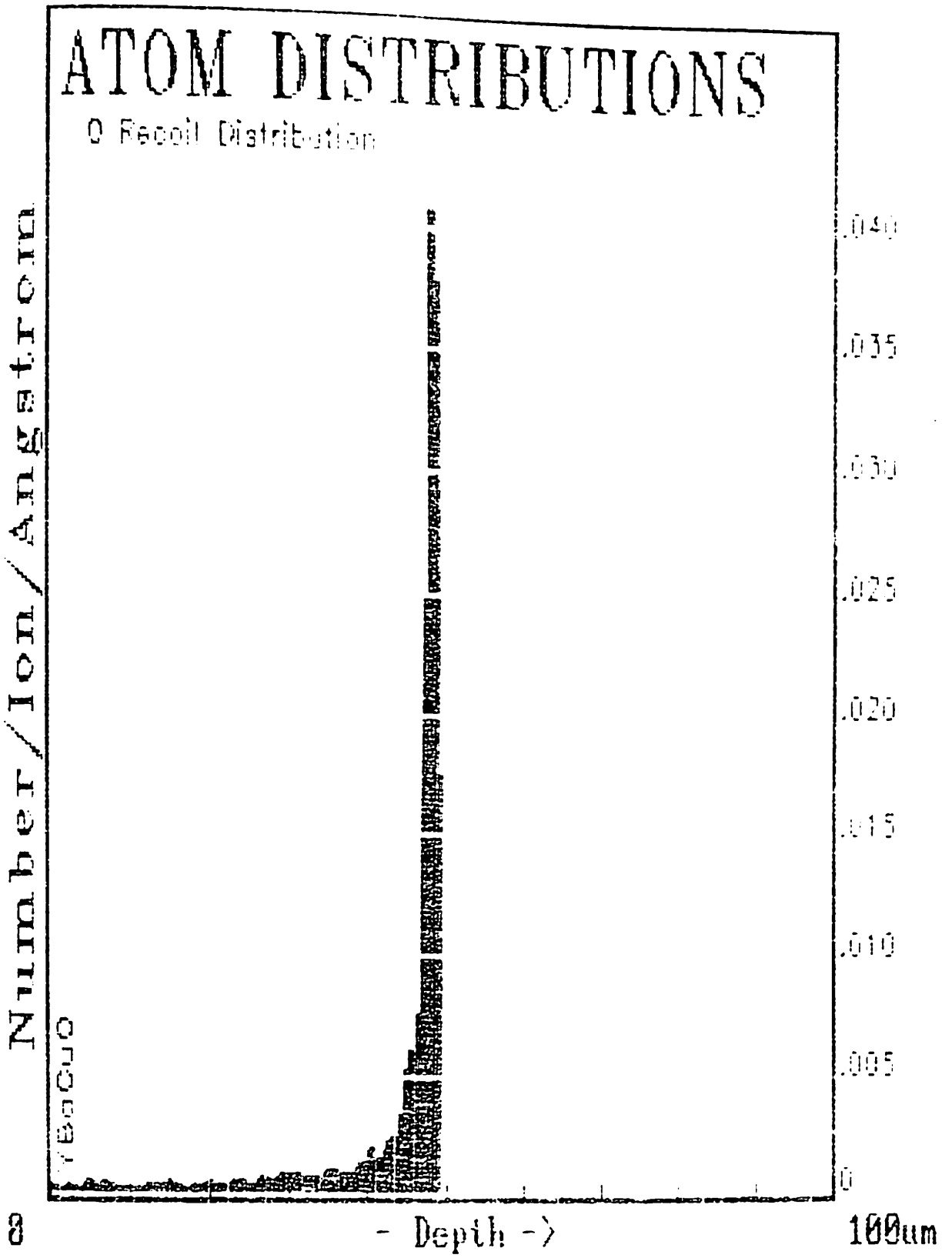

Fig. 4a.5.(d). TRIM plot of oxygen recoil distribution (≡ O target vacancies) created by 75 MeV oxygen in $YBa_2Cu_3O_7$

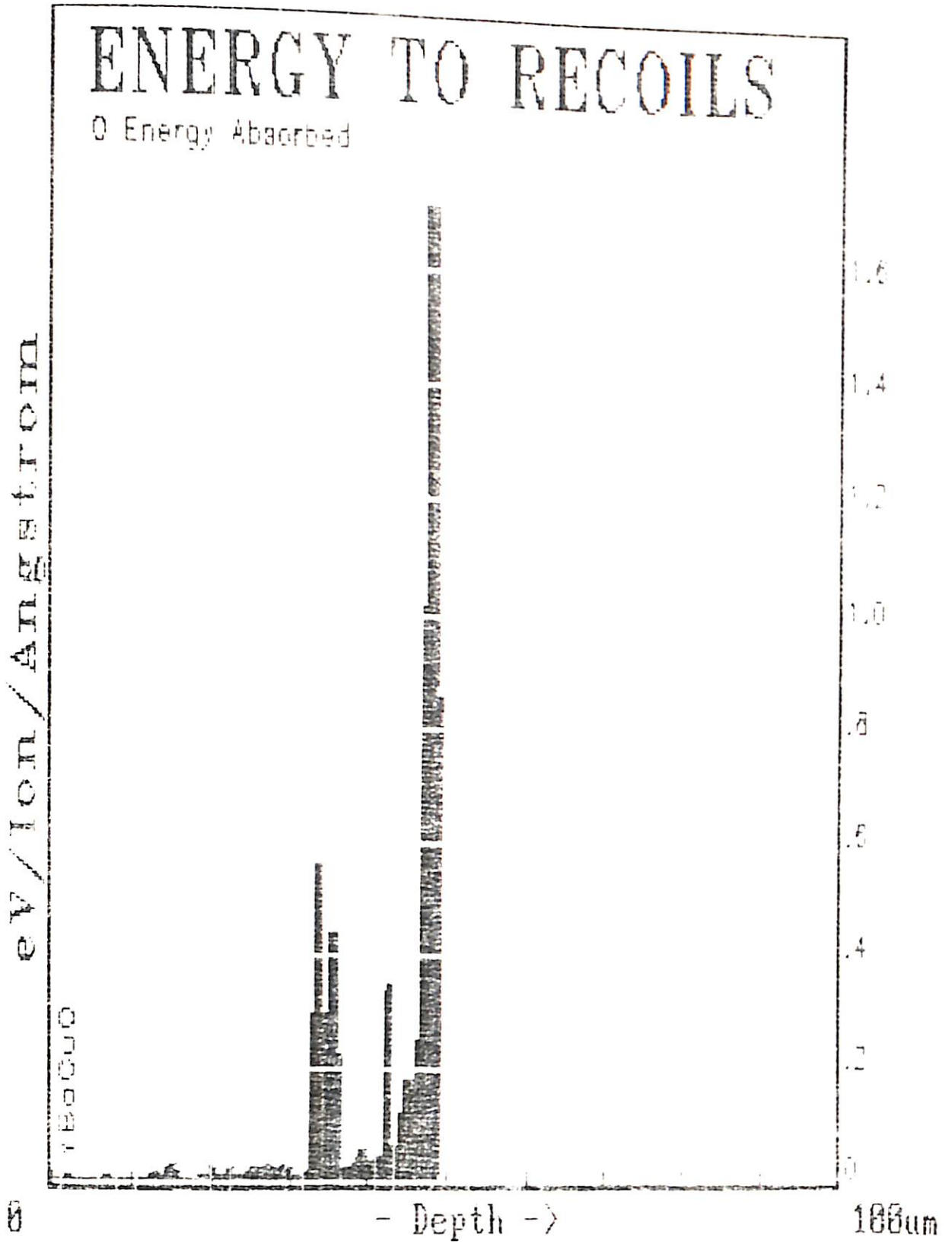

Fig. 4a.5.(e). TRIM plot of energy absorbed by oxygen recoils for 75 MeV oxygen irradiation in $YBa_2Cu_3O_7$

4a.2.2 Results of insitu R vs. dose measurements

Fig. 4a.6 (a,b) shows the variation of normalised resistance (R_n) as a function of the ion dose of the impinging projectiles at ambient temperature (4a.6 (a)) and at low temperature (4a.6 (b)). The low temeperature experiment was planned in such a way, so that the temperature of sample (~100 K) was above the transition temperature Tc of the YBCO target. The resistances at different doses are normalised with respect to the unirradiated value R_0 and the normalisation is done to avoid the different values of initial resistances of different samples. In both the cases, the resistance has been decreased from its initial value as a result of irradiation. However, the striking difference between the two curves are:

(i) for low temeperature irradiation the resistance shows a slight trend of increase at higher doses, while for room temperature irradiation the nature of the change in resistance w.r.t. fluence shows an initial flat region at lower doses, followed by gradual decrease at higher doses.

(ii) the normalised change in resistance ($\Delta R/R_{unirr.}$) is much more in the case of low temperature irradiation than the case at room temperature irradiation (at 1 x 10^{12} cm^{-2} fluence, for low temperature irradiation $\Delta R/R_{unirr} \cong -0.077$ and at room temperature irradiation $\Delta R/R_{unirr} \cong -0.002$).

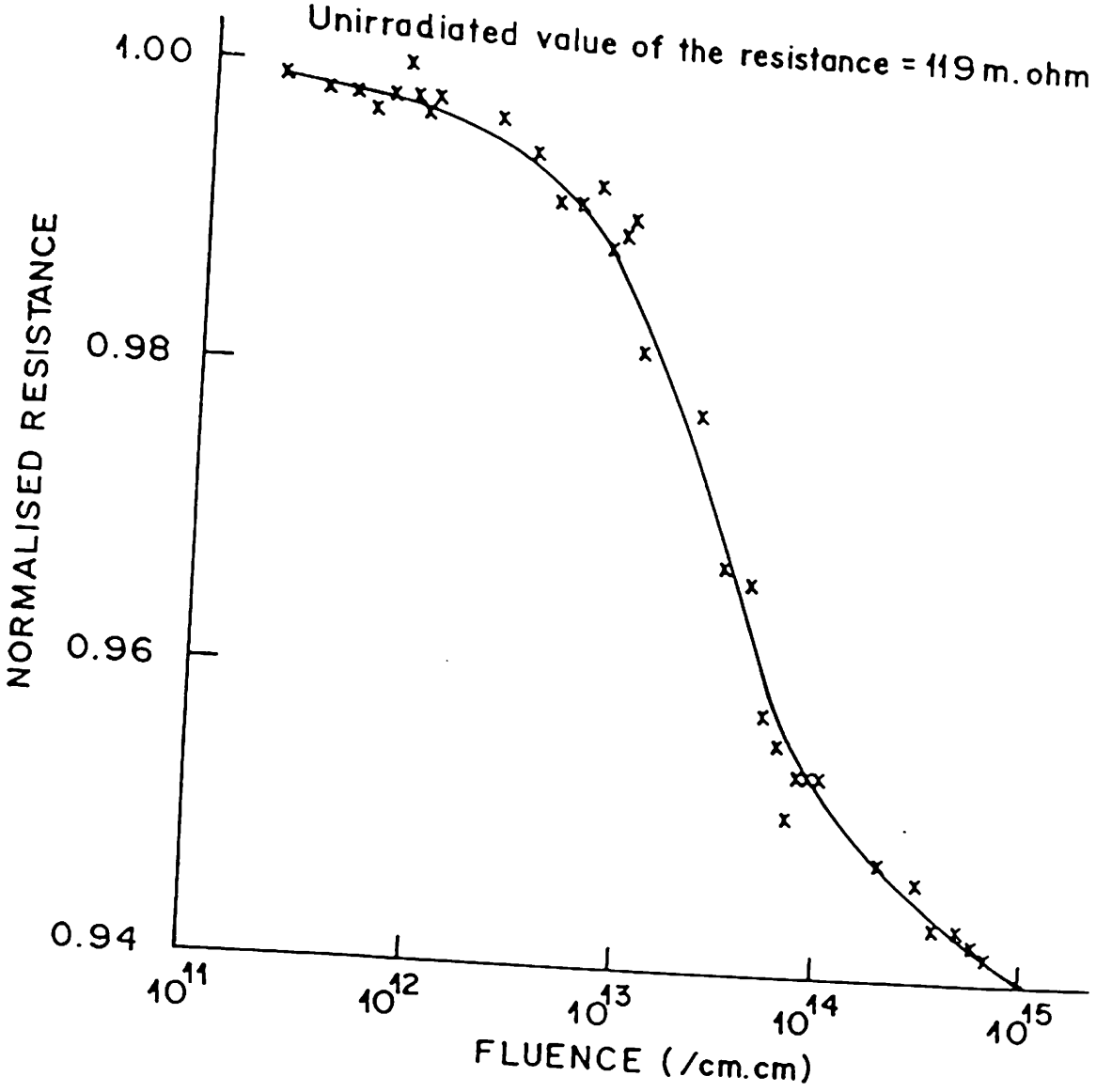

Fig. 4a.6. (a) Insitu variation of normalised resistance (R_n) as function of dose for 75 MeV ^{16}O irradiation at ambient temperature.

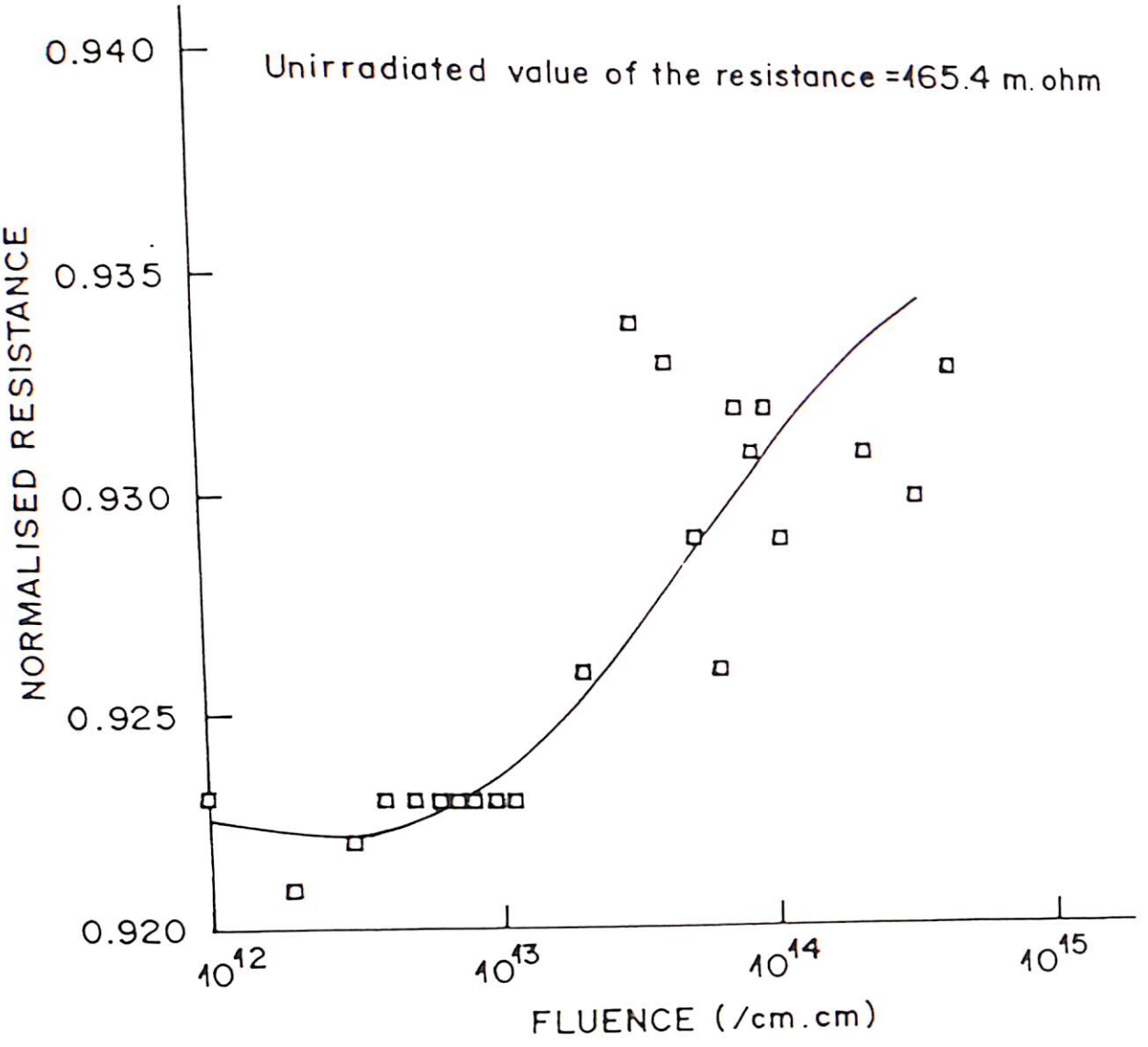

Fig. 4a.6. (b) Insitu variation of normalised resistance (R_n) as a function of dose for 75 MeV ^{16}O irradiation at low temperature.

4a.2.3 Results of XRD

Fig. 4a.7 and 4a.8 show the X-ray diffraction spectra of 75 MeV oxygen irradiated bulk samples at dose 1 X 10^{12}/cm^2 and 4 X 10^{14}/cm^2 respectively. Here the results of room temperature and low temperature is not given seperately, because experiments are carried out ex-situ and once the sample irradiated at low temperature is taken out of the irradiation chamber, it loses it's previous low temperature history. The x-ray diffraction results shows that there is a marked decrease in crystallinity between the samples irradiated at 1 X 10^{12} and 4 x 10^{14}/cm^2. The twin peaks between the values of the diffraction angle 2θ, 32° and 34°, merges at the higher dose. Fig. 4a.9 (a), (b) and (c) show the slow scan of the diffraction spectrum of the oxygen irradiated sample at 4 X 10^{14}/cm^2, between different diffraction angles. The broadening of the peaks shows the degradation of crystallinity by irradiation.

4a.2.4. Results of SEM

Fig. 4a.10 (a), (b) show the surface morphology of unirradiated sample used for oxygen irradiation experiment and 4a.11 (a), (b) show those of irradiated samples at dose 1x10^{11} and 1x10^{13}/cm^2 respectively. The grain size does not seem to change much due to oxygen irradiation as seen from the SEM photographs.

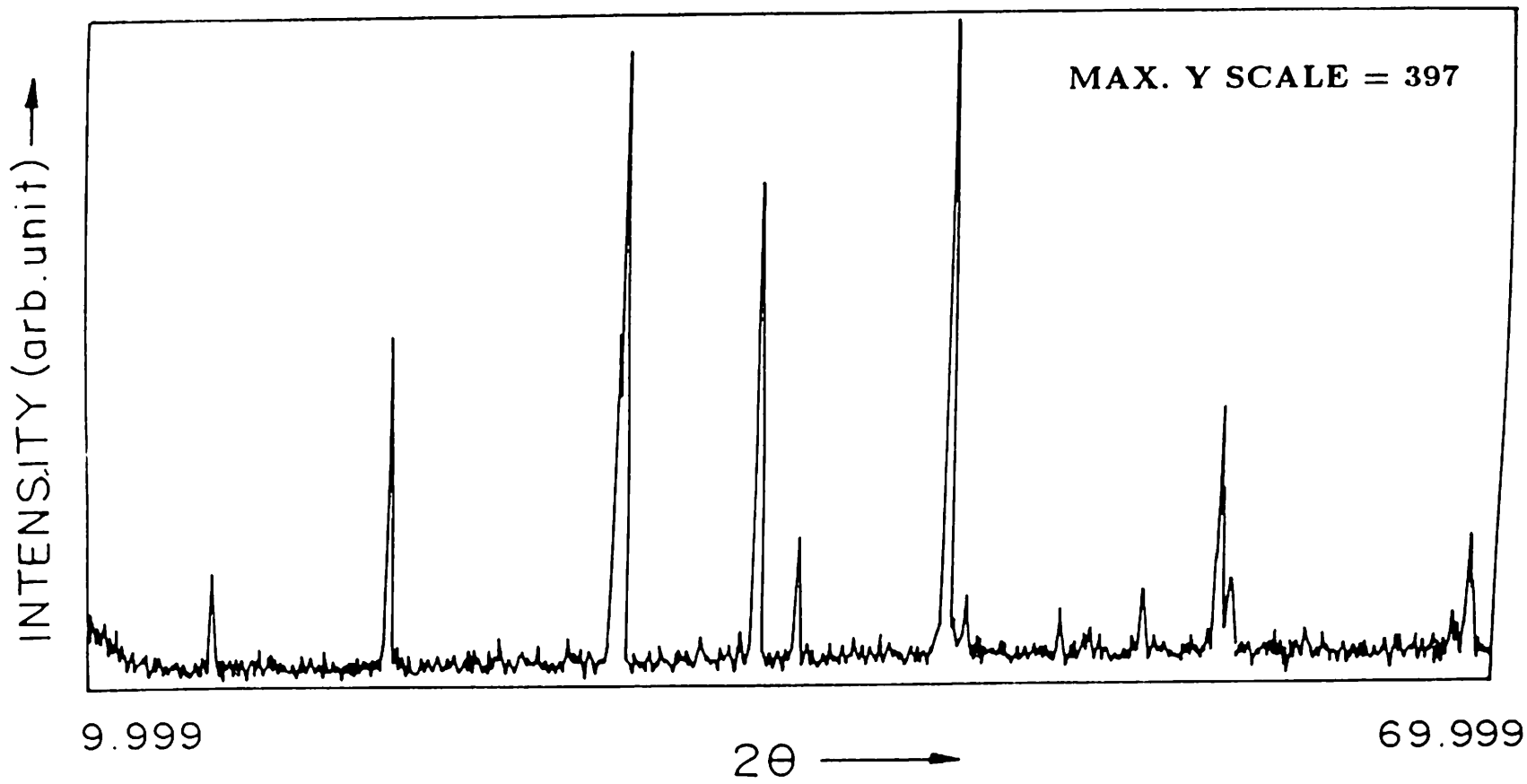

Fig. 4a.7. XRD spectrum of oxygen irradiated bulk YBCO at dose $1 \times 10^{12}/cm^2$.

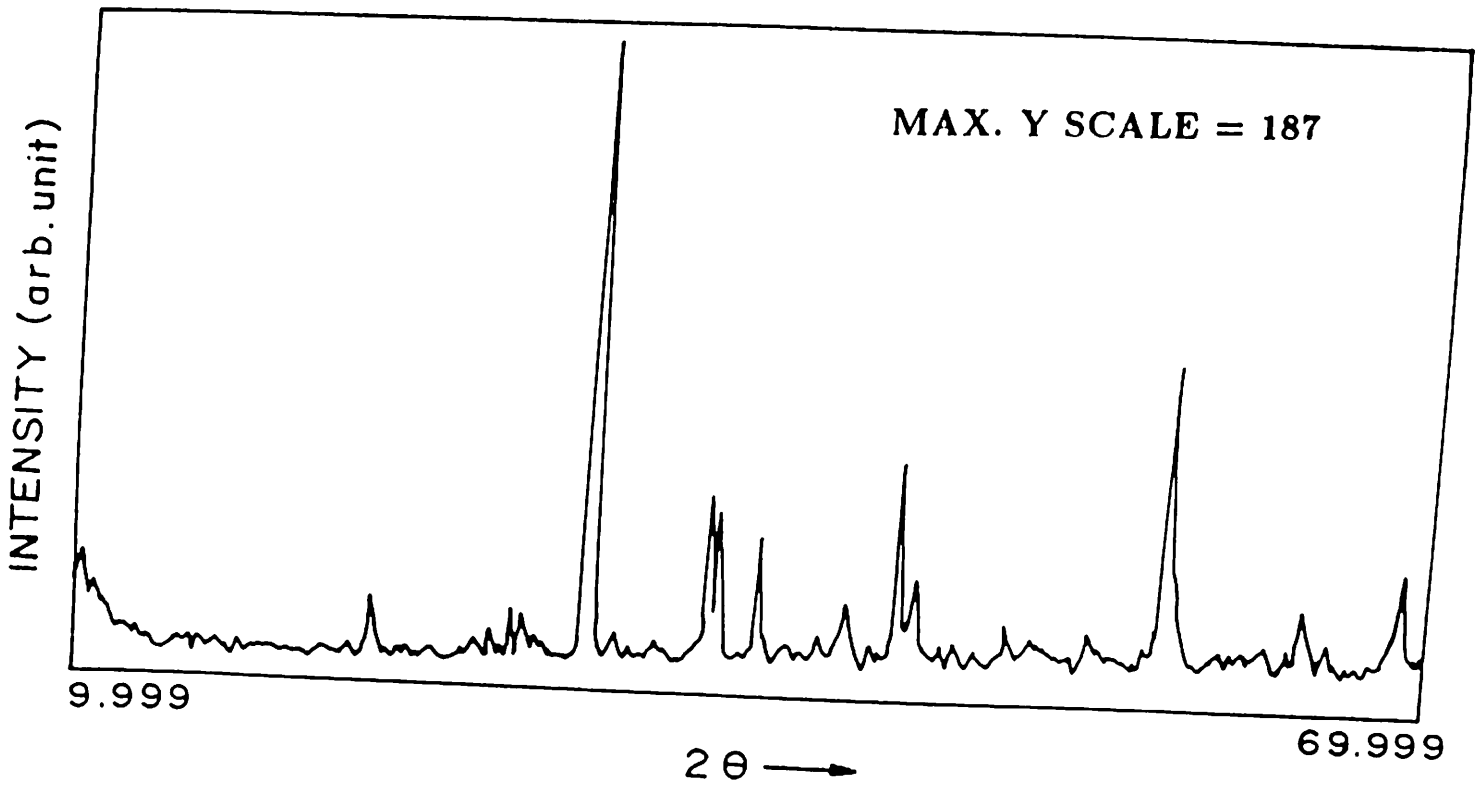

Fig. 4a.8. XRD spectrum of oxygen irradiated bulk YBCO at dose $4 \times 10^{14}/cm^2$.

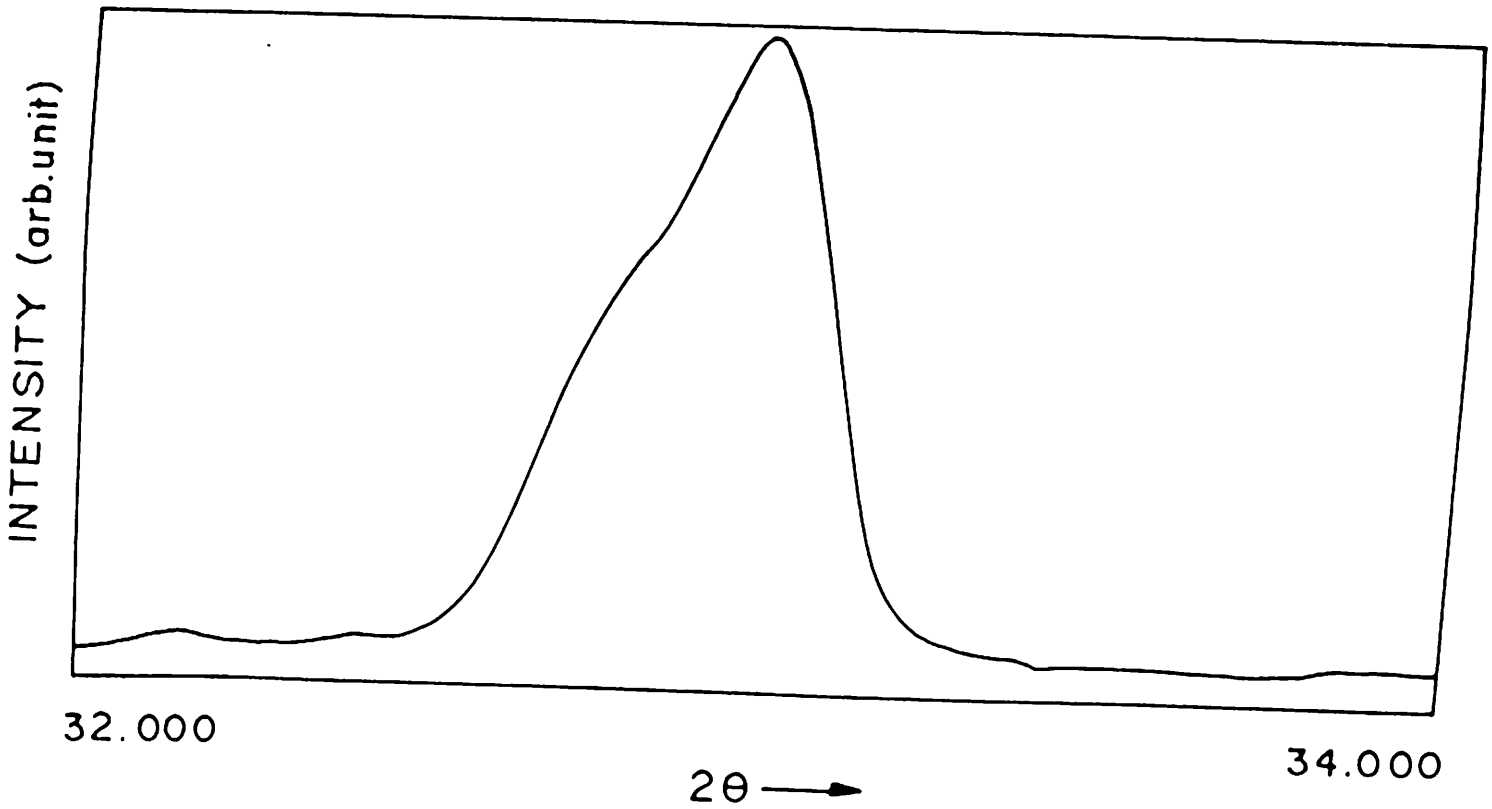

Fig. 4a.9. (a) Slow scan of XRD spectrum of oxygen irradiated bulk YBCO at dose $4 \times 10^{14}/cm^2$.

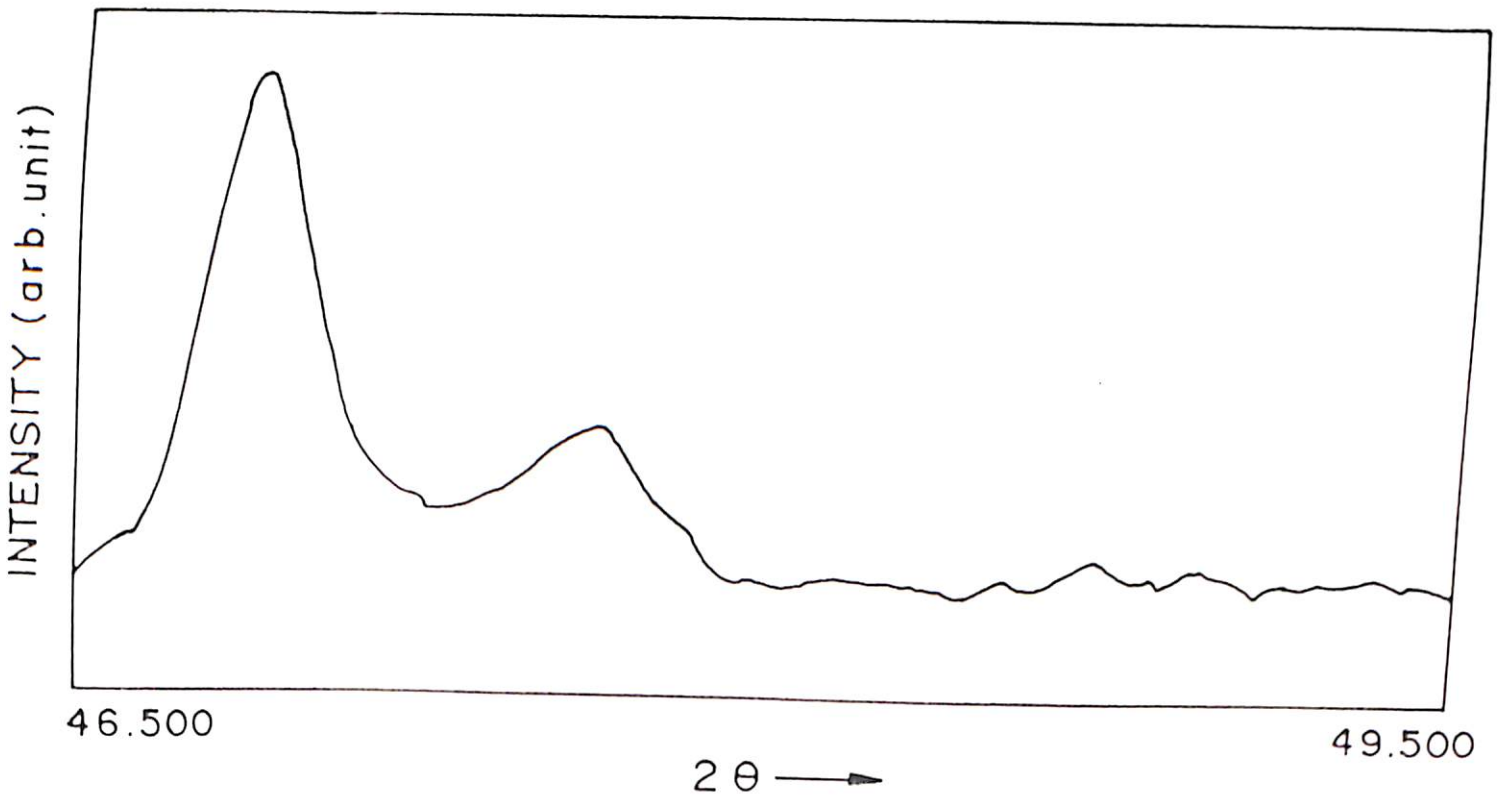

Fig. 4a.9. (b) Slow scan of XRD spectrum of oxygen irradiated bulk YBCO at dose $1 \times 10^{14}/cm^2$.

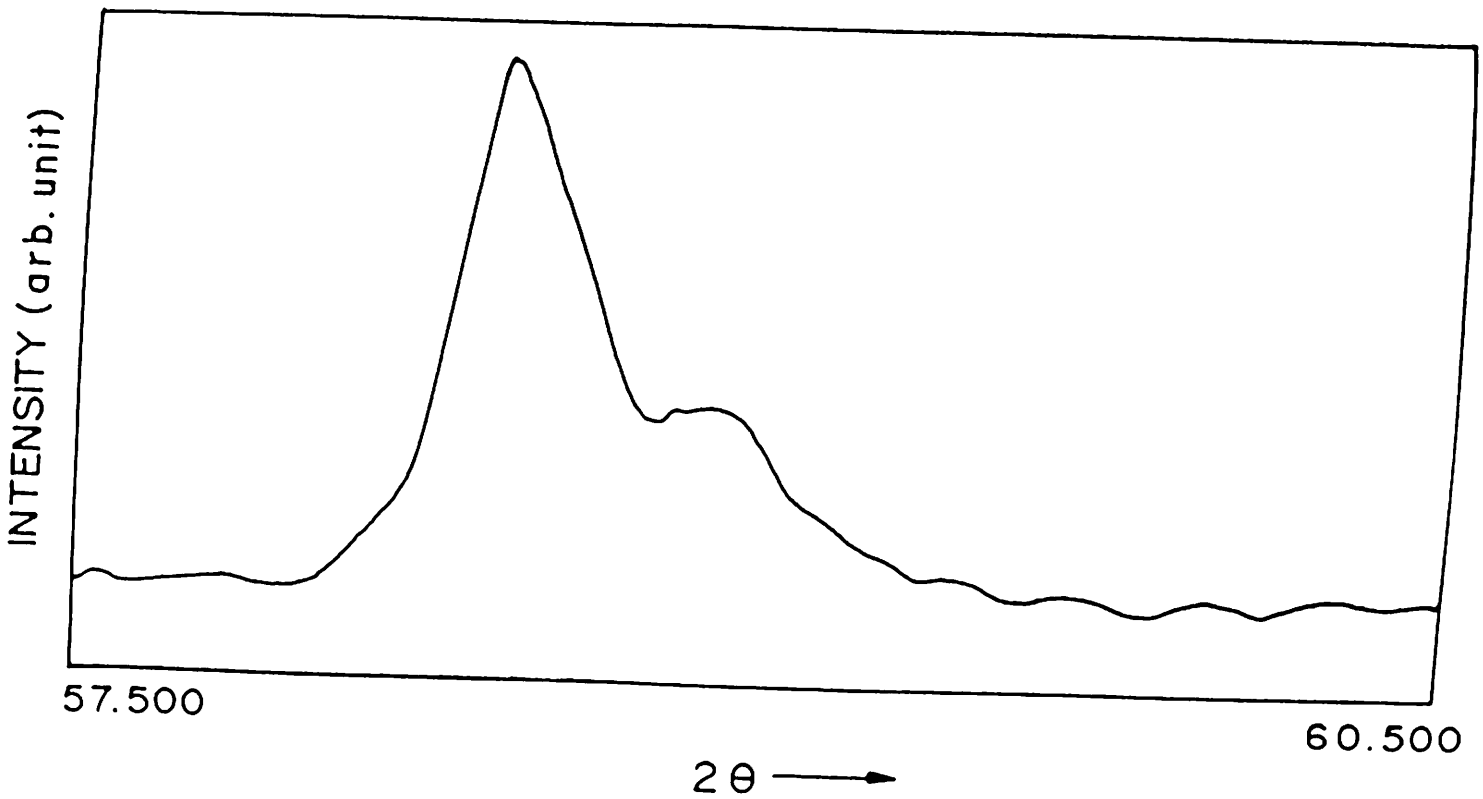

Fig. 4a.9. (c) Slow scan of XRD spectrum of oxygen irradiated bulk YBCO at dose $1 \times 10^{14}/cm^2$.

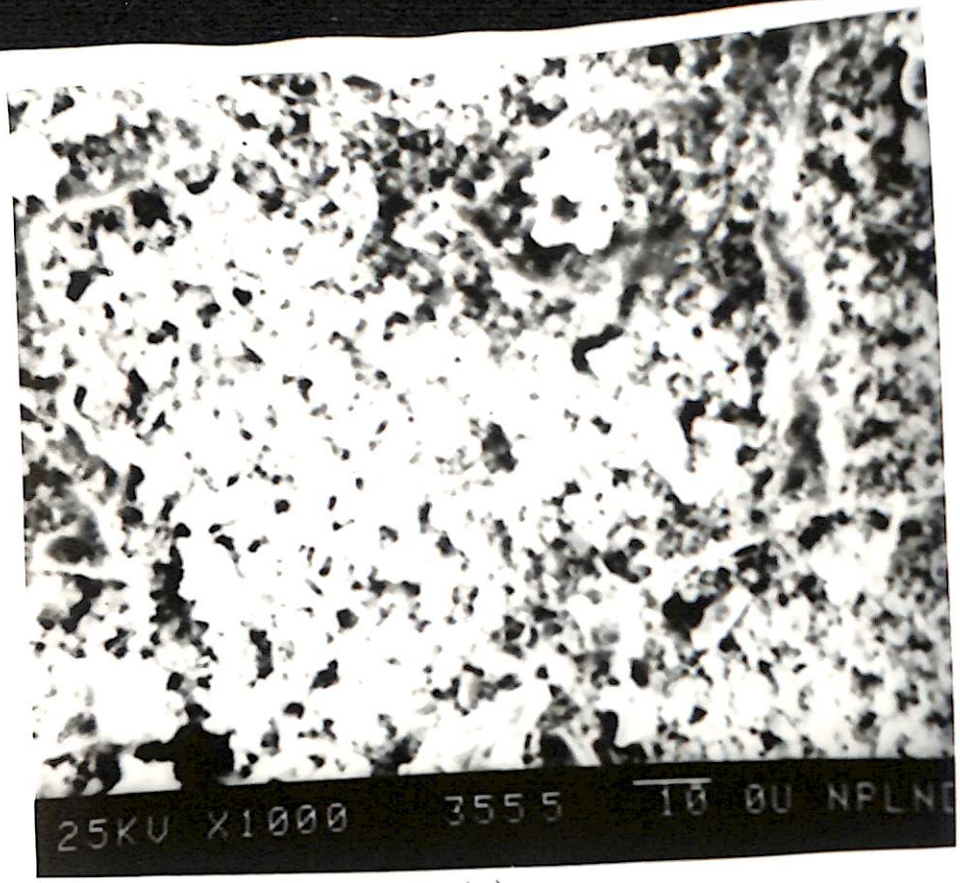

(a)

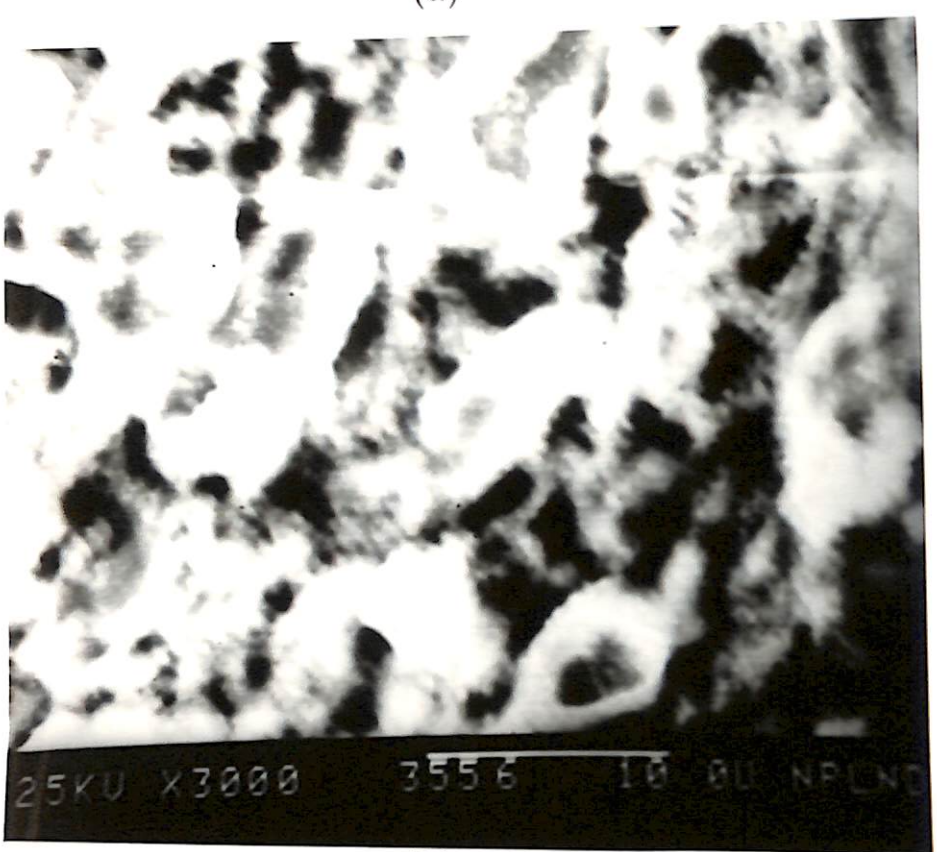

(b)

4a.10. (a), (b) SEM pictures of unirradiated bulk $YBa_2Cu_3O_{7-\delta}$ used for oxygen irradiation at two different magnifications.

But at highest doses it seems that some impurity phases have come to the surface.

4a.2.5. Results of R vs. T measurement

To seperate out the effect of oxygen irradiation on tarnsition temperature of the YBCO bulk sample irradiated at typical dose of 5 x 10^{12}/cm^2, we used two configurations of the samples, namely, planar and tarnsverse, during Tc measurement as shown in fig 4a.12 (a) and 4a.12 (b). Fig. 4a.13 (a) shows the R vs. T curve with the lead arrangement as in fig. 4a.12 (a) and insert. Tc (0) is about 82 K. In the other arrangement (fig. 4a.12 (b)) as shown in fig. 4a.13 (b) the Tc(0) comes down to 79 K. In both the cases Tc (onset) has remained at almost the same value at ~ 85 K.

4a.3. Results of Nickel Irradiation

This section describes the results of 75 MeV ^{58}Ni iirradiation on YBCO bulk samples.

4a.3.1. Projectile parameters

75 MeV ^{58}Ni of charge state 5$^+$ was used. The results of simulation calculation by TRIM for this projectile in YBCO target are listed in table 4a.4. Fig. 4a.14 (a), (b), (c), (d) and (e) show

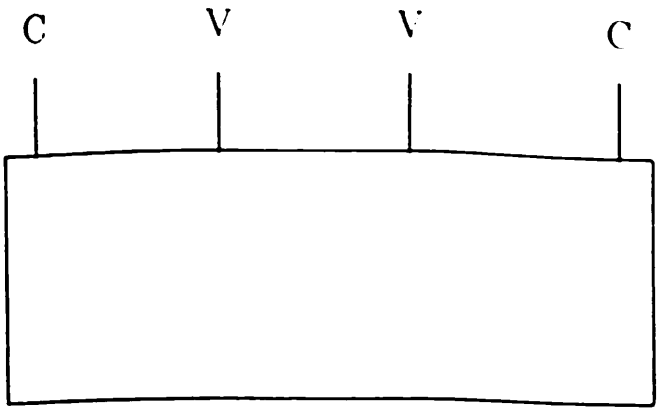

Fig.4a.12(a) Sample connections in planar geometry

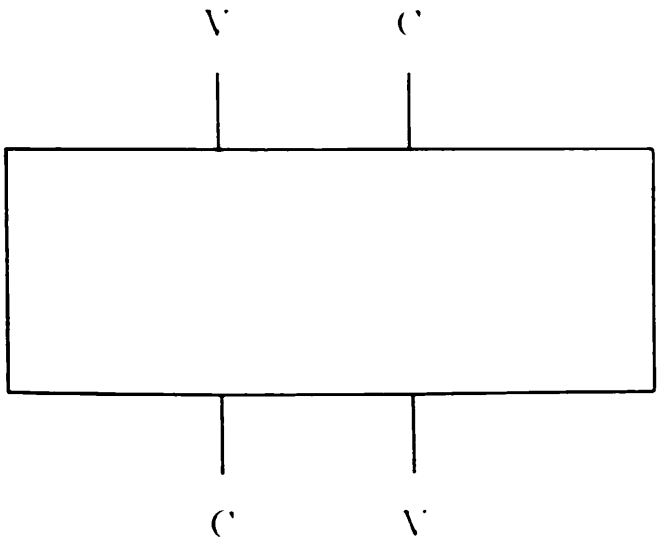

Fig.4a.12(b) Sample connections in transverse geometry

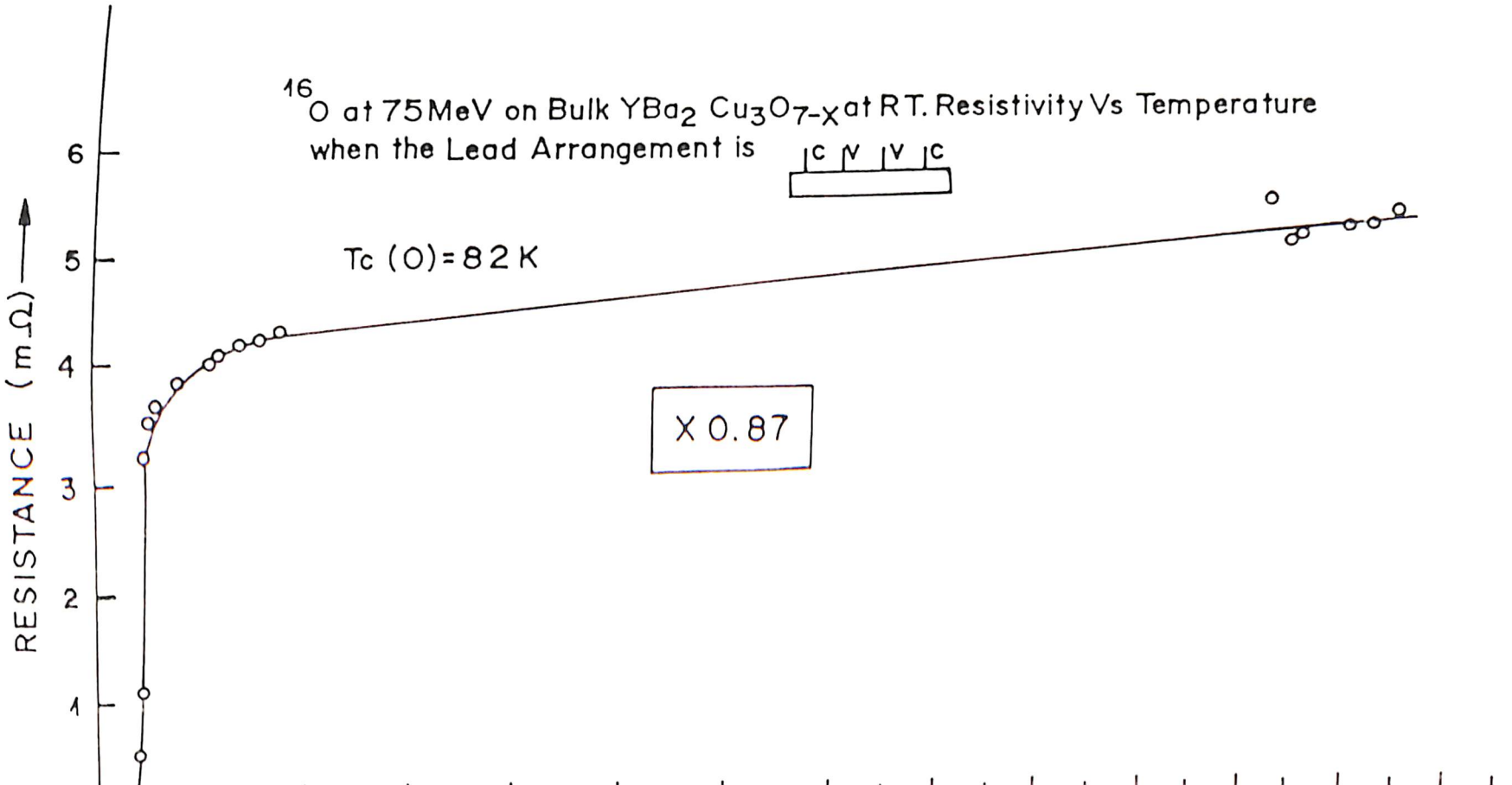
^{16}O at 75MeV on Bulk $YBa_2Cu_3O_{7-X}$ at RT. Resistivity Vs Temperature
when the Lead Arrangement is
C V V C
Tc (O) = 82 K
X 0.87
RESISTANCE (mΩ)
6
5
4
3
2
1

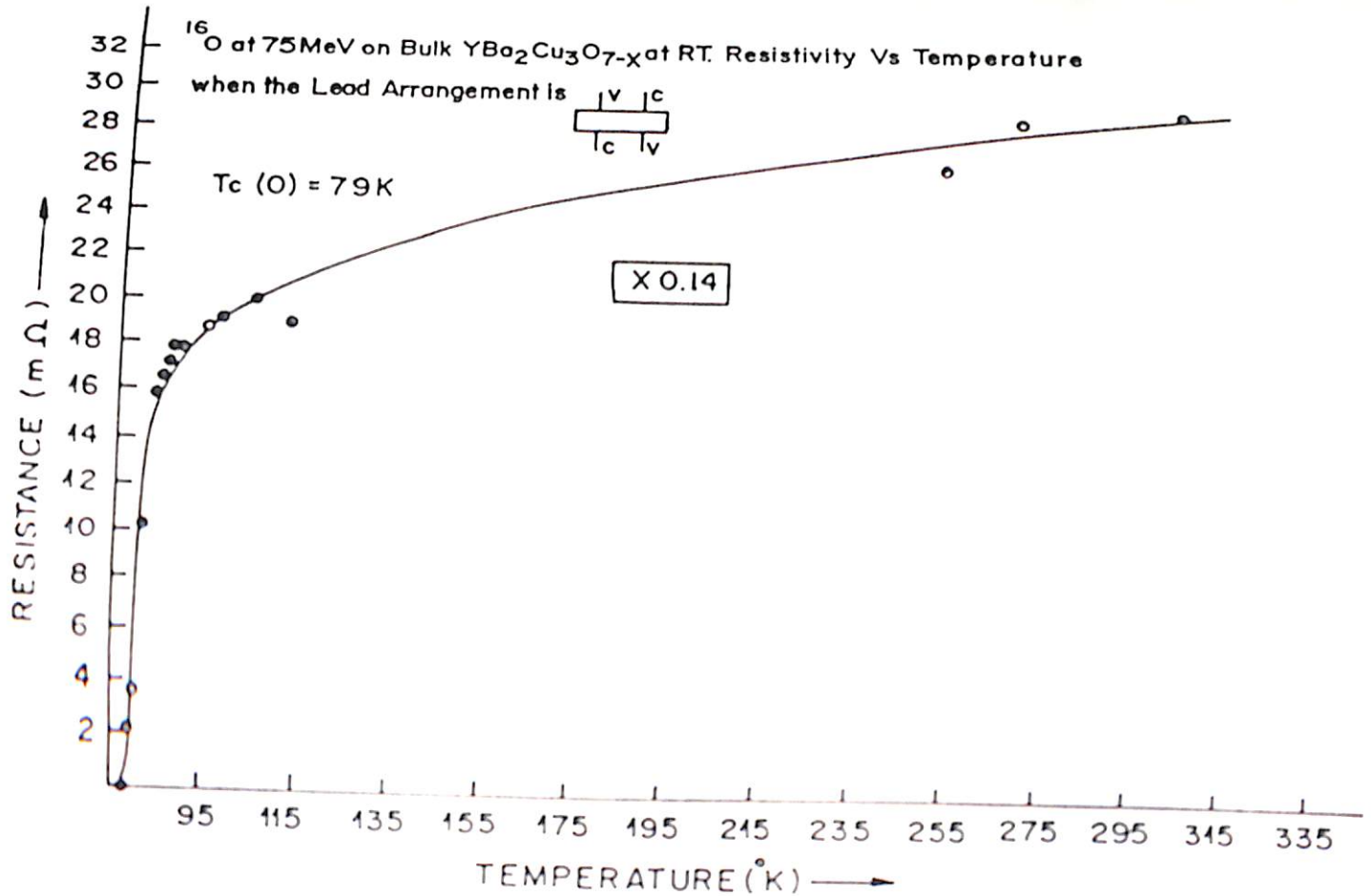

Fig. 4a.13. (b) R vs T of oxygen irradiated bulk YBCO at dose $5 \times 10^{12}/cm^2$ in transverse arrangement.

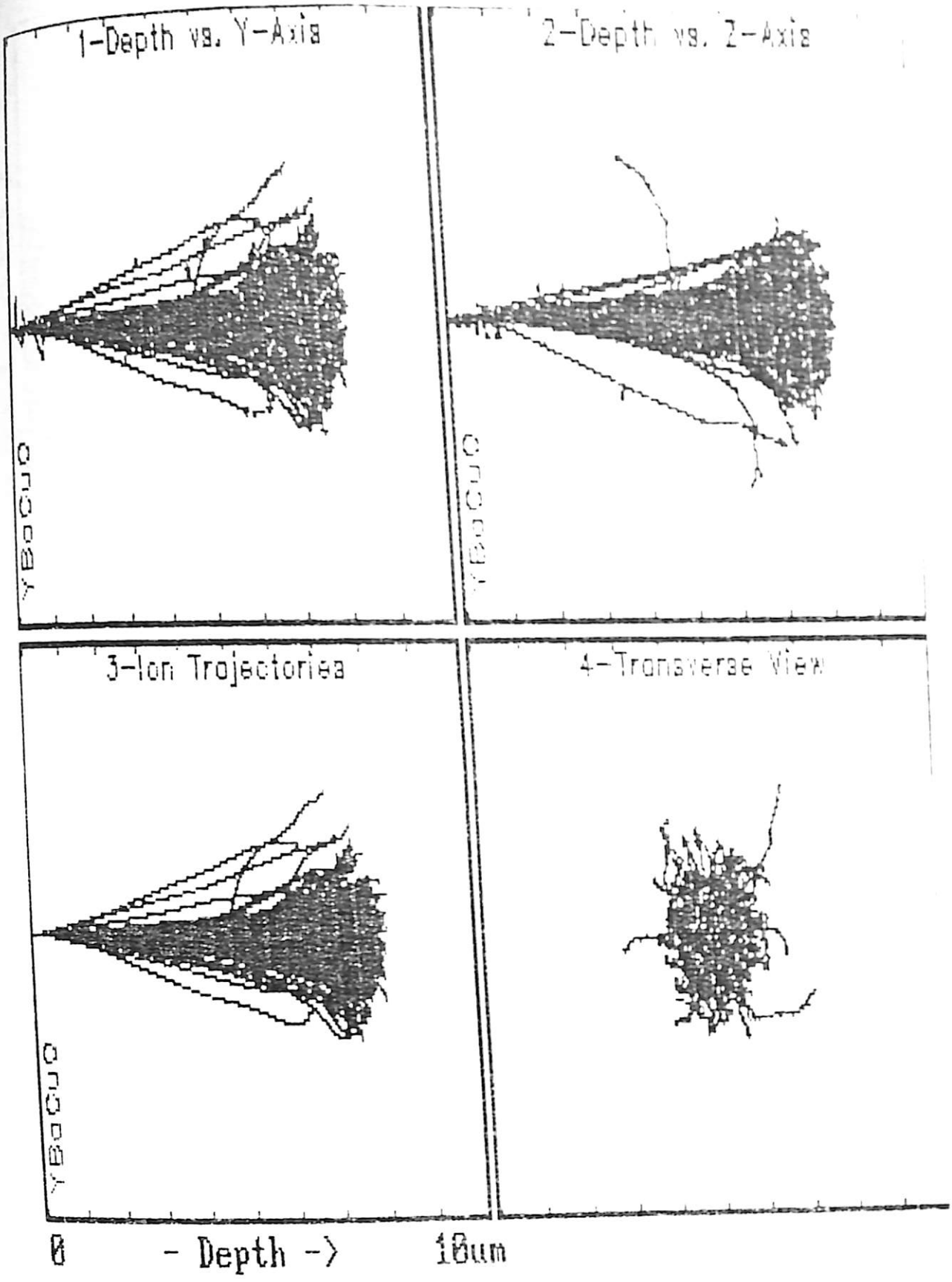

Fig. 4a.14.(a). TRIM plot of 75 MeV nickel trajectory in $YBa_2Cu_3O_7$

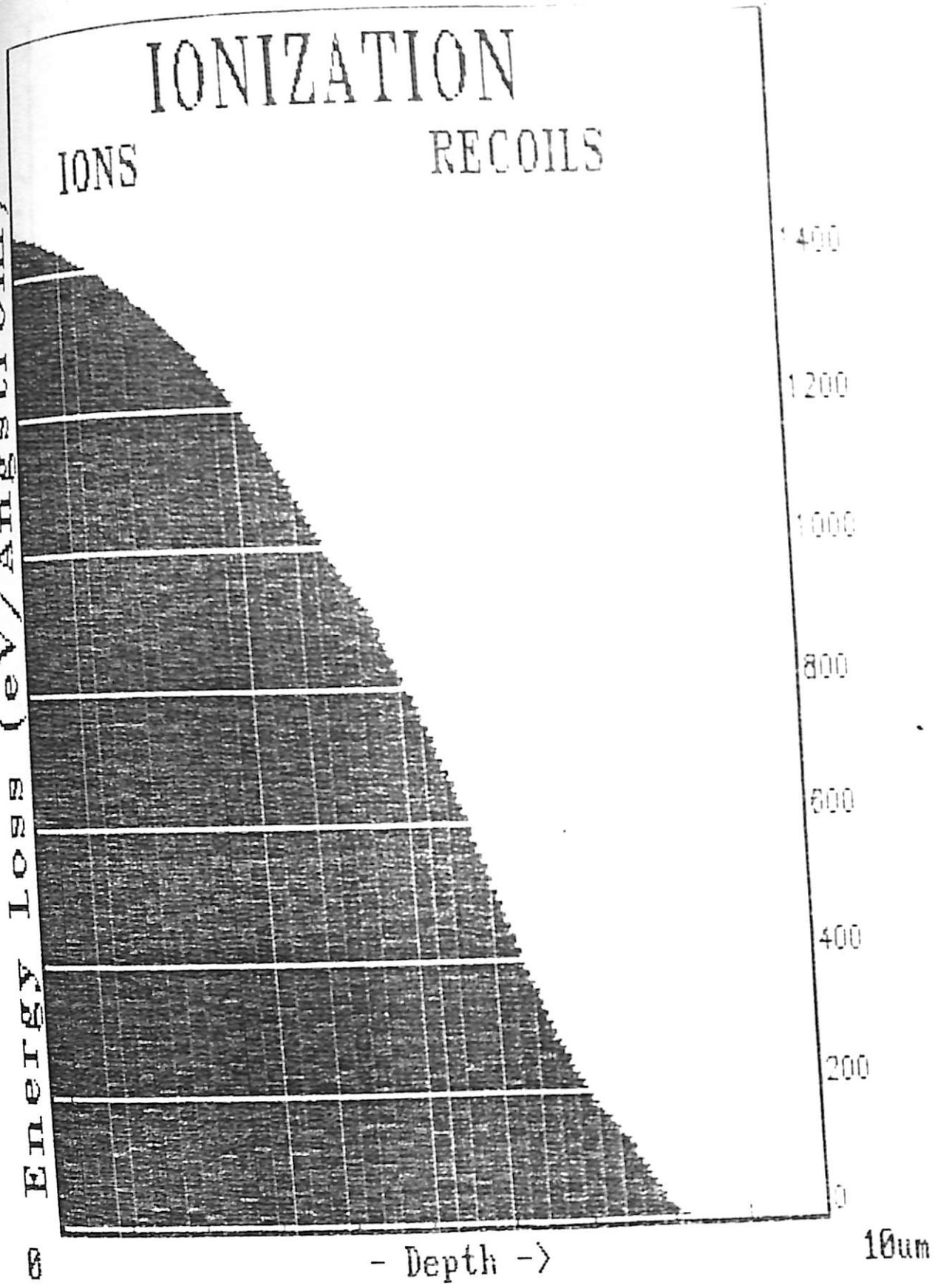

Fig. 4a.14.(b). TRIM plot of ionization by 75 MeV nickel ions and also by the recoils created by the bombarding ions in $YBa_2Cu_3O_7$

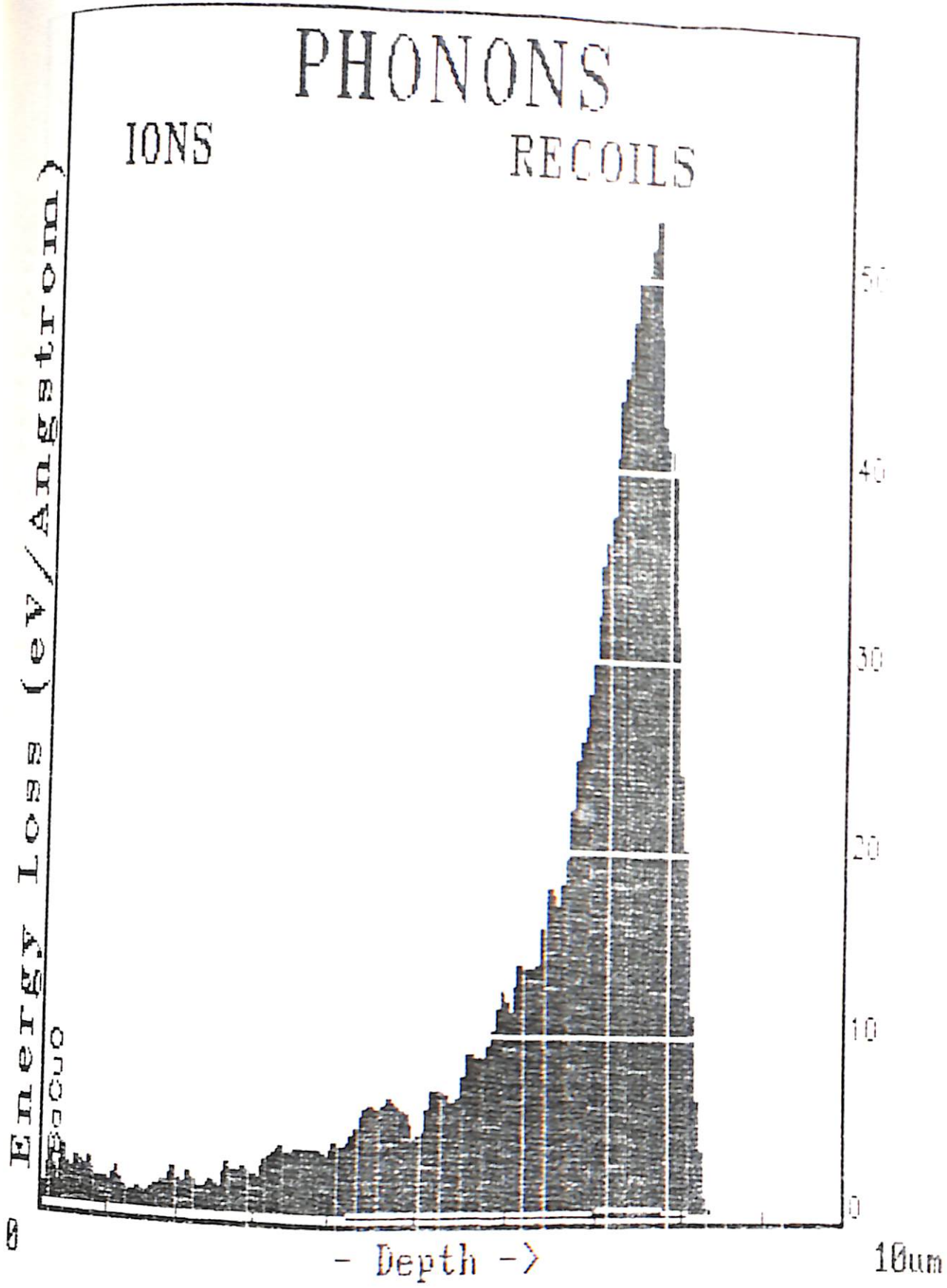

Fig. 4a.14.(c). TRIM plot of phonons created by 75 MeV nickel ions in $YBa_2Cu_3O_7$

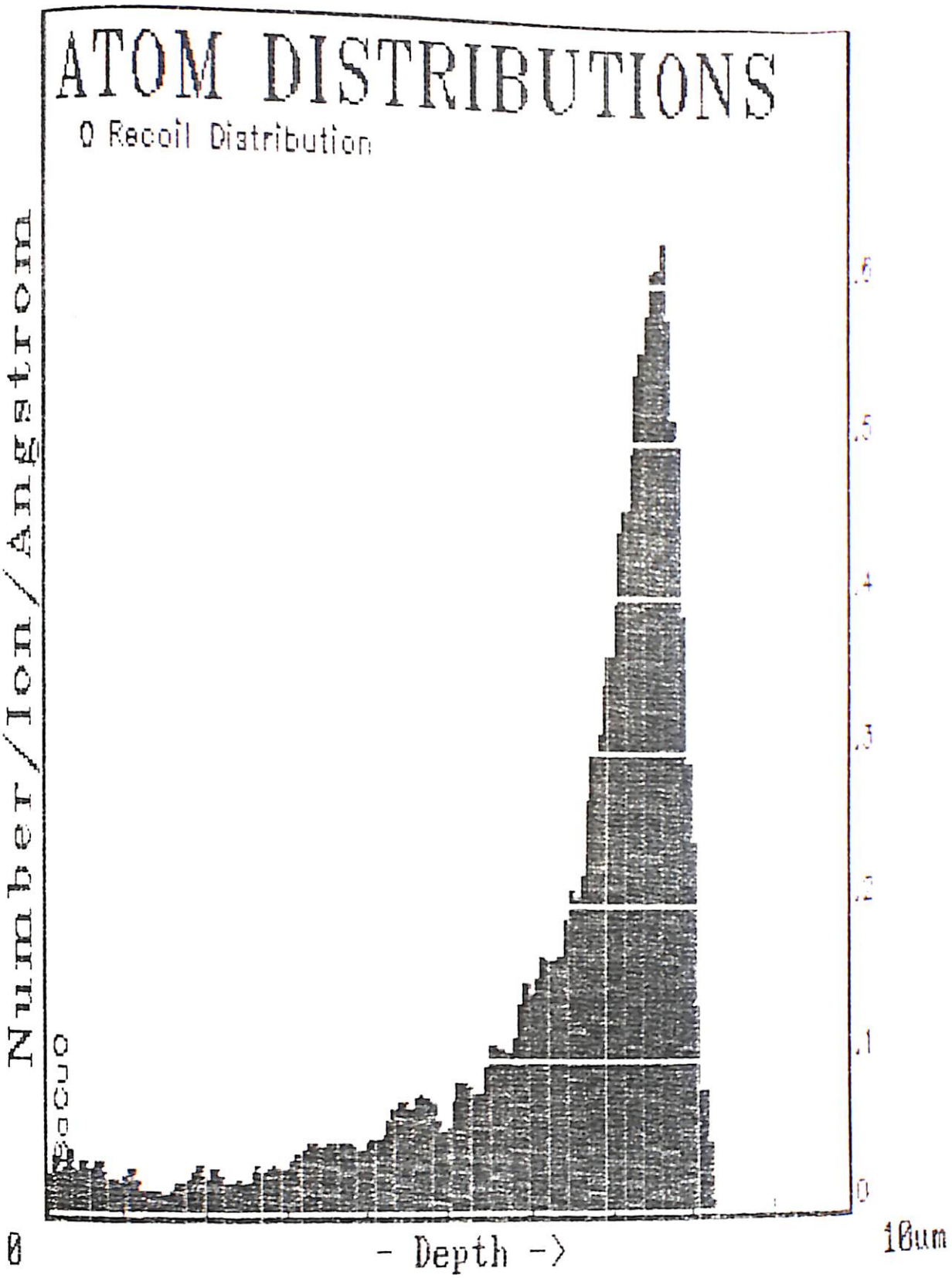

Fig. 4a.14. (d). TRIM plot of oxygen recoil distribution (≡ O target vacancies) created by 75 MeV nickel in $YBa_2Cu_3O_7$

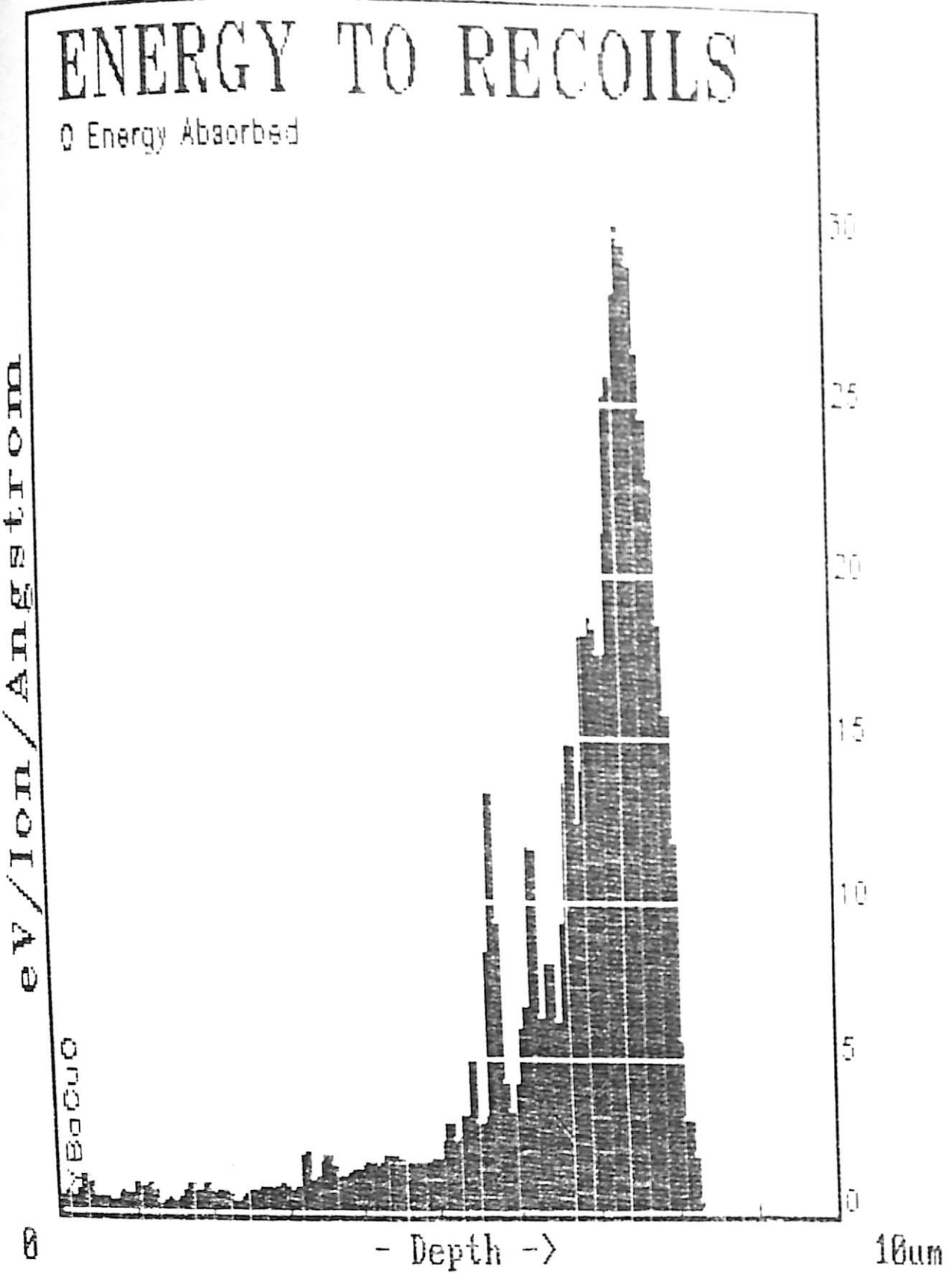

Fig. 4a.14.(e). TRIM plot of energy absorbed by oxygen recoils for 75 MeV nickel irradiation in $YBa_2Cu_3O_7$

the different graphs by TRIM for this projectile-target combination.

TABLE 4a.4

Beam Species	Energy	Rate of Electronic energy loss $(dE/dX)_e$ in eV/Å	Rate of Nuclear energy loss $(dE/dX)_n$ in eV/Å	Range
^{58}Ni	75 MeV	1.46 E+03	3.60 E+00	7.7μm
	10 KeV	1.23 E+01	1.24 E+02	65 Å

4a.3.2 Results of insitu R vs. dose measurement

Fig. 4a.15 (a) and 4a.15 (b) show the insitu variation of normalised resistance (R_n) with fluence for 75 MeV Ni irradiation at ambient and low temeperature. Here also, in low temperature experiment, temperature is kept above the Tc of the target. For room temperature irradiation resistance increases above its unirradiated value at initial smaller doses. It then goes down below its unirradiated value at the dose ~ 6 x $10^{11}/cm^2$. It again starts increasing considerably at dose ~ 2 X $10^{13}/cm^2$ and at a dose 1 X $10^{14}/cm^2$, upto which dose value the room temperature experiment was carried out, the normalised change in resistance

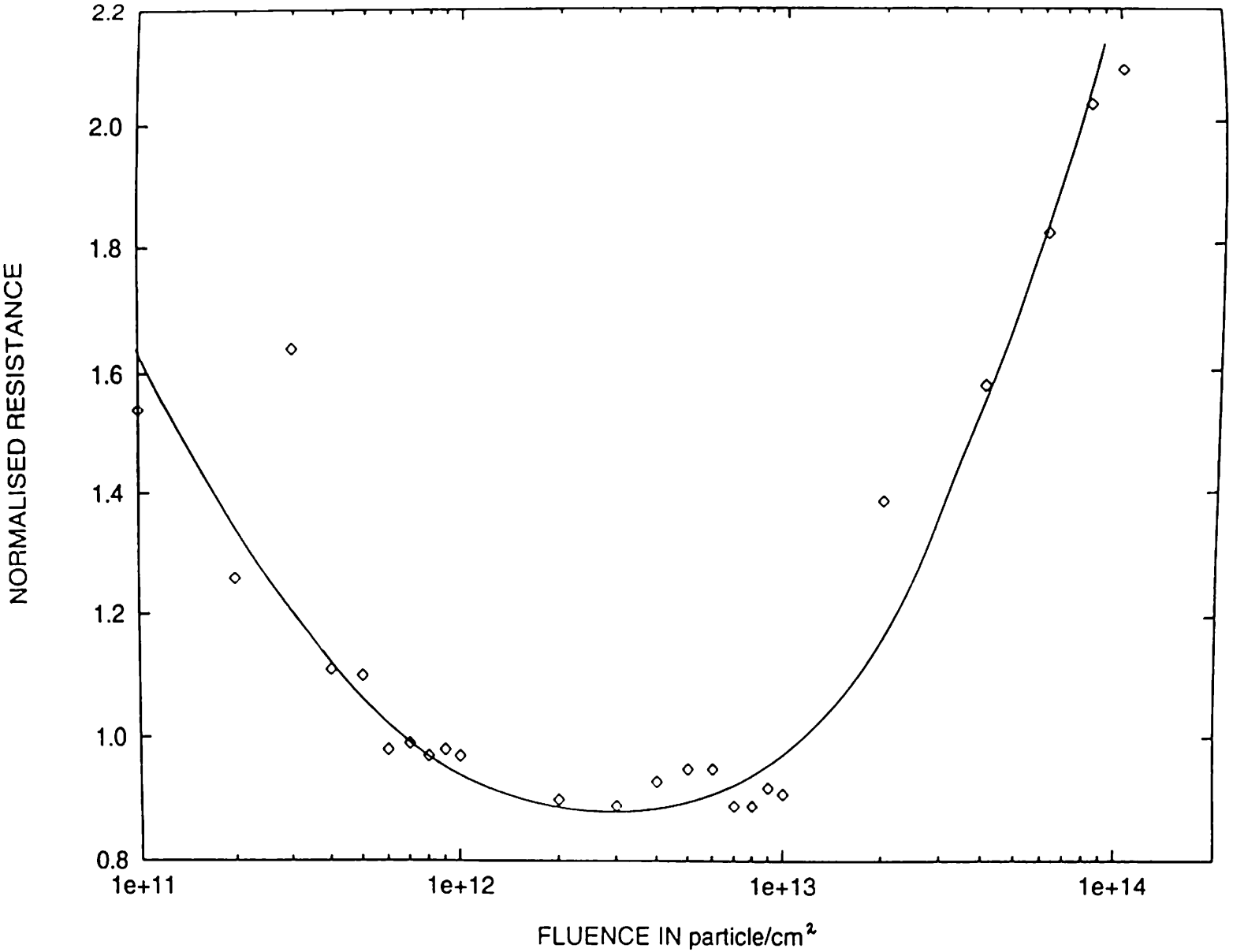

Fig. 4a.15. (a) Insitu variation of normalised resistance (R_n) as a function of dose for 75 MeV ^{58}Ni irradiation at ambient temperature.

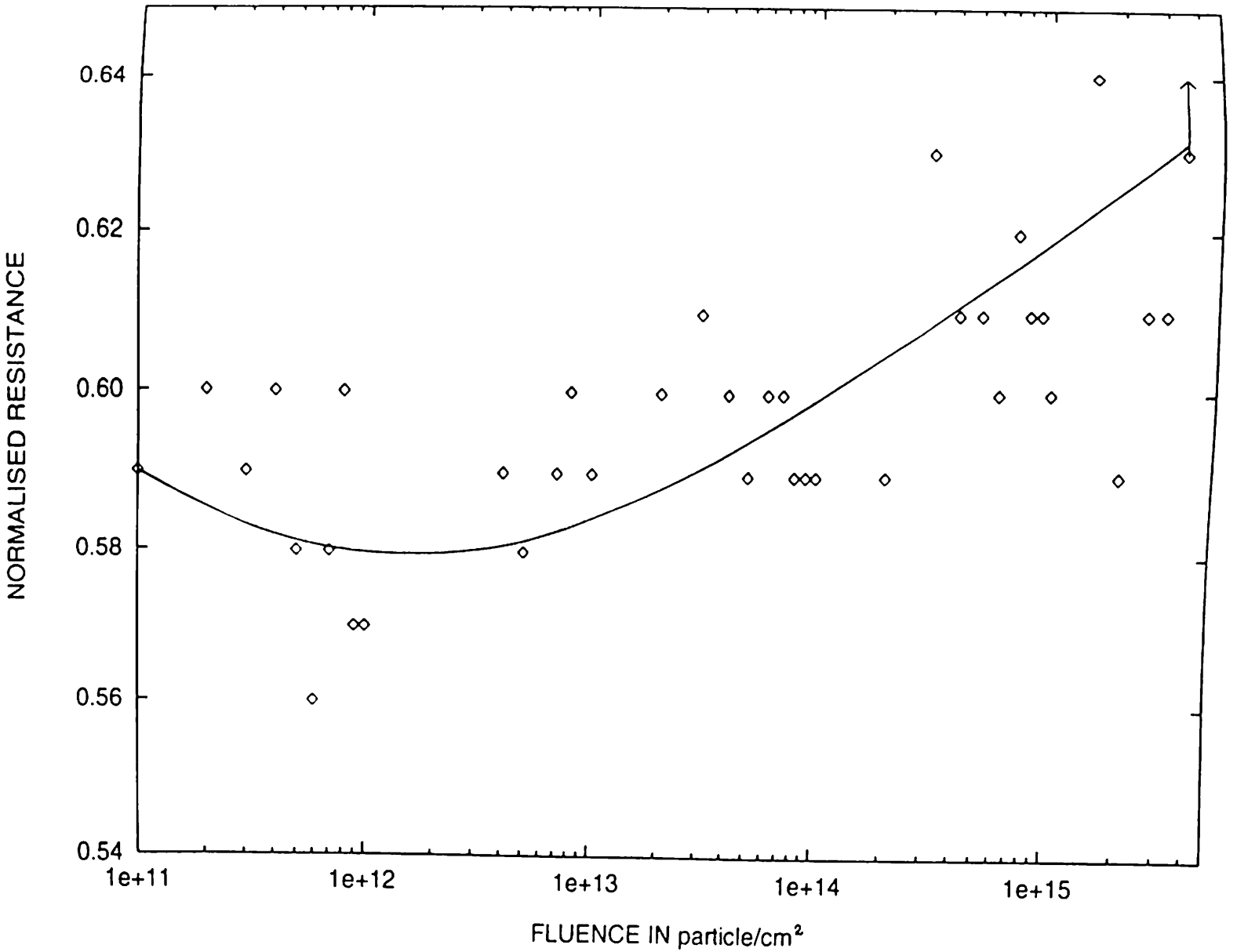

Fig. 4a.15. (b) Insitu variation of normalised resistance (R_n) as a function of dose for 75 MeV ^{58}Ni irradiation at low temperature. The ↑ indicates the sudden increase of resistance beyond that dose.

becomes ~1.09. In contrast, in low temperature irrradiation experiment, the resistance decreases below its unirradiated value even at smaller doses also and this lower value of resistance sustains even at the highest dose of room temperature irradiation, i.e., 1 x $10^{14}/cm^2$. At this value of the fluence, in low temperature case, the normalised change in resistance takes up the value ~ 0.41 which is far different from that value at room temperature irradiation experiment. The low temperature irradiation was continued with further increase in fluence and at a dose ~ 4 X $10^{15}/cm^2$, the resistance jumped to a high value where normalised change in resistance becomes ~ 102.72.

4a.3.3. Results of XRD

Fig. 4a.16 (a), (b), (c) show the X-ray diffraction spectra of 75 MeV Ni irradiated YBCO samples at different doses, namely, 5 X $10^{11}/cm^2$, 1 X $10^{13}/cm^2$ and 1 X $10^{14}/cm^2$ respectively. From the spectra, it is clear that the crystallinity of the sample deteriorated gradually with increasing dose. The twin peaks due to (013) and (103) planes between 32° and 34° diffraction angle, disappear even at a dose of 5 X $10^{12}/cm^2$. The 'c' lattice parameter calculation shows that it does not change from its initial unirradiated value. In the three cases shown in Fig. 4a.16 (a), (b),

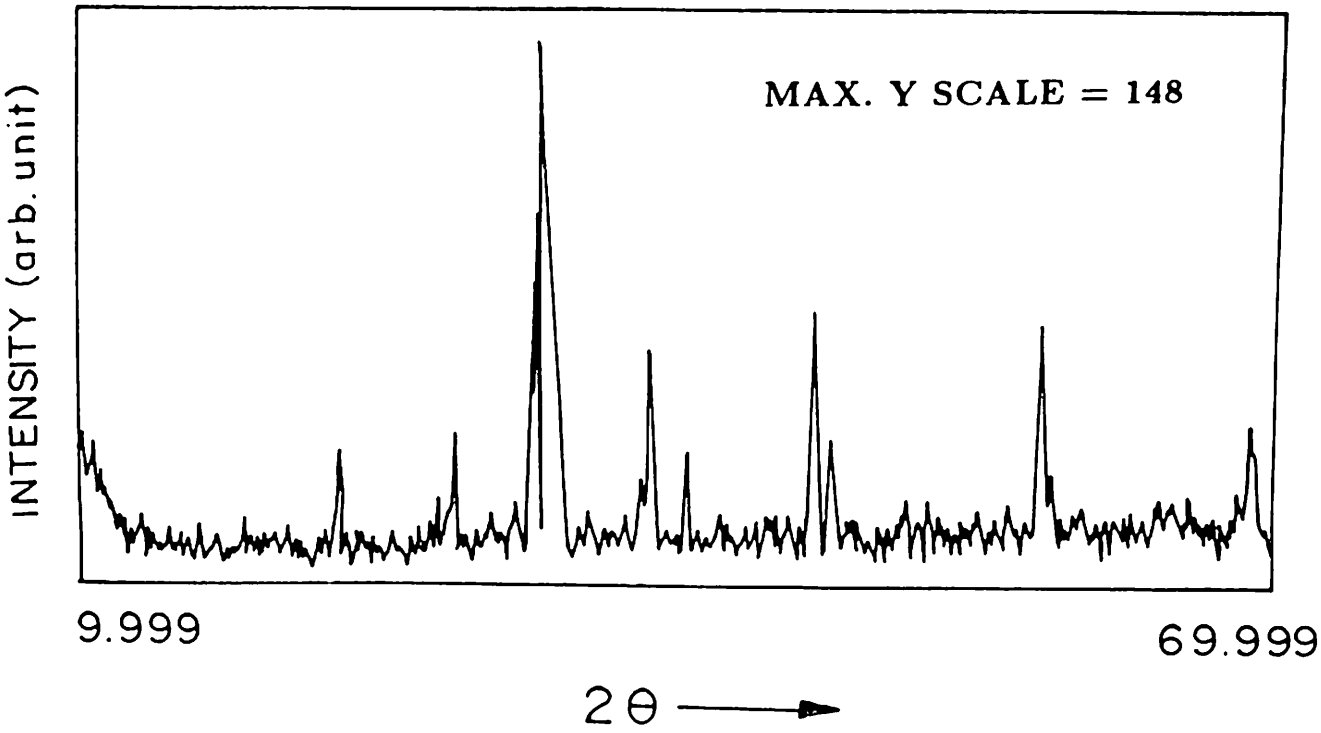

Fig. 4a.16. (a) XRD spectrum of Ni irradiated bulk YBCO at dose $5 \times 10^{11}/cm^2$.

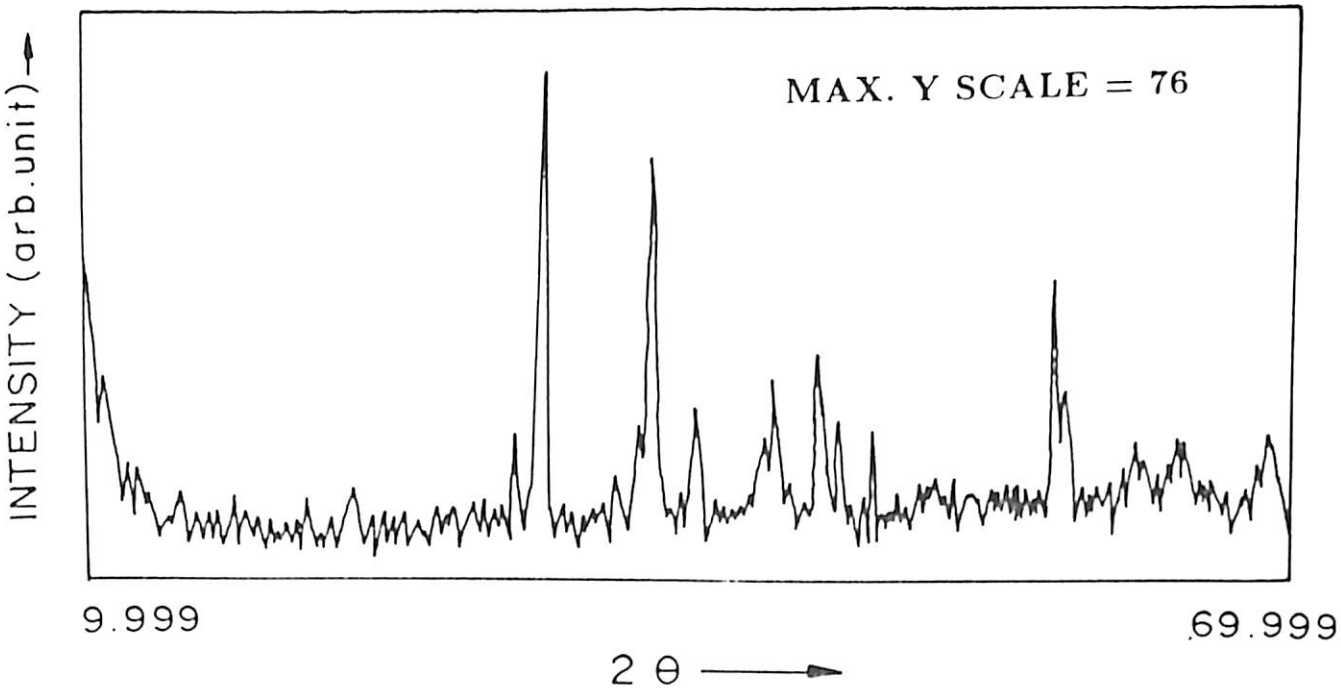

Fig. 4a.16. (b) XRD spectrum of Ni irradiated bulk YBCO at dose $1 \times 10^{13}/cm^2$.

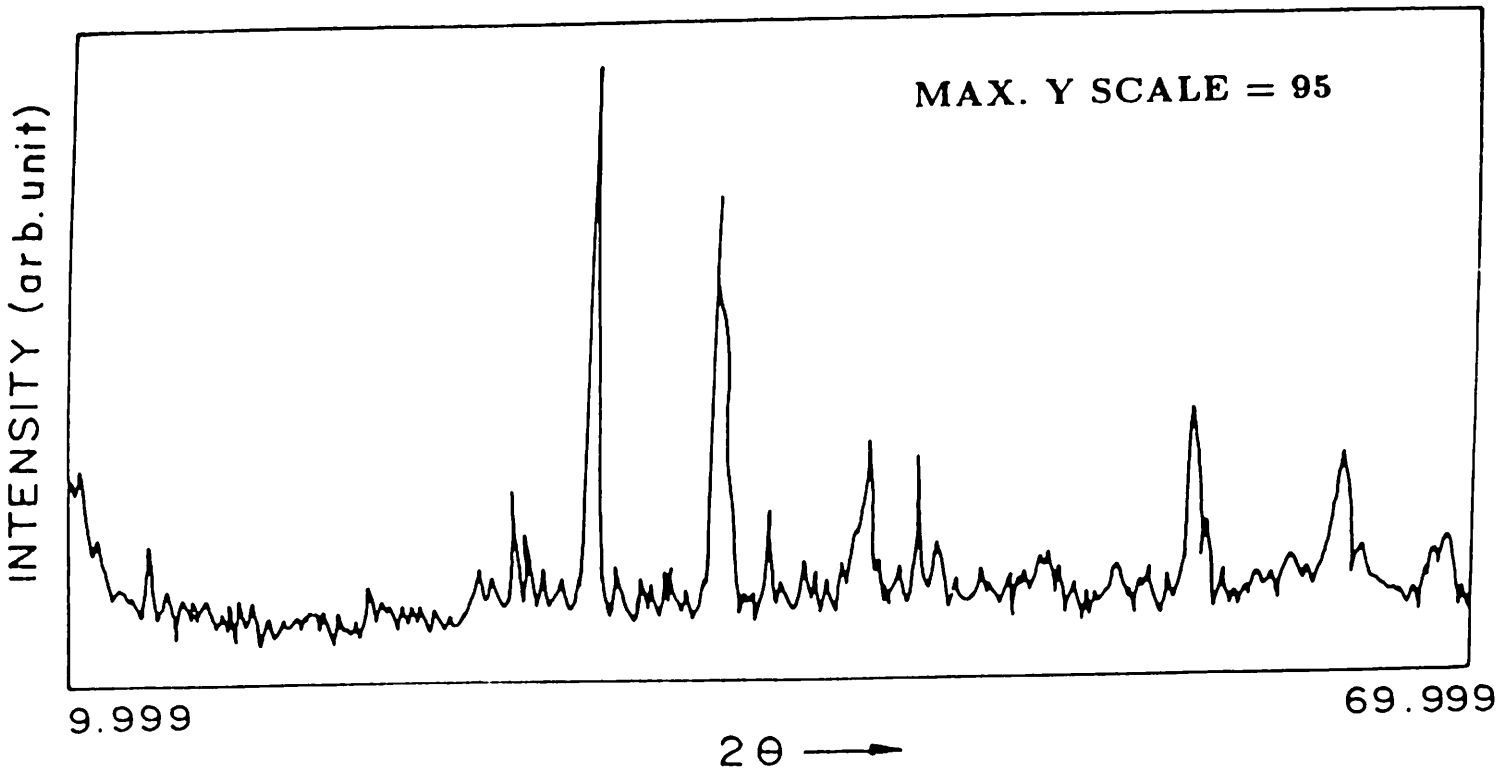

Fig. 4a.16. (c) XRD spectrum of Ni irradiated bulk YBCO at dose $1 \times 10^{14}/cm^2$.

(c), 'c' parameter is calculated as 11.59Å, 11.66Å and 11.62Å respectively. Fig. 4a.17 shows the slow scan of the diffraction spectrum between angle 46° and 48° of a typical irradiated sample at a dose 1 X $10^{14}/cm^2$. The broadening of the peaks shows the degradation of crystallinity due to irradiation.

4a.3.4. Results of SEM

Fig. 4a.18 (a) and (b) show the surface morphology by SEM of the unirradiated sample at two different magnifications. Fig. 4a.19 (a), (b) ,(c) and (d) are the SEM photographs of the 75 MeV Ni irradiated sample at dose values 1 X $10^{11}/cm^2$, 1 X $10^{12}/cm^2$, 1 X $10^{14}/cm^2$ and 1 X $10^{16}/cm^2$. Comparing the two sets of photographs it is clearly visible that at lower doses surface morphology and grain sizes do not change much from that of the unirradiated sample. Only at high dose, the grain size changes.

4a.3.5. Results of R vs. T measurement

Fig. 4a.20 shows the R vs. T curve for the unirradiated sample in 75 MeV Ni irradiation experiment and fig 4.21 (a) and (b) show the R vs. T characteristics of the two YBCO samples irradiated by 75 MeV Ni at two different doses, namely, 5 X $10^{12}/cm^2$ and 1 X $10^{14}/cm^2$. The unirradiated sample shows little bit lower Tc(0) (~80 K), because the Tc of the unirradiated

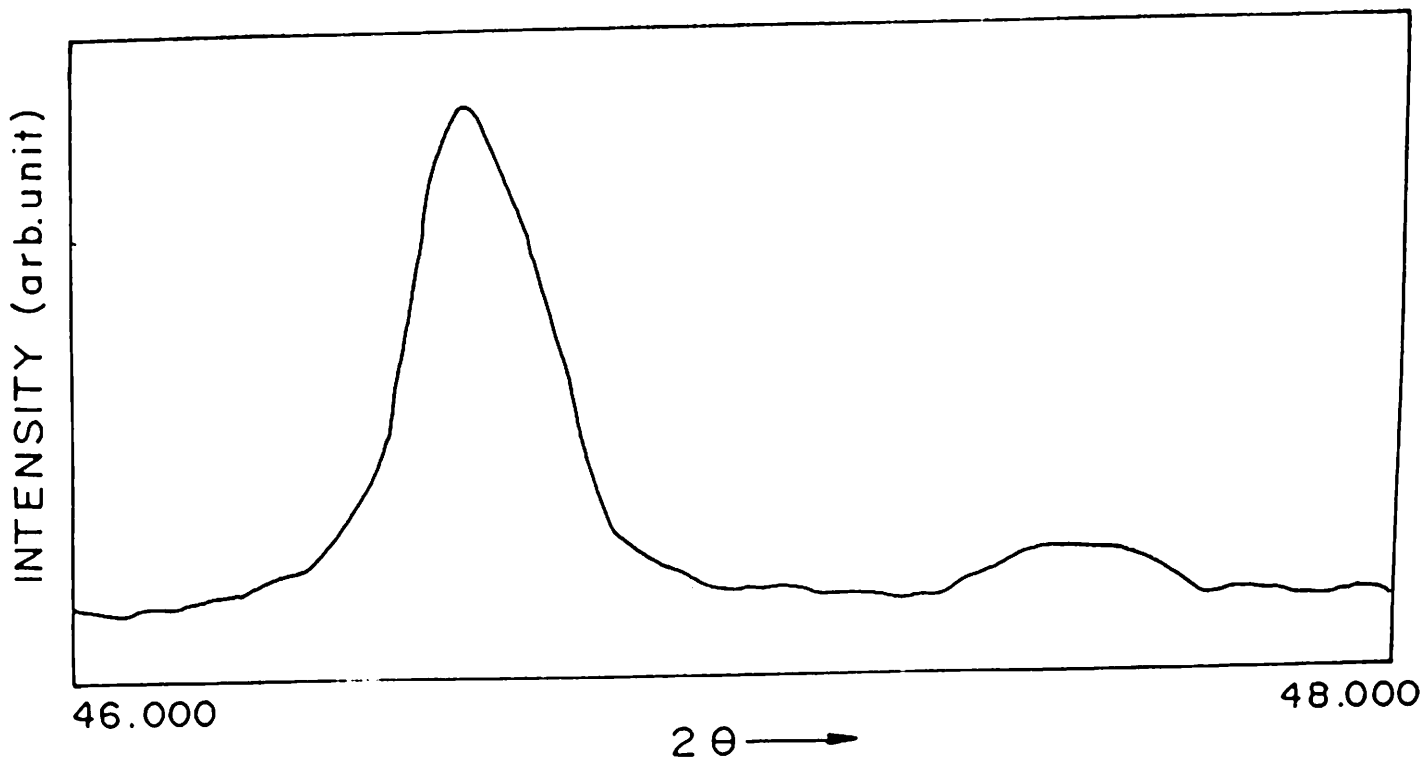

Fig. 4a.17. Slow scan of XRD spectrum of Ni irradiated bulk YBCO at dose $1 \times 10^{14}/cm^2$.

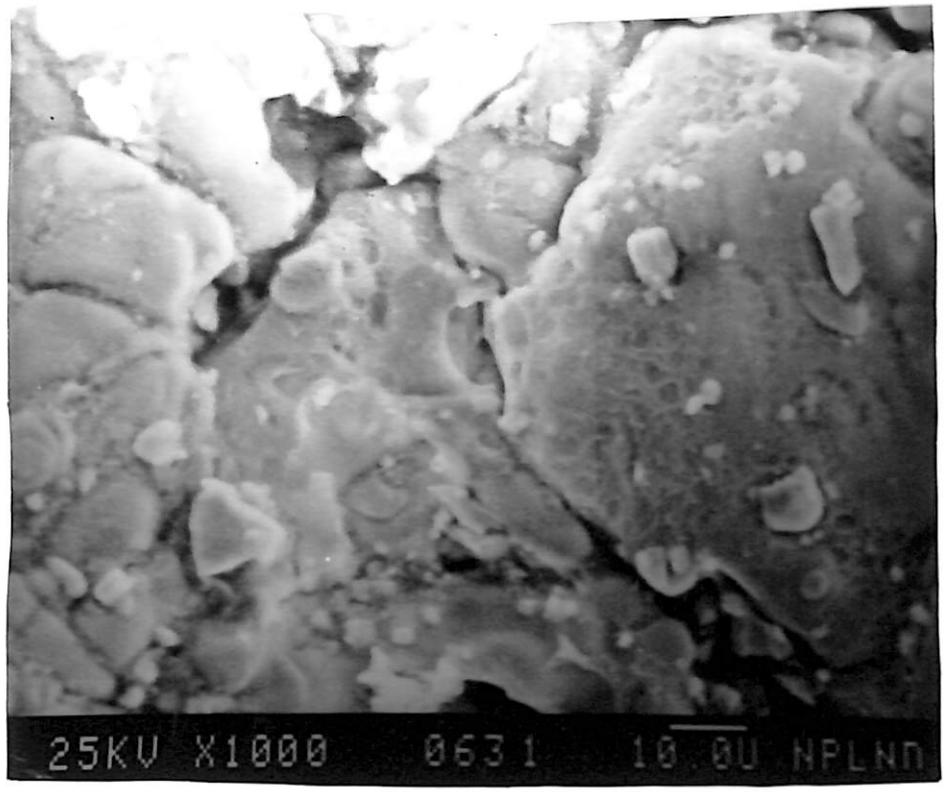

(a)

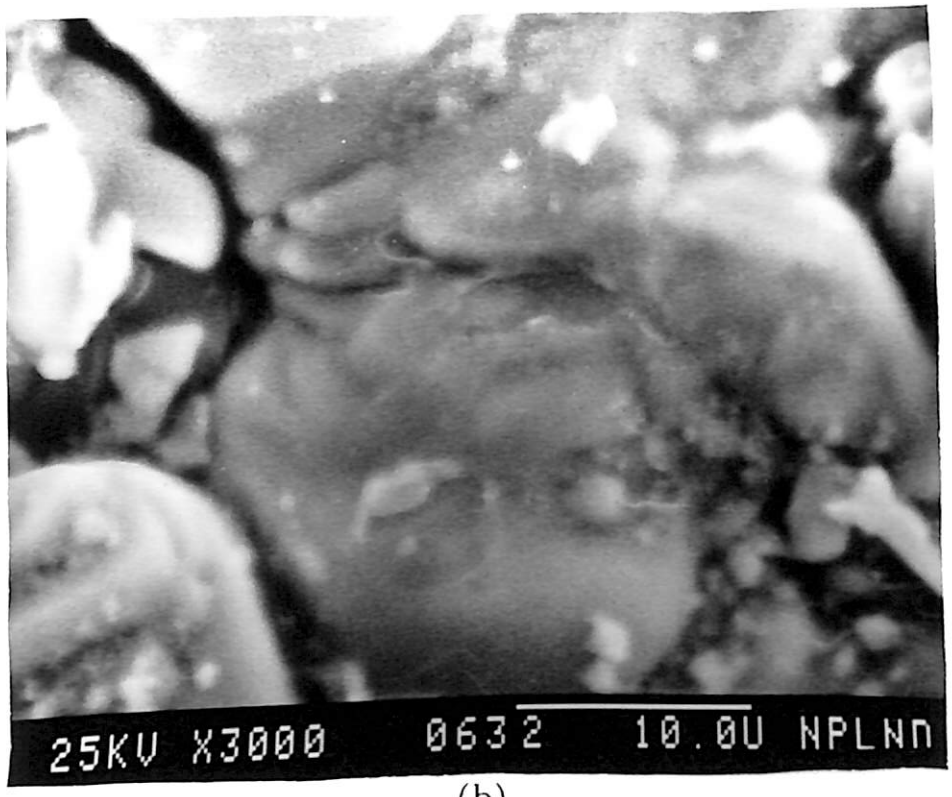

(b)

Fig. 4a.18. (a), (b) SEM pictures of unirradiated bulk $YBa_2Cu_3O_{7-\delta}$ sample used for Ni irradiation experiment at two different magnifications.

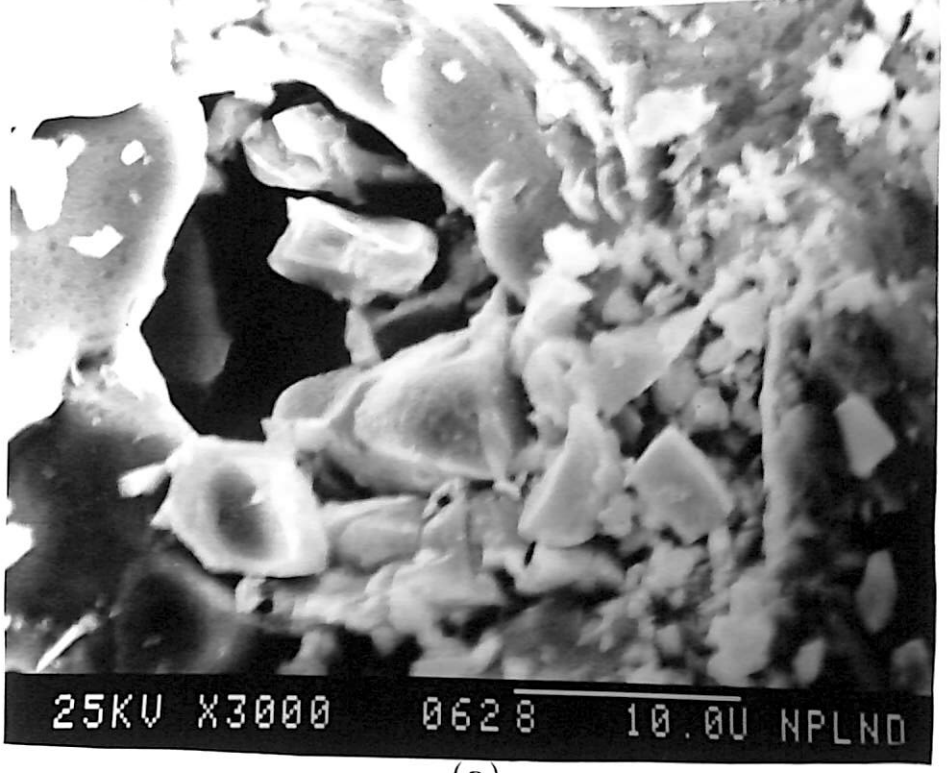

(a)

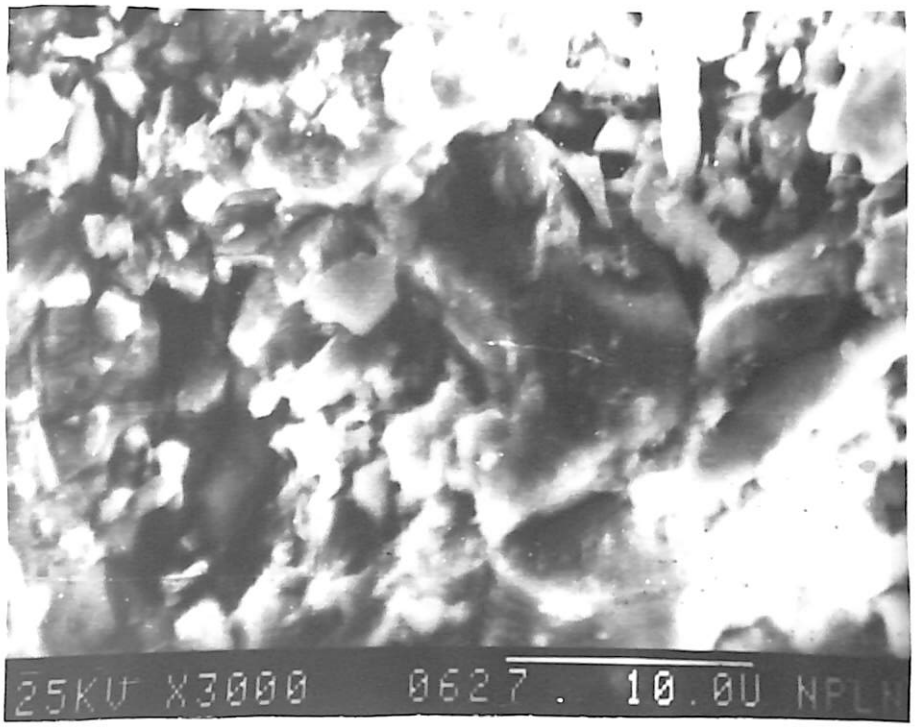

(b)

Fig. 4a.19. SEM pictures of Ni irradiated bulk $YBa_2Cu_3O_{7-\delta}$ sample with dose (a) $1 \times 10^{11}/cm^2$ and (b) $1 \times 10^{12}/cm^2$

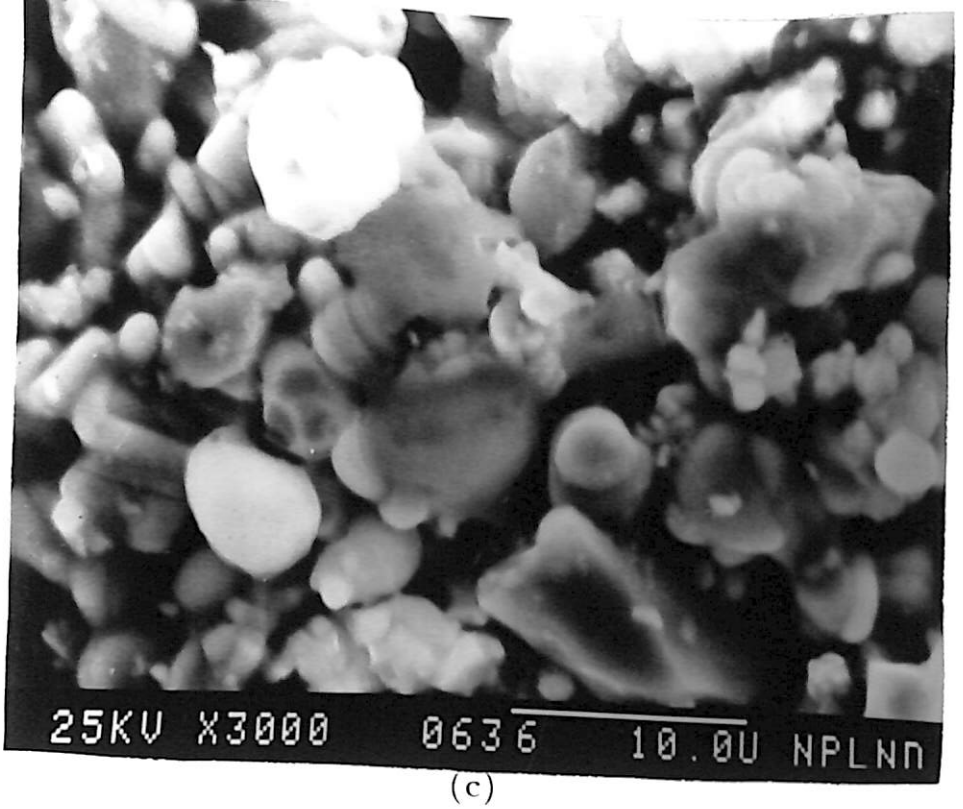

(c)

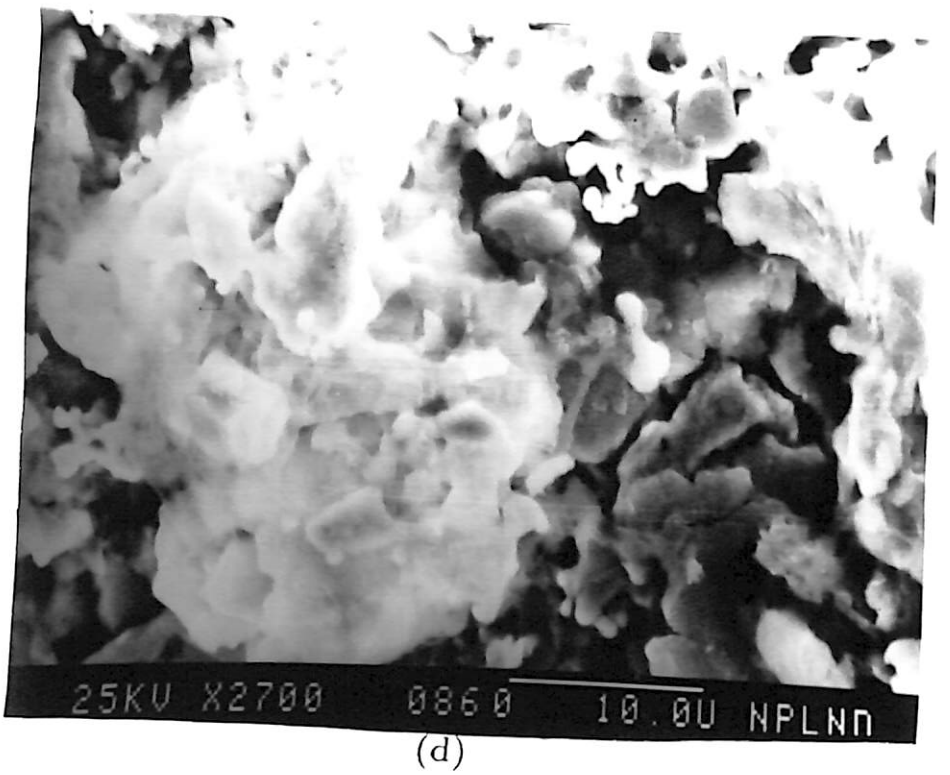

(d)

Fig. 4a.19. SEM pictures of Ni irradiated bulk $YBa_2Cu_3O_{7-\delta}$ sample with dose (c)$1 \times 10^{14}/cm^2$ and (d) $1 \times 10^{16}/cm^2$.

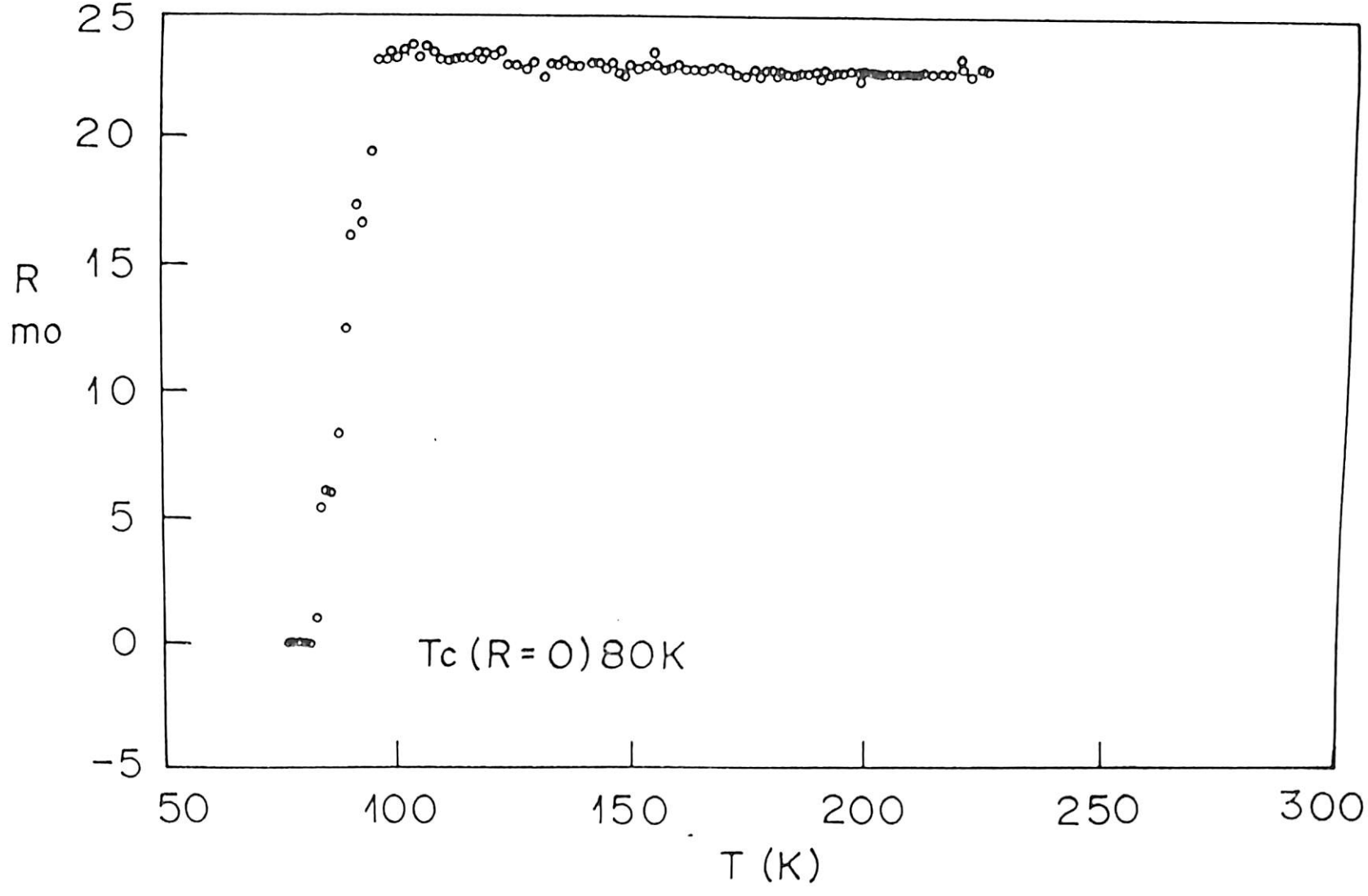

Fig. 4a.20. R vs. T of the unirradiated portion of Ni irradiated bulk YBCO sample.

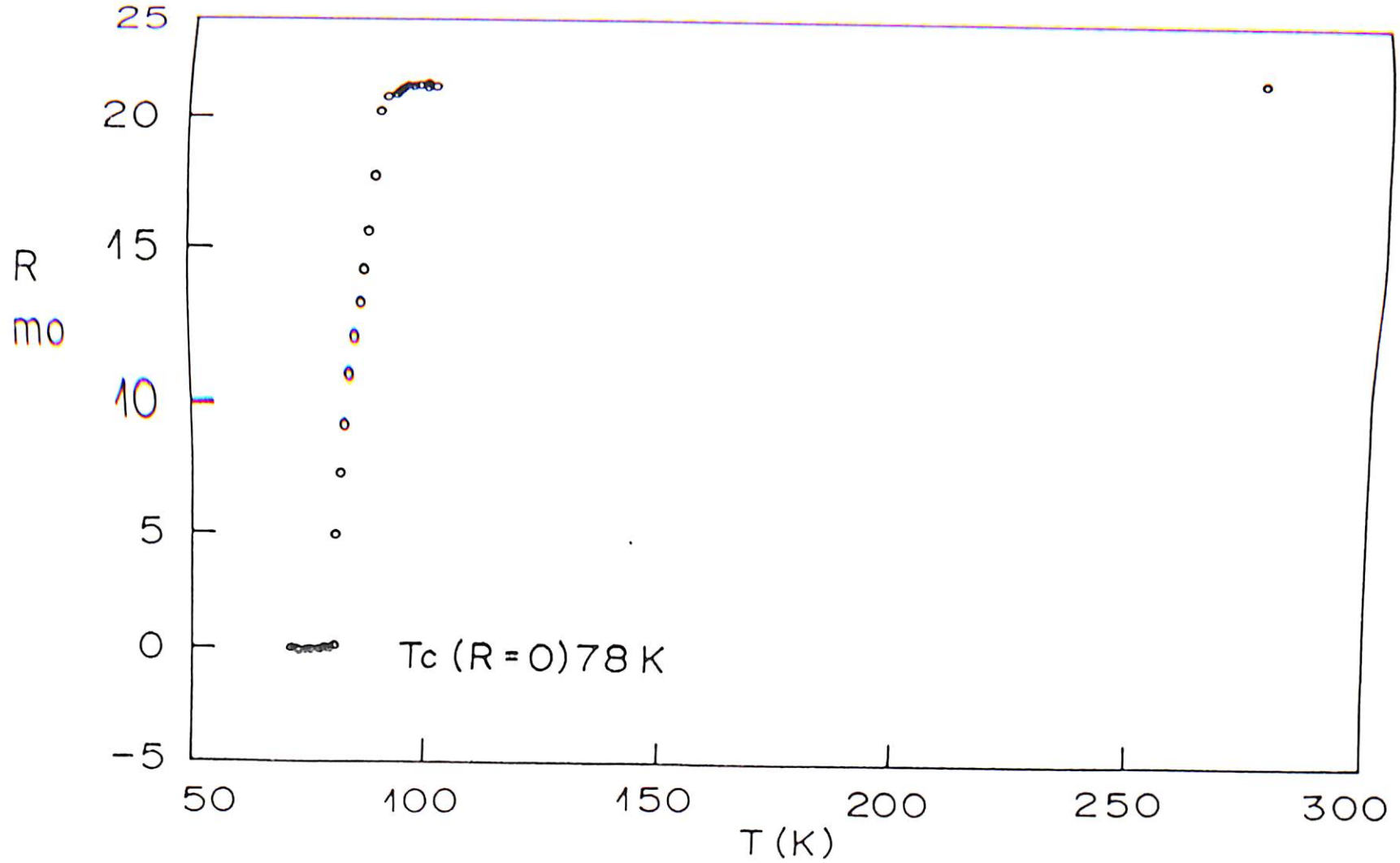

Fig. 4a.21. (a) R vs T characteristic of Ni irradiated bulk YBCO at dose $5 \times 10^{12}/\text{cm}^2$.

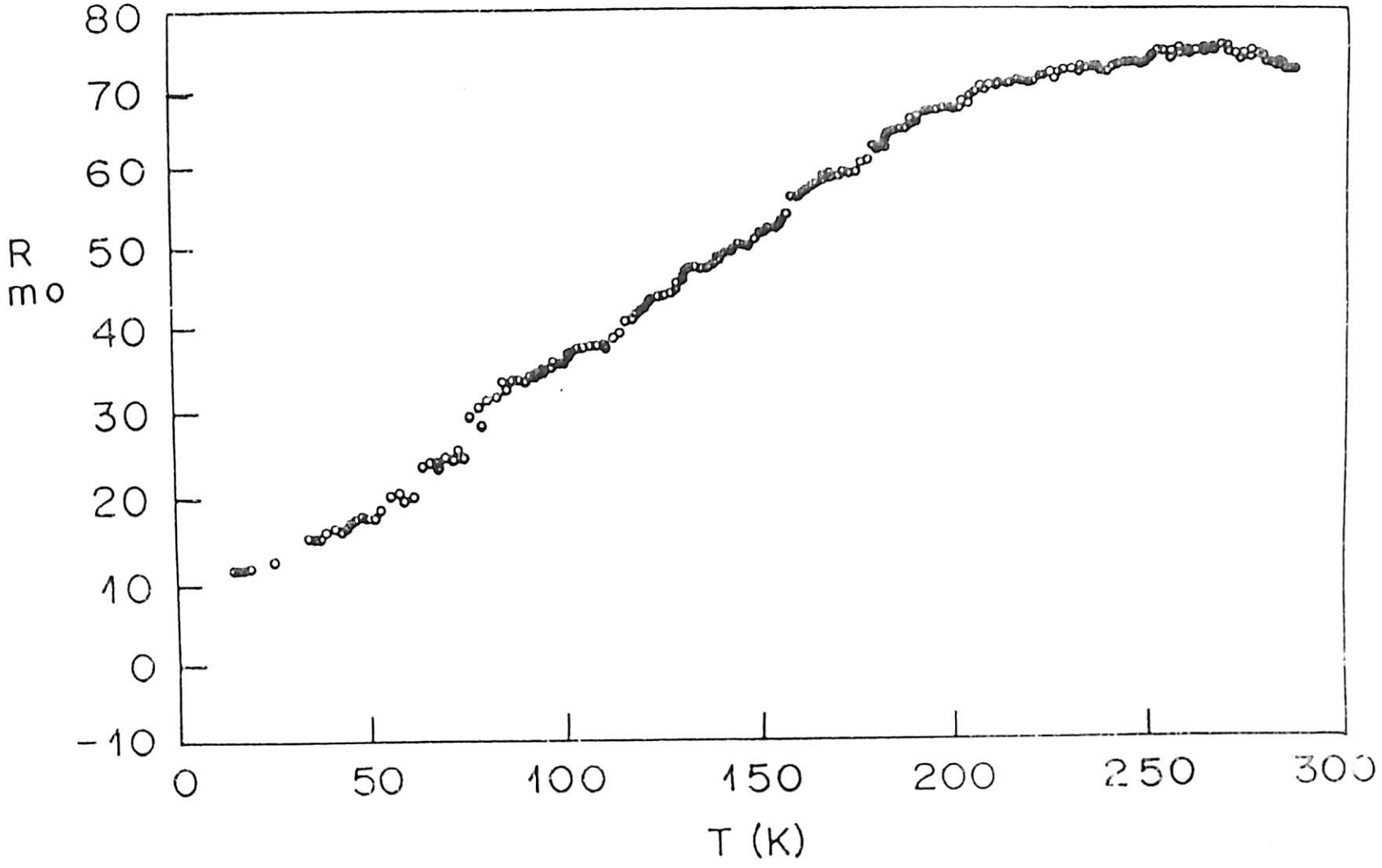

Fig. 4a.21. (b) R vs T characteristic of Ni irradiated bulk YBCO at dose $5 \times 10^{14}/cm^2$.

ample is measured by measuring the Tc of the lower surface of he irradiated sample and the sample for irradiation was kept in vacuum in the irradiation chamber for quite some time and R vs. T measurements are taken after taking out the samples to atmosphere which could degrade the Tc(0) of the sample by some amount. Due to irradiation at smaller doses (~5 X $10^{12}/cm^2$) Tc(0) is seen to be decreased by a small amount (~ 2 K). But at high dose (~ 1 X $10^{14}/cm^2$) the sample lost its superconducting property which is clearly visible from fig 4a.21 (b).

4a.4. Results of Iodine Irradiation

This section will describe the irradiation effect of 100 Mev ^{127}I on bulk YBCO samples.

4a.4.1. Projectile parameters

Fig. 4a.22 (a), (b), (c), (d) and (e) are the TRIM plots of the passage of 100 MeV ^{127}I inside the YBCO bulk target and ionization , vacancies and recoils created due to this irradiation. Table 4a.5 lists the energy loss values of 100 MeV and 10 Kev ^{127}I in YBCO target.

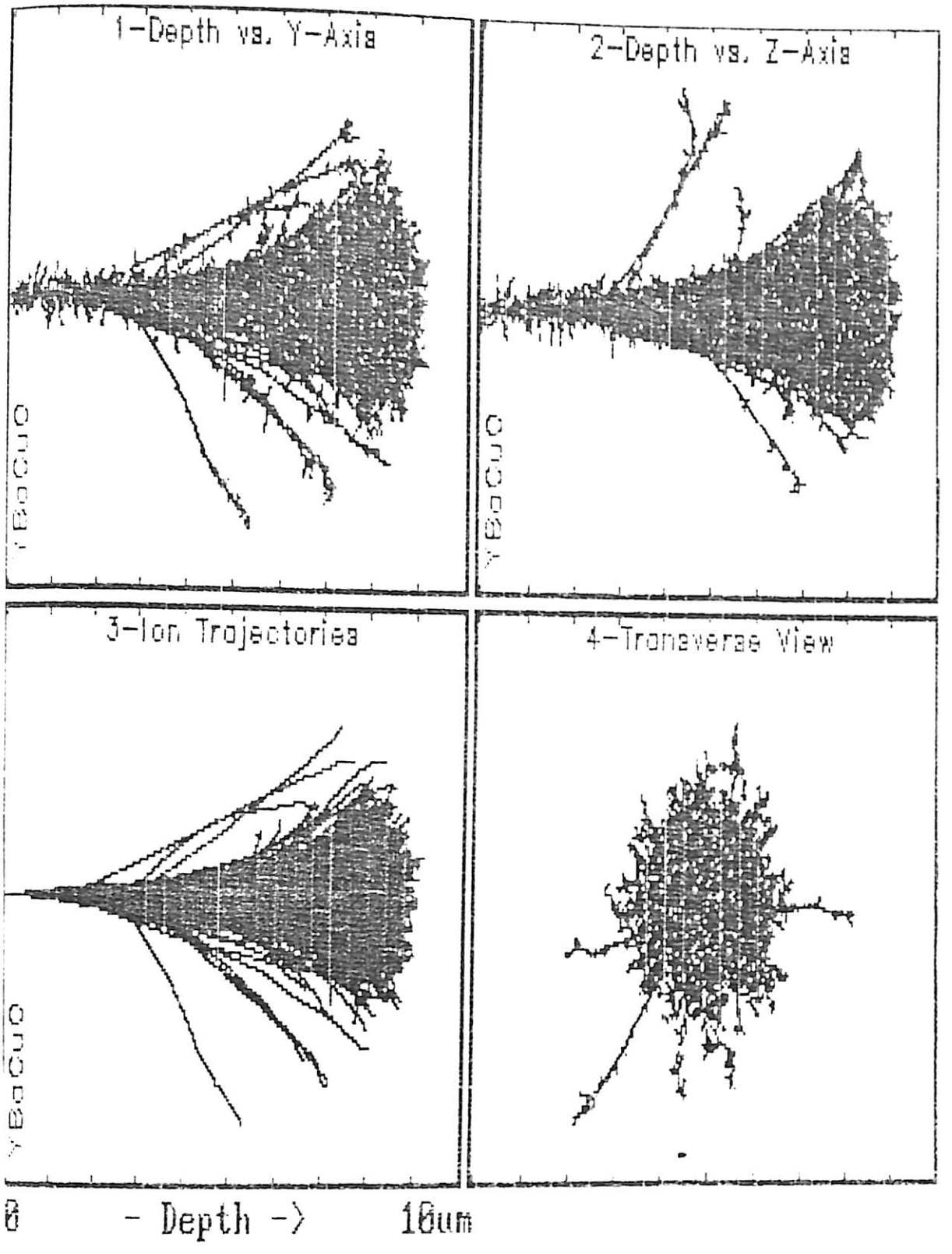

Fig. 4a.22.(a). TRIM plot of 100 MeV iodine trajectory in $YBa_2Cu_3O_7$

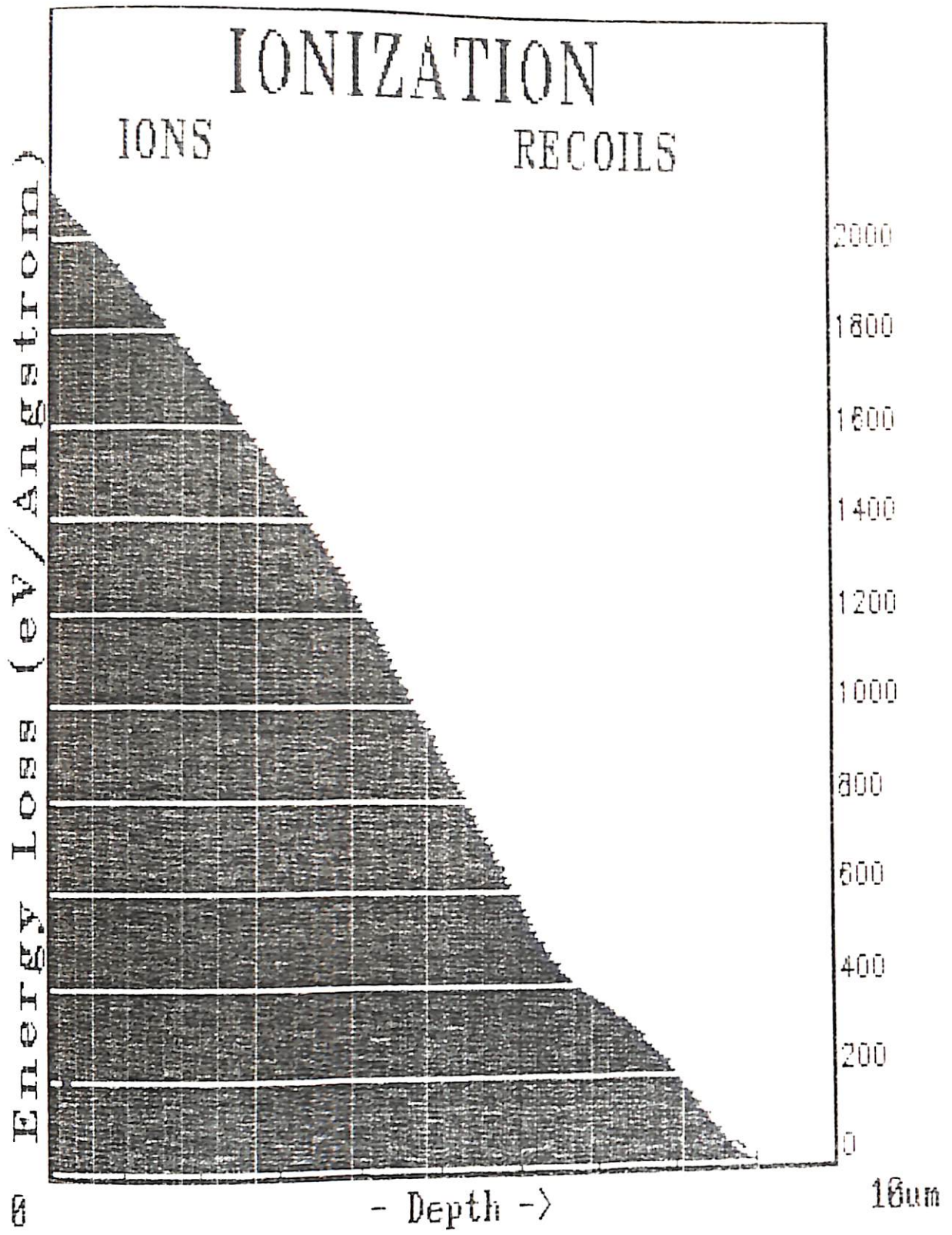

Fig. 4a.22.(b). TRIM plot of ionization by 100 MeV iodine ions and also by the recoils created by the bombarding ions in $YBa_2Cu_3O_7$

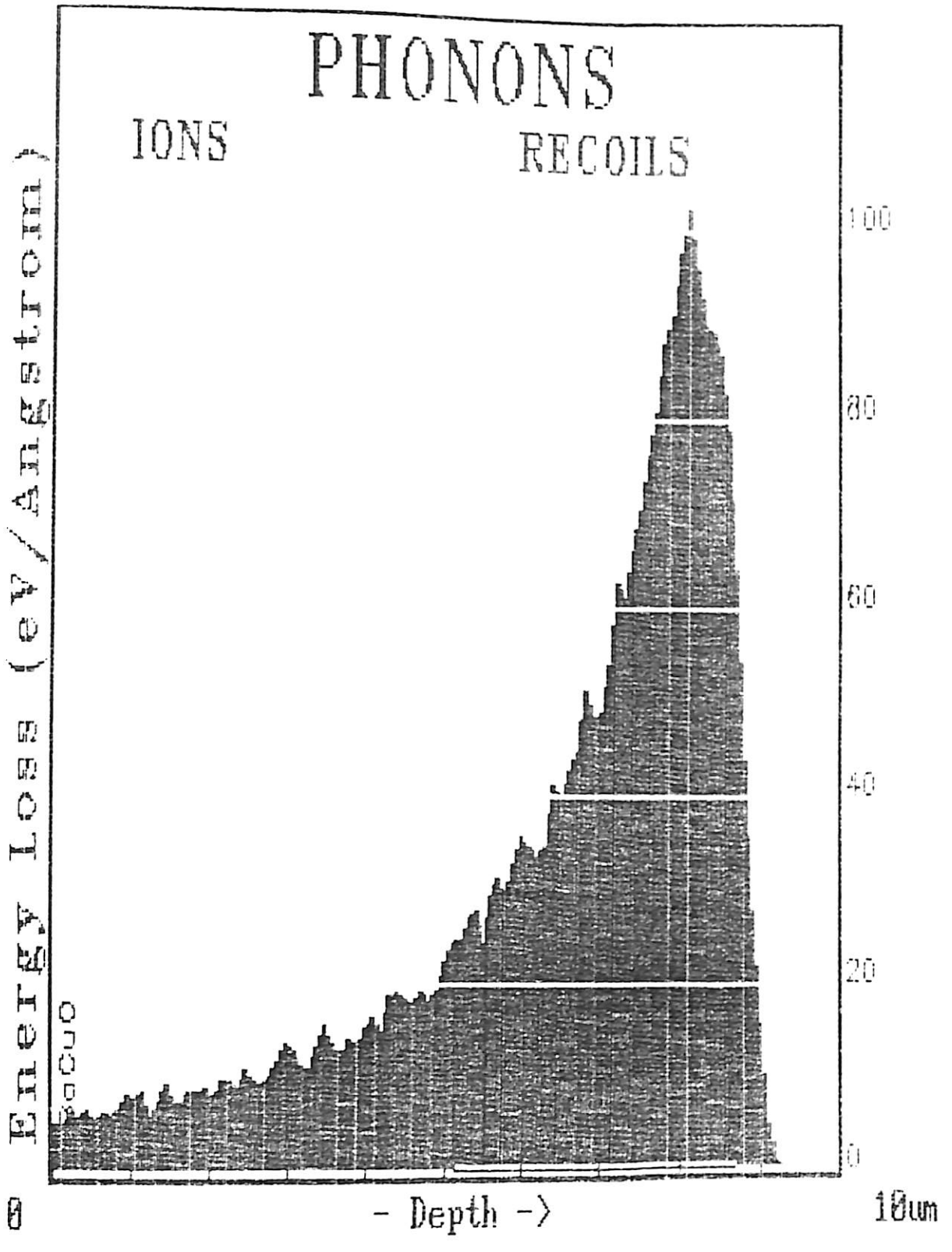

Fig. 4a.22.(c). TRIM plot of phonons created by 100 MeV iodine ions in $YBa_2Cu_3O_7$

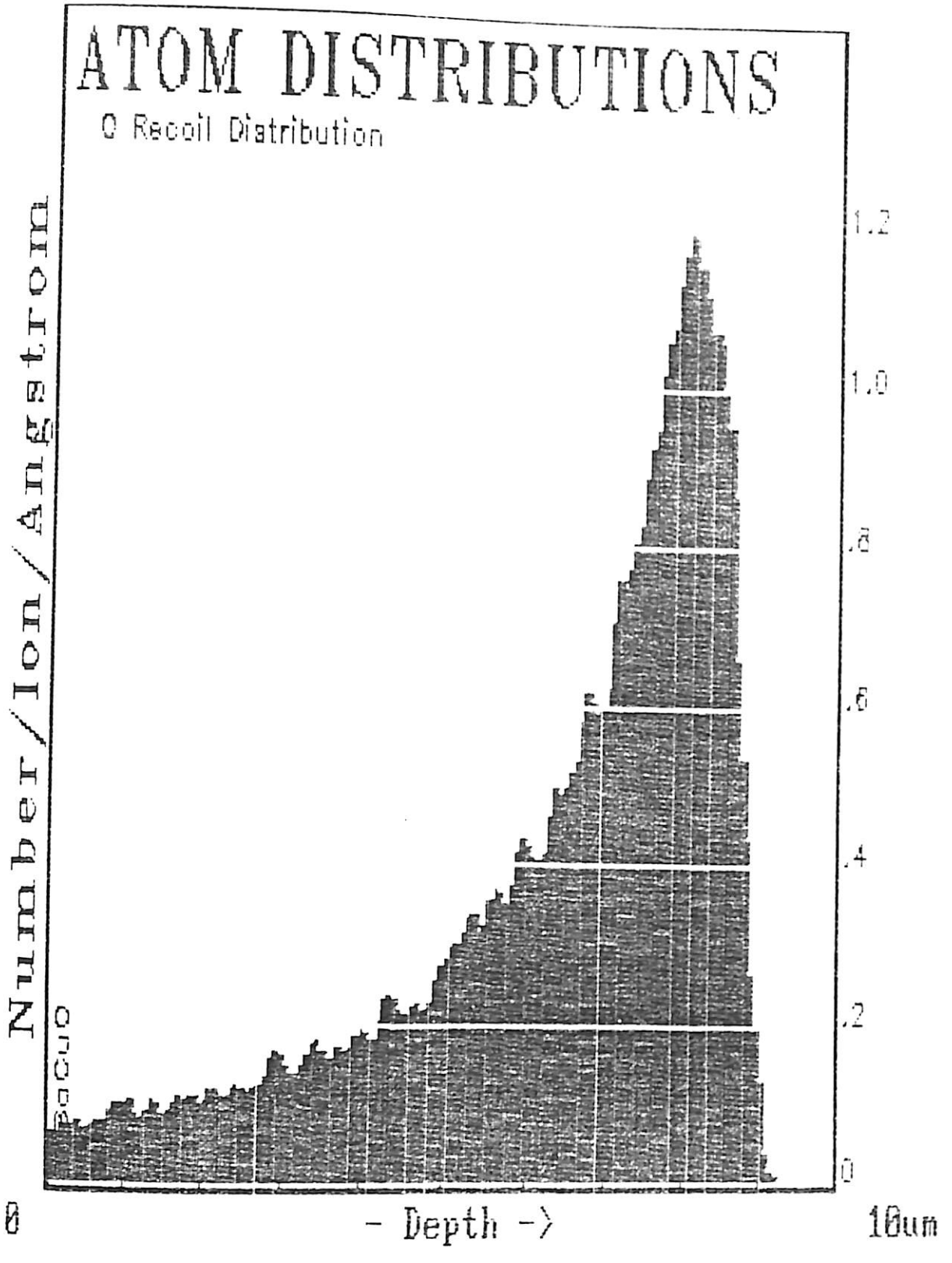

Fig. 4a.22.(e). TRIM plot of energy absorbed by oxygen recoils for 100 MeV iodine irradiation in $YBa_2Cu_3O_7$

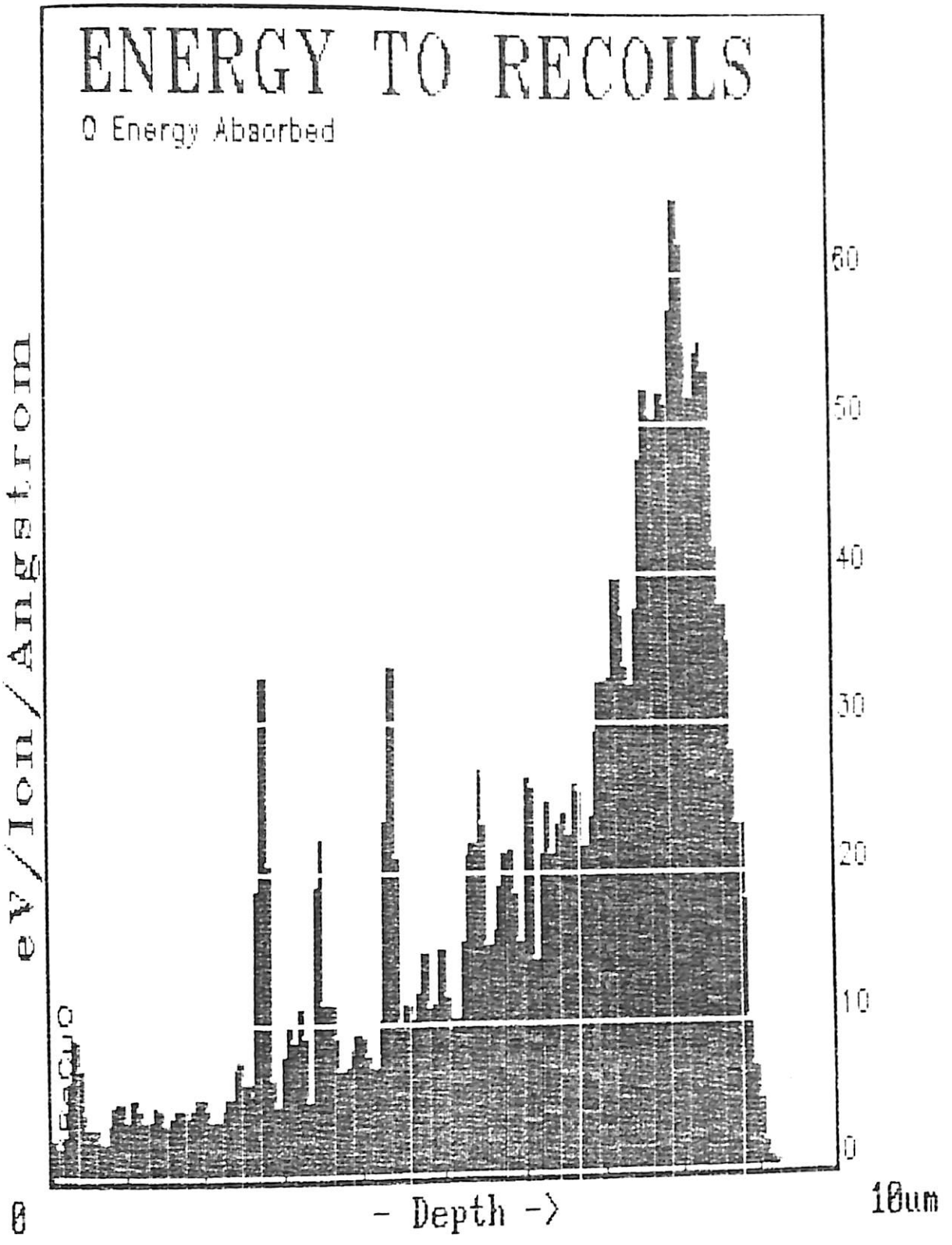

Fig. 4a.22.(d). TRIM plot of oxygen recoil distribution (≡ O target vacancies) created by 100 MeV iodine in $YBa_2Cu_3O_7$

TABLE 4a.5

Beam Species	Energy	Rate of Electronic energy loss $(dE/dX)_e$ in eV/Å	Rate of Nuclear energy loss $(dE/dX)_n$ in eV/Å	Range
^{127}I	100 MeV	2.09 E+03	1.80 E+01	8.32μm
	10 KeV	1.32 E+01	2.04 E+02	57 Å

4a.4.2 Results of R vs. dose measurements

Fig. 4a.23 (a), (b) show the insitu resistance variation of the bulk YBCO samples irradiated by 100 MeV ^{127}I projectiles, at room temperature and low temperature respectively. Although the magnitude of change of normalised resistance brought about by this energetic projectile is small, the nature of the changes are altogether different in the two cases. In the case of irradiation at room temperature the resistance is seen to increase from its initial value of before irradiation and maintains an almost constant value throughout the range of the fluence used in the experiment, i.e., upto ~ 2 x $10^{14}/cm^2$. But for low temperature irradiation, the variation in R with dose shows just the opposite nature than that for the case of room temperature irradiation. At small dose

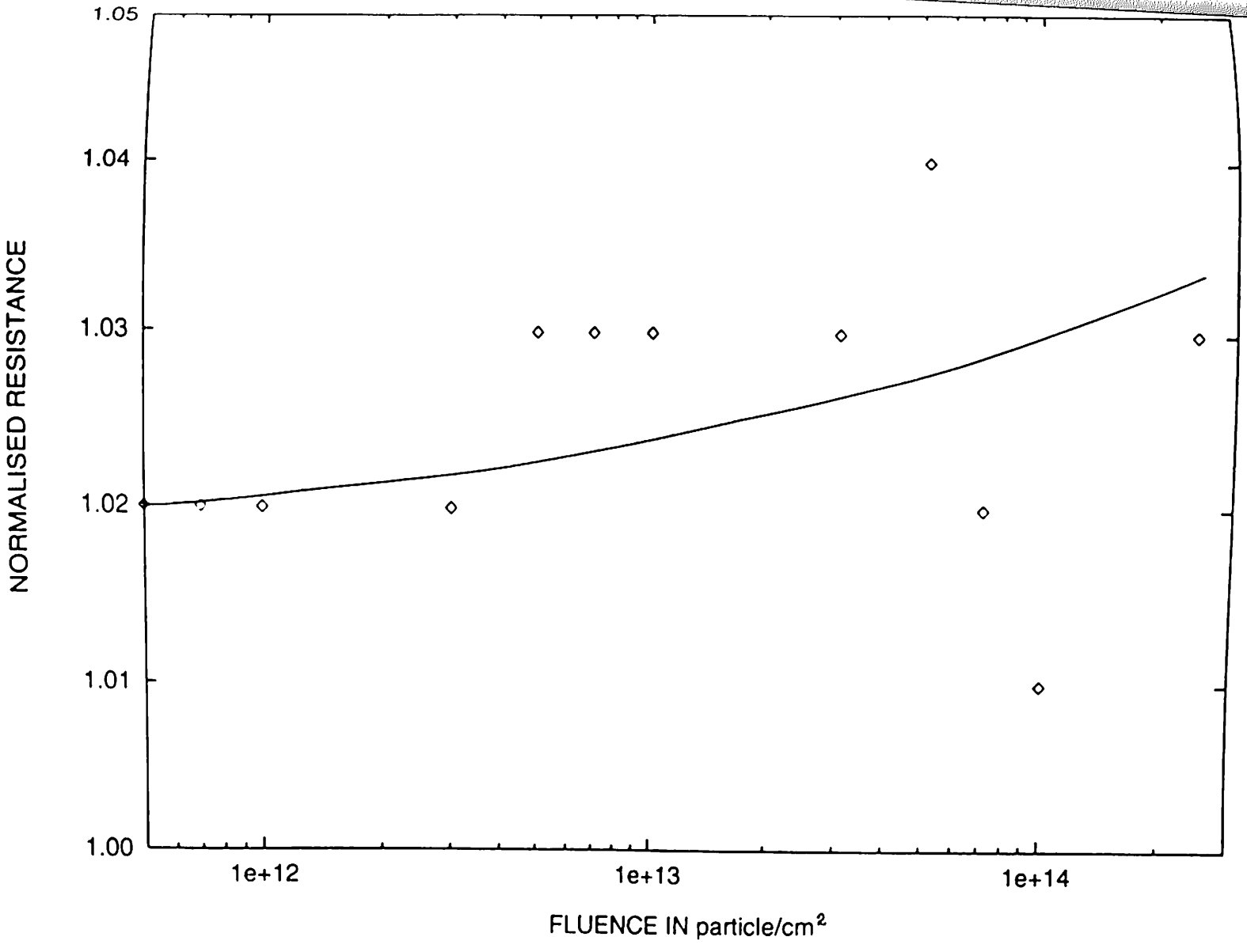

Fig. 4a.23. (a) Insitu variation of normalised resistance (R_n) as a function of dose for 100 MeV ^{127}I irradiation at ambient temperature.

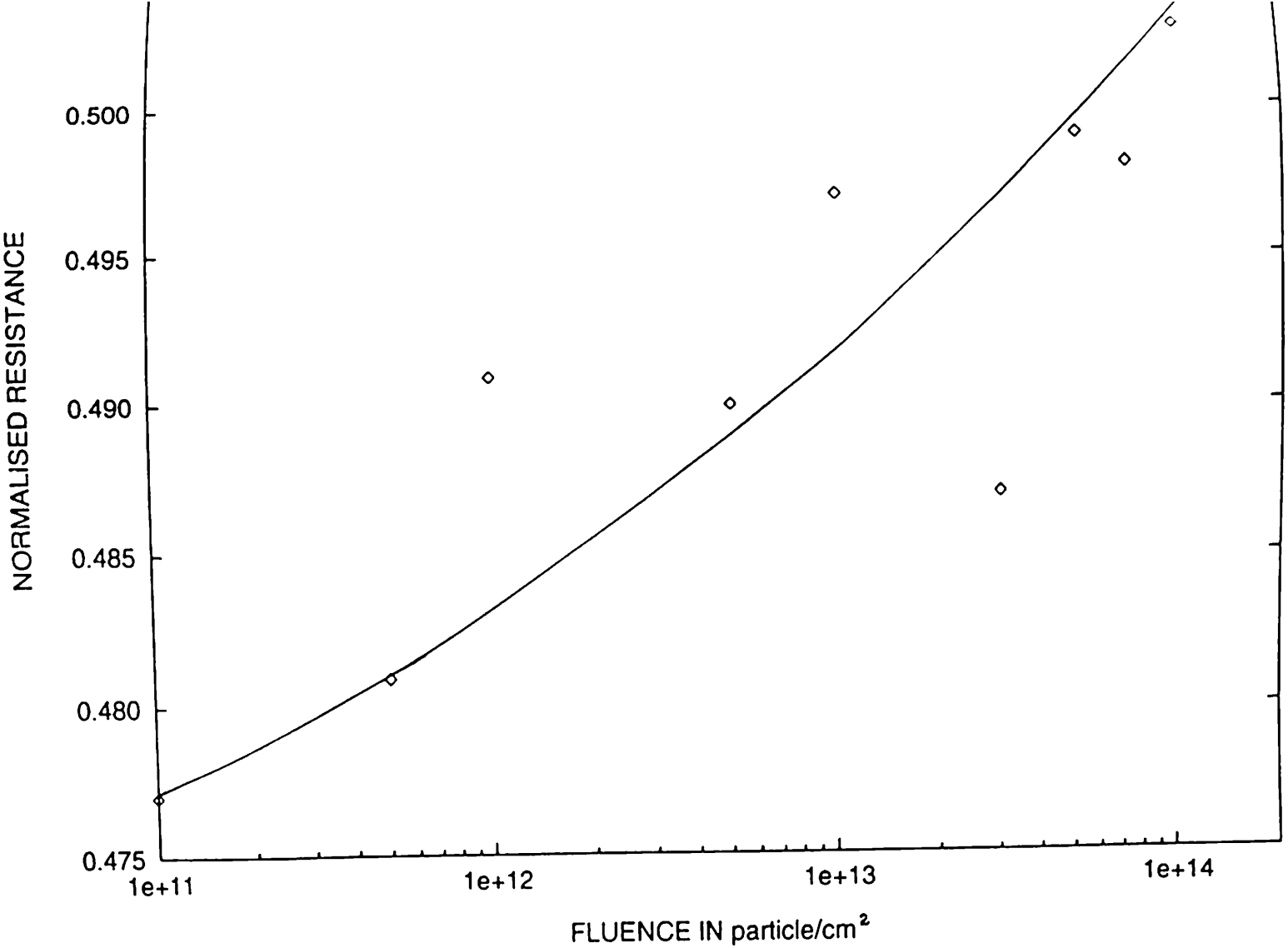

Fig. 4a.23. (b) Insitu variation of normalised resistance (R_n) as a function of dose for 100 MeV ^{127}I irradiation at low temperature.

(~10^{11}/cm^2), the resistance goes down to half of its initial unirradiated value and settles to an almost constant value upto highest dose (~ 10^{14}/cm^2) used in the experiment. It is to be noted here that, anticipating damage of the sample with high current of a heavy particle like ^{127}I, the beam current could not be increased indefinitely, and therefore, the effect at higher doses (beyond 10^{14}/cm^2) remains unexplored. As a quantitative information it is noted here, that at the dose 1 X 10^{12}/cm^2, the normalised change in resistance ($\Delta R/R_{unirr}$) in case of room temperature irradiation becomes .024, while in case of low temperature irradiation, the parameter takes up the value -0.51. The negative sign is indicative of the fact that, resistance has decreased from its initial value.

4a.4.3. Results of XRD

Fig. 4a.24 (a) and (b) show the XRD spectra of unirradiated and 100 MeV ^{127}I irradiated sample respectively. It shows a deterioration of crystallinity due to irradiation. The twin peaks due to (103) and (013) has gone and only one peak of lesser intensity has occured at that place. Calculation shows that the 'c' lattice parameter has also been increased from a value of 11.6502Å to 11.76Å due to irradiation.

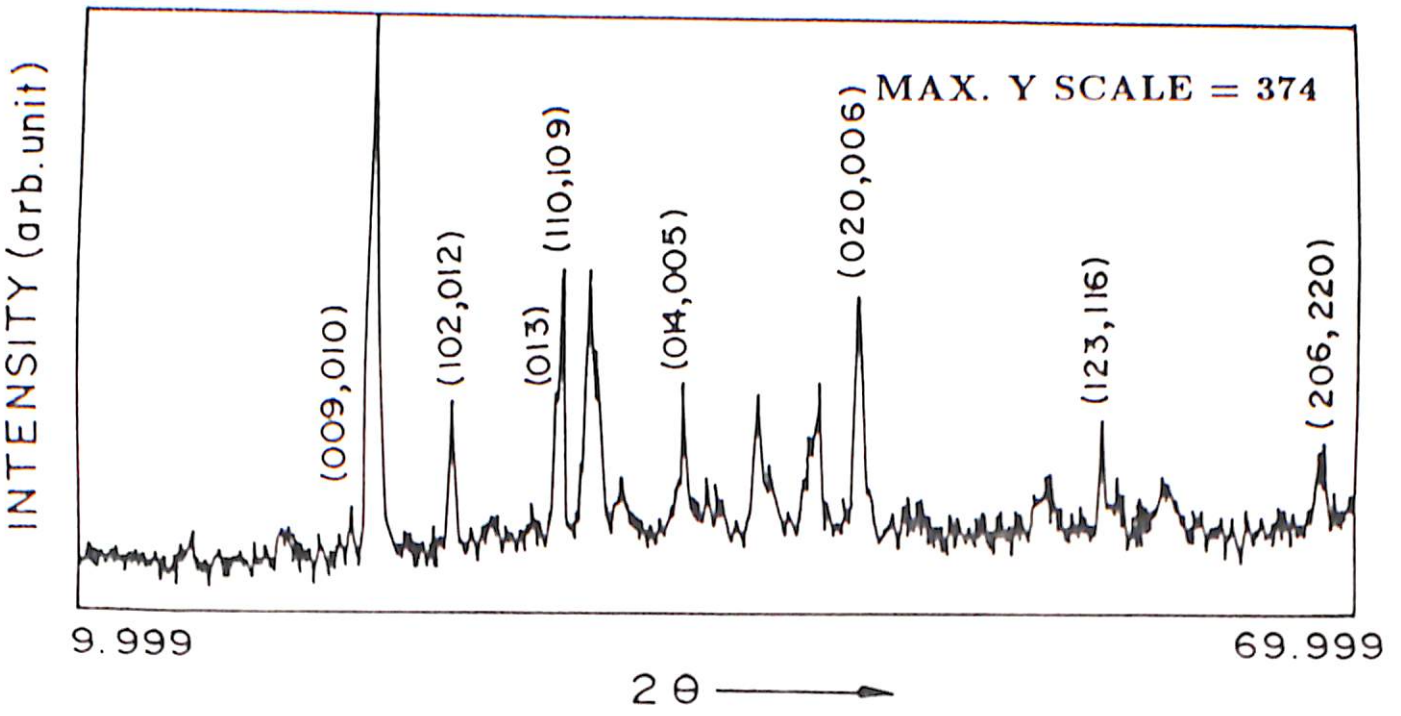

Fig. 4a.24. (a) XRD spectrum of the unirradiated YBCO used in iodine irradiation experiment.

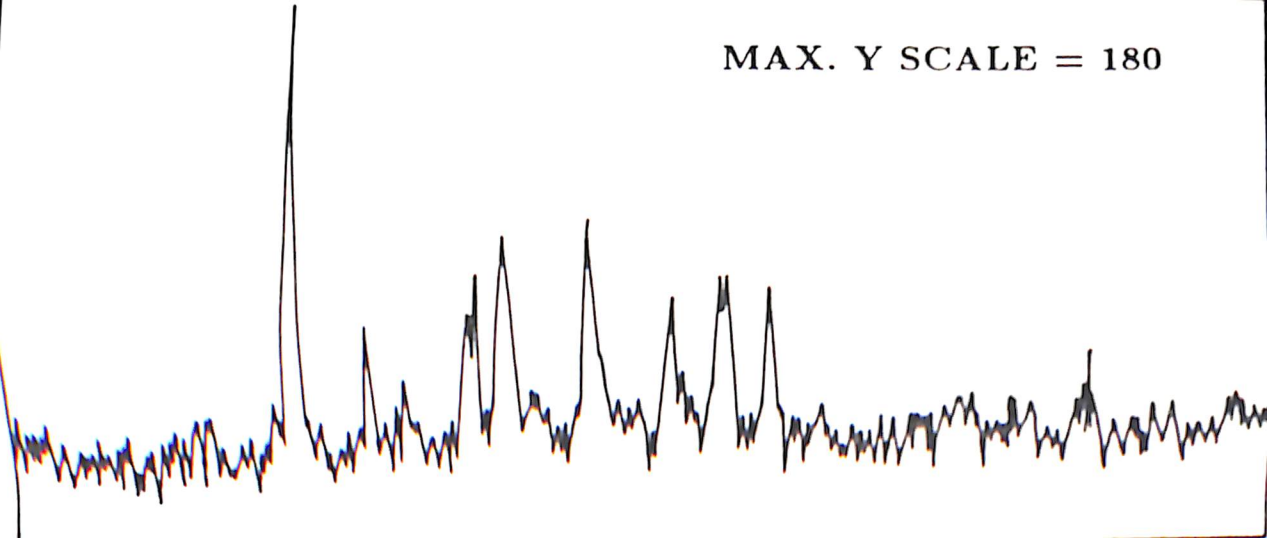
MAX. Y SCALE = 180

4a.4.4. Results of SEM

Fig. 4a.4 (a), (b) show the SEM photographs of the unirradiated sample which show that the grain sizes are sufficiently big and the material is well packed. Fig. 4a.25 (a), (b) show SEM pictures of the irradiated sample with dose 1 x 10^{14}/cm^2 (low temperature irradiated sample) and 4a.25 (c), (d) show that of the sample irradiated with 2.4 x 10^{14}/cm^2 dose (room temperature irradiated sample). The pictures show the formation of craters as big as of 20μm diameter, due to I irradiation. Fig. 4a.25 (c) shows some sort of melting of the grains. This might be the result of heat generation, since that particular sample was irrdaited at ambient temperature.

4a.4.5. Results of R vs. T measurement

The irradiated sample surface becomes highly resistive when taken out of the irradiation chamber. Fig. 4a.26 shows this fact and it also shows that the nature of R vs. T resembled with that of an insulating substance.

4a.5. Results of low Energy Irradiation

Few bulk samples were irrdadiated with 150 Kev ^{14}N beam in the implanter machine of CEERI, Pilani and were characterized

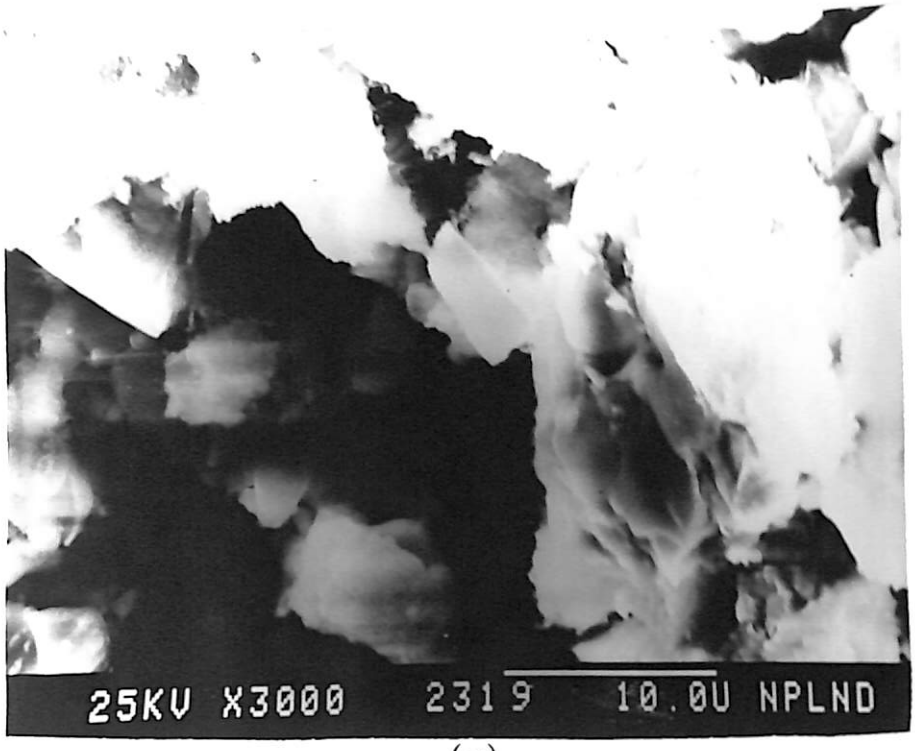

(a)

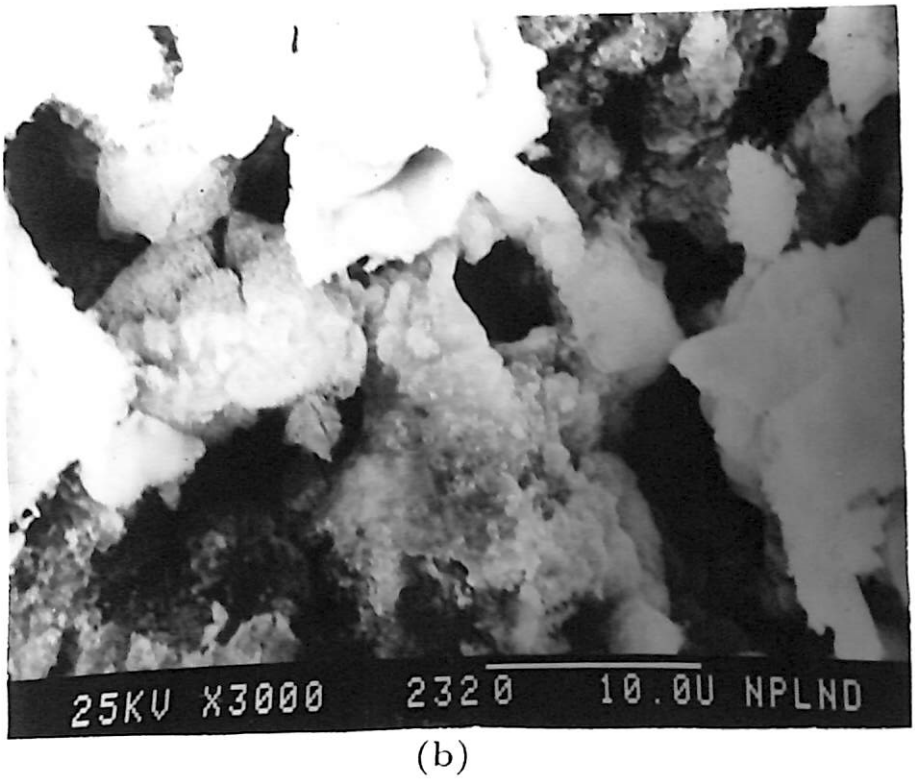

(b)

Fig. 4a.25. (a), (b) SEM pictures of iodine irradiated bulk $YBa_2Cu_3O_{7-\delta}$ sample with dose $1 \times 10^{14}/cm^2$

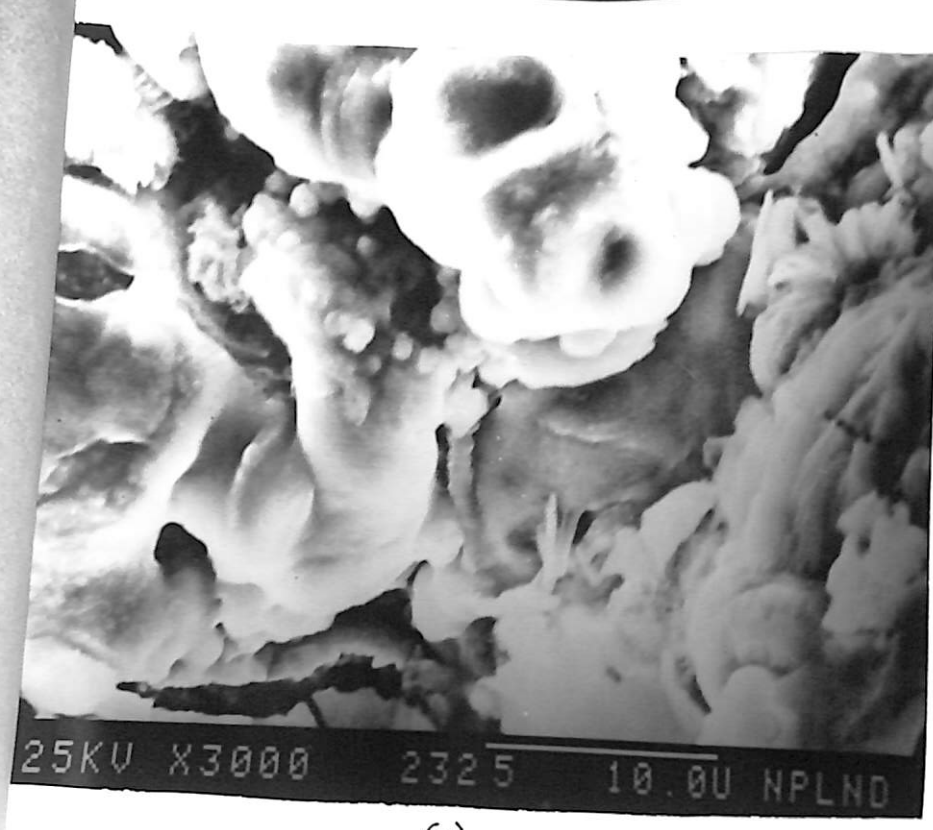

(c)

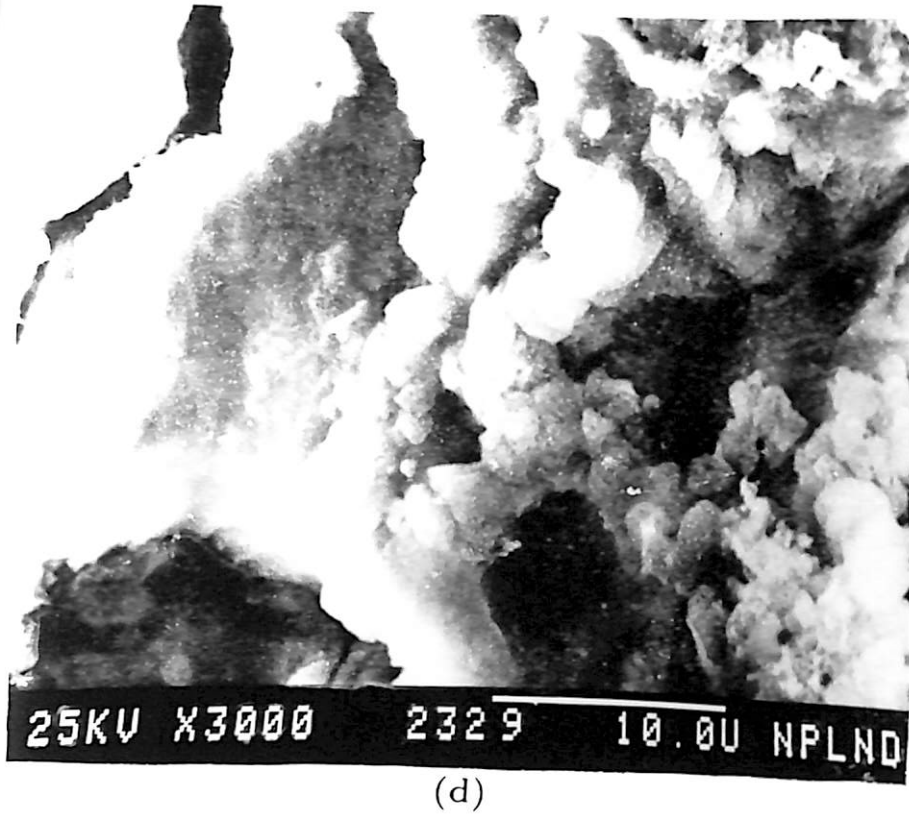

(d)

Fig. 4a.25. (c), (d) SEM pictures of iodine irradiated bulk $YBa_2Cu_3O_{7-\delta}$ sample with dose $2.4 \times 10^{14}/cm^2$

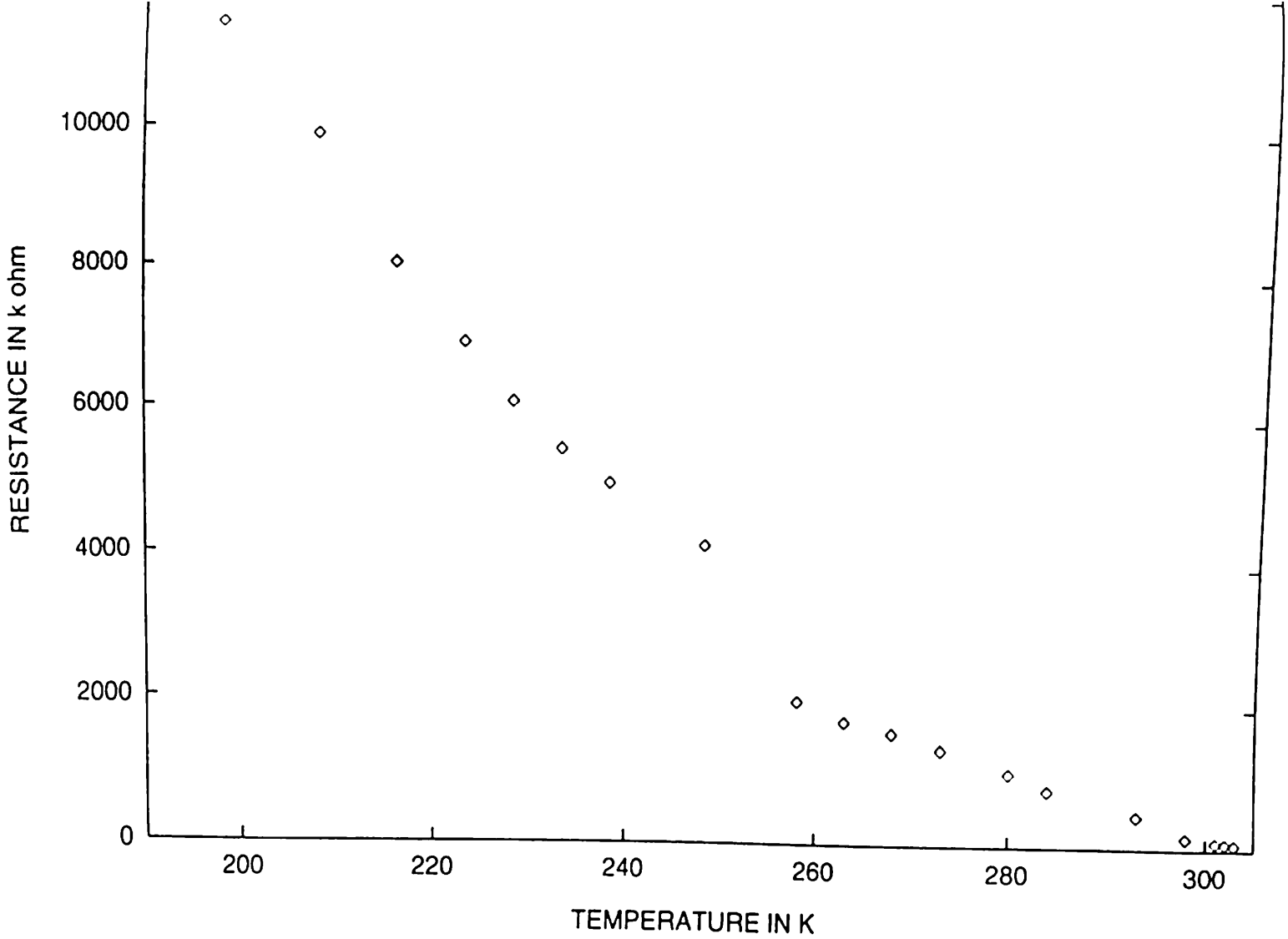

Fig. 4a.26. R vs T of the iodine irradiated sample (dose $\sim 10^{14}/cm^2$).

after irradiation by R vs. T measurement and SEM. The results of these characterizations are described in this section.

4a.5.1. Results of R vs. T measurement

The samples were irradiated with six different doses, 1 x 10^{11}, 1 x 10^{12}, 1 X 10^{13}, 1 x 10^{14}, 1 X 10^{15} and 1 X $10^{16}/cm^2$. Fig. 4a.27 shows the R vs. T of the unirradiated sample and Fig. 4a.28 shows that of the irradiated sample at doses 1 x 10^{11}, 1 X 10^{13} and 1 X $10^{16}/cm^2$. The figures show that Tc_{onset} and Tc(0) remains almost unchanged after irradiation with different doses. Fig. 4a.29 shows a comparision in the R vs. T nature between the unirradiated and irradiated sample at dose 1 X $10^{15}/cm^2$. The fig. shows that although the onset is same, there is a slight tail at downset for the irradiated sample.

4a.5.2. Results of SEM

Fig. 4a.30 show the SEM picture of the surface of unirradiated sample and Fig. 4a.31 (a), (b) show that from the surface of irradiated sample at dose 1 x $10^{12}/cm^2$ and 1 X $10^{16}/cm^2$ respectively. Fig. 4a.30 shows that the surface of the unirradiated sample consists of a mixture of small and big grains. But the SEM pictures of the irradiated sample clearly show that the grain size has been increased considerably. Also, there are

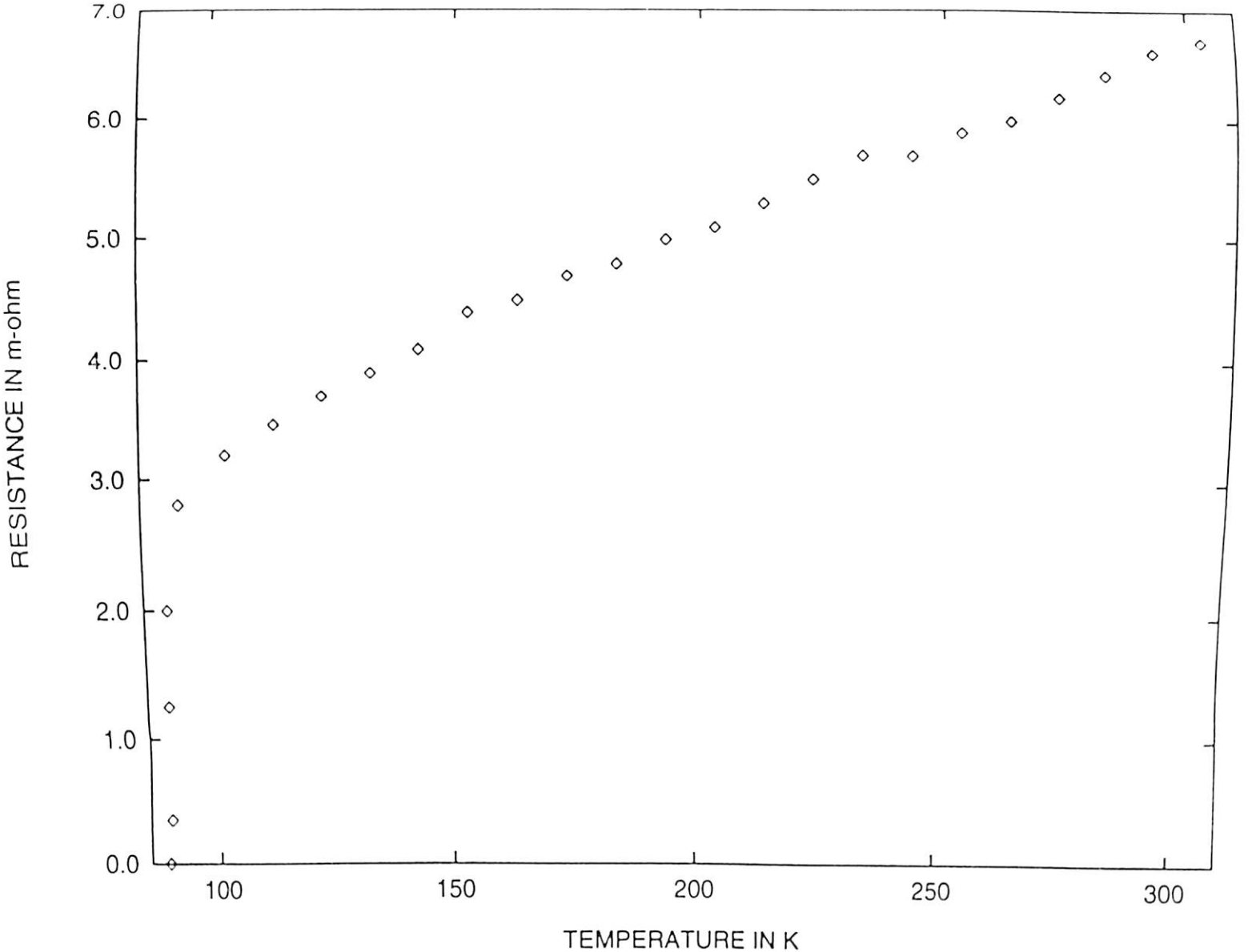

Fig. 4a.27. R vs T of the unirradiated sample used in low energy N irradiation experiment.

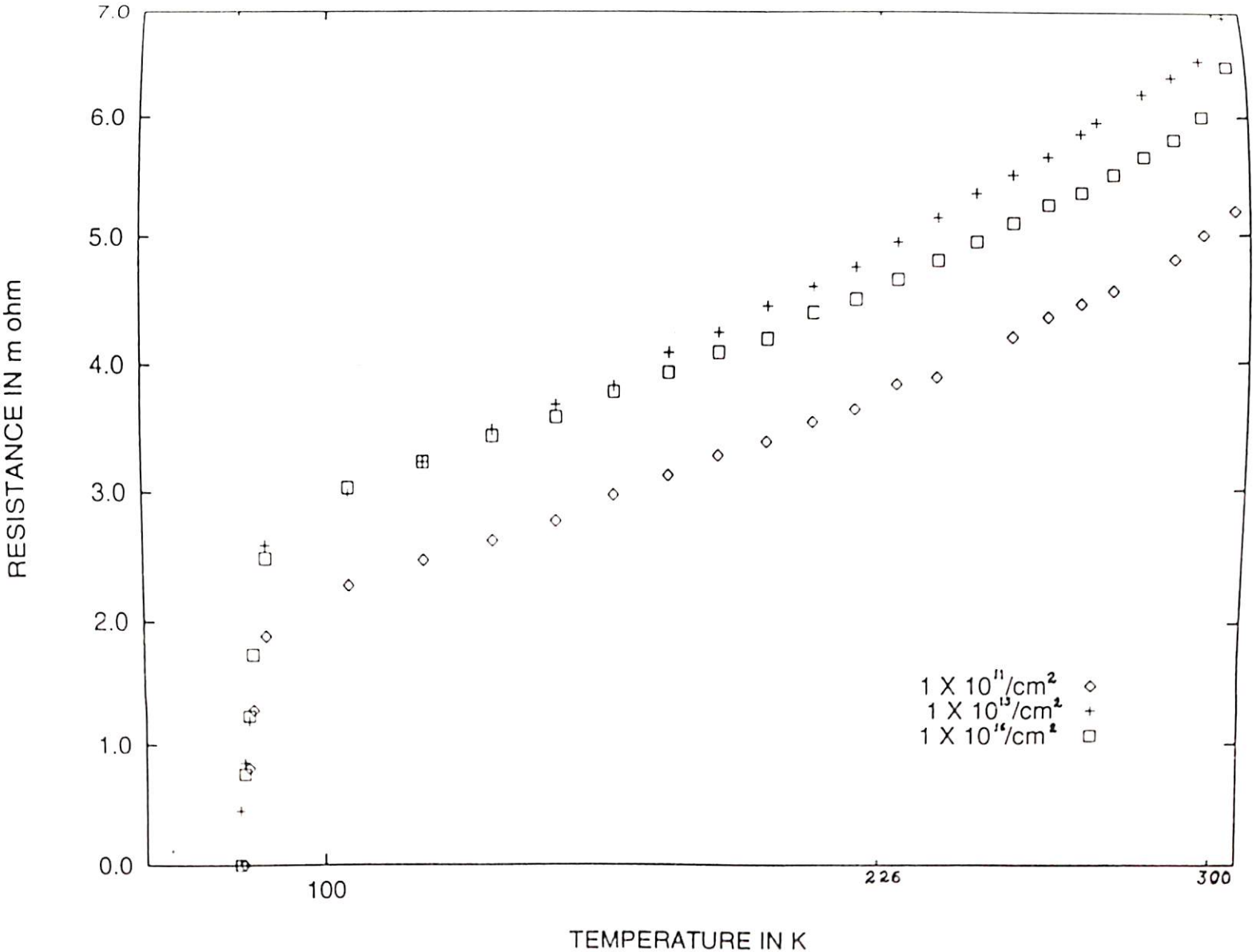

Fig. 4a.28. R vs T of the 150 keV N irradiated bulk YBCO at dose $1 \times 10^{11}/cm^2$, $1 \times 10^{13}/cm^2$ and $1 \times 10^{16}/cm^2$.

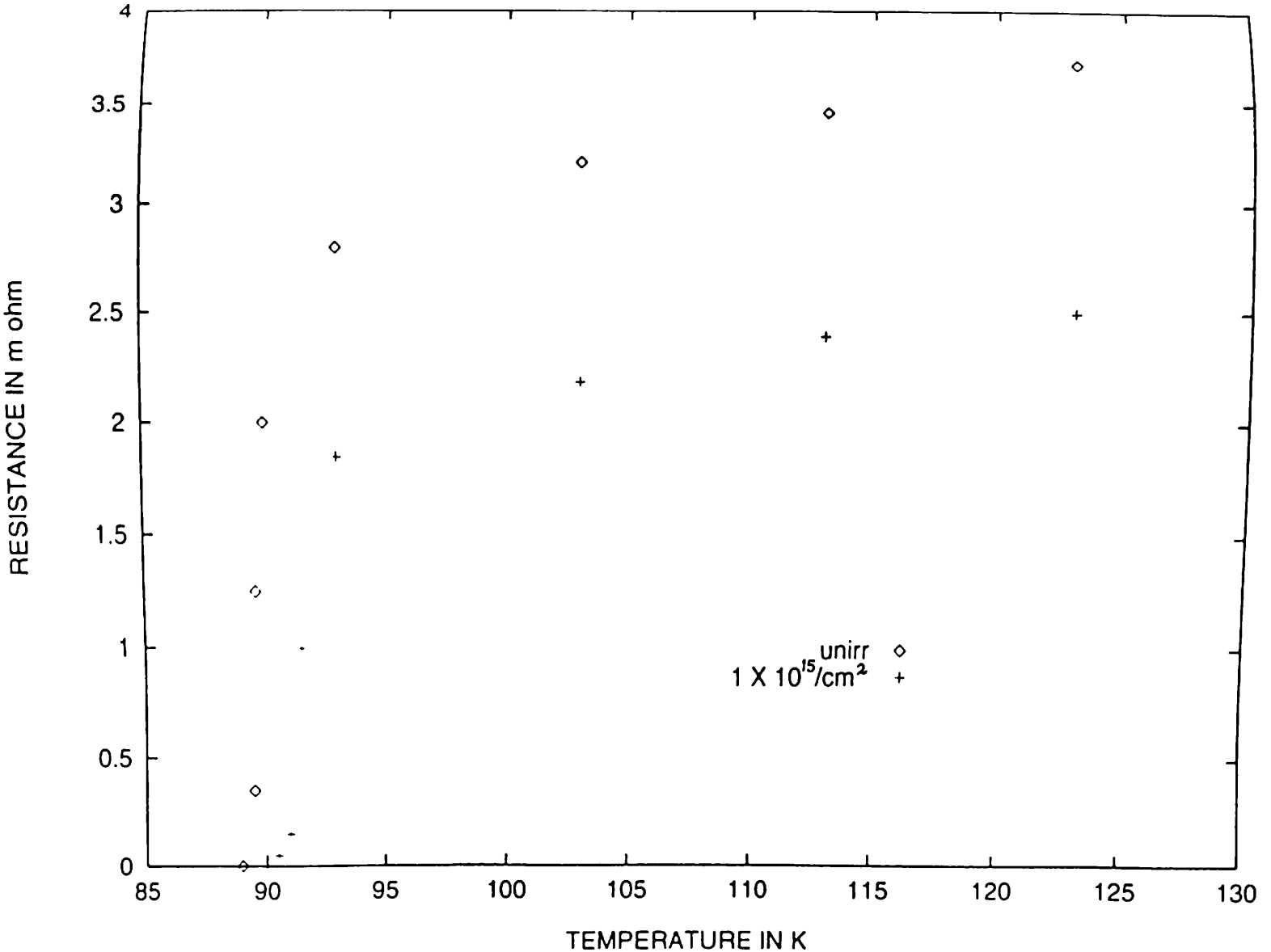

Fig. 4a.29. Comparision of R vs T characteristic of the unirradiated and 150 keV N irradiated (dose = $1 \times 10^{15}/cm^2$) bulk YBCO sample.

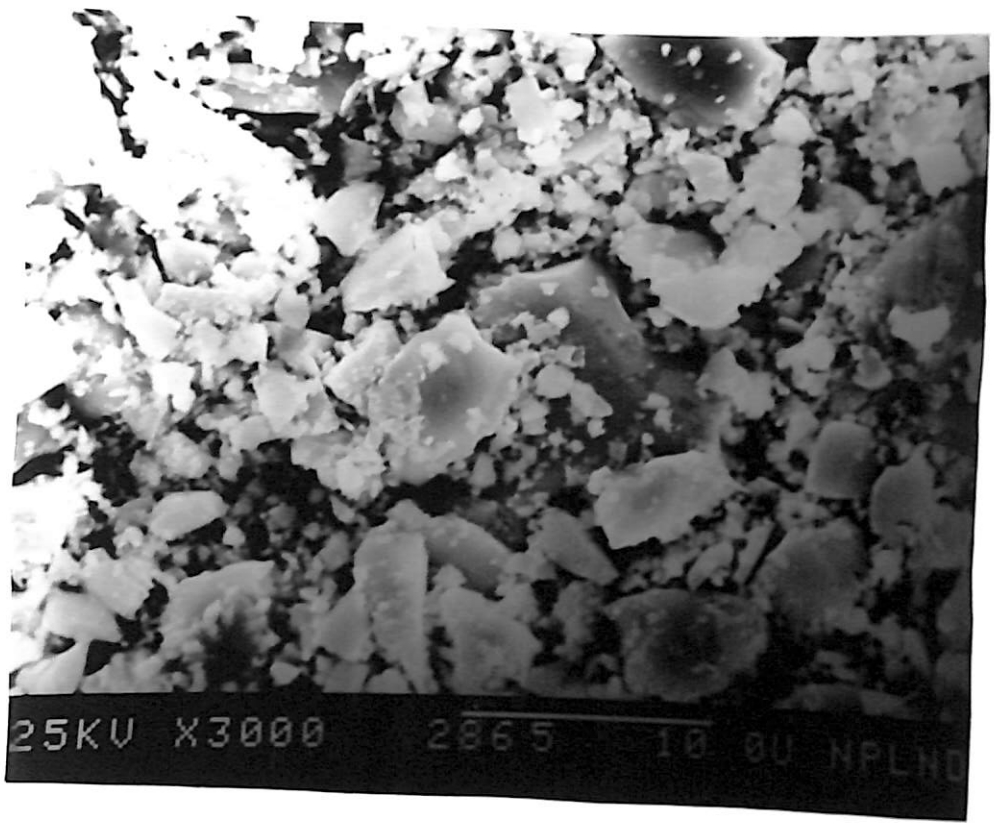

Fig. 4a.30. SEM picture of the unirradiated bulk $YBa_2Cu_3O_{7-\delta}$ sample used for low energy nitrogen irradiation experiment

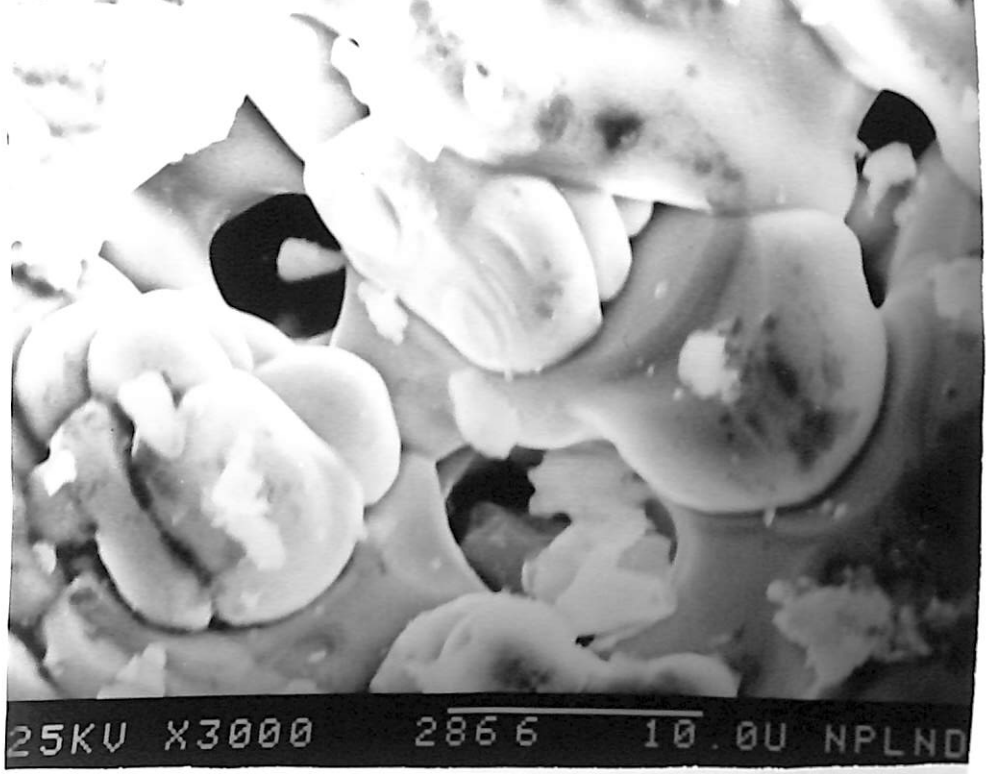

(a)

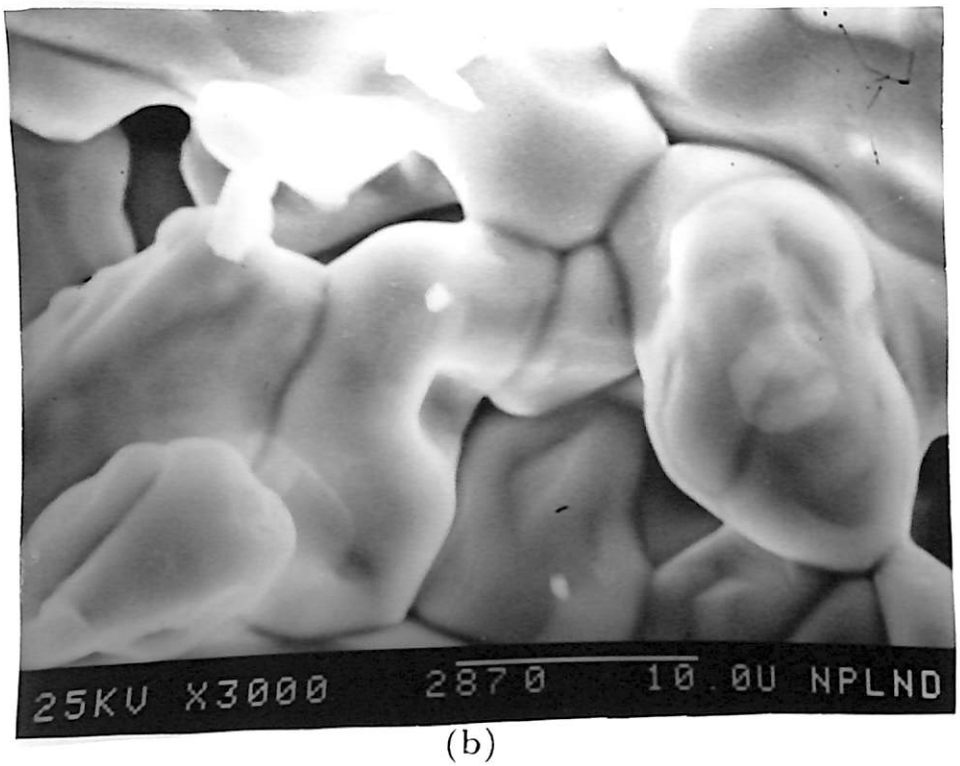

(b)

Fig. 4a.31. SEM pictures of low energy N irradiated bulk $YBa_2Cu_3O_{7-\delta}$ sample with dose (a) $1 \times 10^{12}/cm^2$ and (b) $1 \times 10^{16}/cm^2$

voids created at high dose of irradiation.

4a.6 Thin Film Irradiation Results

Few sputtered deposited thin films of YBCO on YSZ, MgO and $SrTiO_3$ and few laser ablated thin films of YBCO on $LaAlO_3$ substrates are used in the irradiation experiments. The thickness of the films were in the range 500-1000Å. The Tc of the films on YSZ and $LaAlO_3$ were ~ 85°K and those on $SrTiO_3$ and MgO substrates are having a Tc ~ 80 K. The films on YSZ, MgO and $LaAlO_3$ were irradiated by 100 MeV ^{127}I and the films on $SrTiO_3$ were used in the irradiation experiments with 75 MeV ^{16}O. One film on $SrTiO_3$ was tried in ion beam lithography experiment with 150 MeV Ag beam, which did not yield fruitful result due to breaking of the sample. In iodine irradiation experiment, in all the thin film samples the dose of irradiation was limited to lower values, since high dose might cause burning of the film. In iodine irradiation experiment attempt to measure insitu R vs. dose nature of YBCO film on YSZ was failed due to electrical contact problem. In oxygen irradiation experiment insitu sheet resistance variation by Van der Pauw method with dose was calculated. The samples on $LaAlO_3$ got peeled off after irradiation with 100 MeV I at a dose ~ $10^{11}/cm^2$ and the sample on MgO became insulating after exposure to a moderate dose (~ 5 X $10^{11}/cm^2$) of 100 MeV I irradiation.

4a.6.1. Results of sheet resistance vs. dose measurement

The sheet resistance variation with oxygen fluence was measured by standard Van der Pauw method by making four electrical contact at four corners of squarish shaped YBCO thin film sample on $SrTiO_3$ substrate and using the formula, for sheet resistance with reference to the geometry shown in fig. 4a.32 (a) given by,

$$R_s = 4.532 \frac{R' + R''}{2} F\left(\frac{R'}{R''}\right) \qquad \text{(4a.2)}$$

where F(R'/R") is Van der Pauw function. R' is the potential difference between the contacts C and D per unit current through contacts A and B and R" is the potential difference between the contacts A and D per unit current through the contacts B and C.

Fig. 4a.32 (b) shows that the sheet resistance remains almost constant upto a dose of 4 x $10^{13}/cm^2$.

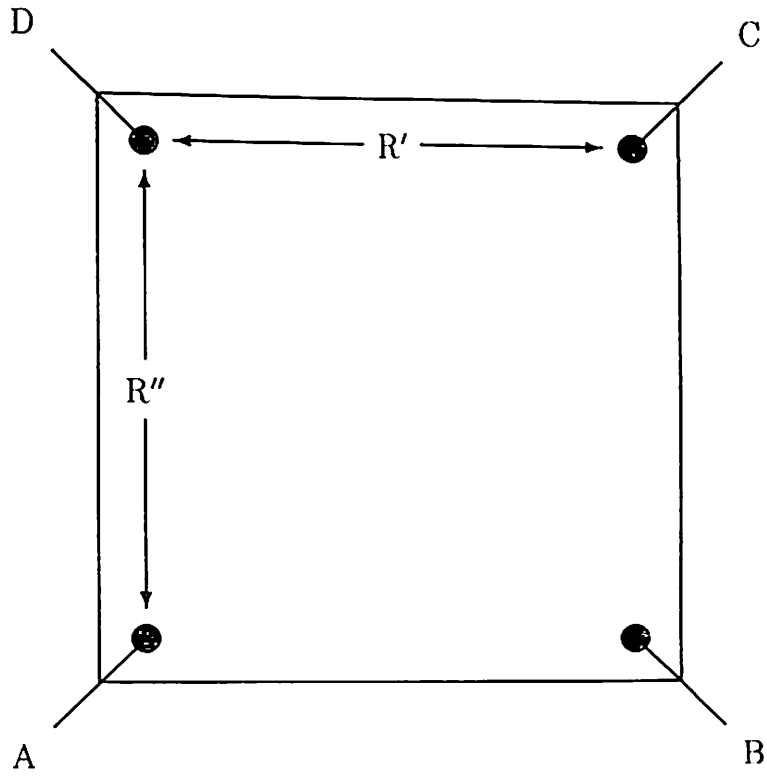

Fig.4a.32(a) Connection geometry in Van der Pauw method

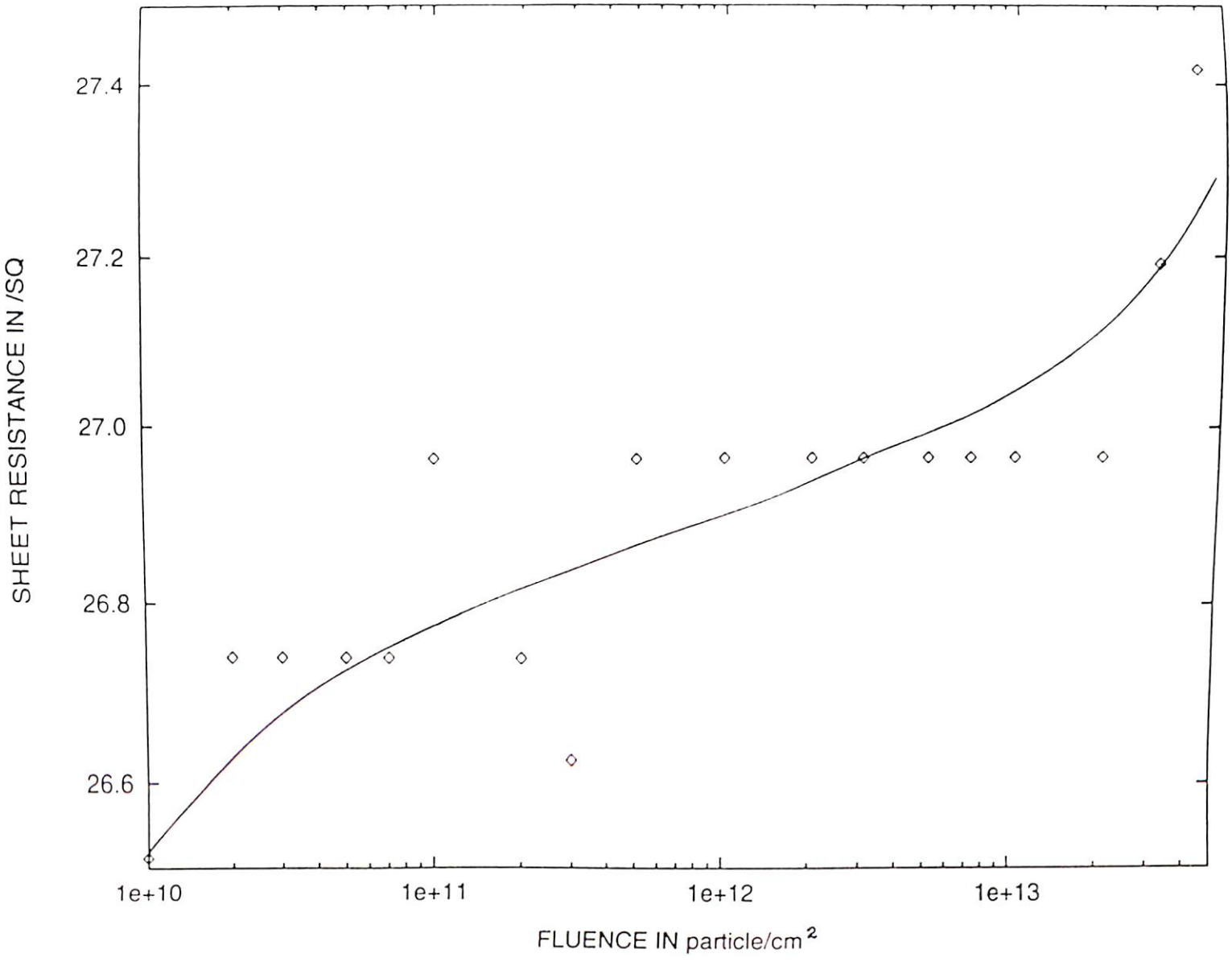

Fig. 4a.32. (b) Insitu variation of sheet resistance with dose for oxygen irradiation on YBCO thin film.

4a.6.2. Results of XRD

Fig. 4a.33 (a), (b) shows the XRD of the unirradiated and irradiated YBCO thin film on YSZ (dose ~ 1 X $10^{11}/cm^2$) by 100 MeV I, respectively. The XRD was taken at unirradiated and irradiated portion of the same sample. The spectra show that although few peaks are lost due to irradiation, some peaks are gained in intensity by a small amount.

4a.6.3. Results of R vs. T measurement

Fig. 4a.34 (a), (b) show the R vs. T curve for the unirradiated and irradiated thin films of YBCO on YSZ substrate. Irradiation was done by 100 MeV I at a dose 1 X $10^{11}/cm^2$. The fig. shows that the thin film sample remains superconducting after irradiation, but its Tc has gone down from 85 K to 82 K.

4a.7. Discussion of the Results

In this section the effect of irradiation of bulk and thin film samples of YBCO with three different energetic ions will be discussed with possible explanation from the results obtained in the different experiments as described in the earlier sections of this chapter.

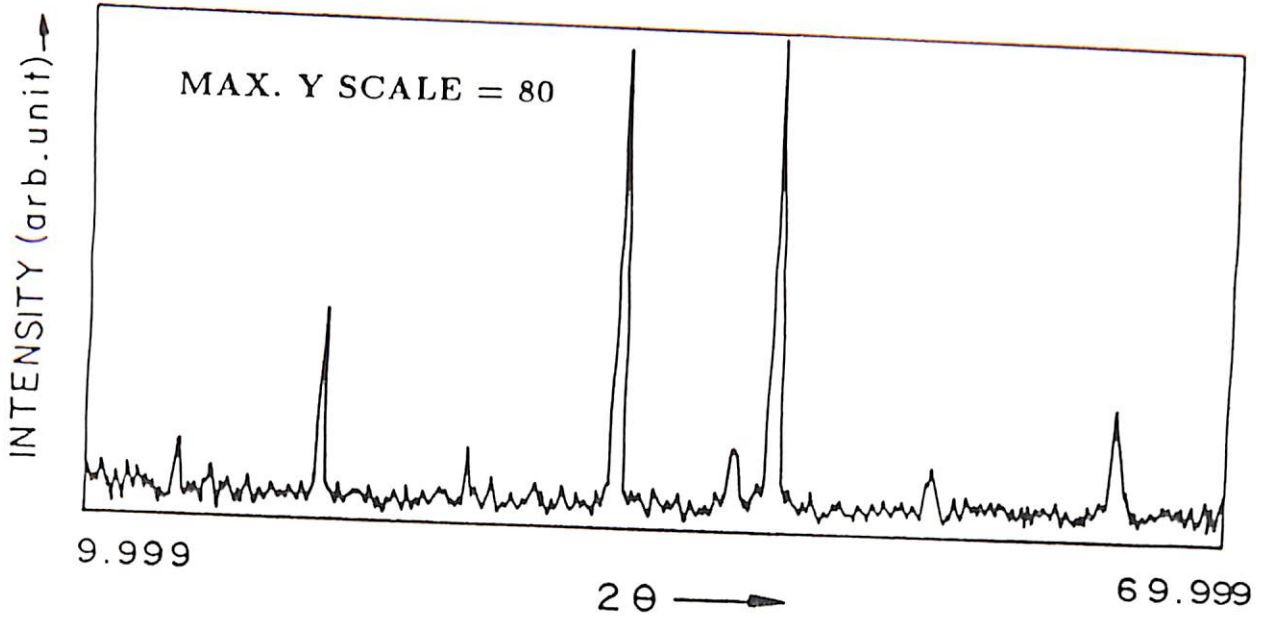

Fig. 4a.33. (a) XRD spectrum of unirradiated YBCO thin film used in iodine irradiation experiment.

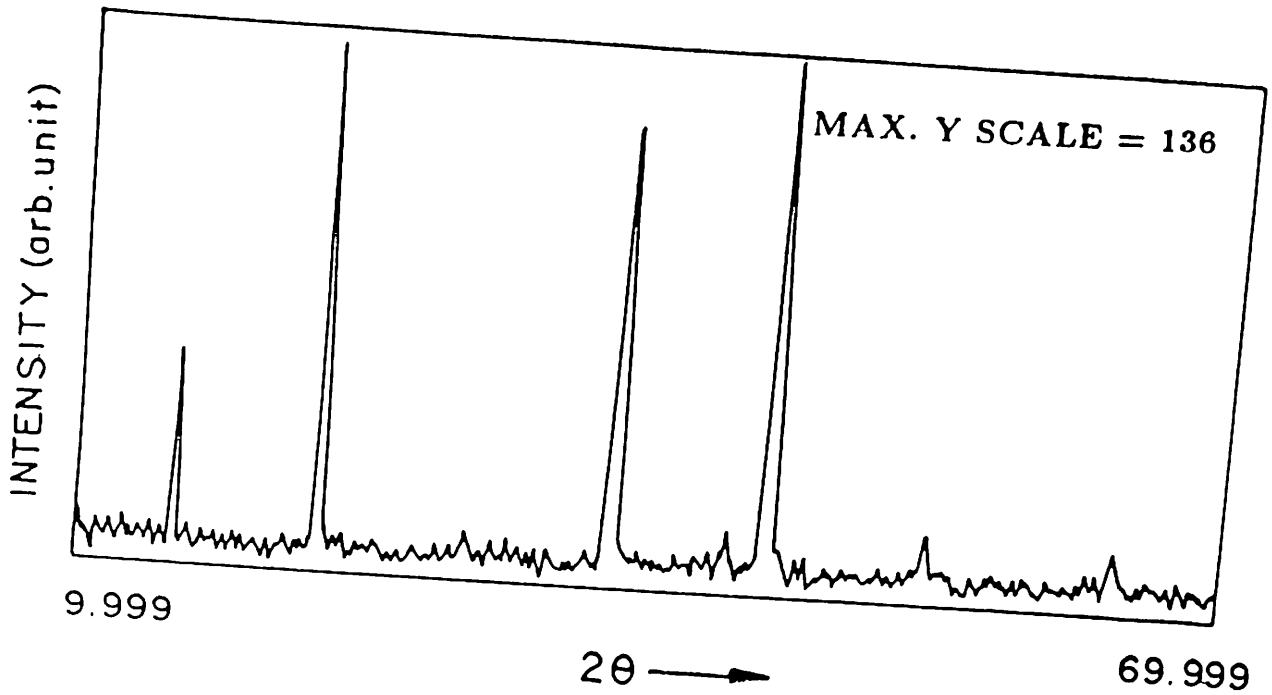

Fig. 4a.33. (b) XRD spectrum of 100 MeV iodine irradiated YBCO thin film.

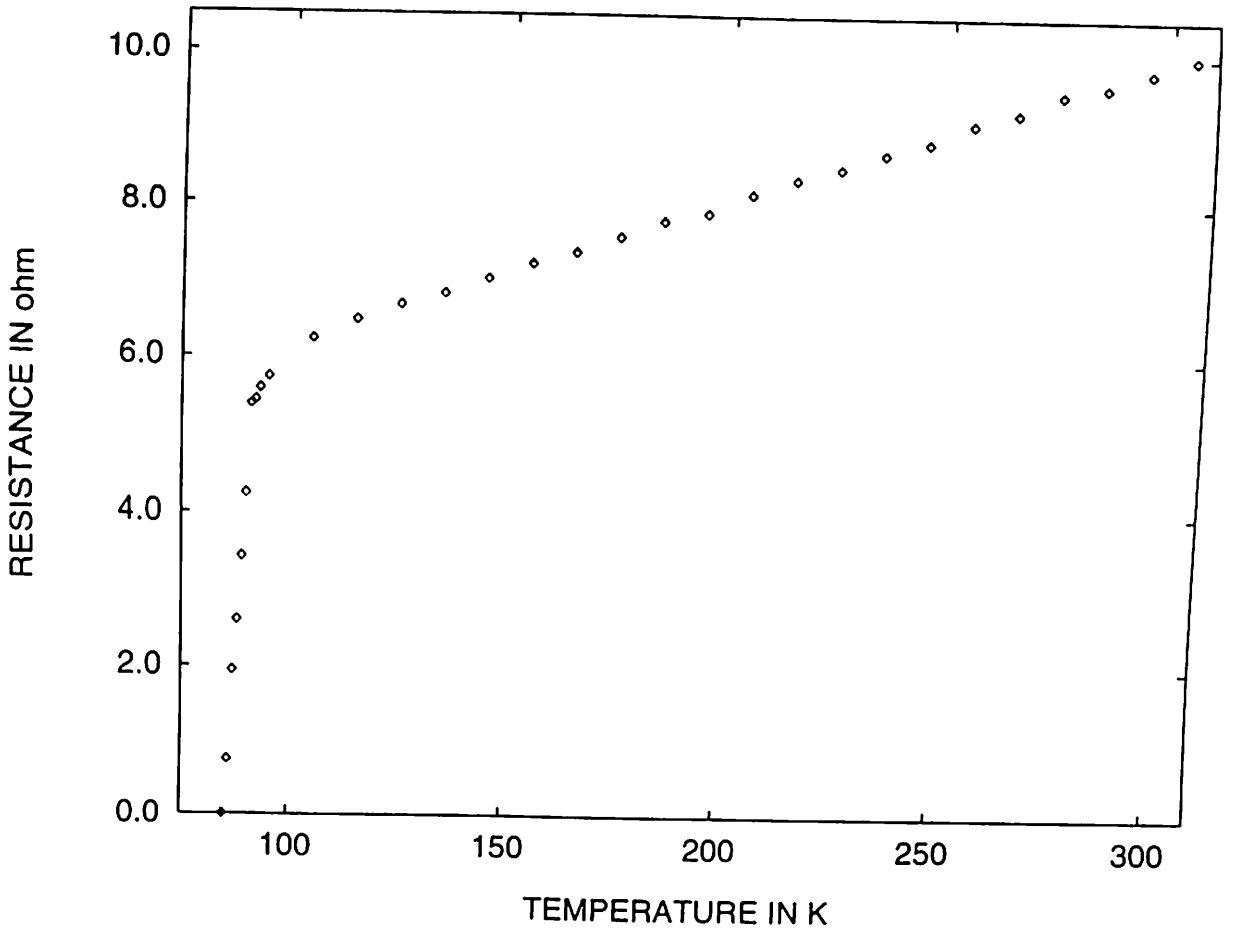

Fig. 4a.34. (a) R vs. T characteristic of the unirradiated YBCO thin film used in iodine irradiation experiment.

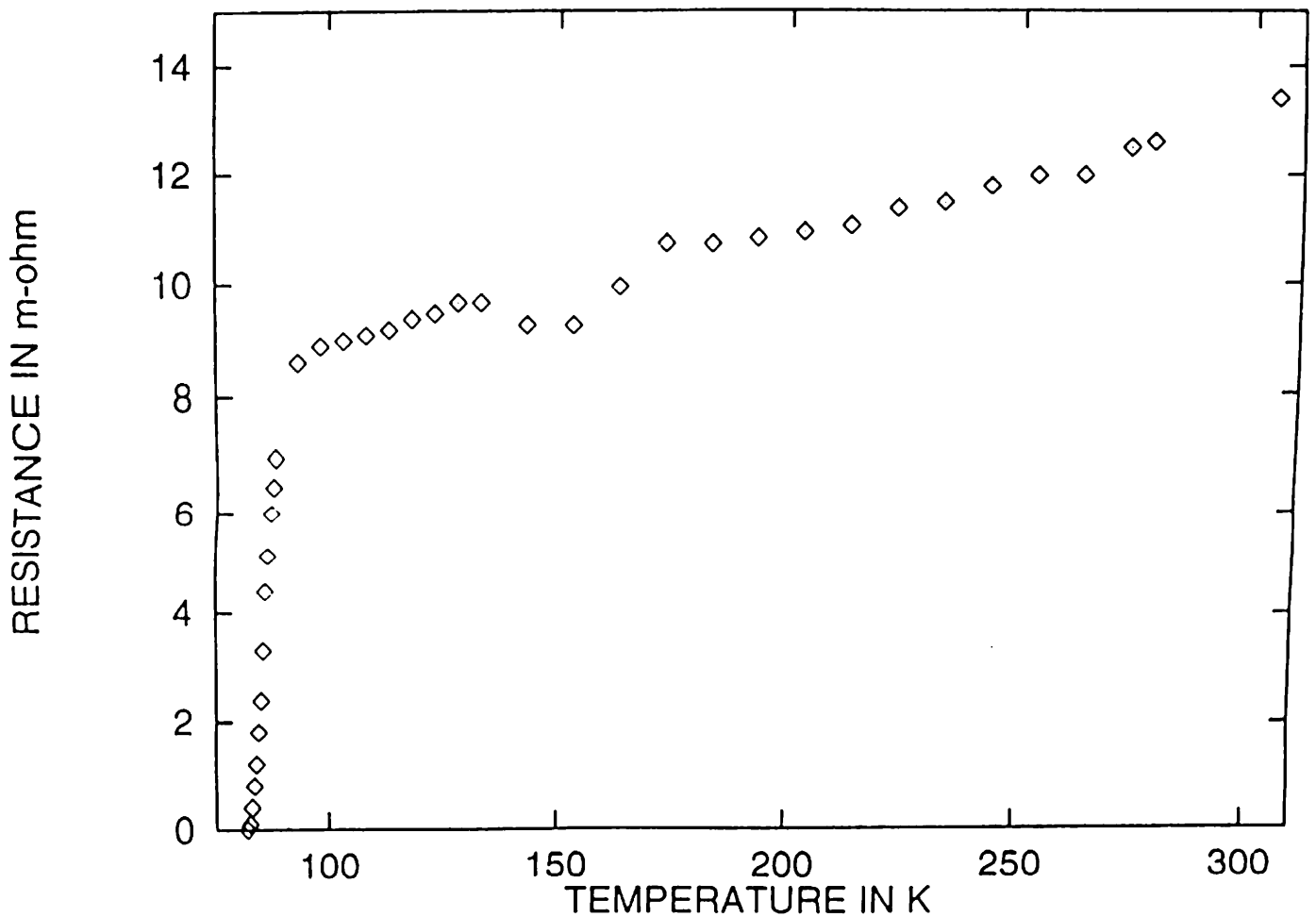

Fig. 4a.34. (b) R vs T characteristic of the iodine irradiated YBCO thin film at dose $1 \times 10^{11}/cm^2$.

The discussion starts with the results of R vs. dose measuremnets. This measurement is performed at two different sample temperatures during irradiation, to find out the effect of sample temperature on the effect of irradiation and to explore some physics of defect creation inside the sample. In all the cases of irradiation with the three different ions, except in case of room temperature irradiation by 100 MeV ^{127}I, the observed resistance is seen to decrease upto certain dose. In order to explain the decrease in resistance from its initial value as a result of irradiation, one must remember the fact that although the projectiles interact with all the atoms in the target, nemely, Y, Ba, Cu and O, during the ions passage, the probability of O atoms in the material getting displaced is highest because this is the lightest atom among the others and also, they are loosely bound in the lattice compared to the other atoms. Since, it is believed that an ordered arrangement of oxygen vacancy is crucial even for normal state metallic conductivity[1], then from the previous argument, the decrease in resistance strongly suggests an improvement of the ordered arrangement of oxygen vacancy upto certain dose of irradiation. This dose is also different for different projectiles. This is because increasing dose means multiplying the number of defects created by a single ion. Since, each projectile has its own energy loss value which is different, the defect density

created by single ion of each species is different from that by the others and therefore, the dose upto which oxygen vacancy ordering prevails over the effects of other defects is different for the three different ions used. In case of iodine irradiation at room temperature, the resistance is seen to increase even at smaller dose. But at this point one should keep in mind that ^{127}I has greatest energy loss value among the three ions and in present study the effect of the doses lower than 1 X $10^{11}/cm^2$ could not be traced because of the unavailability of very low beam current from the accelerator. Therefore, from R vs. dose curve in case of I irradiation at room temperature it can not be inferred that vacancy ordering did not take place at any dose in this case. But the fact which is evident from the R vs. dose curve is that, at dose as low as 1 X $10^{11}/cm^2$, the defect density generated by I ion is sufficient to increase the resistance of the sample. At this point, it is worthwhile to mention the values of normalised change in resistance ($\Delta R/R_{unirr}$) after exposure to a typical dose for the three ions, in case of room temperature irradiation. In case of room temperature irradiation by oxygen ($\Delta R/R_{unirr}$) ~ -0.002, for Ni ($\Delta R/R_{unirr}$) ~ -0.03 and for I, ($\Delta R/R_{unirr.}$) ~ 0.024 at a fixed dose of 1 X $10^{12}/cm^2$. From this it can be seen that only for I, the normalised change in resistance value is positive, i.e., in this case the vacancy ordering seems to be totally counter balanced by the other types of defects produced as a result of irradiation. This fact

can be attributed to be due to high energy loss value of the ^{127}I beam. It should be mentioned here that, initial increase of resistance at the smaller doses in case of Ni irrdaition at room temperature does not corroborate to the explanation given so far. This might be due to the sudden generation of huge number of defects and their inability to relax in smaller time. But over longer time scale they get annealed out and the resistance decreases at larger doses. Now coming to explain the effect of different target temperature during irradiation, it is better to compare the nature of the two variations in normalised resistance (R_n) w.r.t. fluence at two temperatures. If we compare the normalised change in resistance at particular dose (say, 1 X $10^{12}/cm^2$) for the three ions, then we see that the numerical values in case of low temperature irradiation is always greater in magnitude (-0.51, -0.43 and -0.077 in case of I, Ni and O respectively) than those values for room temperature irradiation (.024, -0.03, -0.002 for I, Ni and O) and in low temperature irradiation they are always negative which is indicative of the fact that the resistance has always decreased from its initial value in case of low temperature irradiation. This shows that in case of low temperature irradiation there is a favorable situation for improving the vacancy ordering of the oxygen sites due to ion irradiation and at the same time freezing this situation, thus retaining the ordered vacancy state; this is not the case at room temperature irradiation, since a part of the ordered vacancy

arrangement due to irradiation again gets disordered due to larger amplitude of lattice vibration. Secondly, the change in resistance due to irradiation at low temperature shows a marginal increase in resistance in case of oxygen and cosiderable increase in resistance in case of Ni irradiation. For iodine irradiation, it remains more or less at a constant value upto the highest dose of irradiation carried out. The increase of R_n at higher fluences is due to the creation of other types of defects (point defects, cascades etc.) which have a detrimental effect on conductivity of the sample. But still, upto higher value of fluences, vacancy ordering prevails over the other types of effects in case of low temperature irradiation, which is evident from the fact that at higher fluences also the resistance of the samples remains at lower values than their initial values at higher fluences. In case of Ni irradiation resistance values shoots up to a large value at a particular dose of 3.5 x $10^{15}/cm^2$ in case of low temperature irradiation. This might be due to the fact that the tracks of the ions overlap at this very high dose creating huge defects and also due to lateral straggling of the ions it does not leave much conducting path for the measuring current to flow.

Looking into the R vs. T results, let us first take the results of oxygen irradiation (dose ~ 1 X $10^{12}/cm^2$). Here as described in section 4a.2.5, two configurations of electrical contact is made

for the measurement, namely, transverse and planar. The difference in the results of the R vs. T measurements in these two configurations can be understood on the change in the current percolation path due to radiation damage of the sample. When measurements are done in the tarnsverse mode then we are including two different regions, namely, i) the radiation affected region, ii) the region (lower portion) which is unaffected by the ion beam. On the other hand the planar geometry does not directly account for both the two regions together, probably due to non-uniform current density path between the voltage probes.Now it can be seen from fig 4.13 (a) and (b) that the onset of transition remains almost the same (~ 85 K) in both the cases and in effect it appears that the net result of ^{16}O ion bombardment on YBCO is to increase the width of the superconducting transition. Therefore, it can be definitely concluded from this experiment that the oxygen irradiation has only affected the weak links between the grains. In case of Ni irradiation also, at smaller doses, Tc change is small. Here, to include the irradiated part, the voltage contacts were made on the irradiated zone and to find out the R vs. T of the unirradiated part, the bottom part of the sample was used and one can see that the Tc is degraded little bit due to irradiation. High dose irradiation has made the sample non superconducting. It might be due to the total deterioration of weak links leaving no percolation path for superconducting current to

flow. For iodine irradiation, R vs. T of the lower dose irradiated sample could not be taken. But the higher dose irradiation,like in the case of Ni, has destroyed superconducting properties of the target. But, here, the nature of R vs. T is different from that of the Ni irradiated sample. For Ni irradiated sample, the resistance keeps on decreasing with decrease in temperature. But the iodine irradiated sample shows big increase in resistance with decrease in temperature which is the behavior of an insulator. Therefore, it seems that I, due to its high energy loss value, has affected the intra grain superconductivity also and at high dose it transforms the material to an insulator.

All the XRD spectra confirm the fact that, crystallinity of the sample has been deteriorated as a result of irradiation. The increment of the width of the peaks, as shown in slow scan spectra, also support this fact. But at smaller doses in case of oxygen and nickel, the orthogonality still remains, as is evident from the occurence of the twin peaks of (013) and (103) planes between the diffraction angles 32° and 34°.But at high dose of irradiation orthogonality disappears.

SEM pictures show that there is not much change in surface morphology for lower dose irradiation. But the morphology has changed significantly in case of iodine irradiation where big craters have been formed.

Now to address to the question : "to which energy loss mechanism do we attribute the change in resistance or other properties, as was described in the earlier sections, by the ion irradiation ?", one can refer to the tables 4a.3, 4a.4 and 4a.5. It is seen clearly from these tables that, at this energy range (~75-100 MeV), the electronic energy loss value $(dE/dX)_e$ is significantly higher than the nuclear loss $(dE/dX)_n$ value and $(dE/dX)_e$ remains higher than $(dE/dX)_n$ upto few micron depth of the sample from the surface. Only at the end of the range, where the projectile becomes very much less energetic, $(dE/dX)_n$ becomes dominant. Now XRD, SEM signals come from only few micron thickness of the top surface of the sample. Therefore, whatever the change we are observing in these characterizations, are at the region where $(dE/dX)_e$ is the predominat energy loss factor.

In the context of resistance change of the normal state, a simple model is proposed to judge the role of two different energy loss mechanism. The proposition under the model is : the effects on the material due to electronic and nuclear losses is envisaged to be seperable and that the whole system can be broken up in various sections with the irradiation, affecting the sample differently and having definite geometrical extent. In this context the various thicknesses are defined as under and shown in Fig. 4a.35 (a).

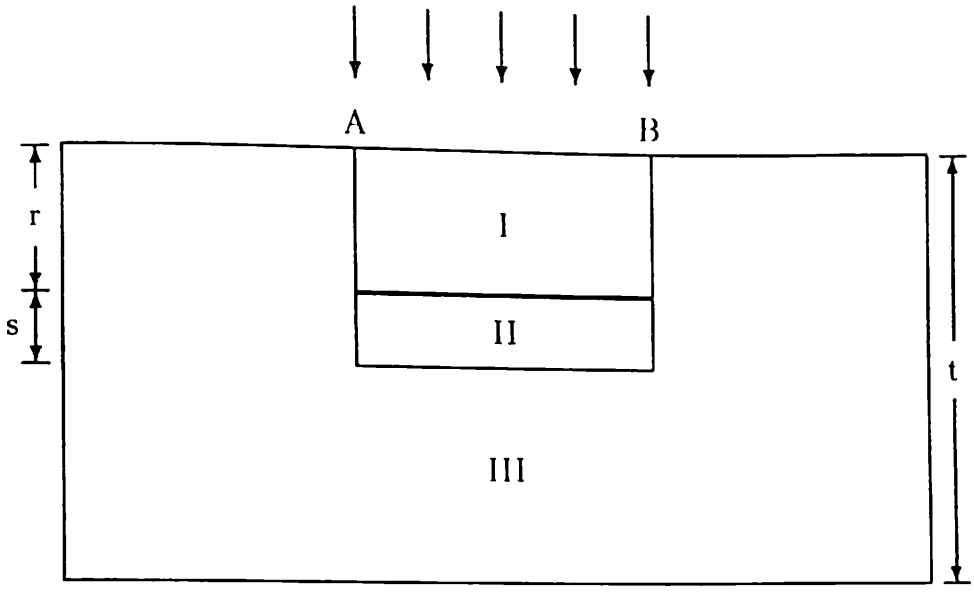

Fig.4a.35(a) Different zones of radiation affected bulk sample

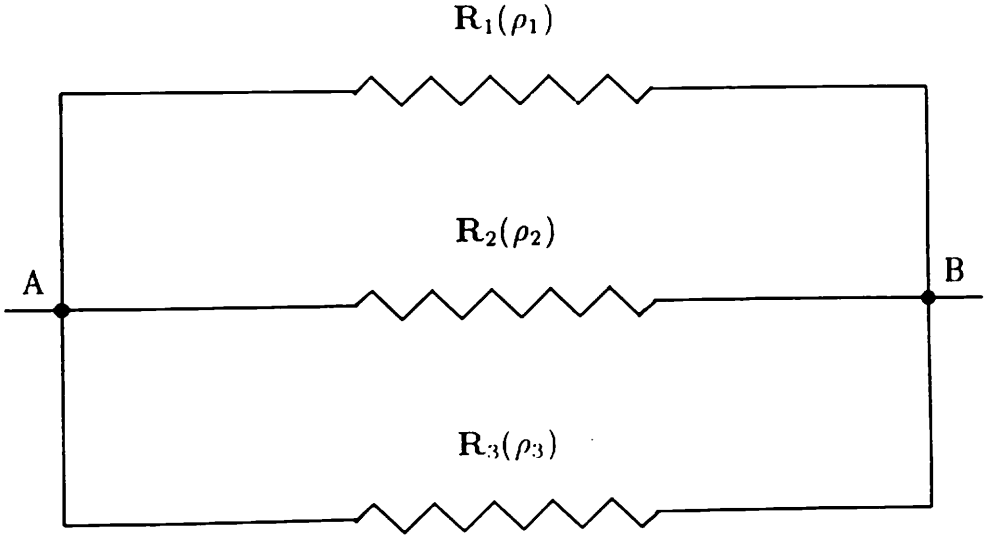

Fig.4a.35(b) Equivalent parallel resistances of the irradiated sample

Sample thickness : t

The extent of electronic loss : d_e (approximately the range of the ion)

The extent of the nuclear loss : d_n (approximately the ion straggling s)

With these fixations of the geometrical parameters and the fact that only a small fraction of the sample is irradiated, the entire target is postulated to be made up of various resistances connected in parallel, as depicted in Fig. 4a.35 (b). Now the various assumptions made, are :

1. The reistivity of zone I is not abruptly changed due to irradiation and due to geometrical considerations the value of the reistance of this zone is much larger than that of zone III, the unirradiated portion. The assumption is based on the fact that the range of the ions used (32 μm maximum, in the three cases) is much less than the thickness of the samples.

2. The reistance of zone II is much larger than that at other zones namely, I and III. This is based on the fact that the resistance of this region is basically confined to the

straggling region which is much smaller in thickness than even the range of the ions.

Now based on the assumptions made above, a simple model is worked out below.

Let us consider only the irradiated portion AB (fig. 4a.35 (a)). The reistivities of three zones are defined as ρ_1, $\rho_2$and ρ_3 corresponding to the resistances R_1, R_2 and R_3. Further R_1 is designated to be affected due to the electronic loss of the ions exclusively and that R_2 due to the nuclear loss. These three resistances are assumed to be connected in parallel such that the total equivalent resistance of I and II is :

$$R = (R_1R_2/(R_1 + R_2)) = R_1 (1 - R_1/R_2) \qquad (4a.3)$$

for $R_2 >> R_1$ and by taylor's series expansion neglecting the higher order terms.

Now the total equivalent resistance between the points A and B is given by,

$$R_{irr} = \{R_1(1 - R_1/R_2)R_3\}/\{R_1(1 - R_1/R_2) + R_3\} \qquad (4a.4)$$

i.e.,

$$R_{irr} = R_3(1 - R_1/R_2) \qquad (4a.5)$$

Eqn, 4a.5 has also been obtained under the assumption that $R_2 >> R_1$ and $R_1 >> R_3$.

Now the change in the resistance due to irradiation can be easily obtained by computing $R_{unirr} - R_{irr}$ and is obtained to be after taylor's series expansion etc. as ,

$$\Delta R = [(\rho_3/d)\{1/t - 1/(t-r-s/2) + (\rho_3(r-s/2)/\rho_1 + (t-r-s/2)^2)\}]/w \qquad (4a.6)$$

where the resistivity is $\rho = Ra/l$ and $a = w.d$ and r,s and t are range , straggling and thickness. The expression clearly relates the resistivity ρ_1 due to electronic loss to the observed variation ΔR. ρ_3 in the expression can be safely assumed to be constant in view of the condition $r << t$ for bulk samples. Thus, we can see clearly that the effect of change in normal state resistivity is a consequence of the changed resistivity coming in due to electronic loss mechanism.

The question now comes that by which mechanism electronic loss affects the materials. Earlier belief was that only insulating substances get affected by this inelastic process. But during the last few years, it has been well established that high levels of linear energy deposition in electronic excitation (usually refrred to as

LET) during swift heavy ion irradiations, can induce structural modifications in metallic systems, such as point defect creation, phase transformation or even latent track formation[2]. As it is understood from the discussion of the results of the present study that YBCO is also sensitive to electronic loss of the energetic projectiles in it and since the behaviour of YBCO in normal state is metallic, we can extend this arguments about the mechanism of affecting the structure by electronic loss for metallic systems to YBCO also.

It has been seen that there is a threshold value of electronic energy loss $(dE/dX)_e$ below which the effect seen is due to elastic collission or radiation annealing, where part of the energy deposited in electronic excitation is converted into atomic motion. This leads to a partial recombination of defects just created, decreasing, for one single ion, the number of produced defects. Above the threshold, a whole new process starts, where effect of damage production in elastic collissions and LET annealing becomes completely negligible as compared to this new process of damage production. It is believed that below threshold, the kinetic energy carried away by the δ-electrons (excited electrons) is converted into atomic vibrations via electron-phonon coupling. The resulting heating up of the lattice might well account for the defect recombination and annealing mentioned above. This

"Thermal Spike" model was invoked years ago for insulating materials[3]. More recently a tentative extension of this model to the metallic system has been made[4].

Coming to the structural modification by electronic energy loss , a "Coulomb Explosion" model which considers the relaxation of the electrostatic potential energy stored in the space charge resulting from the ionization of the atoms, has been used for quite some time for insulators and organic materials[5]. Contrary to what happens in insulator, the life time of the space charge in a metal is extremely short, due to the presence of free conduction electrons. The lifetime, τ, is roughly given by a few 10^{-16} seconds for metals. Nevertheless, for sufficiently high LET levels, when the ionization occurs inside a continuous cylinder, it has been shown[6], that the recoil energy, E_r, acquired by the ionized atoms due to coulomb repulsion can reach 0.1 to few eV. Now, as far as the individual collissions are considered, recoil energy smaller than the threshold energy E_d ($\cong$25 eV) can not lead to a defect creation. In such a scheme, Coulomb explosion appears to be inefficient towards damage creation. But the collective and coherent aspects of the recoils[2] have to be taken into account, so that the concept of the threshold energy, E_d, becomes meaningless. In fact, it has been shown[7] that the spatial and temporal coherence of these excitations

allows an easy coupling to the phonon spectrum. More precisely, low frequency modes are preferentially excited, which occurs (1) for accoustic waves (i.e., $q \cong 0$) and (2) for soft modes (usually at large q values) if any. In the first case, a radial shock wave is generated, whereas in the latter, large amplitude atomic movements are induced. either of these two processes can lead to structural modifications and /or defect creation.

Molecular dynamics calculation shows that as soon as E_r is higher than $\cong$ 1 eV, lattice defects are created. Starting with a crystal in which a preexisting stable Frenkel pair was induced, it was shown[8] that recoil energies as low as 0.2 eV/atom were sufficient to induce the recombination of these frankel pairs in the vicinity of the ion path.

As it was discussed above the results of the irradiation experiments in the present study show that in case of low electronic energy loss value (for oxygen), there is change only in width of transition, whereas in case of high energy loss value (for iodine) the superconducting property has been changed totally and the irradiated sample becomes insulating. Therefore, from our result also it is clear that there is certain value of electronic energy loss for YBCO above which the internal property of the superconducting material is changed, probably, due to the breaking of the Cu-O bonds.

Few samples are irradiated with low energy (150 KeV) nitrogen, because nitrogen is very near to oxygen in the periodic table and was expected to have similar nuclear energy loss value which the 75 MeV O have at the end of its range in YBCO bulk target and is also verified from the TRIM calculation [$(dE/dx)_n$. for 150 KeV O = 11.17ev/Å and $(dE/dx)_n$ for 150 KeV N = 8.16 ev/Å]. In other words the effect of 75 MeV O at the end of the range in YBCO bulk material is experimentally simulated on the surface of YBCO targets by bombarding them with 150 KeV nitrogen. From the result it is seen that there is not much effect of 150 kev N irradiation on the superconducting properties of the YBCO, which in effect can be applied to 75 MeV O at the end of its range. Therefore, from indirect argument it can be said that whatever effect is seen in case of 75 MeV O irradiation is solely due to electronic loss of the ions.

Finally, addressing the thin film irradiation results, it can be said that due to the lack of sufficient number of good quality YBCO thin films, with reproducable properties, thin film experiments could not be properly planned and carried out extensively. Still from the few experiments done on the thin films of YBCO in the present study, few qualitative but correct conclusions can be drawn. In case of oxygen irradiation, not much

change of normal state resistance has been observed in contrast to the result of the similar experiment on bulk samples where a decrease in resistance has been seen. Similar work on thin film was carried out by 25 Mev ^{16}O at 100 K elsewhere[9], where a increase in resistance is observed. It is known to everybody that bulk samples have more intrinsic defects which leaves more scope of improvement than the thin film. The thin films, on the other hand, are much more perfect in structure and exposure to irradaition can only increase the degree of defects increasing the sample resistance. The result of the oxygen irradiation experiment on YBCO thin films can be explained in the light of the above arguments. In case of iodine, the change in Tc from R vs. T measurement indicates the fact that due to its greater electronic energy loss value, iodine perhaps changed the intrinsic superconducting properties of YBCO film.

Therefore, from the irradiation studies it has been observed that there is a definite effect of increasing electronic energy loss of the bombarding projectile on the properties of the superconducting material. In R vs. dose measurements in bulk samples, since the current path follows a parallel circuit, the net change observed, due to the change in a very small thickness on the surface of the sample, is small. This total change not only depends on the value of the energy loss parameter, but also on the thickness of the

affected layer of the bulk sample. For this reason, in case of Ni and I irradiation, although the effect of irradiation may be high, but still the net change is small because the range of these projectiles are small in the material. Thin film samples with exposure to this heavy projectiles might have given sharper changes. Nevertheless, we have been able to detect the differences of changes for different projectiles as discussed in the earlier part of this chapter.Also the different results obtained for the films on different substrates with the exposure to the same energetic particle of almost same order of fluence, showed that the behaviour of the resultant irradiated film not only depends on the energy loss value inside the films, but also the energy loss at the interface of the film and substrate which is different for different substrates.

References

1. G. J. Clark, A. D. Marwick, F. Legoues, R. B. Laibowitz, R. Koch and P. Madakson, *Nucl. Instrum. Meth.*, **B32**, 405 (1988).

2. A. Dunlop, D. Lesueur, P. Legrand and H. Dammak, *Nucl. Instrum. Meth.*, **B90**, 330 (1994).

3. L. T. Chadderton and H. Montagu-Pollock, *Proc. R. Soc.*, **A274**, 239 (1969).

4. M. Toulemonde, C. Dufour and E. Paumier, *Phys. Rev.*, **B46**, 14362 (1992).

5. I. S. Bitensky and E. S. Parilis, *Nucl. Instrum. Meth.*, **B21**, 26 (1987).

6. D. Lesueur and A. Dunlop, *Radiat. Eff. Def. Solids*, **126**, 163 (1993).

7. A. Dunlop, P. Legrand, D. Lesueur, N. Lorenzelli, J. Morillio, A. Barbu and S. Boufford, *Europhys. Lett.*, **15**, 765 (1991).

8. A. Dunlop, D. Lesueur, *Radiat. Eff. Def. Solids*, **126**, 123 (1993).

9. B. Hensel, B. Roas, S. Henke, R. Hopfengartner, M. Lippert, J. P. Strobel, M. Vildic, G. Saemann-Ischenko and S. Klaumunzer, *Phys. Rev.*, **B42**, 4135 (1990).

CHAPTER IV B

THIN FILM BUFFER LAYERS ON Si

In this chapter the deposition of two materials $SrTiO_3$ and MgO as buffer layer for YBCO film on Si and the results of their characterization by different techniques will be described. At the end of the chapter possible interpretations of the results obtained in different measurements will be discussed. $SrTiO_3$ and MgO were chosen as buffer layers because of their amicability with YBCO films as substrate materials.

4b.1. Deposition and Characterization of $SrTiO_3$ Thin Films on Si

$SrTiO_3$ thin films of thickness 1300 Å were deposited on 0.8-1.0 Ω-cm (111) p-type Si substrates by e-beam evaporation from sintered pellets. The base pressure of deposition was 2×10^{-8} mbar and deposition pressure was 5×10^{-6} mbar. Some of the samples were annealed in flowing O_2 at 700°C and 900°C. The thickness of the sample was measured by a surface profilometer. The films were then characterized by Auger electron spectroscopy (AES) and simultaneous heavy ion backscattering (HIBS) and elastic recoil detection analysis (ERDA) and by X-ray diffraction technique (XRD). The results of these characterizations are described in the next few subsections.

4b.1.1. Results of AES

Results of the AES studies of the as deposited and the annealed thin films at 700°C are described in this subsection. Fig. 4b.1 shows the AES spectrum of the surface of the as deposited $SrTiO_3$ film. The spectrum indicates the presence of all the components, i.e., Sr, Ti and O in the film. The surface of the as deposited film is seen to be free from any impurity, which clearly indicates that there is no incorporation of any foreign element from the vacuum chamber even though the deposition pressure was 5×10^{-6} mbar. Fig. 4b.2 (a) shows the AES spectrum of the surface of $SrTiO_3$ film annealed at 700°C in flowing oxygen. In this case we see that besides the presence of the three constituents of the source material, there are two additional elements (sulphur, 149 eV and carbon, 270 eV) present in the sample. Fig. 4b.2 (b)-(d) represents the AES spectra of the annealed film with successive removal of the sample by Ar ions. Although the presence of S is seen only on the top surface of the film, carbon is seen to be present throughout the film. The AES depth profile of the annealed film is shown in fig. 4b.3. This figure confirms that there is no Si interdiffusion into the film. The depth profile also indicates that the concentration of Ti is constant upto a certain thickness below the surface and then diminishes sharply. In contrast the concentration of Sr is almost uniform throughout the thicknes of the film.

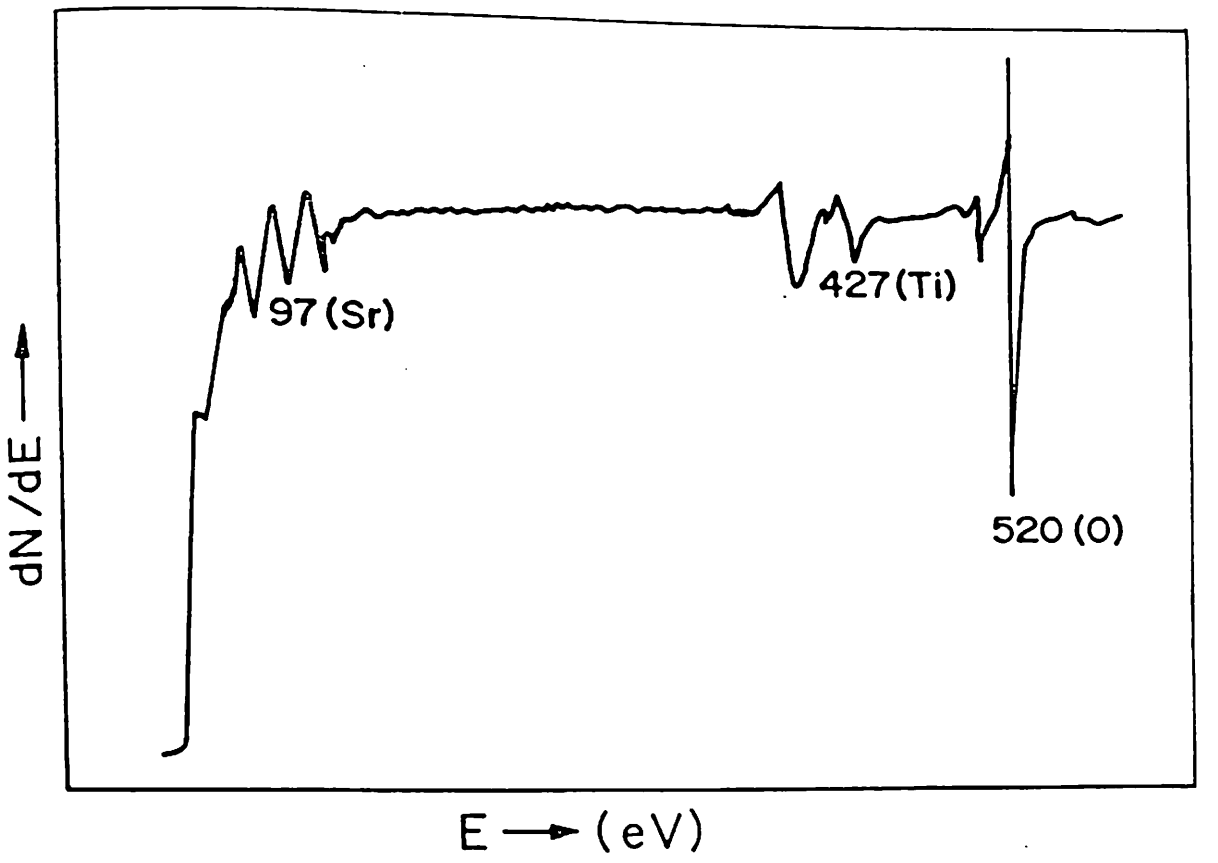

Fig. 4b.1. AES spectrum of the as deposited $SrTiO_3$ thin film.

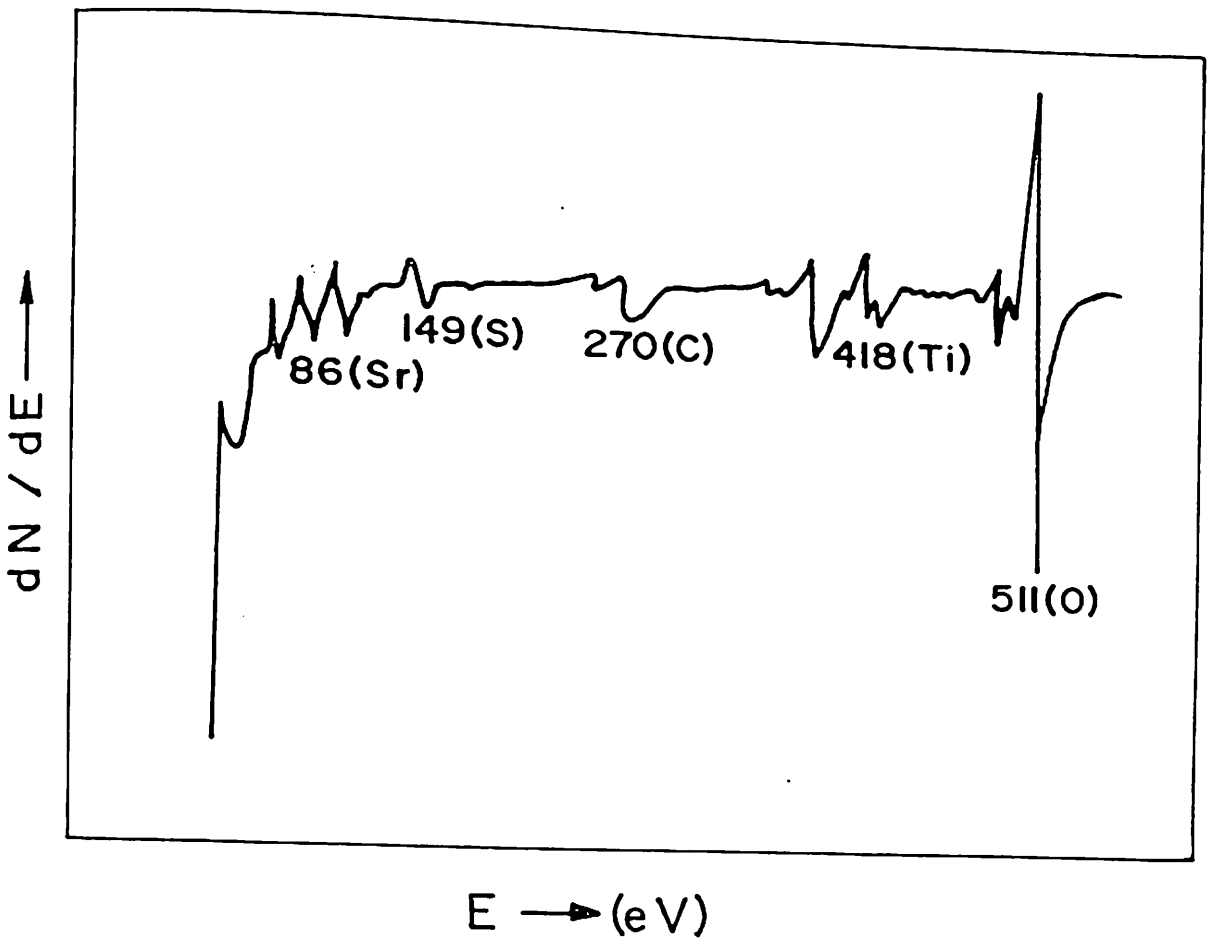

Fig. 4b.2. (a) AES spectrum of the surface of the 700°C annealed $SrTiO_3$ film.

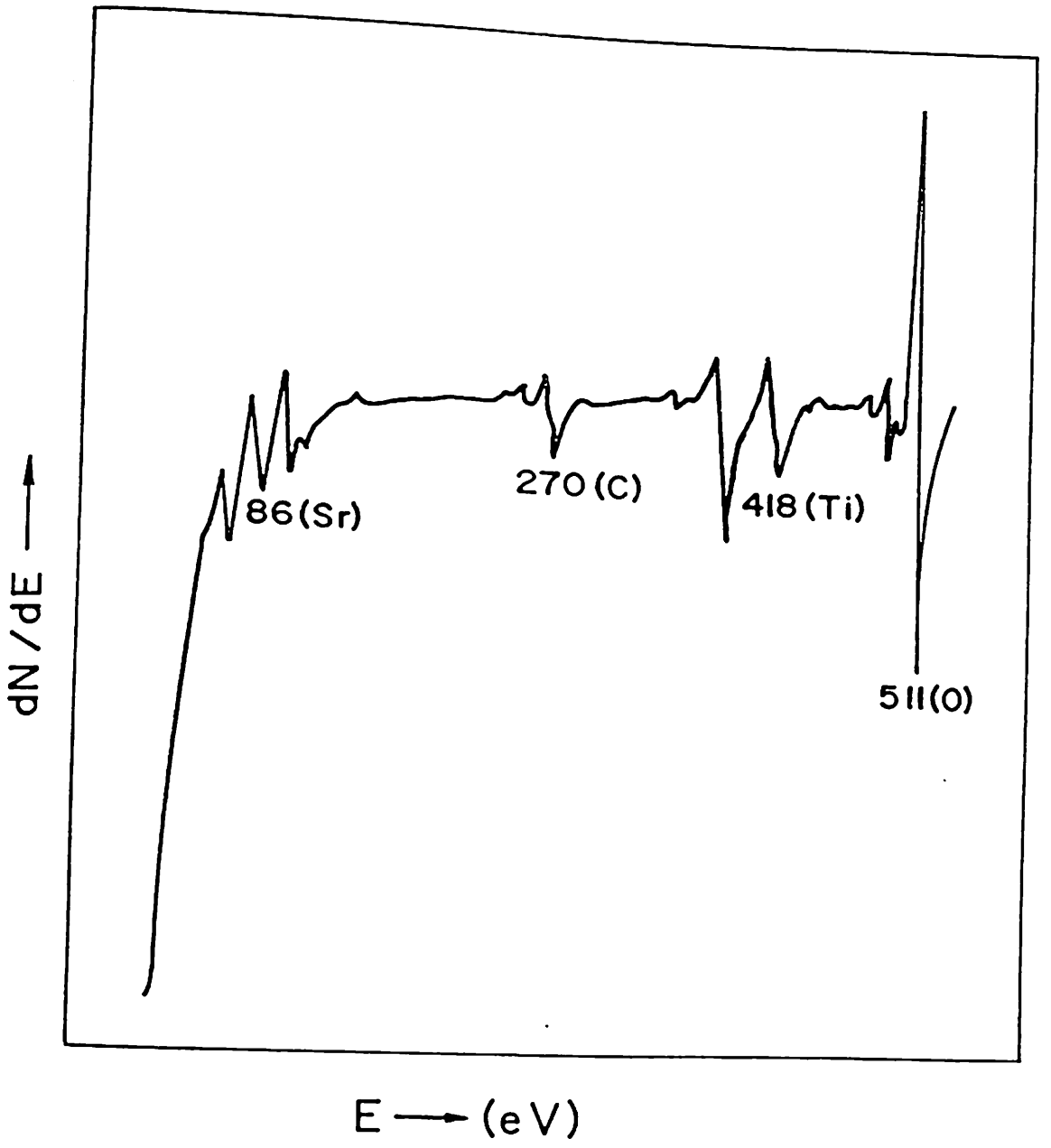

Fig. **4b.2.** (b) AES spectrum of the 700°C annealed $SrTiO_3$ film after 400 s Ar ion etching.

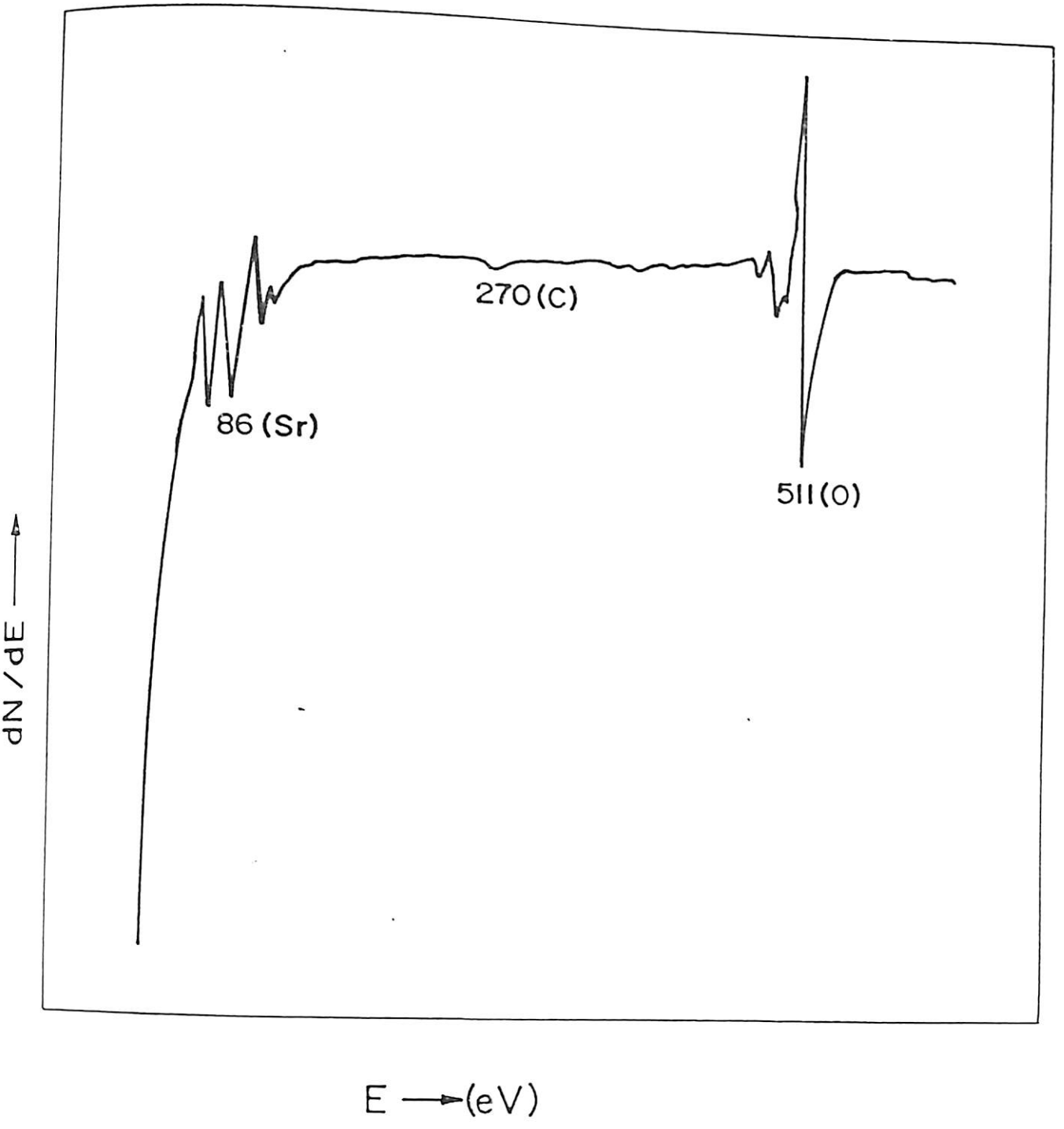

Fig. 4b.2. (c) AES spectrum of the 700°C annealed $SrTiO_3$ film after 580 s Ar ion etching.

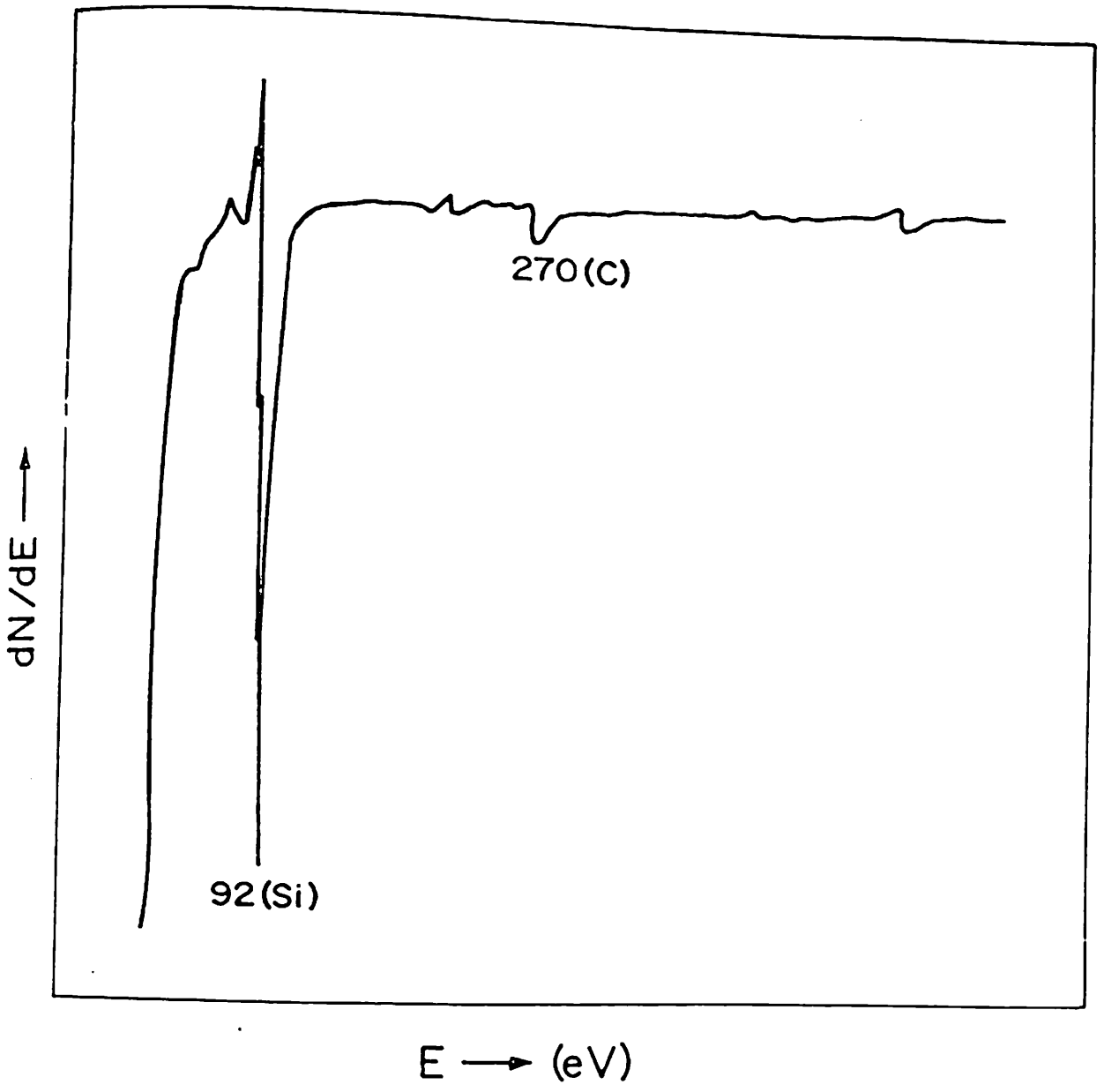

Fig. 4b.2. (d) AES spectrum of the 700°C annealed $SrTiO_3$ film after 760 s Ar ion etching.

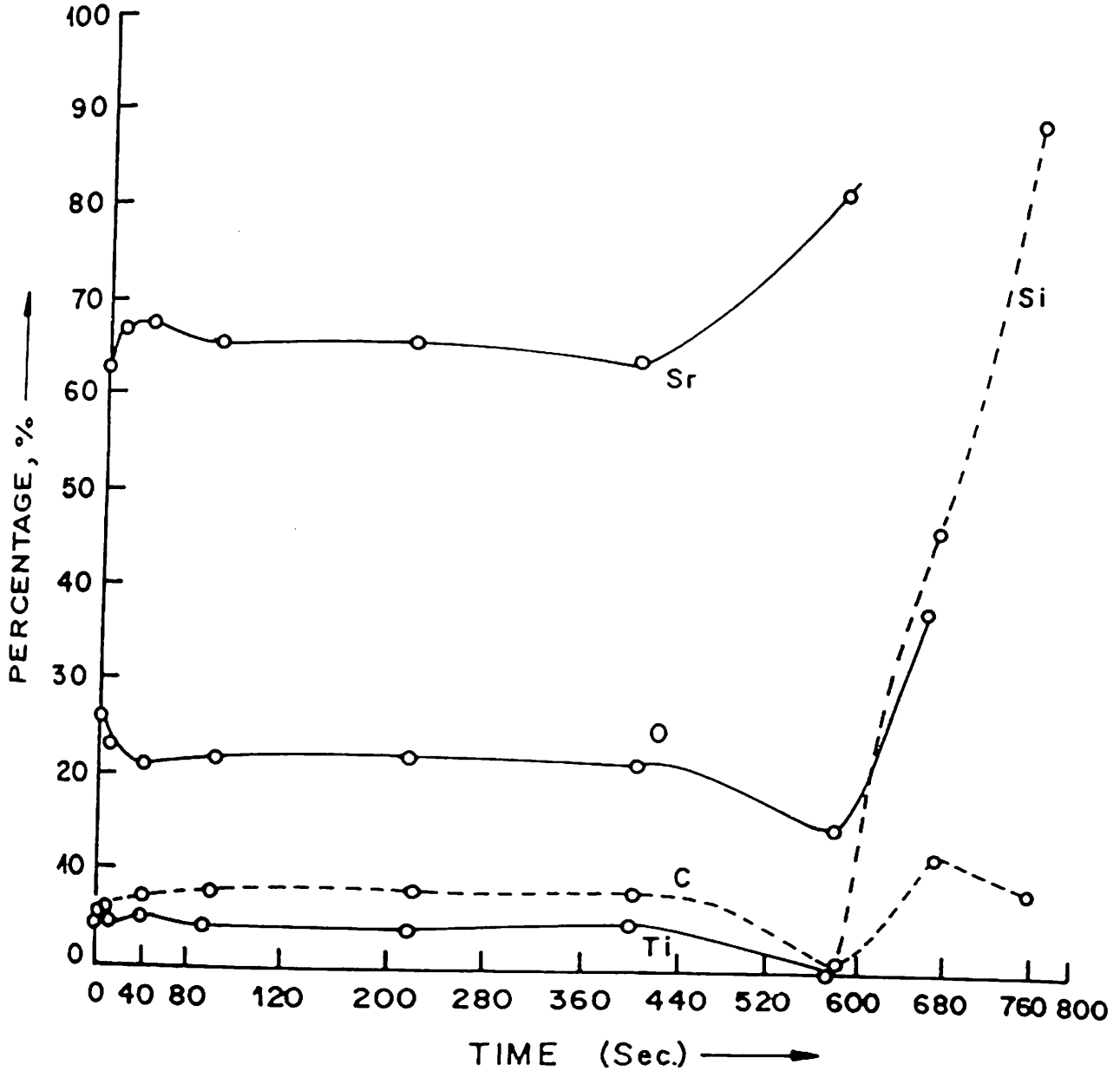

Fig. 4b.3. The percentage atomic concentration as a function of sputtering time (≡ depth) of the 700°C annealed $SrTiO_3$ film on Si.

4b.1.2. Results of HIBS and ERDA

Fig. 4b.4 (a), (b) and (c) show the oxygen recoil spectra of the unannealed samples and of annealed samples at 700°C and 900°C respectively. The figures show that oxygen content reduces in 700°C annealed film. However, it tends to diffuse drastically at higher temperature of 900°C. The backscattering spectra observed in three different types of $SrTiO_3$ film, namely, unannealed and annealed at two different temperature, are shown in fig.4b.5. (a), (b) and (c). The tail at the high energy edge of the Sr peaks are due to the improper amplifier biasing during the Sr peaks are due to the improper amplifier biasing during experiment. Fig. 4b.6 shows the expanded view of the elastic scattering peak due to Sr in annealed and unannealed sample. The high energy edge of the two peaks overlaps with each other which shows that Si atom does not migrate to the surface of $SrTiO_3$ during annealing. For quantitative analysis, the amount of different constituents are found by finding corresponding area under the peak in the spectrum, calculating the differential cross sections $(d\sigma/d\Omega)$of the constituents and also using the $d\Omega$ values of the detector in the HIBS and ERDA. The formulae used for determining differential cross section of backscattering of projectiles and forward scattering of recoils are given below.

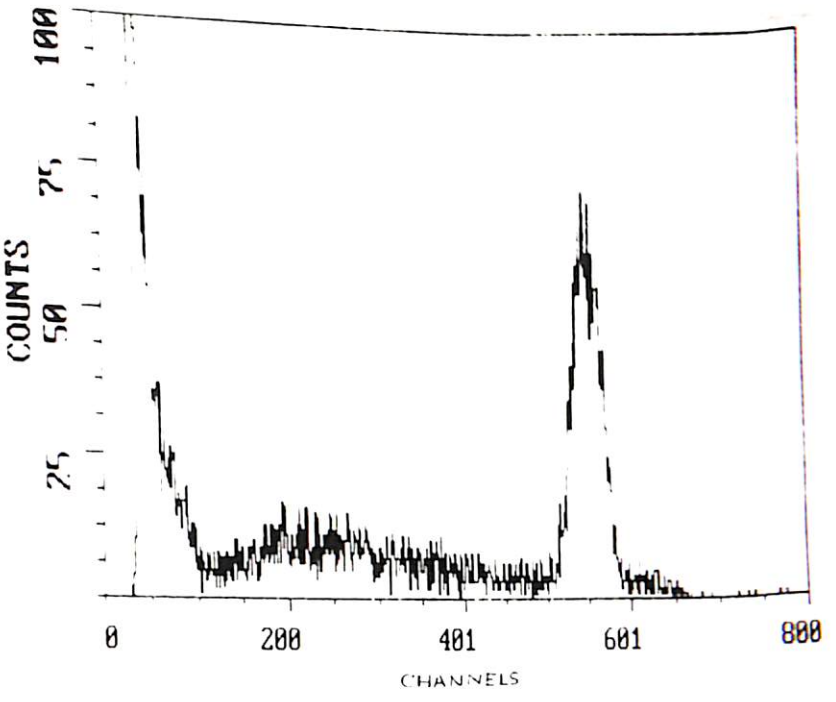

Fig. 4b.4. (a) Oxygen recoil spectrum of as deposited film of $SrTiO_3$.

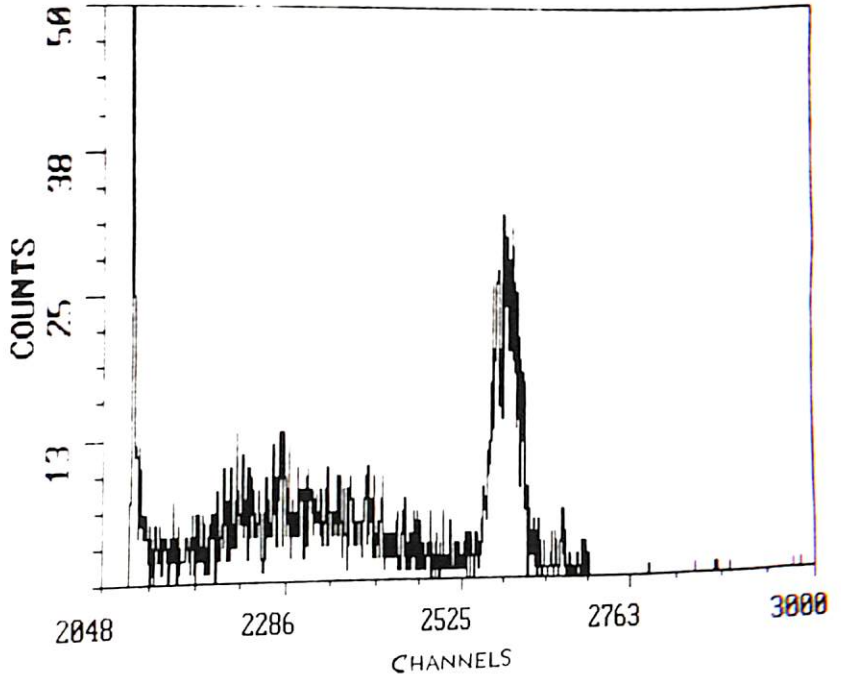

Fig. 4b.4. (b) Oxygen recoil spectrum of 700°C annealed $SrTiO_3$ film.

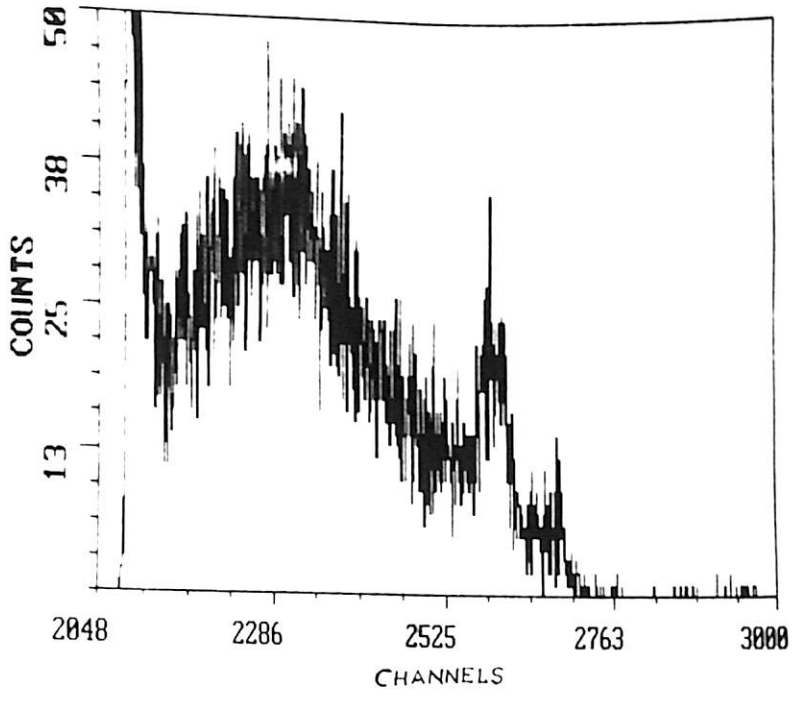

Fig. 4b.4. (c) Oxygen recoil spectrum of 900°C annealed $SrTiO_3$ film.

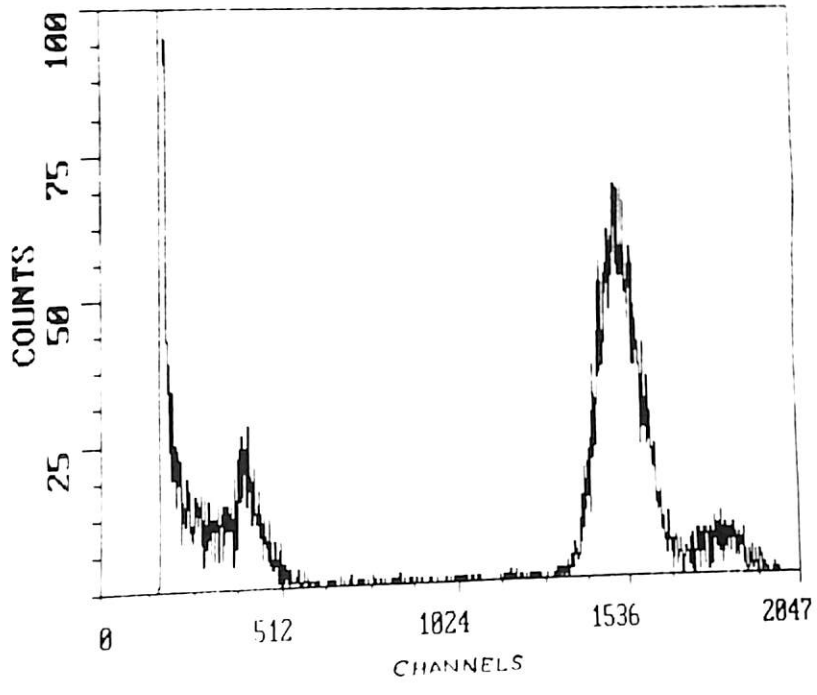

Fig. 4b.5. (a) Backscattered spectrum of as deposited $SrTiO_3$ film.

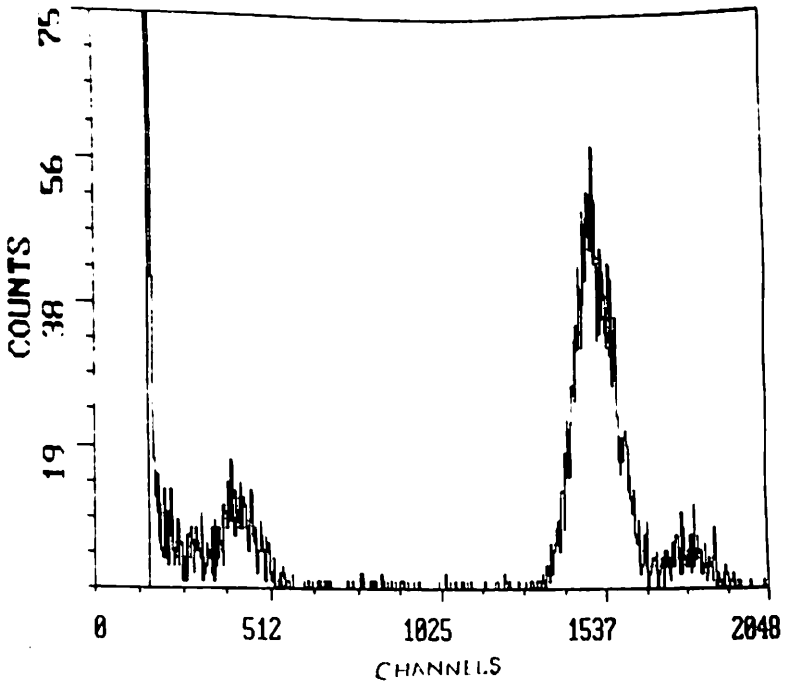

Fig. 4b.5. (b) Backscattered spectrum of 700°C annealed $SrTiO_3$ film.

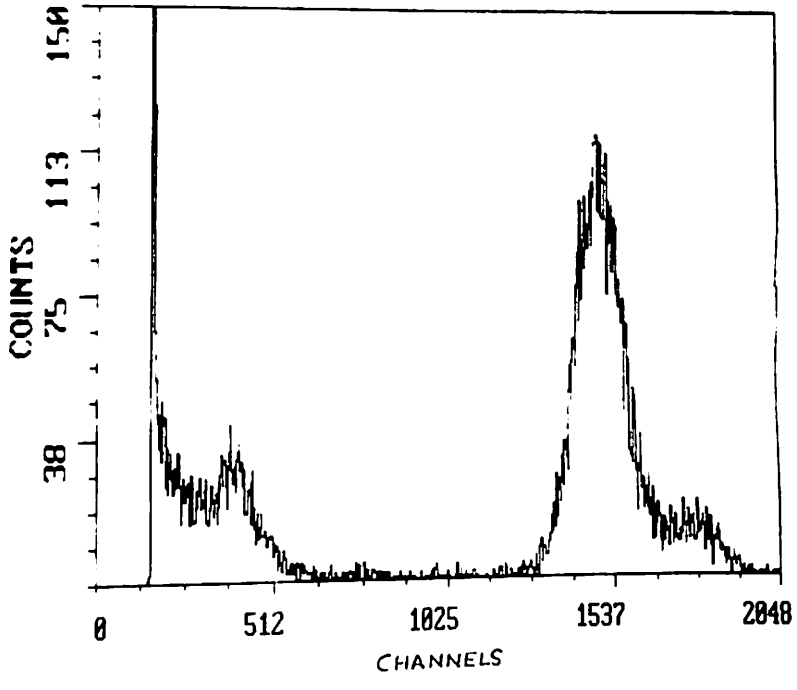

Fig. 4b.5. (c) Backscattered spectrum of 900°C annealed $SrTiO_3$ film.

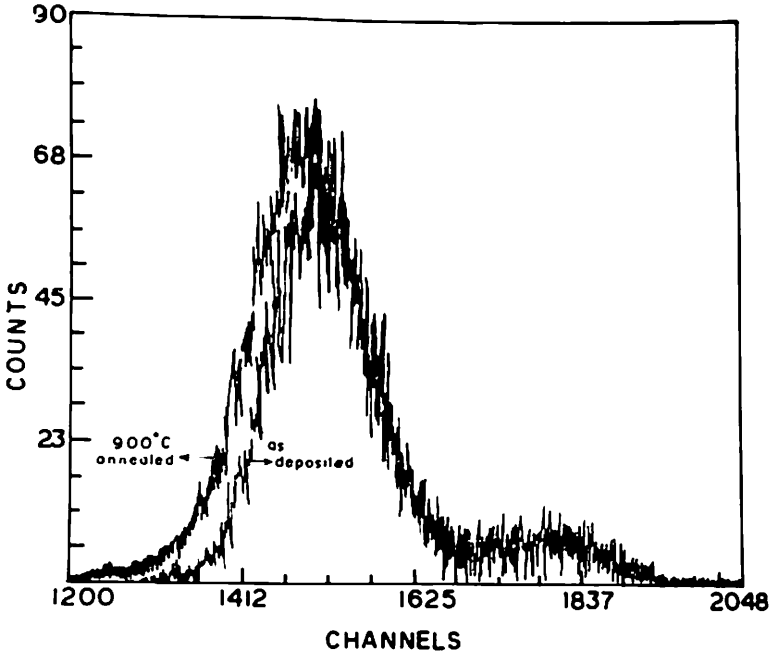

Fig. 4b.6. Expanded overlapped backscattered Sr spectra of as deposited and 900°C annealed $SrTiO_3$ film.

$$\left(\frac{d\sigma}{d\Omega}\right)_{backscatt} = \left(\frac{Z_1 Z_2 e^2}{4E}\right) \frac{4}{\sin^2\theta} \frac{[\{1-\left(\frac{M_1}{M_2}\right)^2 \sin^2\theta\}^{\frac{1}{2}} + \cos\theta]^2}{\{1-\left(\frac{M_1}{M_2}\right)^2 \sin^2\theta\}^{\frac{1}{2}}} \quad \text{(4b.1)}$$

$$\left(\frac{d\sigma}{d\Omega}\right)_{recoil} = \left[\frac{Z_1 Z_2 e^2 (M_1 + M_2)}{2E(d_0) M_2}\right]^2 \frac{1}{\cos^3\phi} \quad \text{(4b.2)}$$

where Z_1, Z_2 and M_1, M_2 are the atomic numbers and the masses of the projectile and target atoms respectively, E is the energy of the projectile and $E(d_0)$ is the reduced beam energy at the scattering position after energy loss in a layer of thickness d_0 at the entrance of the target, θ and ϕ are the backscattering and forward angles respectively. In the above formulae the scattering cross sections are given in laboratory frame of reference.

Calculating by the procedure given above, the stoichiometric ratio of Sr, Ti and O in three differenet cases are listed in table 4b.1. It shows that the prepared samples under study are Sr rich although the starting material was $SrTiO_3$.

TABLE 4b.1

Sample Type	*Ratio*		
	Sr	*Ti*	*O*
unannealed	1.73	1.0	9.8
700°C annealed	1.68	1.0	4.9
900°C annealed	2.2	1.0	1.8

4b.1.3. Results of XRD

Fig. 4b.7 (a), (b) and (c) show the XRD spectra of the $SrTiO_3$ tablet which was used as source material, of as deposited $SrTiO_3$ thin film on Si (111) substrate and 700°C annealed $SrTiO_3$ thin film on Si (111) substrate. Figures clearly show that while the as deposited film is almost amorphous in nature, a (211) orientation has been generated as a result of thermal treatment.

4b.2. Deposition and Characterization of MgO Thin Films on Si Substrates

The second material chosen for buffer layer was MgO also because of its suitability as a substrate material to YBCO thin films. MgO pellets were made by pressing MgO powder and then sintering them at 1000°C. These pellets were used as source in

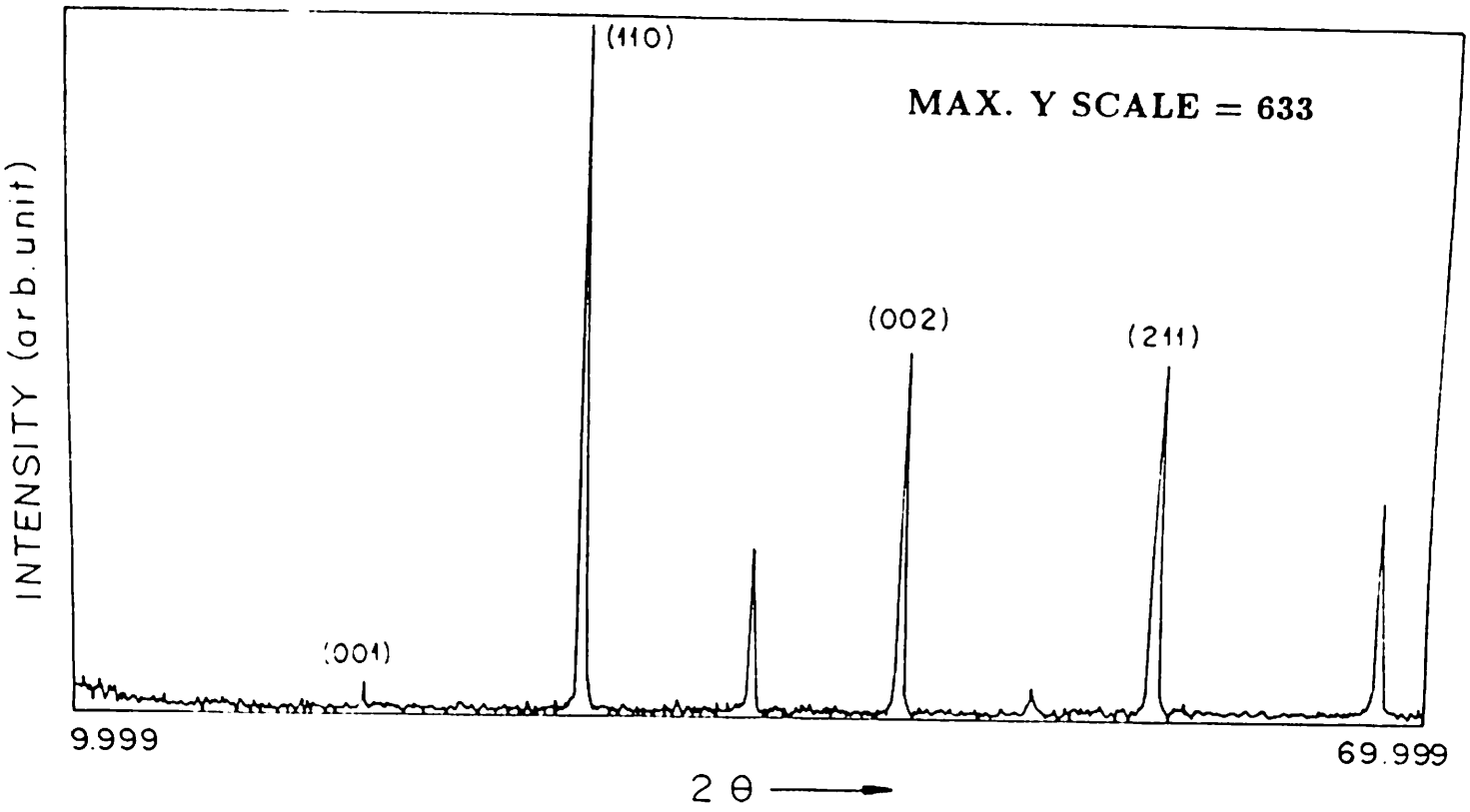

Fig. 4b.7. (a) XRD spectrum of the $SrTiO_3$ pellet used as a source for e-beam deposition of $SrTiO_3$ thin film.

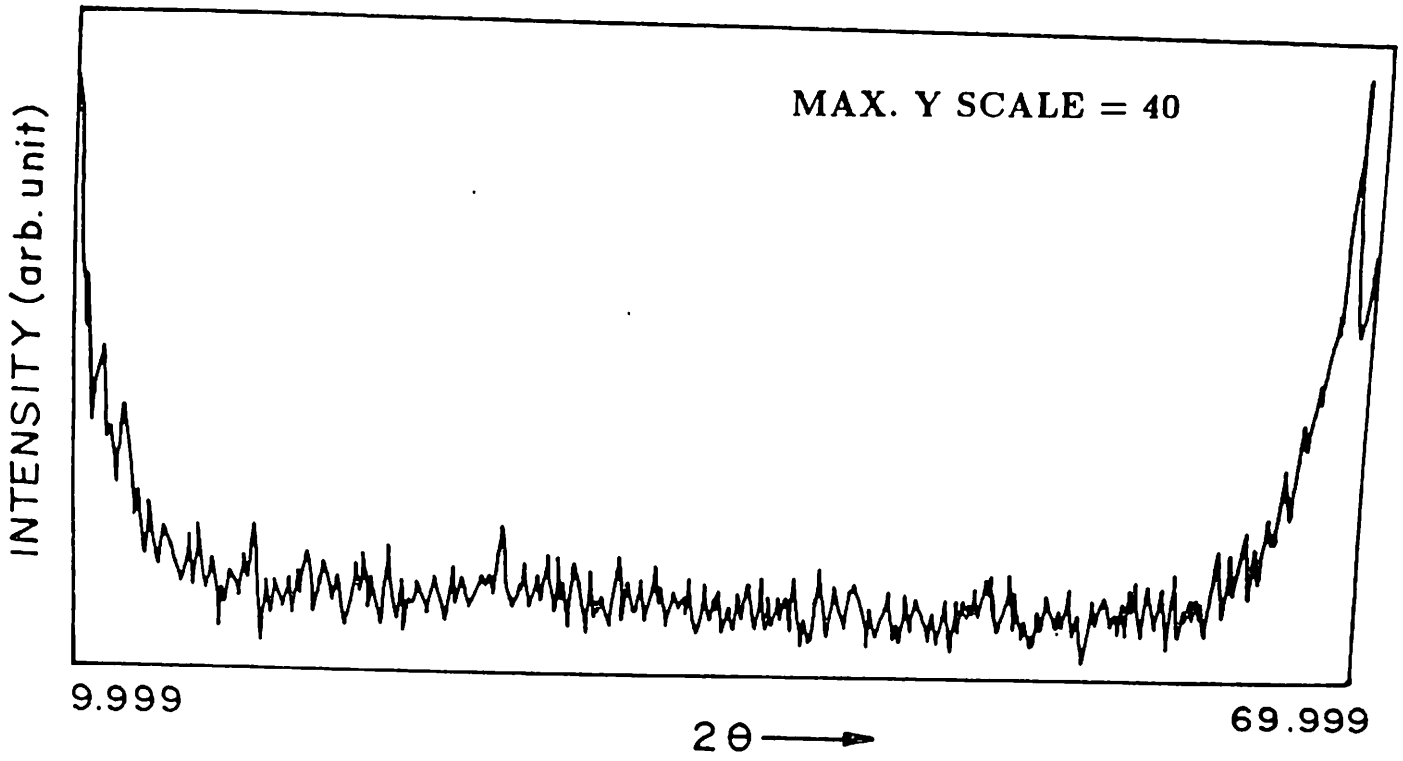

Fig. 4b.7. (b) XRD spectrum of the as deposited $SrTiO_3$ film.

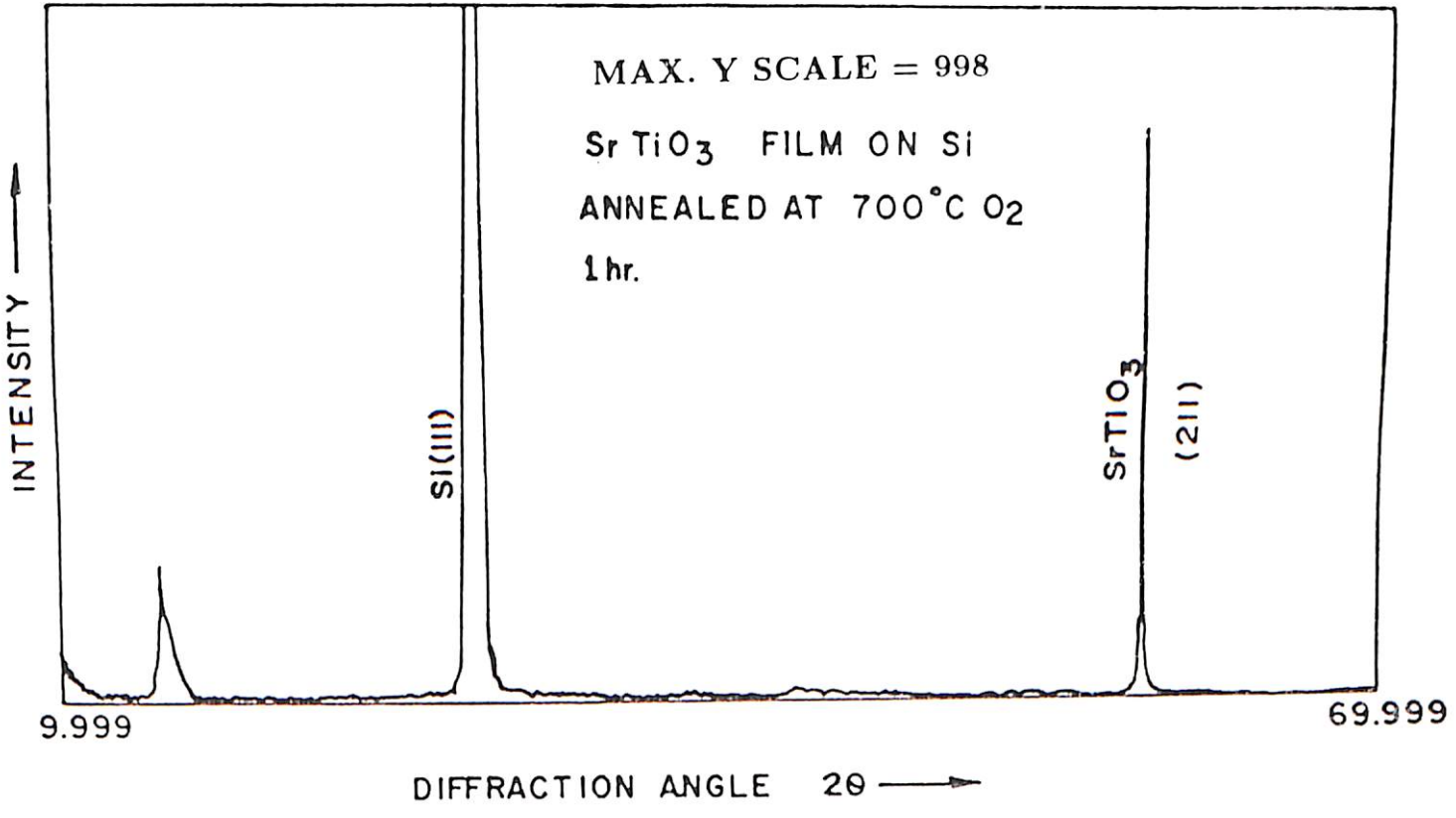

Fig. 4b.7. (c) XRD spectrum of the 700°C annealed $SrTiO_3$ thin film.

the e-beam deposition system. Before deposition the substrates were heated. Because MgO is a hygroscopic material, it absorbs some water vapor during loading into the vacuum chamber. By substrate heating MgO pellets were also heated up and the absorbed water vapor was removed by desorption. The base pressure of deposition was 2 X 10^{-8} torr and the deposition pressure was 6-8 X 10^{-6} torr. The deposition rate was 0.5 Å/sec and the final thickness was 200Å. After removing from the chamber the as deposited films were then annealed at 800°C for 1 hr. Here (100) Si substrates were used as substrate material. The films were then characterized by AES, XPS and XRD, the results of which are discussed in the next few subsections.

4b.2.1 Results of AES

Fig 4b.8 (a) shows the AES spectrum of the surface of the annealed MgO thin film on Si (100) and fig.4b.8 (b)-(d) represents the AES spectra of the same film with sucessive removal of the film by Ar ions. These results show that the film is clean, except the presence of very small amount of carbon on the top surface. Fig. 4b.9 shows the AES depth profiling of the film. This shows that the interface is quite sharp and there is no Si diffusion inside the film. The amount of Mg and O remains constant throughout the depth of the film.

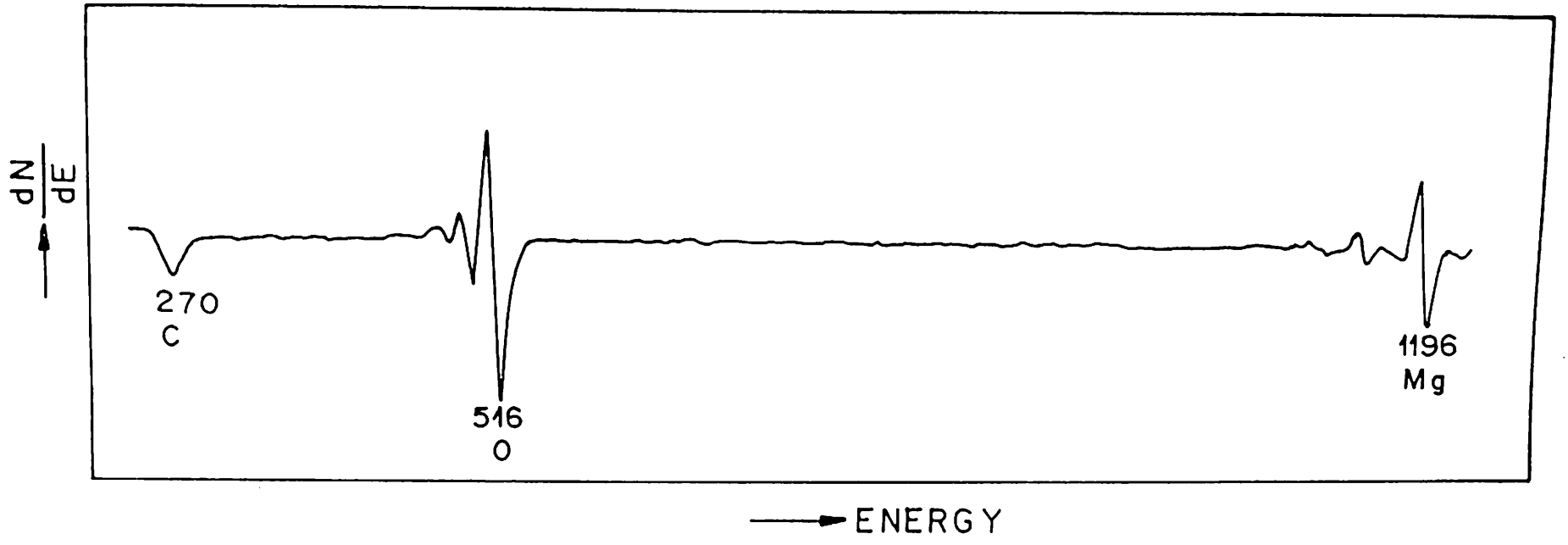

Fig. 4b.8. (a) AES spectrum of the surface of the annealed MgO film.

Fig. 4b.8. (b) AES spectrum of the annealed MgO film after 35 s Ar ion etching.

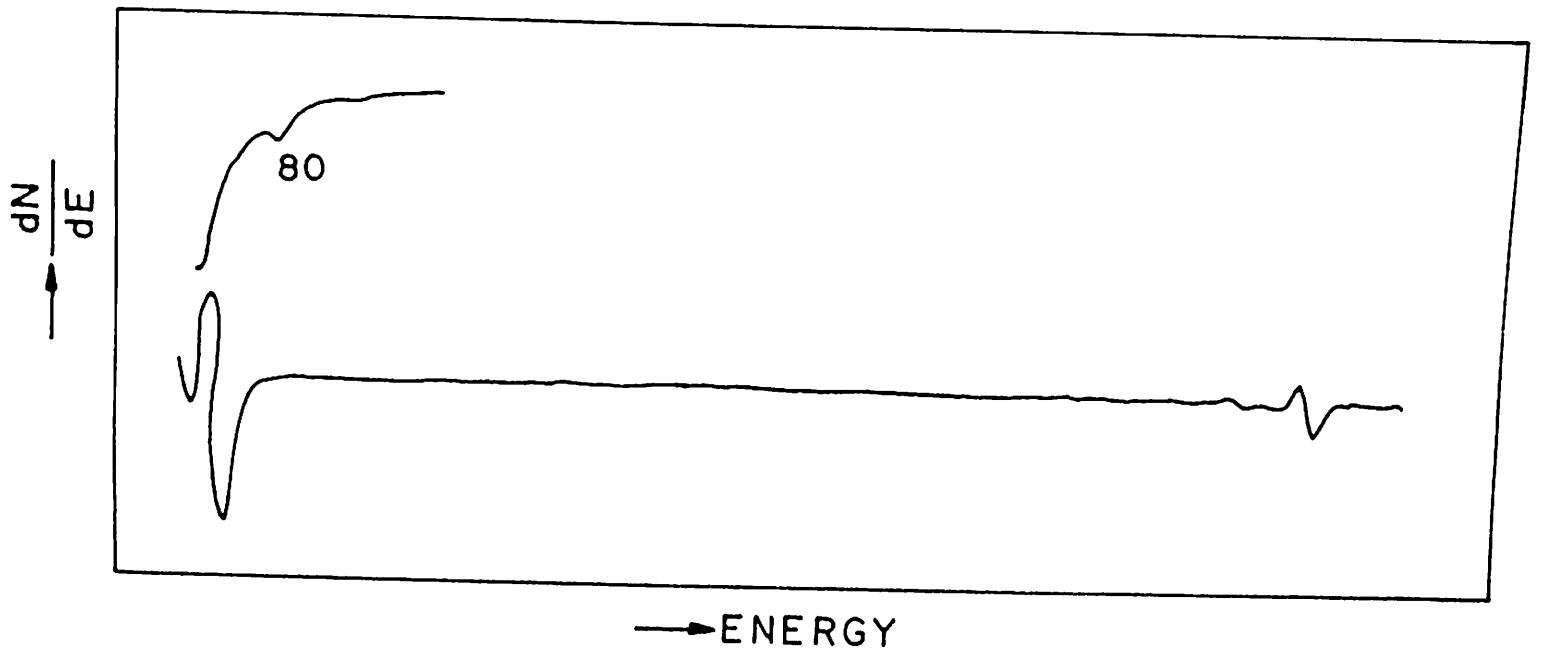

Fig. 4b.8. (c) AES spectrum of the annealed MgO film after 495 s Ar ion etching.

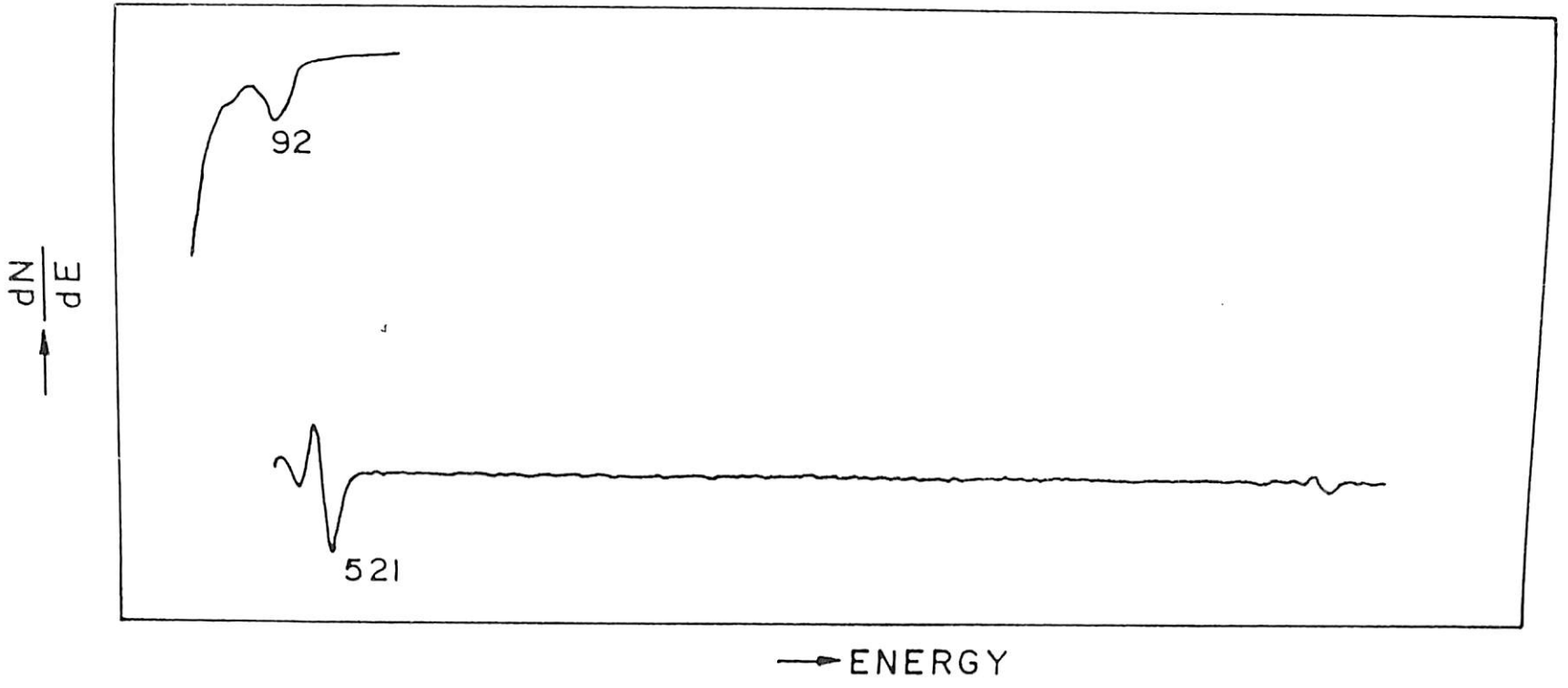

Fig. 4b.8. (d) AES spectrum of the annealed MgO film after 535 s Ar ion etching.

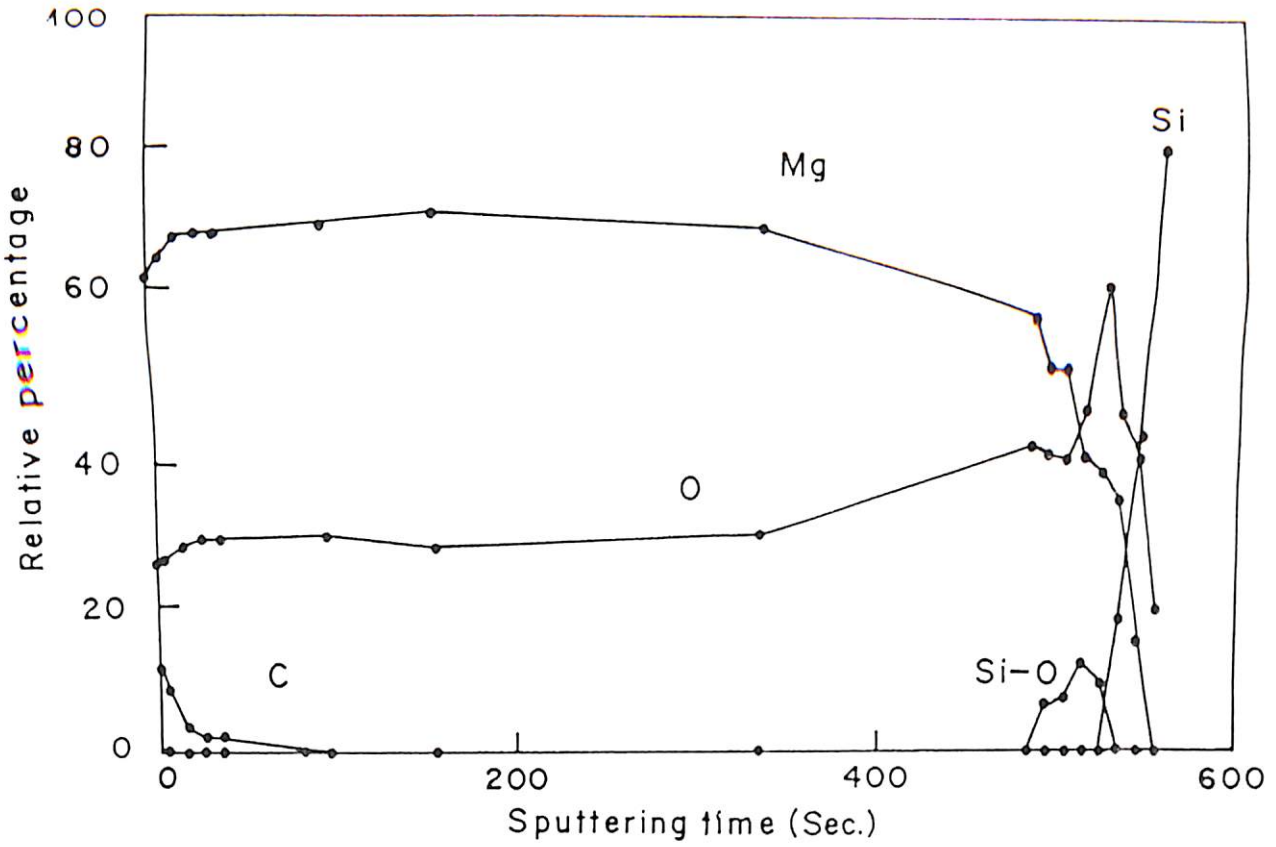

Fig. 4b.9. The percentage atomic concentration as a function of sputtering time (≡ depth) of the annealed MgO film on Si.

4b.2.2. Results of XPS

Fig. 4b.10 (a) shows the XPS spectra of the annealed MgO thin film on Si (100) and fig.4b.10 (b) shows that of the same surface after little bit of sputter cleaning by Ar ion. Like AES results, these figures also show that C is present only at the top surface of the film. Fig. 4b.10 (c), (d) show the finger prints of Mg 2p peak and O 1s peak. Quantitative analysis reveals that Mg and O are present in the film in 1 : 1 ratio. Also the Mg 2p peak is shifted by ~ 3.3 eV due to bonding.

4b.2.3. Results of XRD

Fig. 4b.11 shows the XRD spectrum of annealed MgO thin film on Si (100) substrate. The peak at $2\theta = 57.619°$ is identified as MgO peak of (331) orientation.

4b.3. Discussion of the Results

As was mentioned in first chapter, this growth of buffer layers on Si substrate for subsequent growth of high Tc film on these was undertaken as a preliminary investigation of the feasibility of using superconducting technology in semiconductor industry. Our main goal was to achieve a integrated good quality of buffer layer on Si, where no interdiffusion between Si and the

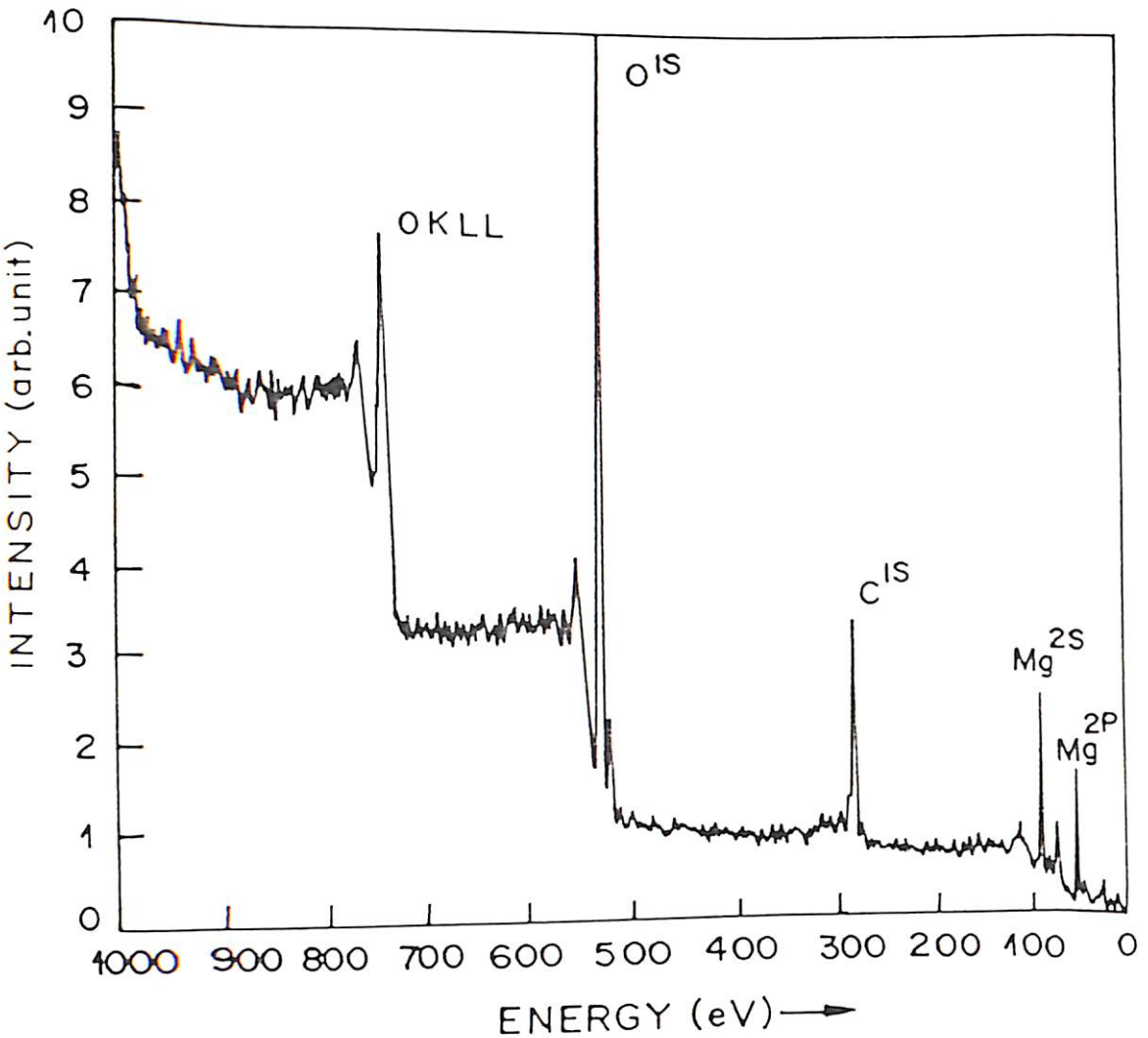

Fig. 4b.10. (a) XPS spectrum of the raw surface of the annealed MgO film.

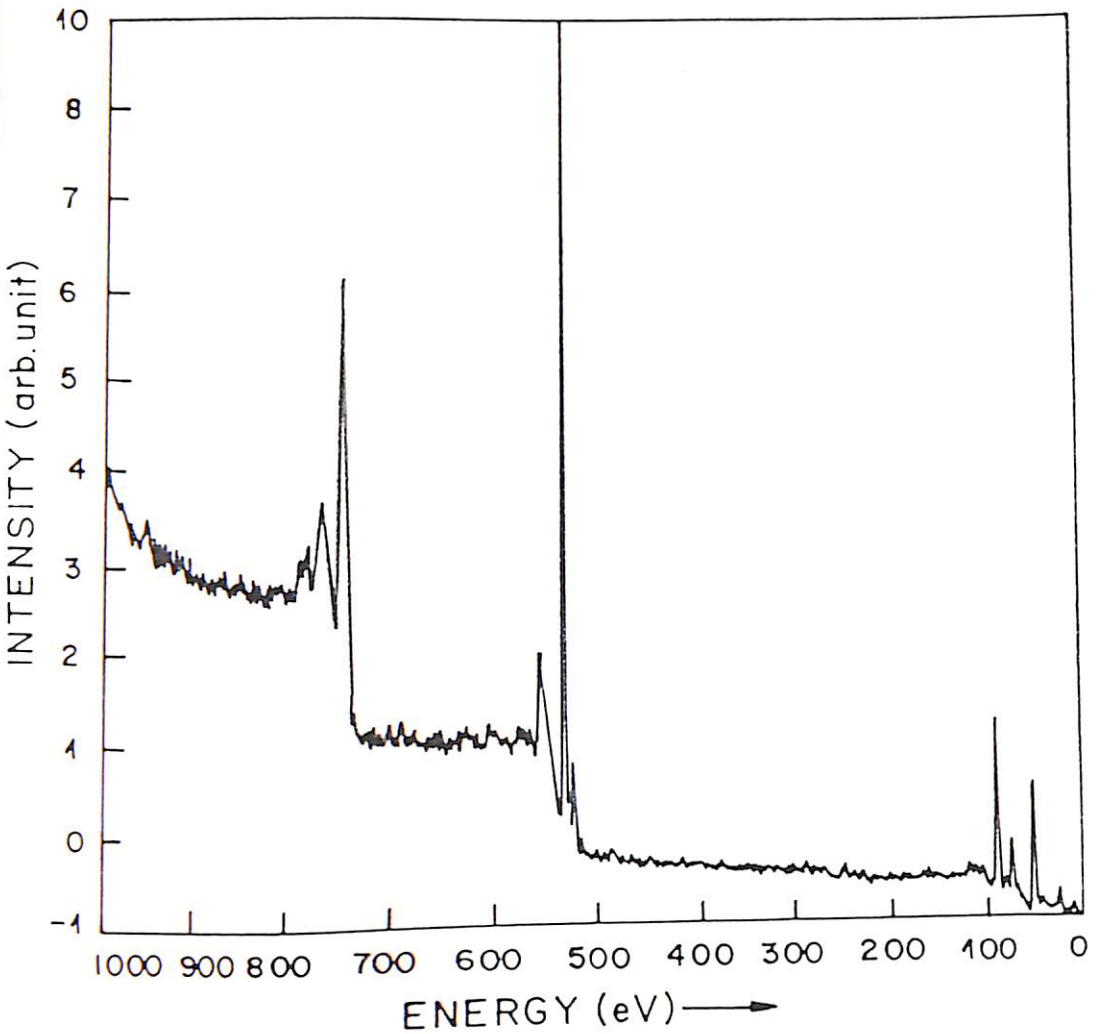

Fig. 4b.10. (b) XPS spectrum of the surface of the annealed MgO film after Ar ion etching for few seconds.

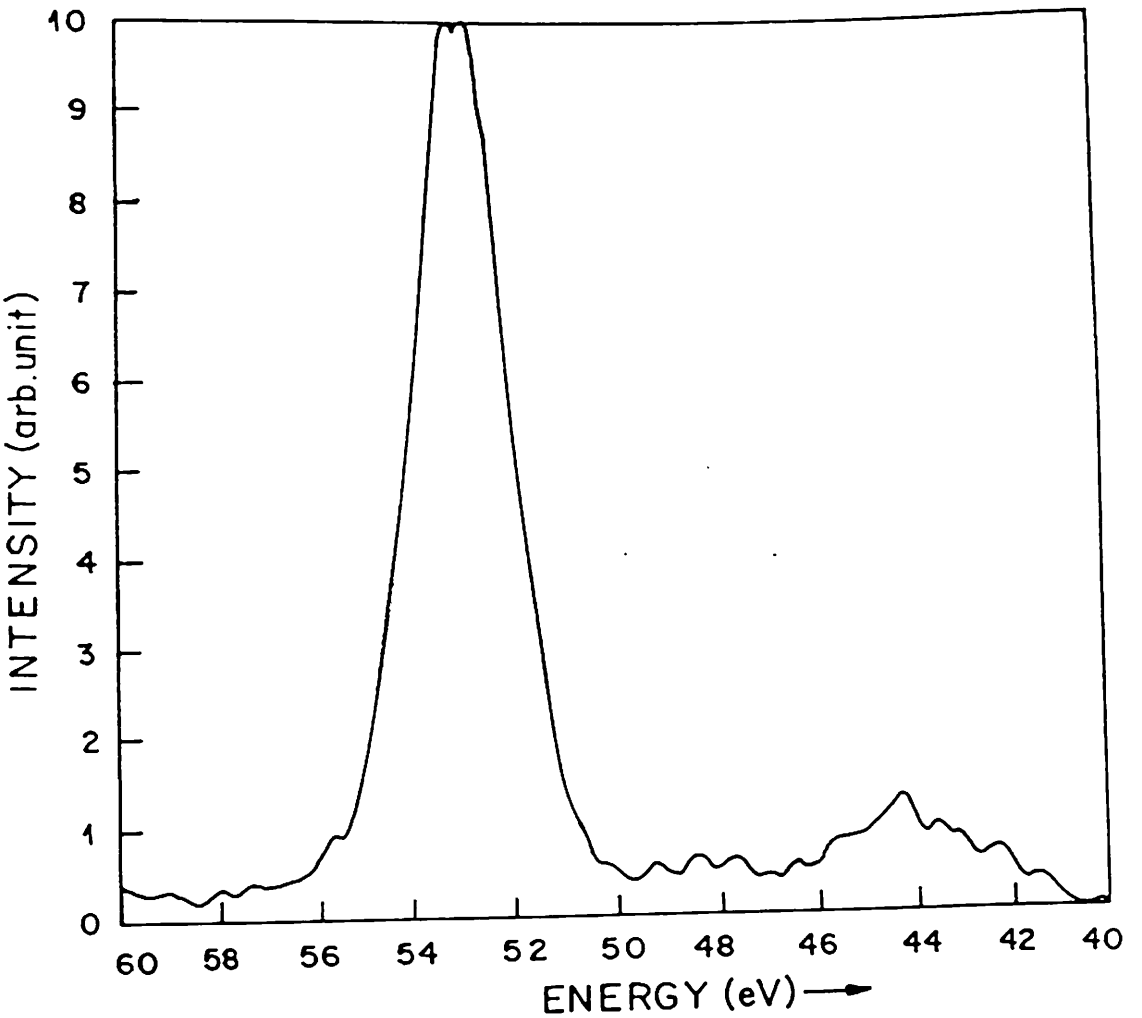

Fig. 4b.10. (c) Finger print of Mg 2p peak in the XPS spectrum of annealed MgO film.

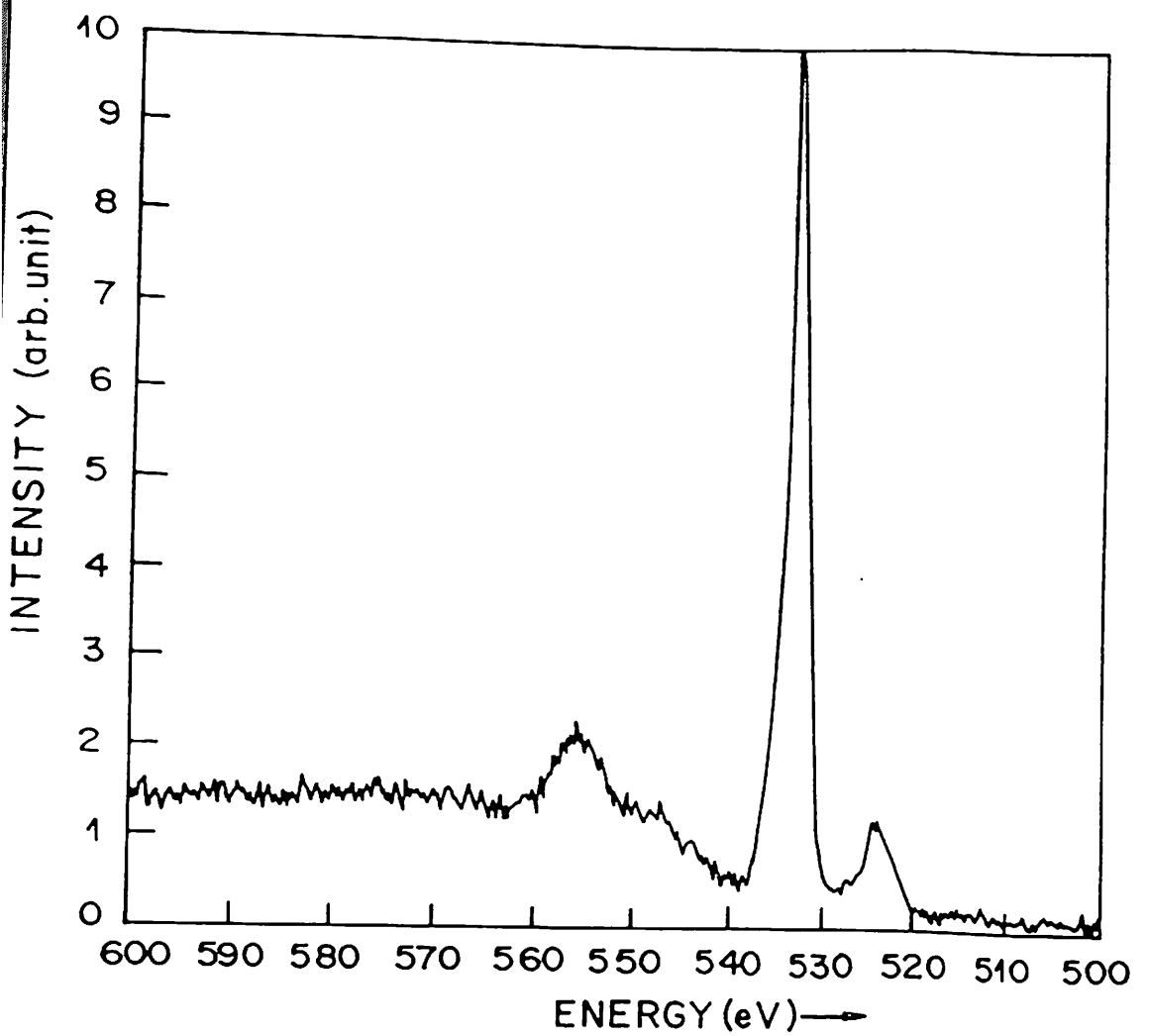

Fig. 4b.10. (d) Finger print of O 1s peak in the XPS spectrum of annealed MgO film.

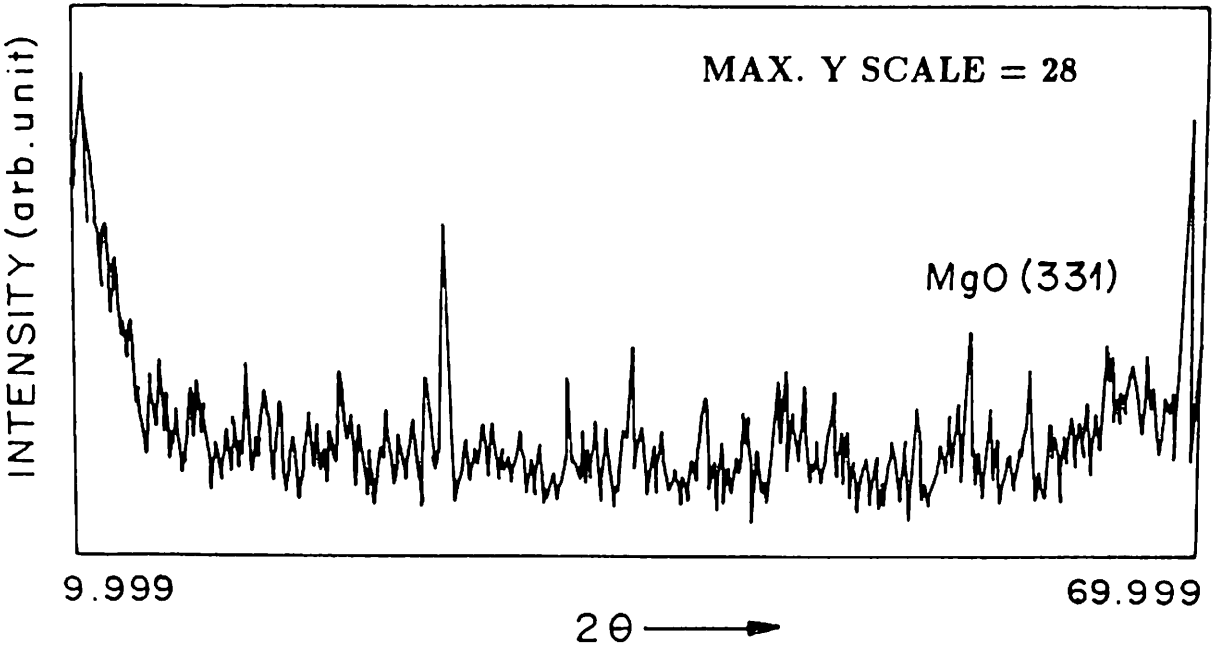

Fig. 4b.11. XRD spectrum of the annealed MgO film on Si (100) substrate.

ıffer layer occurs at high temperature which is necessary in high c film processing. As we describe the results obtained in the resent study, it will be seen that certain amount of success has een achieved in this respect.

From the AES results, it is seen that two types of impurity, C and S, are present in the $SrTiO_3$ film. While S remains only on the top surface of the film, C is seen to be present throughout the film thickness, which is detrimental to the film preparation of '123' compound on the buffered substrate. Now the origin of the two impurities can be envisaged to be due to the high-temperature processing rather than to the film deposition itself. This is based on the reasoning that if the vacuum environment or the source material were responsible for the observed impurities, then even the surface of the as deposited film should have indicated the presence of C and S. However this was not the case as seen in fig. 4b.1 (a). Thus, the only possibility for these impurities to be incorporated remains in the annealing process. The source of C can be attributed to any trace impurity present in the Ar gas feeder line to the sputter gun of the AES system. This is expected as the concentration of the impurity seems to be fairly constant with each sputter layer of the sample. In case of MgO, the problem of incorporation of foreign element has not arisen and except on the top surface of the MgO film, where small amount of C is

present, the film is perfectly clean as revealed by both XPS and AES. This cleanliness of MgO film also consolidates the apprehension of incorporation of C from Ar gas feeder line which was changed before the probing of MgO film. The depth profiling of both $SrTiO_3$ and MgO film confirm one important fact that, there is no Si diffusion inside the deposited thin film as a result of heat treatment. The result of the deepth profiling of $SrTiO_3$ film (fig. 4b.3) can be explained on the basis of the simple fact that the e-beam was focussed to a fine spot and that it was not swept across the sample during deposition. Both these aspects tend to melt the material only in one spot, thus resulting in a non-stoichiometric vapor stream. Also, the local variation in the composition of the sintered pellet will be reflected in the composition variation in the final film deposited on the esubstarte. Further, the condition of the e-beam used can result in partial fragmentation of the material with the high-vapor pressure component evaporating favorably through the deposition time. However, such a situation seems to be favorable, as the initial Sr layer perhaps helps in inhibiting the outdiffusion of Si from the substrate. This is predicted from the results of other workers[1], who have deposited $SrTiO_3$ on Si after depositing an initial SrO layer on it. The result of the depth profiling of $SrTiO_3$ can be approximated to a simple structure comprising of an initial layer of SrO_y and then one of Ti deficient $SrTiO_3$ with the possible

presence of some $SrTiO_3$. This leads us to cojecture that the e-beam evaporation results in the fragmentation of the pellet with Sr and/or SrO_y being predominantly evaporated. In comparison the result of the depth profiling of MgO film is less complicated. It shows (fig. 4b.9) that Mg and O remains constant in amount throughout the film and quntitative analysis of both XPS and AES show that the components (Mg and O) of the film are in the same ration in the film within the experimental error.

The results of the simultaneous HIBS and ERDA of $SrTiO_3$ films also show that there is no Si diffusion inside the film and the film is Sr rich. It also shows drastic reduction of O from the film at very high temperature. This may be due to the fact that the resulting film is not fully stoichiometric $SrTiO_3$ and therefore all the oxygen atoms inside it are not strongly bonded. HIBS also shows a Sr diffusion as a result of high temperature annealing at 900°C. This result is in agreement with the observation of other workers[2].

XRD of $SrTiO_3$ reveals the formation of (211) peak of $SrTiO_3$ as a result of annealing. This is in agreement with the result obtained by other workers[1,3,4], who have deposited $SrTiO_3$ on Si using a focussed e-beam and subsequently annealed the sample in O_2 at 800°C. The result of XRD also confirms the fact that there

is definitely a $SrTiO_3$ phase present in the otherwise non-stoichiometric film. The XRD of MgO also shows the presence of a crystallographic orientation in the annealed MgO film.

Therefore, it is observed from the above results that buffer layers of good integrity have been deposited on Si for subsequent YBCO film deposition. But there are still lot to be improved about these films. In case of $SrTiO_3$ film, although there is no Si diffusion inside the film at high temperature, the stoichiometry of the buffer layer is not correct, which is essential for YBCO film deposition. For getting stoichiometric film, instead of focussing the e-beam at a point, perhaps we need to raster the beam over the $SrTiO_3$ target which was not easily possible in the present case. In case of MgO, stoichiometric MgO film has been deposited without any Si diffusion inside the film at high temperature. But the favorable crystallographic orientation for YBCO film has not been attained, which might be achieved by controlling the substarte temperature during deposition and also by controlling the annealing parameters after deposition.

References

1. H. Mori and H. Ishiwara, *Jpn. J. Appl. Phys.*, **30**, L1415 (1991).

2. Yong Liang, J. Bruce Rothman, Down A. Bonniel, *J. Vac. Sci. Technol.*, **A12**, 2276 (1994).

3. Neung-Ho Cho, Seung-Hee Nam and Ho-Gi Kim, *J. Vac. Sci. Technol.*, **A10**, 87 (1992).

4. Seun-Hee Nam and Ho-Gi Kim, *J. Appl. Phys.*, **72**, 2895 (1992).

CHAPTER IV C

CONCLUSION & FUTURE SCOPE

4c.1. Summary and Conclusion

The present thesis has mainly dealt with the study of irradiation effects on the various properties of the $YBa_2Cu_3O_7$ high Tc superconductor. The samples used in the experiments were the bulk sintered pellets of YBCO. Few experiments have been done on thin films. An attempt has been made to prepare buffered Si substrates for synthesis of the thin film material. This aspect has been addressed by the preparation of two types of oxide thin films as buffer layers on Si wafer. The specific oxides used were : $SrTiO_3$ and MgO. The integrity of the buffer layer on Si was established by heat treatment of the system to as high temperature as 900°C and then subsequent evaluation by surface sensitive techniques of AES, XPS and the high energy backscattering techniques like Rutherford Backscattering (RBS) and Elastic Recoil Analysis (ERDA). In general all the samples were analysed routinely by X-ray diffraction and scanning elctron microscopy.

The main thrust in the present thesis is on the after effects of high energy heavy ion irradiation on the properties of the '123' material. For this the energetic beam were derived from tandem type Van de Graff accelerator with the energy in the range of 75-100 MeV. The chosen projectiles were ^{16}O, ^{58}Ni and ^{127}I. The choice of projectiles was mainly to see the effect of the varying energy loss parameter on the properties of the material and also to

establish the condition of the threshold electronic loss parameter. Material properties were compared both before and after irradiation.

Thus, based on the abridged details of the various experiments done and the results presented in the thesis, following salient conclusions arise. These are indicative of a few of interesting problems that can be taken up for future research in either understanding the basic defect mechanism or even in applied research to generate planar devices.

1) The effect of 75 MeV ^{16}O irradiation (electronic energy loss= 0.17 keV/Å) does not seem to degrade the superconducting properties of '123' system.

2) The effect of 75 MeV ^{58}Ni irradiation (electronic energy loss = 1.45 keV/Å) seems to have the point of inflection with regard to its deleterious effects on the properties.

This is borne out by the fact that when the irradiation is done at room temperature the property does not deteriorate upto a certain dose (~10^{13}/cm^2). Beyond this dose the system shows a monotonous degradation as evidenced by the results of R vs. dose measurements and the Tc measurement on the sample irradiated at the highest dose (1 x 10^{14}/cm^2).

3) To further investigate the aspect of the effect of increasing energy loss the next projectile was ^{127}I and irradiation by it leads us to conclude specifically that the results of ^{58}Ni are correct. In this situation a dose of $\sim 10^{11}/cm^2$ on the sample increases the normal state resistance and yields a decrease in the Tc by about 3K. Unfortunately, irradiation with dose value lower than $\sim 10^{11}/cm^2$ in this case could not be carried out because of unavailability of very low beam current.

4) From all the irradiation experiments it becomes clear that the sample temperature during irradiation has definite involvement in the after effect of irradiation. It turns out in each cases of irradiation at low temperature on the bulk YBCO samples, that normal state conductivity has been improved, most probably by vacancy ordering. This effect has not been observed in case of thin films because they are less prone to the inherent defects and leaves less scope of improvement.

5) Thin film irradiation results suggest that the total effect of irradiation in thin film not only depends on projectile-film combination but also depends on the film-substarte combination.

4c.2 Scope for Future Work

In a nutshell the present thesis has dealt with the study of high energy heavy ion irradiation effects on the properties of high Tc $YBa_2Cu_3O_{7-x}$ superconductor. Variety of techniques have been used in the study of irradiation effects. It is worth mentioning that the most important aspects addressed are the following :

1) Systematic variation of the energy loss parameter by choosing proper ion species.

2) Study of electrical properties on the samples at two distinct temperatures while using any projectile.

3) Study of integrity of buffer layers on Si substrate for large area deposition of HTSC films.

4) Feasibility of ion beam lithography for fabrication of planar devices.

It is ascertained that all these four above mentioned aspects need to be probed further in an extensive and systematic way.

While the present project gives a definite direction to the first problem yet the investigation with regard to change of energy loss parameter in a wide range will be necessary. Presently chosen

ions were ^{16}O, ^{58}Ni and ^{127}I. It will be worth while to include heavier projectiles like ^{181}Ta. At this point one should be careful about the fact that increasing energy of the projectile does not necessarily mean increased electronic energy loss value, because this parameter has a maxima at certain energy value, above which it decreases gradually. For example, in case of oxygen, this maxima occurs at ~ 9 Mev and this energy loss at which the maxima appears increases for heavier projectiles. Therefore, to get higher energy loss after a certain limit for a given projectile, one has to go for heavier projectiles. The restriction of a single ion and changing the energy is not considered to be advantageous as the range in variation of energy loss is not much in the available range of energies. It should be mentioned at this point that, insitu characterization of superconducting samples during irradiation, e.g., R vs. T measurement, a.c. susceptibility measurement etc., which were not possible in the present study, can be taken up for future investigation. These studies are important because exposure of suuperconducting oxides to atmosphere from high vacuum might change their behavior to some extent.

With regard to aspect number 2, a definite goal seems to be defined with regard to associating the role of lattice vibration in conjunction with electronic loss parameter since it is mentioned

in the earlier chapter that the possible mechanism by which electronic loss inflicts structural modification in materials is the coherent aspect of this energy loss. To further elucidate on this it will be worthwhile to study HTSC samples at more target temperatures, viz., 4.2 k, 77 K, ice point and at high temperature.

Aspect 3 is also important from the point of view of application of HTSC in microelectronics area. To this effect successful epi growth of perovskite oxides will be of great help but on large area wafers. This essentially means that techniques such as sputtering or e-beam alone are suitable. It must be pointed out here that, due to unavailability of substrate heating arrangement to high temperature, it was not possible to deposit Mgo or $SrTi0_3$ films at substrate temperature higher than 200°C. Therefore, the effect of variation of substrate temperature on the behavior of the films, specially on their crystallographic orientation, can be taken up as a subject of future investigation.

Aspect 4 is feasible once aspect 1 is established, i.e., a value for threshold S_e at room temperature. Once this gets established, then flood exposure ion beam lithography can be easily achieved by irradiation through e-beam generated metal masks.

APPENDIX I

A BRIEF INTRODUCTION TO TRIM

Introduction

When energetic particles traverse through matter they are slowed down in matter (target) by momentum transfer to target atoms and by exciting the electronic system of the target. The first process is known as 'nuclear stopping' and the latter process is called 'electronic stopping'. The nuclear stopping can be understood by studying the ion-atom repulsive forces and the binary collissions. The electronic stopping is a more complex phenomenon. The estimation of these two losses of the energetic particles inside the matter is very much essential in order to know the trajectories of the ions inside the matter, their total ranges in the target and also to know the distributions of the different types of the defects created inside the matter by the energetic particles. These informations can be obtained either by analytical calculations or by using Monte Carlo simulation methods.

Before describing the simulation process the analytical formulae will be summarised first.

Analytical Formulae

In analytical methods first the binary collission between the

projectile and a target atom is considered and then the formulae are extended for a whole lattice. The most important task for these calculations is to evaluate the interaction potentials. Although there are some negative contribution to the potential in the form of exchange and correlation energies and the attractive potential energy due to the potential well of other neclei, the final result is always a positive potential (repulsive) and considering the screening of the electrons in the target atom, this potential is less than the value of the Coulomb potential $Z_1Z_2e^2/r$. It is formally described by "Coulomb Term" $Z_1Z_2e^2/r$, a "screening factor" ϕ (r/a) $[0 < \phi < 1]$ and a "screening length" 'a'. Fitting the result for several hundred pairs of atoms, a universal screening function is obtained as

$$\Phi_u = 0.1818\exp(-3.2\frac{r}{a}) + 0.5099\exp(0.9423\frac{r}{a}) + 0.2802\exp(-0.429\frac{r}{a}) + 0.02817\exp(-0.2016\frac{r}{a})$$

and the value of 'a' is given by

$$a = \frac{0.8854a_0}{Z_1 23 + Z_2 23}, \quad a_0 = 0.529\ \mathring{A} \quad (Bohr\ radius)$$

Gross deviation can occur for ionic crystal because of rearrangement of electronic distribution or forming of chemical bonds etc.

After fixing the interatomic potential as

$$V = \frac{Z_1 Z_2 e^2}{r} \Phi(\frac{r}{a})$$

the scattering angle is calculated as a function of energy in the C.M. system and impact parameter p. It is standard practice to express this energy and impact parameter as dimensionless parameters as following.

All the lengths are expressed in terms of screening length 'a', i.e., x = r/a and b = p/a and energy is expressed in units of $Z_1Z_2e^2/a$ and it becomes a dimensionless quantity.

$$\varepsilon = \frac{E_{C.M.}}{(Z_1 Z_2 e^2/a)} = \left(\frac{E}{1 + \frac{M_1}{M_2}}\right) / \left(\frac{Z_1 Z_2 e^2}{a}\right)$$

The scattering angle θ and the energy T given to the target atom in an atomic collission are then given by,

$$\Theta(\varepsilon, b) = \pi - 2 \int_{x_0}^{\infty} \frac{d(\frac{b}{x})}{\sqrt{1 - \frac{\Phi(x)}{x\varepsilon} - (\frac{b}{x})^2}}$$

where x_0 is the distance of closest approach and

$$T = \gamma E \sin^2(\frac{\theta}{2}), \text{ where } \gamma = \frac{4M_1M_2}{(M_1+M_2)^2}$$

Using these formulae and expressing E in the expression of T in terms of ε and removing the constant parameters like Z_j, M_j etc., a universal stopping cross section is obtained as,

$$S_n^*(\varepsilon) = \int_0^\infty \sin^2 \frac{\theta(\varepsilon, b)}{2} d(b^2)$$

For insulator target no electrons or holes are available to screen the ionic charges and hence long range coulomb forces are acting far beyond the nearest neighbours in the lattice. The nuclear stopping cross section in this case is given by

$$S_n^* = S_{n_1}^* + \frac{\Phi_\infty^2}{4\varepsilon} ln \frac{T_s}{\hbar\omega}$$

where the first term S_{n1}^* is the usual nuclear stopping term for binary collission.

$$\Phi_\infty = \lim_{x \to \infty} \Phi(x)$$

and T_s is the energy transferred. Here the bound state of the lattice is considered, where the laws of quantum mechanics would not allow energy transfer to these atoms which are less than $\hbar\omega$ i.e., a few 10^{-2} eV.

The damage cross section can be written as,

$$S_d^* = \varepsilon \int_0^{b_d(E_d)} \sin^2 \frac{\theta}{2}\, d(b^2)$$

E_d is defined as kinetic energy necessary for parmanently removing an atom or ion from its lattice site, beyond the region of spontaneous recombination. For ceramic materials E_d is of the order of 30-90 eV. Energies of this magnitude are transferred only in close binary encounters with impact parameter $b \leq b_d$ where $T(b_d) = E_d$. Typically $b_d \leq 10$, $p_d \leq 1$Å. So damage production is very little affected by ionic character of the projectile or target.

Electronic Stopping

Historically the electronic stopping was calculated for point charges, such as protons. The main feature of electronic stopping is that the lower the ion velocity becomes, the lesser are the stopping power contributions of high density regions (i.e., the inner shell of the target atoms). This means at low velocities only the outer shells or even just valence or conduction electrons are responsible for the electronic stopping.

For practical application requiring high precision, the formula used for electronic stopping of point charges is

$$\frac{1}{S_e} = \frac{1}{S_{LO}} + \frac{1}{S_{Hi}}, \quad S_{LO} = C_0\sqrt{E}, \quad S_{Hi} = \frac{C_1}{E}\log\left(\frac{C_2}{E} + C_3 E\right)$$

For heavy ions the electronic stopping is given by,

$$S_e(v) = Z_{eff}^2(v)\, S_p(v)$$

where Z_{eff}(v)=effective charge of the projectile for scattering target electrons and S_p(v) = stopping power for protons at the same velocity v as the heavy ions.

Z_{eff} can be taken as the average charge as seen by the electrons of the target and hence the value of Z_{eff} is expected to fall within the boundaries, i.e., $Z^* < Z_{eff} < Z$, where Z is the nuclear charge of the ion (responsible for electron scattering close to the ion nucleus) and Z^* is the charge state of the ion (responsible for electron scattering at large seperation from the nucleus). By appropriate averaging over all possible encounters

$$Z_{eff} = Z^* + 0.05(Z - Z^*)\left(\frac{v_0}{v_F}\right)^2 \ln\left(1 + \left(\frac{2\Lambda v_F}{a_0 v_0}\right)^2\right)$$

where v_F denotes the Fermi velocity of the target material and v_0 is the Bohr velocity (usually $v_F \cong v_0$).

Monte carlo calculations

The advantage of Monte Carlo method over analytical methods are : It allows the explicit consideration of surfaces and interfaces, the rigorous treatment of elastic scattering with any number of different target atoms in multiatomic targets, and finally it yields the full distribution functions rather than a few moments of such distributions. It is also easy to include recoil cascades which in turn yields all the information on sputtering, ballistic mixing and defect production.

The major limitation of this method is that it is inherently a computer time consuming procedure. This problem has been alleviated by using effective programs.

Physical Assumptions Used In The TRIM Code

The TRIM (Transport and Range of Ions in Matter) program, as other simulation programs, follows a large number of individual ion histories in a target. Each history begins with a given position, direction and energy of the ion. The ion is then followed through a sequence of collisions with the target atoms with the assumption of straight free flight path between collisions. The particle's energy is reduced after each free flight path by the amount of electronic energy loss and then (after the collision) by the so called nuclear energy loss which is the result of transferring momentum to the target atom in the collission. Each ion's history is terminated either when the enrgy drops below a pre-specified value or when the particle has moved out of the front or rear surface of the target. The target is considered as amorphous with atoms at random locations which means that any directional properties of the crystal lattice are ignored. Thus it actually describes the implantation into amorphous materials, and neglects channeling effects which may become important at low-dose and low-energy implants where

fraction of the ions may get steered through open passages (plannar or axial) along certain directions in crystalline structures. At high energies, the acceptance angles become small but channeling nevertheless persists.

Monte Carlo simulations are based on the binary collission model. The assumption breaks down at very low energies where deflection may occur even at large seperations from the target nucleus. In this case the ion may interact with more than one target atom at the same time and errors may be introduced by treating such collissions seperately with very small free flight paths in between. Nevertheless the TRIM results yield quite satisfactory agreement with experimental data.

At high energies the TRIM code is quite efficient as it takes into account the natural increase in free flight paths; a particle's free flight path between noticable collisions is long at high energies and is steadily reduced in the course of slowing down. The TRIM program contains provisions for dealing with very high energies and includes relativistic electronic energy loss and straggling for higher energies. For ion energies below 1 MeV/a.m.u., the electronic straggling however, was found to be of little importance for the projected range profiles and is usually neglected. Some kind of electronic straggling at low energies can be introduced by the

built in option of treating the electronic energy loss as dependent on the distance of closest approach in the individual collissions.

The presently described computer program is available for targets of several layers of different composition. The program provides output for one and two dimensional distributions of ion range and energy deposition, as well as the reflection and transmission characteristics of planar targets.

Atomic Collissions

The scattering of the ion by the target atoms is not only an important process of slowing down the incident ion by momentum transfer to the target atoms, but also determines the geometry of the particle trajectories. In the TRIM program a simple analytic expression of high accuracy is used which has often been named the "magic formula". This formula is based on very simple geometric considerations and gives the scattering angle θ in C.M. system as

$$\cos\frac{\theta}{2} = \frac{p+\rho+\delta}{\rho+r_0}$$

where δ is an empirically fitted correction term.

In TRIM program, the appropriate realistic repulsive potential used is

$$V = \frac{Z_1 Z_2 e^2}{r} \Phi(\frac{r}{a})$$

ϕ is the screening function and given by the universal formula as given earlier. This form of ϕ is chosen because, first of all, it is based on a number of several hundred individually calculated biatomic potentials, secondly, it compared well to more than hundred experimentally determined poetentials and thirdly and finally, quite good agreement between range predictions and experiments could be obtained when using this kind of potentials.

For the sake of computer efficiency, the universal screening function and magic formula are not used at energies $E >> Z_1 Z_2 e^2/a$. At such high enrgies all noticable deflections and energy transfers take place at rather small impact parameters where the potential is very close to an unscreened coulomb potential. In this case computer time is saved by using a potential which varies from coulombic through an $r^{-1.5}$ to r^{-2} potential for which the deflection angle and transferred energies can be obtained in a simple analytic way, providing about the same precision in the high energy regime as the magic formula does in the low energy region.

From the known scattering angle θ in the c.m system, the deflection angle ψ of the ions trajectories in the laboratory system is obtained by,

$$\Psi = \arctan \frac{\sin \theta}{\cos \theta + \frac{M_1}{M_2}}$$

For determining the new ion direction in three dimensional space we need - besides of the polar angle ψ - another (azimuthal) angle ϕ which is selected randomly between 0 and 2π for amorphous materials. The energy transferred to the target atom in the collision is given by,

$$T = \frac{4M_1M_2}{(M_1 + M_2)^2} E \sin^2 \frac{\theta}{2}$$

Simple estimates of energy deposition

In the first version TRIM program, a rough analytical estimate is performed in order to obtain such results as (i) how much of the recoil energy is going into ionization processes (important in damage in insulators, particularly ionic crystals and

organic substances) and (ii) how much of energy is going into collisional damage (no. of vacancies produced in the cascade) and (iii) how much of the recoil energy is absorbed in sub-threshold collisions in the cascade where the energy is transferred in phonons (heat).

For a first order estimate, after determining the energy available for nuclear damage E_υ, the no. of displaced atoms (produced vacancies) is calculated by the well known "modified Kinchin-Pease" model.

$$\nu = 1 \qquad \text{if} \qquad E_d < E_\nu < 2.5\,E_d$$

$$\nu = 0.8\frac{E_\nu}{2E_d} \qquad \text{if} \qquad E_\nu \geq 2.5E_d$$

As a result of these calculations, the ionization caused by recoiling atoms (in eV) and the number of vacancies produced are provided as standard output of the TRIM program.

Using these simple estimates or performing more rigorous studies or recoil tarnsport with the extended TRIM-CASC code, it was often observed that the cascading recoils (particularly if they are lighter than the incident projectile) cause more ionization in the target than the incident ions themselves.

Free flight path and impact parameter selection

The TRIM program saves computer time by using a concept of extending the free flight path between collisions at higher energies. This is a very special feature of TRIM code and requires some careful considerations about the deflection angles and transferred energies. For high energy incident particle the total cross section for interaction with the target atoms is very small, while at lower energies the cross sections increase and the mean free flight path decreases accordingly. The connection between the cross section and the mean free flight path L is given by the following expression

$$\pi p_{max}^2 L = N^{-1}$$

where N is the atomic density in the target.

For each collision in the TRIM code the impact parameter and the azimuth angle is obtained from random numbers R_n ($0 < R_n < 1$) according to

$$p = \sqrt{R_n}\, p_{max}, \quad \Phi = R_{n+1} - 2\pi$$

If at very high energies the mean free flight path L becomes extremely large, an independent check is performed such that the electronic energy loss over that free flight path does not exceed five percent of the energy. If that would be the case , the ion's free flight path would be reduced accordingly.

Electronic energy loss

TRIM program treats electronic energy loss as independent of nuclear energy loss. The reasons are of two folds : The pragmatic reason is the increased computer efficiency mainly through the priviously discussed concept of extended free flight paths. The other more important reason is the lack of satisfactory theoritical descriptions or experimental data of the impact parameter dependence of the electronic energy loss in the solids.

The electronic energy loss is simply obtained by,

$$\Delta E_e = L\,N\,S_e(E)$$

where $S_e(E)$ is the electronic stopping cross section. For non-elementary target Bragg rule is used which states that every target atom species is contributing to the stopping power proportional to its abundance.

Layered target structures, surfaces

TRIM code is set up to correctly treat various layers of different materials as well as front and rare surfaces. The way to handle this is straight foroward : after the ion (recoil) has moved its mean free flight path along its new direction into the position x, y, z, two random numbers are called to determine the impact parameter and azimuth angle ϕ; from these known data the position of the next target atom is calculated and checked, whether it is located inside one of the layers or infront or behind the target. In the last case the target atom is encountered and the ion (or recoil) is moving on with no deflection or nuclear energy loss, becoming a candidate for reflected or transmitted ion (or a sputtered particle if it is a recoil atom). Otherwise if the target layer is determined, a target atom of this layer is selected as the next collision partner.

Selection of target atoms in multiatomic materials

The selection of target atoms is performed in the TRIM code by ramdom numbers, assuming the probabilities of encounters being proportional to their stoichiometric abumdance, i.e., oxygen

is encountered twice as frequent as Si in an SiO_2 target. This is by no means trivial and actually it was a matter of some concern whether the lighter atom should have smaller cross section than heavier ones, thus favouring collisions with the heavier components beyond their stoichiometric fraction. The basic idea is to let the potentials take care of this situation without imposing any arbitrary cut offs, such as smaller p_{max} for lighter atoms as compared to heavier ones. This means that sufficiently large impact parameters for all target atoms are allowed, but it is expected, for example, at a given large impact parameter, that a light target atom with a lower interaction potential will cause only minimal deflection and energy tarnsfer as compared to a heavy component. This concept is also supported by the fact that the atomic radii and also the range of interactions as calculated from overlapping solid state HFS atoms, are by no means smaller for light atoms than for heavy ones. The difference between light and heavy target atoms turns out to lie in the magnitude of the potential, but not in the range of interaction.

APPENDIX II

PUBLICATIONS

LIST OF PUBLICATIONS

1. An analysis of electron beam evaporation of $SrTiO_3$ on Si substrates, **Sanjit K. Das**, P.K.Ashwini Kumar and S.K.Sarkar, *J.Phys. : Condens. Matter* , 6, L445 (1994).

2. Effect of sample temperature on the irradiation effects of energetic particles in the YBCO system, **S.K.Das**, P.K.Ashwini Kumar and S.K.Sarkar, D. Kanjilal and L.Senapati, *Vacuum* , **46**, 227 (1995).

Papers presented at National Symposia :

1. High energy (MeV) irradiation effects on high Tc superconducting materials, **Sanjit K. Das**, P.K.Ashwini Kumar, *National Symposium of Physics and Chemistry of High Temp. Superconductors* (1991).

2. Effect of ^{58}Ni irradiation on the resistivity and surface microstructure of $YBa_2Cu_3O_7$, **Sanjit K. Das**, P.K.Ashwini Kumar, S.K.Sarkar, *Ninth National Symposium On Radiation Physics* (1991).

3. Synthesis of thick superconducting films of $YBa_2Cu_3O_{7-x}$ by spin technique, P.K.Ashwini Kumar, **S.K.Das**, S.K.Sarkar, *Third Annual General Meeting of the Material Research Society of India* (1992).

4. Preparation and analysis of $SrTiO_3$ thin films on Si substrates, **Sanjit K. Das**, P.K.Ashwini Kumar & S.K.Sarkar, *Indian Science Congress* (1993).

Papers accepted in International Symposia :

1. Normal state resistivity variation of superconducting $YBa_2Cu_3O_{7-x}$ bulk with dose due to Ni and O ions irradiation at 75 MeV, **Sanjit K. Das**, P. K. Ashwini Kumar and S. K. Sarkar, L.senapati and D. Kanjilal, *Twelfth International Conference on the Application of Accelerators in Research and Industry* , Nov. 2–5, 1992,Denton, Texas, USA [Abstract].

2. Effect of electronic energy loss on the surface microstructure and crystallinity of the heavy ion irradiated superconducting $YBa_2Cu_3O_{7-x}$' P.K. Ashwini Kumar, **Sanjit K. Das**, S. K. Sarkar, D. K. Suri, K. D. Kundra, L. Senapati and D. Kanjilal, *Twelfth International Conference on the Application of Accelerators in Research and Industry* , Nov. 2–5, 1992, Denton, Texas, USA [Abstract].

3. Study of annealing behaviour of $SrTiO_3$ thin films by simultaneous HIBS and ERDA, **Sanjit K. Das**, P. K. Ashwini Kumar, S. K. Sarkar, D. Kabiraj and D. K. Avasthi, *The Seventh International Conference on Radiation Effects in Insulators* , Sep. 6–10, 1993, Nagoya, Japan [Abstract].

4. Effect of 75 MeV ^{16}O and ^{58}Ni irradiation on the normal state resistivity and crystallinity of bulk $YBa_2Cu_3O_{7-x}$, **Sanjit K. Das**, P. K. Ashwini Kumar, S. K. Sarkar, D. Kanjilal, *Third European Symposium RADECS'95* , Sept. 18–22, 1995, Areachon, France.

ergamon

Vacuum/volume 46/number 3/pages 227 to 228/1995

0042-207X/95 $9.50+.00

0042-207X(94)00050-6

ct of sample temperature on the irradiation effects nergetic particles in the YBCO system

P K Ashwini Kumar and S K Sarkar, *National Physical Laboratory, New Delhi 110012, India*

al and L Senapati, *Nuclear Science Center, New Delhi 110067, India*

for publication 8 June 1994

s at 75 MeV incident energy have been used to study the irradiation effects on the normal state nce variation with fluence. The studies conducted include the measurement of resistance variation ose due to the ion used. The samples were the bulk sintered pellets of $YBa_2Cu_3O_{7-x}$ maintained at l temperature (T ~ 300 K) and low temperature (T ~ 100 K). In the case of a sample irradiated at normal rature there is a continuous decrease in resistance with dose, while in the other case there is a minimal e in the resistance vs fluence curve. These experimental results reveal that the sample temperature has ial effect on the damage mechanism.

tion

covery of superconductivity above about 50 K in some cuprates[1] led to a spurt[2-4] in research into these materials. fter, attempts were made to see the effects of energetic ns on the normal and superconducting properties. With to this aspect, it has been well established[5] that whenever traverses through matter it loses its energy via two pro- namely, the first one by the ion–target electron inter- called the electronic energy loss (Se), and the other one on–target atom interaction, called the nuclear energy loss ith regard to the particular case of ionic irradiations on nductor like $YBa_2Cu_3O_7$, it has been shown that there is hold value for Se, above which the material undergoes a change in the properties, i.e. the normal state resistance crease very sharply, the ion on its passage through the al leaves a permanent track and, also, the superconductor a sudden deterioration in its properties. While most of the nents reported to date have focused attention on the ion– interaction, with the sample at normal temperature or at mperature, the present paper describes the results of work with ^{16}O on a $YBa_2Cu_3O_7$ bulk sample held at ambient rature and also at low temperature (~ 100 K) but greater ne T_c. The results are explained on the basis of the effect of e temperature on the role of ion irradiation with regard to ge creation.

imental

samples of $YBa_2Cu_3O_{7-x}$ were made by the standard solid reaction technique[6]. The starting materials were Y_2O_3, $BaCO_3$ and CuO. The materials of proper stoichiometry were thoroughly mixed, ground and pelletised to circular discs measuring about 25 mm in diameter. The calcination was done at 900 C and the sintering was done at 930 C. The pellets were checked to be superconducting at about 90 K. For irradiation experiments the samples were cut into rectangular bars measuring $10 \times 3 \times 2$ mm^3. The samples were irradiated by 75 MeV oxygen beam from a 16 MV Tandem Accelerator (PELLETRON) at the *Nuclear Science Center*. The samples mounted on the glass epoxy were fixed on a cold finger cooled by liquid nitrogen. The glass epoxy mount ensured that the temperature of the materia was above the transition temperature. The vacuum in the chamber during irradiation was maintained at about 5×10^{-6} mbar. A standard four probe technique using constant current source and nanovoltmeter was employed to measure the variation of resistance with fluence *in situ*. The data were taken at about 5 min after stopping the beam, so that the short lived transient effects were equilibrated. The ion fluence was varied between 1×10^{11} cm^{-2} and 1×10^{15} cm^{-2}. The fluence of the beam was determined by counting the number of particles bombarding the sample using a current integrator and a counter. The secondary electrons coming out of the sample were suppressed by an electrostatic suppressor.

Results and discussions

Figures 1 and 2 show the variation of normalised resistance (R/R_0) with dose for the sample kept at ambient temperature and at low temperature, respectively. In both the cases the resistance has been decreased from its initial value as a result of irradiation. However, the striking difference between the two curves are

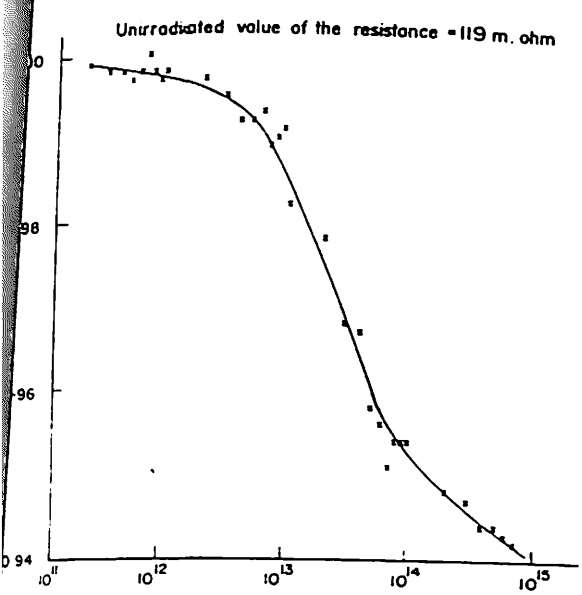

1. Variation of normalised resistance with fluence of 75 MeV for target at ambient temperature.

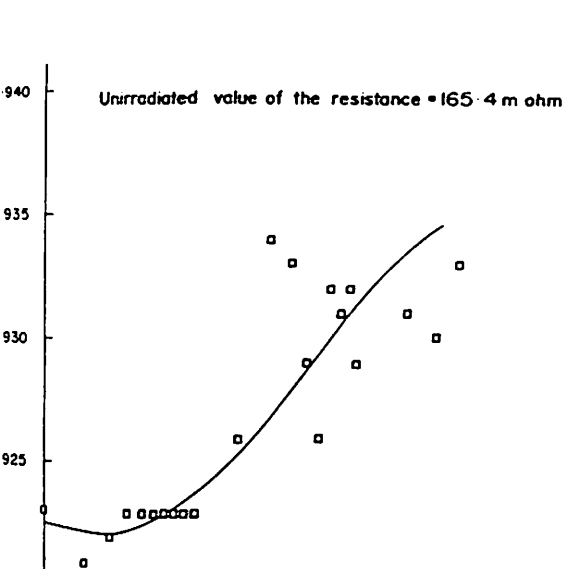

2. Variation of normalised resistance with fluence of 75 MeV at low temperature.

for low temperature irradiation the resistance shows a slight trend of increase at higher doses, while for room temperature irradiation the nature of the resistance wrt fluence shows an initial flat region at lower doses, followed by a gradual decrease at higher doses;

the normalised change in resistance ($\Delta R/R_{unirr}$) is much more in the case of low temperature irradiation than the case at room temperature irradiation (at 1×10^{12} cm^{-2} fluence, for low temperature irradiation $\Delta R/R_{unirr} \approx -0.077$ and at room temperature irradiation $\Delta R/R_{unirr} \approx -0.002$).

rder to explain the decrease in resistance from its initial s a result of irradiation, one must remember the fact that although the projectile, i.e. O ions, interacts with all the atoms in the target, namely Y, Ba, Cu and O, during its passage, the probability of O ions getting displaced is highest because O is the lightest atom amongst the others and, also, they are loosely bound in the lattice compared to the other atoms. Since it is believed that an ordered arrangement of oxygen vacancy is crucial for even normal state metallic conductivity[8], then from the previous argument the decrease in resistance strongly suggests an improvement of the ordered arrangement of oxygen vacancy as the major effect of the oxygen irradiation in our $YBa_2Cu_3O_{7-x}$ bulk sample. Also, the possible incorporation of oxygen in the $YBa_2Cu_3O_{7-x}$ lattice at the end of the projectile's range might be a factor in reducing the resistance of the samples from its initial value. At this point, it is worthwhile to compare the nature of the two variations in R_n vs fluence at two temperatures. The larger value of $\Delta R/R_{unirr}$ for low temperature irradiation shows that there is a favorable situation for improving the vacancy ordering of the oxygen sites due to ion irradiation and at the same time freezing this situation, thus retaining the ordered vacancy state; this is not the case at room temperature irradiation, since a part of the ordered vacancy arrangement due to irradiation again gets disordered due to a larger amplitude of lattice vibration. Secondly, the change in resistance due to irradiation at low temperature shows a very marginal increase of R_n at higher fluences, leading to the creation of other types of defects (point defects and cascades etc.), which have a deteriorating effect on conductivity. From the nature of the two curves, it seems that up to a fluence of about 10^{14} cm^{-2} the vacancy ordering phenomenon prevails over the other types of effects. The result of the present experiment may be compared with that of the work on a thin film irradiated by 25 MeV ^{16}O ions at 100 K (ref 6). In the case of the thin film, the resistance of the irradiated sample is always more than the unirradiated value, while in the present case of the bulk sample it is always less. This anomaly seems to be due to the fact that bulk samples used in the present study may have more intrinsic imperfections compared to the thin film.

Acknowledgements

The authors are grateful to the Director, National Physical Laboratory and the Director, Nuclear Science Center, New Delhi for their continuous encouragement during the course of the work. One of us, SKD, is grateful to the Director, National Physical Laboratory, for the award of a senior research fellowship. The co-operation of the Pelletron accelerator crew is gratefully acknowledged.

References

[1] J G Bednorz and K A Muller, *Z Physik*, B64, 189 (1988).
[2] T Terai, T Masegi, T Takahashi, Y Enomoto and S Kubo, *Jpn. J Appl Phys*, 29, L2053 (1990).
[3] A D Marwick, G J Clark, Nucl Instrum Meth, B37/38, 910 (1989).
[4] D Bourgoult, S Boufford, M Toulmonde, D Groult, J Provost, F Studert, N Ngyuen and B Raveau, *Phys Rev*, B39, 6549 (1989).
[5] M Toulmonde, *Nucl Instrum Meth*, B19/20, 120 (1987).
[6] B Hensel, B Roas, S Henke, R Hopfengartner, M Lippert, J P Strobel, M Vildic, G Saemann Ischenko and S Klaumunzer, *Phys Rev*, 42, 4135 (1990).
[7] D Kanjilal, S Chopra, M M Narayanan, I S Iyer, V Jha, R Joshi and S K Dutta, *Nucl Instrum Meth*, A328, 97 (1993).
[8] G J Clark, A D Marwick, F Legoues, R B Laibowitz, R Koch and P Madakson, *Nucl Instrum Meth*, B32, 405 (1988).

J. Phys.: Condens. Matter 6 (1994) L445–L448. Printed in the UK

LETTER TO THE EDITOR

An analysis of electron beam evaporation of $SrTiO_3$ on Si substrates

Sanjit K Das, P K Ashwini Kumar and S K Sarkar

National Physical Laboratory, Dr K S Krishnan Road, New Delhi 110012, India

Received 6 June 1994

Abstract. Thin films have been prepared by electron beam evaporation of strontium titanate ($SrTiO_3$) on bare (111) p-type silicon substrate held at room temperature. The as deposited films were annealed at 700 °C in flowing oxygen to compensate for any loss of O from the sample. The as deposited and the annealed samples were analysed by Auger electron spectroscopy (AES). The AES analysis shows that there is no trace of Si present in the bulk of the film and the Si/film interface is fairly sharp. The results are discussed in the light of the usefulness of the e-beam deposition of $SrTiO_3$ for preparation of a buffer layer on an Si substrate for the deposition of high-T_c superconducting materials in thick- and thin-film form.

Ever since the discovery of the occurrence of a high transition temperature in some cuprates by Bednorz and Muller [1] there has been a spurt of research activity in ceramic superconductors. The system $YBa_2Cu_2O_7$ (YBCO) has been studied extensively both in bulk and film form (thin and thick). The films have been formed on a variety of substrates such as crystalline $SrTiO_3$ [2], MgO [3], $LaAlO_3$ [4], $LaGaO_3$ [5], YSZ [6] and bare and buffered Si [7,8]. Deposition of an $SrTiO_3$ thin film has been attempted recently by using magnetron sputtering [9] and pulsed laser deposition [10]. The aim has been to use the dielectric layer in the IC technology. The interest in the last type of substrate is that this is available in large dimensions and that once a YBCO superconductor can be synthesized on such materials, a revolutionary change can be brought about in the technological advantage of high-T_c ceramic. Attempts have been made to grow the YBCO films on buffered Si and some success has been achieved. In this context an attempt has been made to use $SrTiO_3$ film as a buffer layer on Si for preparing a thick film of YBCO. While the '123' film could be made by the spin on technique, the adhesion of these films has posed a serious problem with a resultant low conductivity of the sample. To understand this situation a preliminary study to analyse the $SrTiO_3$ thin film prepared by e-beam deposition was undertaken. Some of the salient features of the results are presented in this letter.

In the present study 0.8–1.0 Ω cm (111) p-type Si substrates were used. These were cleaned thoroughly by the standard RCA technique with a final dip in buffered HF. The wafers were loaded into the deposition system immediately after the cleaning step. The $SrTiO_3$ pellets required for the deposition were made from the powder, which was pelletized to circular discs of about 25 mm diameter. The pellets were sintered at 1600 °C for about 24 h. The deposition was done in the Varian VT 118A UHV system by e-beam evaporation. Before commencing the deposition the substrates were heated to about 200 °C for about 1 h and then allowed to cool down to room temperature. The base pressure was 2×10^{-8} mbar and the deposition pressure was 5×10^{-6} mbar. The thickness of the after the heating process.

sample was 1300 Å as measured by a surface profilometer and the rate of deposition was 1 Å s^{-1}. Some of the samples were annealed in flowing O_2 at 700 °C in a microprocessor controlled high-temperature furnace with a temperature stability of ±0.1 °C (Tempress Omega Junior-I). The AES spectra were taken of the as deposited and the annealed samples in a Varian surface analysis system equipped with a single-pass CMA and Ar sputter gun for depth profiling.

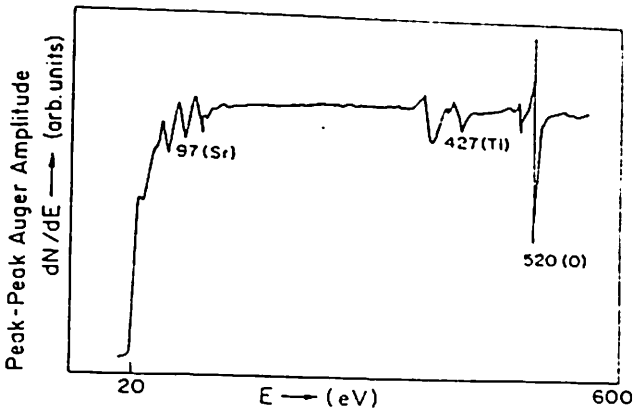

Figure 1. The Auger electron spectrum of the as deposited $SrTiO_3$ thin film.

Results of the AES studies of the as deposited and the annealed thin films are reported here. Figure 1 shows the Auger spectrum of the as deposited sample at the surface, which is indicative of the presence of all the components, i.e., Sr, Ti and O. It is observed that the surface of the film is free from any impurity, which clearly indicates that there is no incorporation of any foreign element from the vacuum chamber even though the deposition pressure was 5×10^{-6} mbar. The spectrum shown in figure 2(*a*) is that of the surface of the annealed film. In this case we see that besides the presence of the three constituents of the source material there are two additional elements (sulphur, 149 eV, and carbon, 270 eV) present in the sample. While this can be expected to be due to the environment during heat treatment yet it is surprising that C is present throughout the thickness of the film as seen in figure 2(*a*)–(*d*). Figure 2(*b*)–(*d*) represents the AES spectra of the annealed film with successive removal of the sample by Ar ions. Now the origin of the two impurities can be envisaged to be due to the high-temperature processing rather than to the film deposition itself. This is based on the reasoning that if the vacuum environment or the source material were responsible for the observed impurities, then even the surface of the as deposited film should have indicated the presence of C and S. However, this was not the case as seen in figure 1. Thus, the only possibility for these impurities to be incorporated remains in the annealing process. The presence of S is seen only in the top surface layer and is thus not of serious concern. On the other hand the presence of C is detrimental to the film preparation of '123' compound on the buffered substrate. The source of this C can be attributed to any trace impurity present in the Ar gas feeder line to the sputter gun of the AES system. This is expected as the concentration of the impurity seems to be fairly constant with each sputter layer of the sample. However, the Auger analysis does confirm one thing, namely, there is no diffraction of Si from the substrate into the film, thus at least confirming the usefulness of the deposited film as a good buffer layer except for the presence of the impurities, which, are, however, not uncontrollable. The depth profile of the annealed sample (figure 3) indicates that the concentration of Ti is constant up to a certain thickness below the surface and then diminishes sharply. In contrast the concentration of Sr is almost uniform throughout the thickness of the film. This can be attributed to the simple fact that the e-beam was focused to a fine spot and that it was not swept across

the sample during deposition. Both these aspects tend to melt the material only in one spot, thus resulting in a non-stoichiometric vapour stream. Also, the local variation in the composition of the sintered pellet will be reflected in the composition variation in the final film deposited on the substrate. Further, the conditions of the e-beam used can result in partial fragmentation of the material with the high-vapour-pressure component evaporating favourably through the deposition time. However, such a situation seems to be favourable, as the initial Sr layer perhaps helps in inhibiting the outdiffusion of Si from the substrate. O is also seen to be present throughout the sample and is partially compensated by annealing. The results of the depth profiling an be approximated to a simple structure comprising of an initial layer of SrO_y and then one of Ti-deficient $SrTiO_3$ with the possible presence of some $SrTiO_3$. This leads us to conjecture that the e-beam evaporation results in the fragmentation of the pellet with Sr and/or SrO_y being predominantly evaporated. The fact that the film partly comprises stoichiometric $SrTiO_3$ is confirmed from the x-ray diffraction, which reveals a 211 peak corresponding to the dielectric. This is in agreement with the result obtained by other workers [11], who have deposited $SrTiO_3$ on Si using a focused e-beam and subsequently annealed the sample in O_2 at 800 °C.

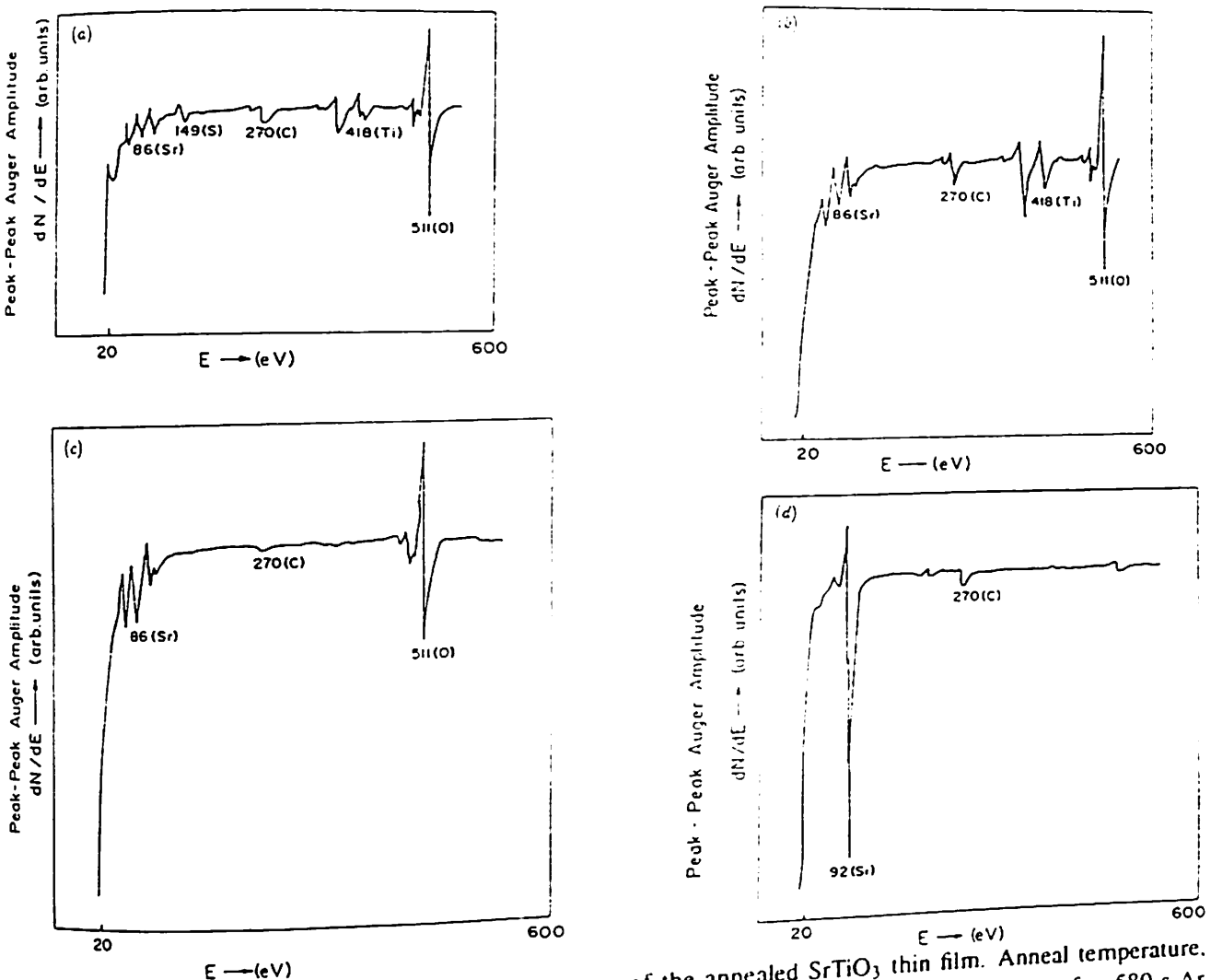

Figure 2. The Auger electron spectrum of the annealed $SrTiO_3$ thin film. Anneal temperature, 700 °C; 1 h in O_2. (*a*) Surface of the sample; (*b*) after 400 s Ar ion etching; (*c*) after 580 s Ar ion etching; (*d*) after 760 s Ar ion etching.

While this is only a preliminary study a detailed evaluation is being undertaken to assess the utility of the material in thin-film form in VLSI/ULSI technology and as a buffer layer in the synthesis of high-T_c films.

It has been shown that the $SrTiO_3$ films can be deposited successfully by direct e-beam evaporation of a sintered pellet of the ceramic. It has been seen by AES analysis

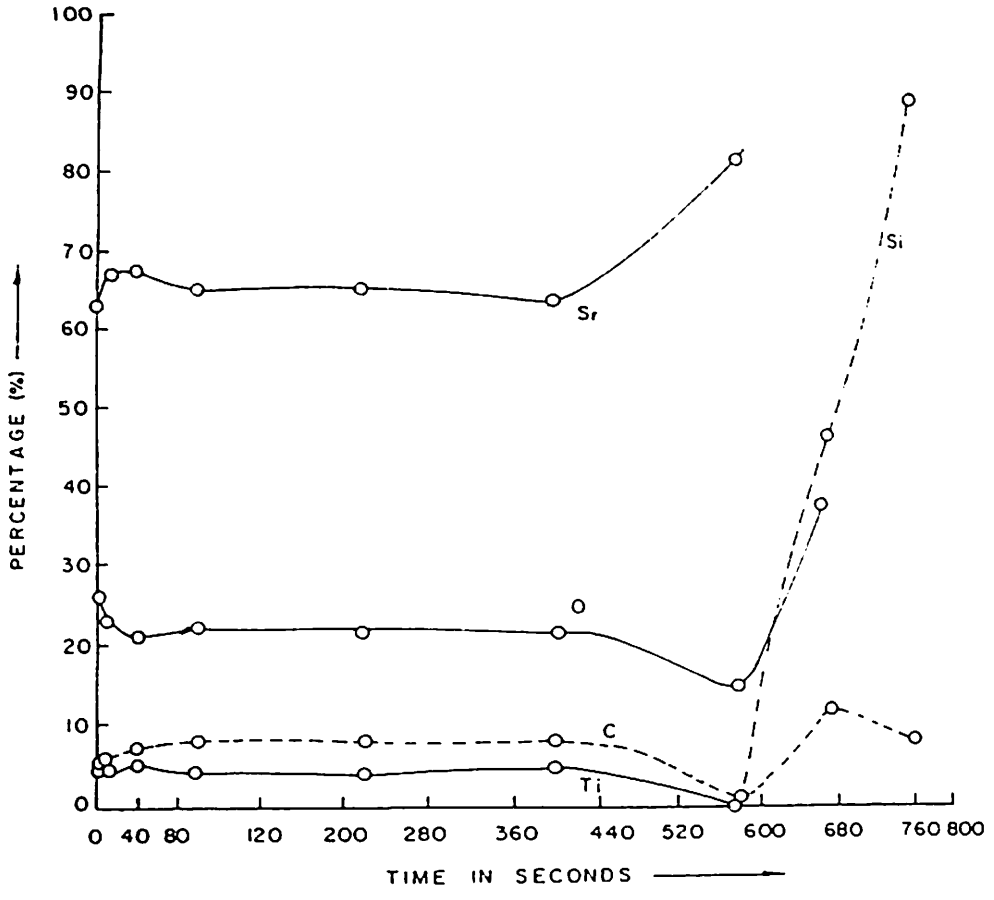

Figure 3. The percentage atomic concentration as a function of sputtering time (depth) of the annealed $SrTiO_3$ thin film on Si.

that the deposited films when subjected to high-temperature treatment do not contain Si thus confirming the integrity of the layer for use as a buffer for high-T_c thin-film synthesis. Detailed investigations are under way to study the system by high-energy nuclear techniques.

The authors are thankful to the Director of the National Physical Laboratory for his continuous encouragement to undertake this work. One of us (SKD) is thankful for the award of a senior research fellowship. Special thanks are also due to Dr J K N Sharma and his staff for taking the AES spectra.

References

[1] Bednorz J G and Muller K A 1986 *Z. Phys.* B **64** 189
[2] Buda J D, Chisorlin M F, Feenstra R, Lounds D H, Norton D P, Boatner L A and Christen D K 1991 *Appl. Phys. Lett.* **58** 2174
[3] Ushida T, Higashiyama K, Hirabayashi I and Tanaka S 1991 *Supercond. Sci. Technol.* **4** 445
[4] Kuhn M, Horn R, Klinger M and Hinkin J H 1991 *Supercond. Sci. Technol.* **4** 471
[5] Levy A, Fslk J P, Kastner M A, Gallagher W J, Gupta A and Kleinsassar A W 1991 *J. Appl. Phys.* **69** 4439
[6] Venkatesan T, Chase E Q, Wu X D, Inam A, Chang C C and Shokohi P K 1988 *Appl. Phys. Lett.* **53** 243
[7] Magero Campero A, Turner L G and Kendall K 1988 *Appl. Phys. Lett.* **53** 2566
[8] Chourasia A R, Chopra D R, Bensoula A and Ruzakowskim P 1992 *J. Vac. Sci. Technol.* A **10** 115
[9] Neung-Ho Cho, Seung-Hee Nam and Ho-O Kim 1992 *J. Vac. Sci. Technol.* A **10** 87
[10] Roy D, Peng C J and Krupanidhi S 1992 *Appl. Phys. Lett.* **60** 2478
[11] Moni H and Ishiwara H 1991 *Japan. J. Appl. Phys.* **30** L1415